Charles University in Prague
Faculty of Mathematics and Physics

**DOCTORAL THESIS**

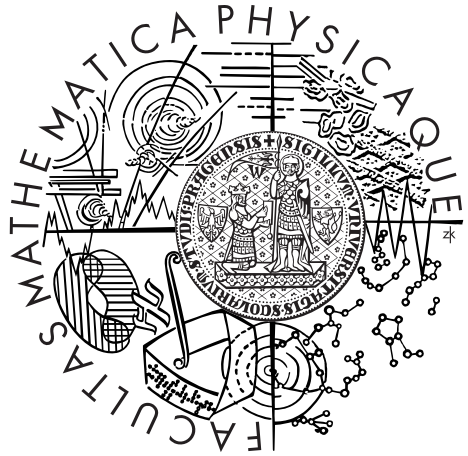


Jakub Seidl

# Anomalous diffusion of plasma in tokamak edge region

Institute of Theoretical Physics

Supervisor: Doc. Ing. Ladislav Krlín, DrSc.

Branch of study: Theoretical physics, astronomy and astrophysics

Prague 2012

## Acknowledgements

I would like to express my gratitude primarily to my supervisor, Dr. Ladislav Krlín, whose passion for the field is admirable and hardly can remain without reflections on the spirits of his co-workers. He provided me with many valuable discussions, especially on the topic of ion transport in turbulent plasmas presented in the last chapter. My great thanks go to Dr. Jan Horáček who introduced me very enthusiastically to the topics of probe measurements in tokamak edge and theory-experiment comparison. I am very grateful also to Dr. Anders Henry Nielsen from Technical University of Denmark for an access to ESEL code and for many very fruitful discussions on the topic of turbulence modelling. He was always well-minded and open for discussion. Also all other colleagues from IPP Prague deserve my thanks for all the inspiration they gave me. And at last, but not least, I believe that more than half of the credit for this work goes to my family whose support during last few years was exceptional. Thank you.

This work was partly supported by grants GAP205/11/2341, GAP205/10/2055, GAP205/12/2327, by MSMT Project # LM2011021 and the project SVV 261301 of the Charles University in Prague. The access to computing and storage facilities owned by parties and projects contributing to the National Grid Infrastructure MetaCentrum, provided under the programme "Projects of Large Infrastructure for Research, Development, and Innovations"(LM2010005) and to the CERIT-SC computing and storage facilities provided under the programme Center CERIT Scientific Cloud, part of the Operational Program Research and Development for Innovations, reg. no. CZ. 1.05/3.2.00/08.0144 is highly appreciated. Experimental data provided by Dr. Jan Horacek and used in Sec. 5.6 are highly appreciated.

Prohlašuji, že jsem tuto disertační práci vypracoval samostatně a výhradně s použitím citovaných pramenů, literatury a dalších odborných zdrojů.

Beru na vědomí, že se na moji práci vztahují práva a povinnosti vyplývající ze zákona č. 121/2000 Sb., autorského zákona v platném znění, zejména skutečnost, že Univerzita Karlova v Praze má právo na uzavření licenční smlouvy o užití této práce jako školního díla podle §60 odst. 1 autorského zákona.

V Praze dne 17.12.2012 Jakub Seidl

## Abstrakt

**Název práce:** Anomální difuze plazmatu z okrajové turbulentní oblasti tokamaku

**Autor:** Jakub Seidl

**Školící pracoviště:** Ústav fyziky plazmatu AV ČR, v.v.i.

**Vedoucí disertační práce:** Doc. Ing. Ladislav Krlín, DrSc., ÚFP AV ČR

**Konzultant:** RNDr. Radomír Pánek, Ph.D., ÚFP AV ČR

**Abstrakt:** Tato práce poskytuje stručný úvod do problematiky turbulence plazmatu v okrajové vrstvě tokamaku a diskutuje některé aspekty anomální difuze plazmatu v této oblasti. V rámci modelování turbulence generované výměnnou nestabilitou je s užitím kódu ESEL zkoumán vliv paralelního transportu, a to především charakteru paralelních proudů, na vlastnosti turbulentních struktur s přihlédnutím k možnostem experimentálního ověření. Na základě modelovaných charakteristik turbulence je pak diskutován vliv fluktuací na měření elektrostatických sond v okrajové vrstvě tokamaku v režimu vysoké srážkovosti. Srovnání modelu s měřením provedeným na tokamaku ASDEX Upgrade vysvětluje některé neočekávané výsledky experimentu, jako například přítomnost 'hrbu' ve frekvenčních spektrech potenciálu plazmatu. Dále je vysvětleno chování korelační funkce hustoty měřené na dvou prostorově separovaných Langmuirových sondách v oblasti magnetické separatrix a je poukázáno na nejednoznačnost metody měření vorticity plazmatu pomocí sady plovoucích Langmuirových sond. V závěrečné části je pak modelován transport těžších příměsí plazmatu v prostředí turbulentního elektrostatického potenciálu. V prostředí driftové turbulence je identifikována změna směru radiálního pohybu částic v závislosti na typu částice jako důsledek nestabilního pohybu těžších slabě ionizovaných částic v kladných potenciálových strukturách. Výsledky jsou srovnány s driftovým přiblížením zanedbávajícím Larmorův poloměr částic.

**Klíčová slova:** Tokamak, turbulence plazmatu, anomální difuze, elektrostatické sondy, výměnná nestabilita

## Abstract

**Title:** Anomalous diffusion of plasma in tokamak edge region

**Author:** Jakub Seidl

**Tutoring institution:** Institute of Plasma Physics AS CR, v.v.i.

**Supervisor:** Doc. Ing. Ladislav Krlín, DrSc., IPP AS CR

**Consultant:** RNDr. Radomír Pánek, Ph.D., IPP AS CR

**Abstract:** This work provides brief introduction to the topic of plasma turbulence in tokamak edge region and several aspects of anomalous plasma diffusion are discussed. We use numerical code ESEL to model interchange turbulence and investigate properties of turbulent structures in different regimes of parallel transport. Means of experimental verification of the results are discussed. Results of the modelling are then used to interpret unexpected results experimentally obtained by electrostatic ball-pen probes on tokamak ASDEX Upgrade, mainly appearance of a 'bump' in power spectra of measured plasma potential. Next, we explain behaviour of cross-correlation function of density signals measured by two spatially separated Langmuir probes in the vicinity of magnetic separatrix and we point out an ambiguity in interpretation of results of vorticity measurement made by set of floating Langmuir probes. In the last part, transport of plasma impurities by electrostatic turbulent potential is modelled. We identify reversal of radial particle velocity for particles with higher mass-to-charge ratio and explain it as a result of unstable particle trajectories on positive potential structures. The transport of particles with fully resolved cyclotron orbits is compared with drift approximation.

**Keywords:** Tokamak, plasma turbulence, anomalous diffusion, electrostatic probes, interchange instability

# Contents

# 1. Introduction

Nowadays, there is a high demand for development of new types of energy sources. This comes as a reaction on two fundamental limitations of conventional sources based on burning of fossil fuels, i.e. limited amount of fossil fuels accessible at reasonable cost and large amounts of carbon dioxide released by the process of burning into the atmosphere. Recently, especially the issue of carbon dioxide emissions and their impact on global climatic and biospherical changes were largely discussed. Even though this discussion is still far from being resolved, it is evident that energy production based on principles with reduced carbon cycle and not limited by availability of some 'rare' commodity are essential for a future energy production.

Currently exploited non-fossil sources of energy have issues of their own which limit their usability as a global substitute of fossil burning. As a result of crisis in Japan nuclear power plant Fukushima in 2011, discussion about future use of nuclear power plants has been raised again and they have been recently banned in several countries due to strong concerns about risks connected with leaks of radioactive or toxic material in case of any accident. On the other hand, renewable energy sources based on exploitation of energy of natural processes like wind, hydropower, sunlight, tides or geothermal heat, are often bound only to the (limited number of) places with favourable environment. Moreover, they may strongly interfere with the environment, alter (not only) surrounding landscape and biosphere and their power output is dependent on strength of the natural source, which may be fluctuating very strongly.

Nuclear fusion is an alternative concept of energy production which utilizes the fact that the nuclear binding energy of light atoms mostly strongly increases with their atomic number (see Fig. 2.1) and thus combining two lighter atoms into heavier one will release the spare energy. This is just opposite of nuclear fission, where the energy is released by splitting of heavy atoms. The main advantages of fusion process would be the large power-gain per mass of the fuel and abundance of the fuel (mainly deuterium, which forms cca. $0,015\%$ of hydrogen atoms in the see water). Compared to renewable sources, the power source would not be subject to any fluctuations and its safety compared to nuclear power plants would be significantly higher.

The idea of production of energy due to fusion reactions was first raised by Atkinson and Houtermans [7] in the twenties of the 20th century as an explanation of power production by the sun and at the beginning of 1930s first experimental fusion of two deuterium atoms with simultaneous release of energy was successfully accomplished. The interest in nuclear fusion strongly rose after the second world war when a military research focused on development of a hydrogen bomb. After its successful construction there was a strong optimism that the route to a civil utilisation of the fusion power will be of similar difficulty as in the case of atomic bombs and nuclear power plants (first controlled reaction made in 1942; first atomic bomb constructed in 1945; first civil nuclear power plant built in 1954). This optimism, however, was strongly exaggerated and even though the military research on this topic was declassified in 1958 and strong international cooperation

started, controlled nuclear fusion remains one of the biggest scientific and technological challenges today. After 50 years of research, construction of tokamak ITER, the first reactor that is expected to demonstrate energy production larger then its input power, started just recently in 2007.

In order to reach nuclear fusion, it is necessary to heat fuel to the temperatures of the order of $10^8$K ($10^4$ eV). At this temperature, the matter exists in an ionized state called plasma, consisting of separate ions and electrons. Since the individual plasma particles are charged, they are subjected to electromagnetic forces and it is possible to utilize electromagnetic field in order to influence plasma behaviour. This allowed A. Sacharovov and I. Tamm to design device (later called tokamak) capable of confining hot plasma in a toroidally shaped magnetic field. Tokamak concept became famous in 1968 when Russian tokamak T-3 reached record electron temperature of 1 keV. This record, even though disbelieved at first, triggered high interest of scientific community in the tokamak concept and for a long time suppressed development of other concepts. For more details of early history of tokamaks, see e.g. [136].

This work focuses on study of plasma behaviour in the edge region of tokamak device. Even though this region, with its relatively low plasma density and temperature, does not contribute to the fusion reactions themselves, it is crucial for future success of tokamaks in several ways. First, it is the region where plasma touches the first wall and therefore behaviour and conditions in the edge region may significantly influence plasma-wall interaction and wall degradation. This problem is most severe in the case when hot and dense plasma objects are present, as in the case of edge localized modes (ELMs) that spontaneously appear in some modes with improved confinement (H-mode, see chapter 2.4). Secondly, properties of the edge region naturally form boundary conditions for the central region and may very significantly improve or degrade plasma and energy confinement, if outward transport in the edge region is reduced or enhanced, respectively. Moreover, for any diagnostic, heating or fuelling system that wants to reach the core, it is necessary to penetrate the edge region first. Its properties then may influence functionality of the system.

At first, plasma edge transport was considered to be driven by collisional processes [70]. This led to overestimation of confinement time during the design of first devices and to significant underestimation of plasma losses, so called problem of anomalous diffusion. Search for explanation of high magnitude of observed outward transport was hot topic of nuclear fusion for a long time. In the last 15 years it was recognized and generally accepted that dominant role in transport processes in the edge region may be attributed to presence of turbulent structures in this region [88, 31]. The edge turbulence naturally arises as a consequence of magnetic configuration of the tokamak device and nonuniformity of the plasma. Then, coherent turbulent structures that are self-consitently formed may advect significant amounts of plasma density or energy outward. This work aims to contribute to the discussion of properties of the edge turbulence itself and properties of induced plasma transport, which are nowadays subjects of an intensive research.

This work is organized as follows. First, in chapter 2, principle of thermonuclear fusion is briefly explained and basic geometry and principle of tokamak is described. Experimental observations of turbulence in tokamak edge and its transport properties are summarized in chapter 3. Chapter 4 presents basics of theory of

plasma transport, with plasma treated either as single particles (section 4.1) or as a fluid (section 4.3). Section 4.4 discusses reduction of fluid equations introduced in previous chapter to 2D plane perpendicular to magnetic field. In chapter 5, we present results of our simulations with interchange fluid model ESEL and discuss properties of turbulence structures under different assumptions on transport along magnetic field lines. The results of ESEL simulations are used also in the chapter 6 to interpret and discuss several results obtained by experimental measurements using probe diagnostics. Finally, transport of individual particles (mainly plasma impurities) in the potential field generated by tokamak edge turbulence is studied in chapter 7. Each of the chapters 5, 6 and 7 firts contains brief introduction to its topic (Secs. 5.1, 6.1 and 7.1-7.4) followed by our results (Secs. 5.2-5.7, 6.2-6.5, 7.3 and 7.5-7.7).

# 2. Fusion basics and tokamak concept

## 2.1 Thermonuclear fusion

As was already mentioned in the introduction chapter, controlled thermonuclear fusion is one of the most promising candidates for future sustainable energy source. Compared to conventional power systems, the $CO_2$ emissions are in the optimistic case expected to be 100 times lower then in coal burning systems and about 2 times lower than in fission power plants [156], however with somewhat higher cost of energy (without assuming any carbon tax on a conventional sources, factor of 2 was estimated in [156]).

Similarly to the concept of nuclear power plants, concept of fusion facility is based on energy release caused by transmutation of atoms. Figure of nuclear binding energies per nucleon (Fig. 2.1) shows that up to the iron, the binding energy per nucleon in most cases increases with mass number, while for elements heavier then iron, it slowly drops down. This is a consequence of competition between short-ranged (exponentially decaying) strong binding force and electrostatic repulsion between positively charged protons in the nuclei. While nuclear fission utilizes the right part of the curve, where the energy is released by breaking heavy nucleus apart, the nuclear fusion is focused on the left part, where energy can be released by fusing two light nuclei into a heavier one. There are several nuclear reactions that could possibly be utilized, however when cross-section of the reaction together with its optimum temperature is taken into account, the deuterium-tritium reaction

$$ {}^{2}_{1}D + {}^{3}_{1}T \rightarrow {}^{4}_{2}He\,(3.5\text{MeV}) + {}^{1}_{0}n^{0}\,(14.1\text{MeV}) \tag{2.1} $$

comes out as the best candidate with the highest cross-section at the lowest temperature. Unfortunately, about 80% of the energy is released in the neutron part of the reaction. This is associated with problems with reduced lifetime and functionality of reactor materials and systems in the environment with high neutron fluxes, activation of the materials or demands on biological shielding. Moreover, tritium is a radioactive isotope which brings further problems with fuel retention in plasma-facing components (PFC) of the reactor. The retention of the tritium has not been thoroughly investigated so far, but it is expected to be similar to retention of deuterium [119]. High risk of tritium is in its chemical similarity to the hydrogen that allows its easy penetration into biological systems. Due to this concerns, even though the D-T reaction is reaction of the first choice at this point of research, there exist other candidates that will be probably taken into consideration (even though more difficult to ignite) after controlling D-T reaction is mastered. Another problem of D-T reaction is a relative rareness of the tritium isotope. To solve this issue, interaction of fusion neutrons with lithium in a special blanket is planned,

$$ {}^{1}_{0}n^{0} + {}^{6}_{3}Li \rightarrow {}^{4}_{2}He + {}^{3}_{1}T. \tag{2.2} $$

This process is refered to as tritium breeding and is expected to provide tritium self-sustainability for the reactor.

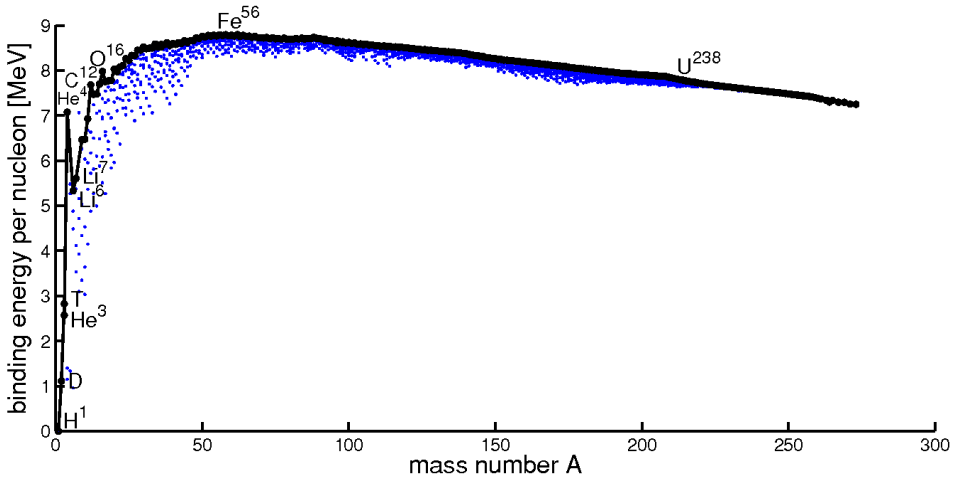


Figure 2.1: Binding energy per nucleon as a function of mass number $A$. Most common and most stable isotopes are marked with black solid line. Plotted data adopted from [9].

In order to ignite plasma, i.e. produce sufficient energy output from the fusion that will compensate all radiation losses and maintain the plasma temperature, criterion derived by Lawson [92] must be fulfilled. Nowadays, it is usually expressed as a condition in form of triple product that relates plasma density $n$, energy confinement time $\tau_E$ and central ion temperature $T$ for ignition of D-D reaction [154]

$$nT\tau_E \geq 3 \cdot 10^{21} \text{ keV} \cdot \text{s} \cdot \text{m}^{-3}. \tag{2.3}$$

There are different strategies how to maximize the Lawson's triple product. In inertial fusion, the confinement times are very small (pulse duration in order of nanoseconds) which must be compensated by increased density. On the other hand, magnetic confinement relies on confining rather low-density plasma ($n \approx 10^{20}$ m$^{-3}$) for the times in order of seconds at temperatures $T \approx 10^4$ eV. After more than half a century of research, there are several concepts of fusion devices, each in different state of development and struggling with different kinds of problems. To name the most common:

- **Laser fusion** is based on the concept of inertial confinement and relies on rapid compression and heating of a fuel to the fusion parameters as illustrated in Fig. 2.2. In laser fusion, as the outer layer of a small target is rapidly heated by high-energy laser beams, it expands outwards, compressing and heating the inner part of the fuel pellet due to reaction force. If the compression and heating is sufficiently strong, fusion reactions appear in the center, that further heat and ignite surrounding parts of the fuel pellet. No additional means of confinement are required, the fuel is confined fully by its inertia. The main difficulties of the inertial confinement come from the necessity to efficiently couple the laser light energy to the target and efficiently (adiabatically) compress the fuel. There are also strict requirements on the symmetry of the pellet and uniformity of the surface heating and if not fulfilled, Rayleigh-Taylor instabilities develop [8], diverting large part of the energy from the inward flux, thus preventing ignition in the central part.

Despite of these technical difficulties, inertial confinement is at present time one of the two most promising fusion concepts.

- In **Z-pinch** device, large electric current is driven in the plasma. This creates magnetic field that compresses the plasma due to the Lorentz force (illustrated in Fig. 2.2). Interestingly, history of Z-pinch goes down to the 1790, when first experiments with discharging high electric energy into a metal wire were made (see [61] and reference 12 therein). At the beginning of fusion research, Z-pinch concept was considered very promising. However, due to presence of strong magnetohydrodynamic (MHD) and Rayleigh-Taylor instabilities, the main focus was later shifted in favour of Z-pinch competitors. Nowadays, Z-pinch is, among other applications, investigated as a strong X-ray or neutron source.

- **Reversed field pinch** (RFP) is a pinch with axisymmetric toroidal configuration. The plasma is confined by poloidal magnetic field created by toroidal plasma current and by toroidal field created partly by plasma currents and partly by external magnetic field coils. The name comes from the fact, that the toroidal field reverses its direction near the plasma edge. In steady-state, the reversed configuration is maintained by a nonlinear dynamo effect. Compared to the tokamak concept, RFP does require much weaker toroidal magnetic field (comparable in magnitude to the poloidal field) and thus has smaller demands on power input and supporting infrastructure. On the other hand, complicated feedback system is needed to stabilize and control magnetohydrodynamic modes, whose non-linear dynamics is still not fully understood.

- **Tokamak** concept has currently the most developed physics basis among fusion devices with magnetic confinement [101]. It is a toroidal device, similarly to RFP, but with significantly larger toroidal field generated by external coils. This toroidal field largely improves the confinement, but on the other side significantly increases operational costs. Twist of magnetic field lines by poloidal component of the magnetic field, necessary to prevent drifting of plasma to the wall, is generated mainly by externally induced toroidal currents flowing in the plasma. Main toroidal current is in standard scenarios driven by transformer effect with plasma as a secondary transformer circuit. This limits tokamak operation to pulsed regime. Tokamak concept will be discussed in more detail in the following sections.

- **Stellarator**, in contrast to tokamaks, generates necessary twist of magnetic field lines by adjusting the externally imposed magnetic field. This requires very complicated geometry of magnetic field coils and brings difficulties with coils manufacturing and with diagnostics and theoretical description of stellarator plasma. On the other hand, this approach can avoid complexity of tokamak's current drive systems and allow, in principle, steady-state operation of the device.

Among others, also concept of hybrid reactors is nowadays intensively discussed. It is a middle-step between fusion and fission power plant. A fusion device,

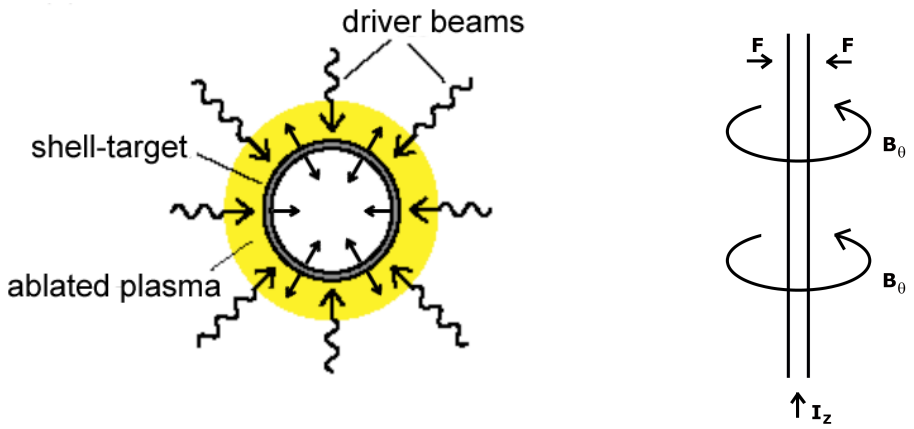


Figure 2.2: Left: Illustration of principle of target heating and compression in laser fusion. Right: Illustration of Z-pinch principle.

that does not have sufficient fusion energy gain factor $Q$, is coupled to a conventional fission reactor and serves as a source of neutrons. Then, it is possible to maintain fission reaction with only subcritical amount of fission material, thus increasing control over the reaction and eliminating the risk of uncontrolled chain reaction.

Size of the device with magnetic confinement is limited from the bottom by many factors, such as confinement and stability of the plasma, ratio of tritium breeding or neutron shielding [101]. At present time, the world largest tokamak, ITER [1], is under construction in France by a consortium of seven countries. It is assumed that it will be the first tokamak capable of achieving fusion power $P_{fusion}$ higher then power $P_{in}$ required to keep a steady-state plasma, with fusion energy gain factor $Q = P_{fusion}/P_{in} \approx 10$. Even when this goal is achieved, another facilities will be needed before a commercial fusion power plant becomes available. High energy gain factor $Q$ is a first step only and future devices will have to achieve engineering efficiency $Q_{eng} > 1$, which takes into account efficiency of all systems involved in the power plant. The most important goals of post-ITER facilities will be to demonstrate all the technologies and their economical competitiveness, scalability and operability on large scales ([101] and references therein).

## 2.2 Principle of tokamak

The name 'tokamak' originates in Russian. It is an abbreviation of 'toroidalnaya kamera i magnitnaya katushka', which means 'toroidal vessel with magnetic winding'. Obviously, the name itself describes basic construction scheme of the tokamak illustrated in Fig. 2.3. It is a ring-shaped vacuum vessel (torus) with D-shaped or circular (older tokamaks) cross section. In order to maintain the fusion process, plasma particles must be confined in the central part of the vessel, otherwise the plasma would quickly cool down and loose its density by contact with walls. For this purpose, the vessel is surrounded by several systems of magnetic

[1] http://www.iter.org/

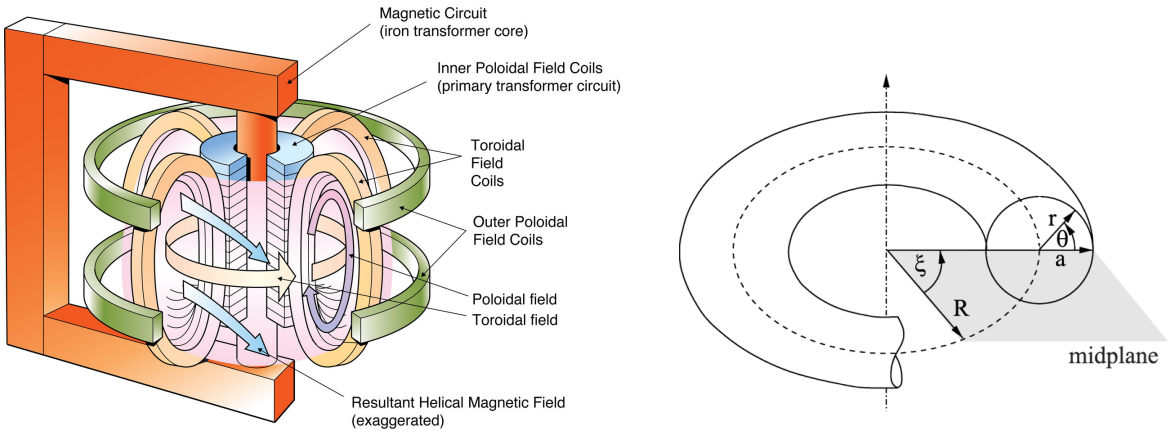


Figure 2.3: Left: Illustration of tokamak scheme. Right: Illustration of toroidal coordinates $r, \theta, \xi$ on a torus with major radius $R$ and minor radius $a$.

coils that create required magnetic field which keeps the plasma confined inside the vessel.

Charged particles in a strong magnetic field are forced to move mainly along magnetic field lines. Therefore, the strong toroidal magnetic field (in orders of $\approx 1$ T) created by toroidal field coils is the primary means of confining plasma particles. The field described in toroidal coordinates (see Fig. 2.3) is

$$B = \frac{B_0 R}{R + r\cos\theta} \tag{2.4}$$

with on-axis field $B_0$. This field itself, however, is not sufficient for long-term plasma confinement, because purely toroidal closed field lines circulating the torus result in curvature and $\vec{\nabla}B$-drifts (4.21) on the plasma particles. The drifts are charge dependent and the ions and electrons become verticaly separated, creating vertical electric field that moves the plasma by $\vec{E} \times \vec{B}$ drift (4.13) outwards.

This issue was solved by introducing poloidal component of the magnetic field. This field twists the field lines into helical field, consequently (in common case) forming structure of nested magnetic surfaces. Every field line then can be found moving along the surface of corresponding magnetic surface. In this configuration, the force due to magnetic field curvature on a particle passing along field line changes sign as the field line appears below or above the magnetic axis. As a result, plasma electrons and ions do not separate and do not create the unfavourable vertical electric field. This compensation mechanism, however, does not work in a boundary region with open field lines and drive due to magnetic field curvature is an important part of transport processes in this region, as will be shown in Chap. 5.

The poloidal magnetic field is created partly by external poloidal field coils and partly by toroidal plasma current inside the vessel. The current is driven by transformer effect with plasma as a secondary circuit and primary winding in form of solenoid going through the torus center. On top of that, there are also other magnetic systems responsible e.g. for plasma shaping or position feedback.

Tokamak vessel possess azimuthal symmetry and can be conveniently described by toroidal coordinate system shown in Fig. 2.3. To reflect dependence of magnetic

field on radial position (2.4), part of the poloidal cross-section with $-\pi/2 < \theta < \pi_2$ is often referred as low-field side (LFS), the rest of the cross section as high-field side (HFS). Sometimes, terms inboard and outboard are used instead. Size of a tokamak is usually described in the toroidal coordinates by its major radius $R$ and minor radius $a$. Both radii may vary by an order between different tokamaks. Major radius of nowadays operated tokamaks ranges from several decimetres (e.g. GOLEM tokamak $R = 0.4$ m) to several meters (JET with $R = 2.96$ m) and minor radius $a$ from several centimetres (GOLEM with $a = 0.06$ m) to several meters (JET with $a_V = 2.1$ m in vertical direction and $a_H = 1.25$ m in horizontal direction). Size of ITER tokamak that is currently under construction is planned to be $R = 6.2$ m and $a_H = 2$ m.

## 2.3 Tokamak boundary

In the tokamak boundary region, magnetic field lines, in contrast to the central part, are not closed. Instead, on both ends they are connected to material parts of the tokamak. This region is referred to as scrape-off layer (SOL). SOL is located next to the region of closed field-lines and both regions are separated by last closed flux surface (LCFS) - (magnetic) separatrix. There are two main types of tokamak plasma, divided by the means how the SOL is created.

- In **limited plasma** the separatrix on some toroidal position directly touches a material surface (limiter, see Fig. 2.4). The limiter penetrates through all magnetic surfaces outside the separatrix and therefore magnetic field lines outward the separatrix are open, connected to the limiter, or to some other material surface. Plasma that gets into the SOL quickly hits the limiter and the region is effectively 'scraped-off'. Even though some tokamaks still use this configuration, it is unfavourable for several reasons. Since the limiter and confined plasma are in direct contact, impurities and neutrals released by plasma-wall interaction can easily penetrate through the separatrix. Moreover, the limiter is exposed to high heat fluxes, which further amplify the impurity release.

- In **diverted plasma** the separatrix does not get into contact with material surfaces. Instead, by applying external poloidal magnetic field with direction opposite to the poloidal component of magnetic field inside the vessel, an X-point (sometimes more than one) is created (Fig 2.4). X-point prevents contact of the main plasma with the walls and localizes most of the plasma-wall interaction into a divertor region, where the divertor tiles are carefully designed to withstand high heat fluxes. This configuration allows tokamak to reach higher energies stored in the central plasma, compared to limited plasma, without a risk of damaging the plasma facing components.

  The divertor tiles can be localized far from the main plasma, which limits core contamination by impurities released due to sputtering process during plasma-wall interaction and localizes neutral recycling processes mainly into a divertor region.

Both cases are schematically depicted in Fig. 2.4.

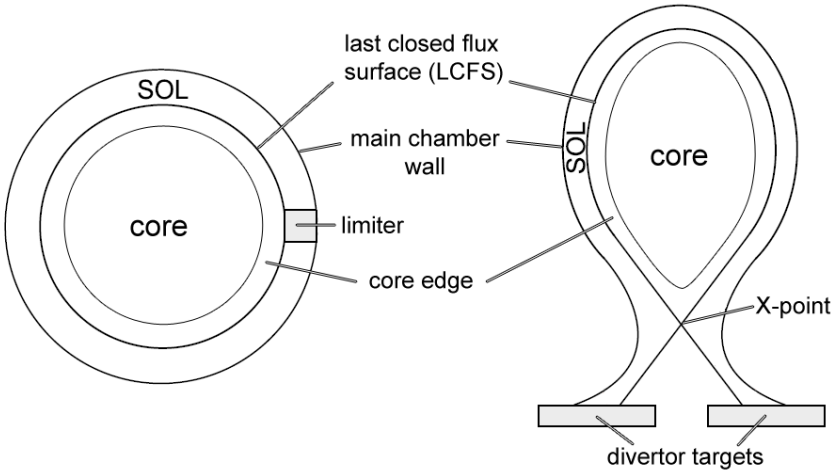


Figure 2.4: Sketch showing limiter (left) and divertor (right) configuration in the poloidal cross-section.

Definition of the term plasma edge in the literature is somewhat unclear. In some cases it denotes only region of closed field lines in the vicinity of separatrix (core edge in Fig. 2.4), in other cases its meaning includes also region of open field lines (SOL and wall-shadow region). In this work, plasma edge or edge plasma will denote core edge together with SOL and wall-shadow, while edge region will denote core edge only.

## 2.4 L-mode and H-mode

In 1982, H-mode [6], a new high-confinement mode, was discovered on tokamak ASDEX. In this mode the energy confinement time is strongly improved compared to what is measured in the standard low-confinement mode (L-mode). This is caused by reduction of effective heat and particle diffusivity at the plasma edge. A strong shear of poloidal plasma rotation is observed near the LCFS [57] and it is generally believed that it results in creation of edge transport barrier by decorrelating turbulence structures and thus strongly suppressing the turbulent transport. In H-mode, in the inner vicinity of LCFS a region of high radial pressure gradient called pedestal is formed (see Fig. 2.5). The pedestal is supported by the edge transport barrier that suppresses radial turbulent transport and prevents transition back to L-mode profiles. The pedestal is, however, not stable in typical H-mode conditions and it periodically collapses due to peeling-ballooning MHD instability generating large convective structures, ELMs (edge localized modes) [154, 142]. ELMs can carry very large heat fluxes and quickly erode material surfaces inside tokamak. The question of ELM mitigation is therefore one of the most intensively studied questions in the field today.

The spontaneous transition from L-mode to H-mode (L-H transition) occurs only with sufficient plasma heating power and even after 40 years of intensive study, its mechanism is still not understood. It is likely that coupling of different turbulent modes may play an important role in the formation of the H-mode barrier [40] which motivates study of edge turbulence in L-mode, even though the main

operating regime of future tokamaks will be H-mode or some more advance mode.

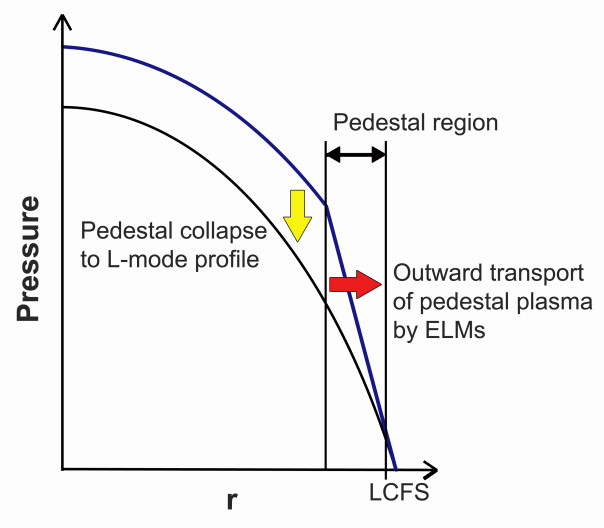


Figure 2.5: Schematic illustration of radial pressure profile in pedestal and its collapse associated with appearance of ELMs.

## 2.5 Plasma-wall interaction

When plasma particles hit solid surface, several physical processes can occur [154]. To name the most important, plasma particles may be neutralized and trapped inside the solid material, possibly undergoing chemical reaction. They may also knock atoms out of the solid into the plasma or be scattered back themselves.

During physical sputtering, incident plasma particles knock atoms of the solid material out into the plasma. The released particles become ionized in the plasma and their species form a new fraction of the plasma. Atomic mass of released particles is typically significantly larger than that of the ions of main plasma. Divertor tiles are usually made of carbon, beryllium or wolfram compounds, but plasma impurities may be composed from virtually any particle species present in any plasma facing component (PFC) such as first wall, diagnostics, etc., or in the air trapped in cavities of PFC material. The rate of physical sputtering differs between materials as shown in Fig. 2.6. The yield of the process is dependent mainly on the mass and energy of incident ions and the sputtering may, with some probability, occur any time plasma particle hits the solid. Particles of the solid are sputtered by momentum transfer from incident particles and therefore the sputtering process induced by plasma electrons may be neglected compared to that induced by plasma ions. Larger fraction of heavy plasma impurities scattered from PFC and incidenting back on the same material surface could even lead to uncontrolled sputter erosion of the material [120, 146].

Plasma particles incidenting on the PFC may chemically react and become chemically bound to the solid material. This process has typically very low energy threshold [120] and is relevant especially for carbon PFC, because carbon is highly chemically active with hydrogen isotopes of the main plasma. This leads to tritium

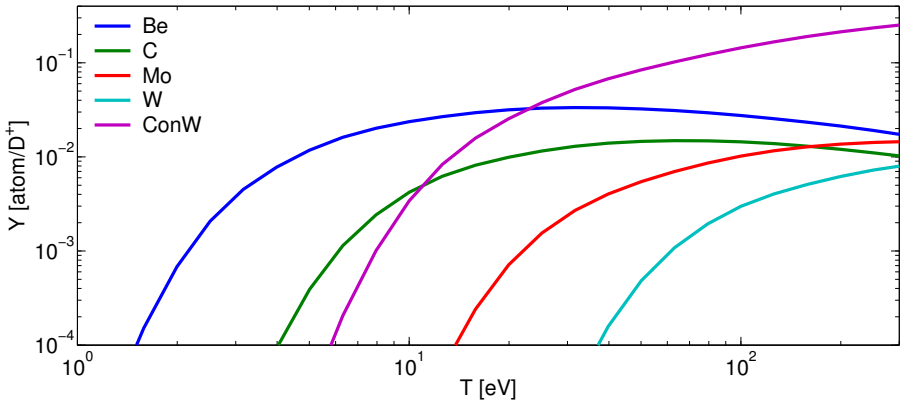


Figure 2.6: Dependence of physical sputtering yield of different materials on temperature of incident plasma ions. Data adopted from [120].

retention by chemical reaction with the eroded carbon, which is one of the negative aspects of current tokamak design, as mentioned earlier.

Part of the incident ion flux is neutralized and scattered back into the plasma. In the plasma, the neutral atoms are gradually ionized by collisions with plasma particles and increase local plasma density by process called recycling. Especially in diverted plasma recycling process may form dense cloud of neutrals in the vicinity of divertor tiles and largely increase local plasma density. This leads to divertor detachment from the SOL plasma, reducing heat load on the divertor tiles and having consequences on properties of turbulent transport in the SOL as will be shown in Secs. 4.4.4 and 4.4.5.

Note that plasma-wall interaction processes are non-linear functions of plasma ion energy and therefore it is not sufficient to estimate wall erosion, recycling and impurity release on the basis of mean plasma temperature near the solid surface. Fluctuations of the turbulent plasma may be intermittent and small fraction of events (e.g. ELMs in H-mode) may be responsible for majority of surface-interaction processes.

## 2.6 Plasma impurities

Impurities of the main hydrogen plasma may be released from solid surfaces by plasma-wall interaction, intentionally as a part of spectroscopic diagnostics, a part of an experiment or as a product of fusion reactions (helium ash). Their presence increases complexity of the edge plasma by atomic processes and their impact on plasma parameters may be both positive and negative.

Historically the most severe problem was cooling of the main plasma by impurity radiation that in first tokamaks formed the main source of energy losses [154, 146]. The radiation depends strongly on atomic mass $Z$, being lower for lower $Z$ species. The low-$Z$ impurities are fully ionized for temperatures around 1 keV and hence they contribute only by bremsstrahlung radiation. On the other hand, high-$Z$ impurities retain part of the electrons and their line radiation largely increases the total radiated power. It is therefore beneficial to use low-$Z$ materials for PFC and materials based on carbon are often used for that purpose. Unfortu-

nately, not all effects of using low-$Z$ impurities are beneficial and e.g. radiation of not-fully ionized low-$Z$ impurities in the edge, when localized poloidally or at $q = 2$ rational surface, may destabilize the plasma and cause density limit disruptions [146].

On the contrary, volumetric power-loss caused by impurities may have beneficial consequences when located in the SOL, because it spreads out part of the energy of usually highly localized plasma-wall interaction events. This lowers requirements on the parameters of PFC material and increases their lifetime.

Presence of impurities in the core leads to fuel dilution. Since the total plasma pressure summed over all plasma species is limited by MHD instabilities ($\beta$-limit [154]), electrons released by the impurities together with impurity ions themselves may occupy a major fraction of the allowable pressure, hence limiting amount of fuel that can be contained in the plasma.

In the first approximation, impurities at given radius are quickly homogenized over poloidal and toroidal directions by rapid parallel transport and transport of impurities from their source into the core plasma is often treated as 1D problem described by cross-field diffusion coefficient $D_\perp$ and pinch velocity $v_{pinch}$ [146]:

$$-\Gamma_{\perp,imp} = D_\perp \frac{\partial}{\partial r} n_{imp} + v_{pinch} n_{imp}. \tag{2.5}$$

The transport equation is not directly related to any physical diffusive or convective process and measured values of transport coefficients $D_\perp$ and $v_{pinch}$ are anomalous (see Sec. 3 for explanation), $D_{\perp,imp} \approx 1\ \mathrm{m^2 s^{-1}}$ and $v_{pinch,imp} \approx 10\ \mathrm{ms^{-1}}$. It describes the overall rate of transport only, regardless of the real transport mechanism. In Chap. 7 we will investigate movement of plasma impurities in the potential field of edge turbulence and discuss role of the turbulence in impurity transport process.

# 3. Anomalous plasma transport in tokamak edge

## 3.1 Collisional, neoclassical and Bohm diffusion

At the beginning of fusion research, it was assumed that transport in the tokamak edge is dominated by collisional processes [70]. Collisional transport of plasma can be described by diffusion equation resulting in radial density flux $\Gamma_n$ given by Fick's law [30]

$$\Gamma_n = -D_n^c \frac{\partial}{\partial r} n \tag{3.1}$$

with coefficient of perpendicular particle diffusion due to Coulomb collisions and ambipolar effects [19]

$$D_n^c = (1 + \frac{T_i}{T_e}) r_{L,e}^2 \nu_{ei} \tag{3.2}$$

where $T_i$ and $T_e$ are ion and electron temperature, respectively, $r_{L,e}$ is electron cyclotron radius. Transport of heat and momentum may be described similarly by momentum diffusion coefficient $D_\mu^c$ and ion $D_{\chi,i}^c$ and electron $D_{\chi,e}^c$ heat diffusivity [19]:

$$D_\mu^c \approx \frac{3}{8} D_{\chi,i}^c \tag{3.3}$$

$$D_{\chi,i}^c = 2 r_{L,i}^2 \nu_{ii} \tag{3.4}$$

$$D_{\chi,e}^c = 4.66 r_{L,e}^2 \nu_{ee}. \tag{3.5}$$

Characteristic spatial scale of the diffusion process at temperature $T_j$ is given by Larmor radius $r_{L,j}$ of electrons ($j = e$) or ions ($j = i$) with charge $q_j$ and mass $m_j$,

$$r_{L,j} = \frac{\sqrt{e T_j m_j}}{q_j B}. \tag{3.6}$$

The time scale is represented by frequency of collisions between electrons, $\nu_{ee}$, electrons and ions, $\nu_{ei}$ and between ions, $\nu_{ii}$, [19]

$$\nu_{ei} = Z\sqrt{2}\nu_{ee} = \frac{\sqrt{2} Z n_e e^4 \ln\Lambda}{12\pi^{3/2} \epsilon_0^2 m_e^{1/2} T_e^{3/2}} \tag{3.7}$$

$$\nu_{ii} = \left(\frac{m_e}{2m_i}\right)^{1/2} \left(\frac{T_e}{T_i}\right)^{3/2} \nu_{ei} \tag{3.8}$$

where $e$ and $m_e$ are charge and mass of plasma electrons, $Ze$ and $m_i$ are charge and mass of plasma ions, $n_j$, $T_j$ are density and temperature of each species, $\epsilon_0$ is vacuum permittivity and $\ln\Lambda$ is Coulomb logarithm.

For typical values of density and temperature in tokamak edge, $n \approx 10^{19}$ m$^{-3}$ and $T \approx 100$ eV, the value of classical collisional diffusion coefficient is in the order of $D_n \approx 10^{-4}$ m$^2 \cdot$ s$^{-1}$ and for deuterium plasma $D_\mu/D_n \approx 25$, $D_{\chi,i}/D_n \approx 60$ and $D_{\chi,e}/D_n \approx 2.5$ [39]. These all are very small values that led to large

expectations during design of first fusion devices. Moreover, Eqs. (3.2-3.5) scale as $1/B^2$, predicting large impact of strength of magnetic field on plasma confinement. Unfortunately, it was very soon observed that experimentally measured cross-field particle diffusion coefficient $D_{n,exp}$ is significantly larger, with values in the order of 1 $\mathrm{m}^2 \cdot \mathrm{s}^{-1}$ [26]. Behaviour of $D_{n,exp}$ on many magnetic confinement devices was observed to fulfil semi-empirical relation [30, 154]

$$D_{n,exp} \approx \frac{1}{16}\frac{T_e}{eB} \equiv D_B \tag{3.9}$$

where $D_B$ is called Bohm diffusion coefficient. Contrary to the collisional diffusion (3.2), $D_B$ increases with $T_e$ which is clearly unfavourable for achieving fusion plasma parameters. Moreover, since $D_B \sim 1/B$, scaling of confinement time in real devices is much weaker then predicted from collisional theory and this brings significant difficulties in achieving parameters of plasma necessary for fusion reaction. Physical mechanism responsible for observed values of $D_{n,exp}$ remained unexplained for a long time and it was often referred as a problem of anomalous diffusion. Nowadays, radial transport induced by presence of convective turbulence structures is generally recognized as a mechanism that can enhance effective radial diffusion to the experimentally observed levels [88, 31].

In tokamaks, classical cross-field diffusion described by Eqs. (3.2-3.5) may become enhanced by effects of toroidicity of the device. This is referred to as neoclassical diffusion and neoclassical effects may dominate by one or two orders over classical Coulomb collisions [67] (even though still being significantly smaller than observed Bohm diffusion). For the case of low collisionality, important contribution to the radial transport may come from particles that are trapped by mirror effect due to change of $|B|$ along magnetic field line. Such particles are oscillating in so called bannana orbits. Distribution of trapped and untrapped particles may significantly differ and the resulting anisotropy of pressure tensor drives net outward flux [67]. Estimate of neoclassical diffusion coefficient in this regime is given by effective collisional frequency of trapped particles $\nu'$ (which is larger then collisional frequency of untrapped particles $\nu$, $\nu' \sim \nu R/r$), radial width of the banana orbits $\Delta r \sim q r_{L,e}/\sqrt{r/R}$ and fraction of particles that are trapped $N_{tr} \sim \sqrt{r/R}$ [154]

$$D_{nc,bannana} \sim N_{tr}\nu'(\Delta r)^2 \sim q^2 \nu (r/R)^{-3/2} r_{L,e}^2. \tag{3.10}$$

For sufficiently collisional plasmas ($\nu > 1$) such anisotropy is destroyed by collisions forcing particles to skip from/into trapped mode frequently. On the other hand, parallel mean-free path in collisional plasma is short, allowing presence of non-negligible parallel pressure gradient. The source of this gradient is build-up of charge, particles and pressure due to non-divergence-free part of diamagnetic flux. Such parallel pressure gradient naturally drives return parallel flows and currents known as Pfirsch-Schlüter (PS) flows (currents) [146]. In highly collisional regime parallel friction of these flows induces radial fluxes in the direction of major radius [146, 67]. Note that in cylindrical geometry the diamagnetic flux would be divergence-free and there would be no drive for radial transport of this type. Net flux averaged over the whole flux surface can be in the lowest order written in

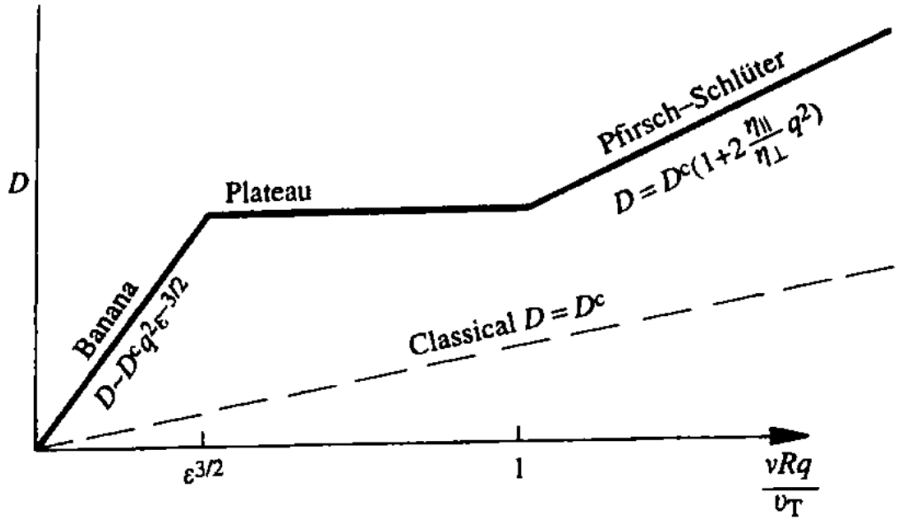


Figure 3.1: Dependence of diffusion coefficient $D_n$ on collision frequency $\nu$. $\epsilon$ is inverse aspect ratio of relevant magnetic surface $\epsilon = r/R$ and $v_T$ is thermal velocity. [154].

diffusive form (3.1) with diffusion coefficients [67, 68]

$$
\begin{aligned}
D_n &= D_n^c + D_n^{nc} \approx (1 + 1.3q^2) D_n^c && (3.11)\\
D_\mu &= D_\mu^c + D_\mu^{nc} \approx (1 + 1.6q^2) D_\mu^c && (3.12)\\
D_{\chi,i} &= D_{\chi,i}^c + D_{\chi,i}^{nc} \approx (1 + 1.3q^2) D_{\chi,i}^c && (3.13)\\
D_{\chi,e} &= D_{\chi,e}^c + D_{\chi,e}^{nc} \approx (1 + 1.6q^2) D_{\chi,e}^c && (3.14)
\end{aligned}
$$

where subscripts $c$ and $nc$ denote classical and neoclassical diffusion coefficient, respectively, and $q$ is safety-factor.

For collisionality in middle range between banana and PS regime, $(r/R)^{3/2} < \nu < 1$, the collisional transport is dominated by particles with small parallel velocity and diffusion coefficient stays roughly constant [154]. The resulting scaling of diffusion coefficient with collisionality is schematically depicted in Fig. 3.1.

We should note that expressions (3.11-3.14) were derived on the basis of assumption of closed field lines (averaging over flux surfaces was performed) and should not be directly aplicated on situation in SOL with open field lines because of two main effects [39]. On one side, the radial flux induced by (PS) flows is poloidally dependent, stronger in low-field side then on high-field side. Therefore, when flux surface averaging is not possible, local value should be used. On the other hand, open field lines present local sinks for plasma and act against build-up of charge, density and pressure caused by compressibility of diamagnetic flux that drives the PS flows. Authors of [39] therefore argue that in the vicinity of low-field side midplane the two mechanisms compensate each other and standard neoclassical diffusion coefficients (3.11-3.14) can be used.

## 3.2 Langmuir probes

The most common and the simplest diagnostics for measurement of fluctuations and transport of edge plasma is electrostatic Langmuir probe - simple electrical sensor located inside the plasma. The spatial resolution of the sensor given by its size is often $\approx$ 1 mm, with temporal resolution up to the order of MHz. In some configurations, the time resolution may be, however, limited by capacitive effects of the electronics [72, 73]. This makes Langmuir probe ideal for diagnostics of rapid transport events associated with plasma turbulence. Unfortunately, direct presence of the probe inside the plasma limits its applicability to the edge region only and if located deeper in the main plasma, the probe may get damaged by large heat fluxes. Means of save probe penetration deeper into the plasma are still subject of a research [75]. Also interpretation of measured quantities is not fully straightforward, as we will discuss in the following paragraphs.

When voltage is applied on the probe, measured current scales with local electron temperature $T_e$, density $n$ and plasma potential $\phi$ as [77, 100, 145]

$$I = I_s^+(n, T_e)\left(1 - e^{(V - V_{fl}(T_e,\phi))/T_e}\right) \tag{3.15}$$

where $I_s^+$ and $V_{fl}$ is ion saturation current and floating potential, respectively. Relation (3.15) is referred as I-V characteristics of the probe and it is a consequence of formation of sheath layer at the boundary of plasma and solid materials. Mobility of electrons along magnetic field lines is higher than that of ions and more electrons than ions are lost to the wall. This leaves plasma with positive potential compared to the wall and the electric field limits number of electrons that can enter the area. Due to Debye shielding in the plasma [30, 154], the potential drop is restricted mainly to the distance of several Debye lengths from the material surface, to the layer called sheath. The Debye length $\lambda_D$ is defined as

$$\lambda_D = \sqrt{\frac{\epsilon_0 T_e}{ne^2}} \tag{3.16}$$

where $\epsilon_0$ is permittivity of vacuum.

$I_s^+$ is the maximum positive current (due to ions) that can reach the wall. As Eq. (3.15) shows, it is measured for large negative biasing potential $V$. The maximum ion current is basically proportional to plasma density $n$, ion charge $Z_i$ and to ion sound speed $c_s$ [146],

$$I_s^+ = AeZ_i n c_s \tag{3.17}$$

$$c_s = \sqrt{\frac{T_e + Z_i T_i}{m_i}} \tag{3.18}$$

where $A$ is a factor describing influence of probe surface area and effects of ion acceleration to the sheath, $T_i$ is ion temperature and $m_i$ ion mass.

Measured value of $I_s^+$ is usually used for determination of $n$. In this case local (fluctuating) values of $T_e$ and $T_i$ should be known. However, to obtain $T_e$ and especially $T_i$ fluctuations with Langmuir probe is very problematic. Therefore $c_s$ is often replaced by its value $\bar{c}_s$ based on mean temperature and either fixed value of ion temperature itself $T_i \approx$ const. or fixed value of $T_e/T_i \approx$ const. is assumed. This, indeed, brings underestimation of density fluctuations in the places with

large temperature fluctuations and their overestimation in the places where the fluctuations are small. Moreover, factor $A$ may be dependent on $T_i$ [145] which brings another source of error, estimated in [72] for conditions of TCV tokamak by a factor $A(T_i)/A(T_i = 0) \approx 2$.

Similarly to the situation with $I_s^+$, the current measured by the probe saturates at some minimum value $I_s^-$ when sufficiently large positive bias voltage $V$ is applied. This effect is not described by simplified model (3.15) and more complicated expression is needed to describe the full I-V characteristics. Note that due to larger mobility of electrons it usually holds that $I_s^- \gg I_s^+$. Information obtained from the electron saturated part of I-V characteristic is rarely used in the measurements of tokamak edge plasma and we will therefore stick with model (3.15) and in the rest of the work we will neglect any influence of saturation of electron current.

$V_{fl}$ describes potential on the solid surface without external biasing that is related to the plasma potential as

$$V_{fl} = \phi - \alpha T_e. \tag{3.19}$$

Term $\alpha T_e$ describes height of the potential drop in the sheath caused by high mobility of electrons that are quickly lost to the surface, leaving plasma biased positively [146],

$$\alpha = \frac{1}{2} \ln \left( \frac{1}{2\pi} \frac{m_i}{m_e} \frac{T_e}{T_i + T_e} \right). \tag{3.20}$$

Typical value of $\alpha$ in tokamak edge plasma is $\alpha \approx 2.5 - 3$.

Both quantities $I_s^+$ and $V_{fl}$ (or all three quantities $n$, $T_e$, $\phi$) can be simultaneously obtained from fit of the whole I-V characteristics (3.15) measured by sweeping probe that periodically changes biasing potential $V$ applied on the probe, thus scanning over the whole range of I-V characteristics. Another option is to use separate probes that are either negatively biased (for $I_s^+$) or electrically floating (for $V_{fl}$). The sweeping technique allows measurement of plasma density, temperature and potential simultaneously at the same place at the price of worse temporal resolution. This is due to the fact that measurement over many values of biasing potential has to be made before single value of $n$, $T_e$ and $\phi$ is obtained. The measurement with several separate probes fast measurements of $I_s^+$ and $V_{fl}$, but estimation of $n$ and $\phi$ has to be based on previously stated assumptions on $T_e$ and $T_i$ behaviour. Moreover, such simultaneous measurement of $I_s^+$ and $V_{fl}$ is not spatially localised which brings complications in interpretation of the data by physical models. There exist several other, non-perturbing, diagnostic techniques capable of measuring edge plasma properties (see e.g. [145, 146]), however Langmuir probes are still the most often used due to their small spatio-temporal resolution. Cross-comparison of different diagnostics shows that density measurement by Langmuir probes agrees with other diagnostics well, up to the factor of 2 [146].

## 3.3 Experimental observations of edge plasma fluctuations

Since the first measurements in tokamaks, large fluctuations of plasma density in tokamak edge have been observed. The relative density fluctuation level $\sigma_n/\langle n \rangle$ in

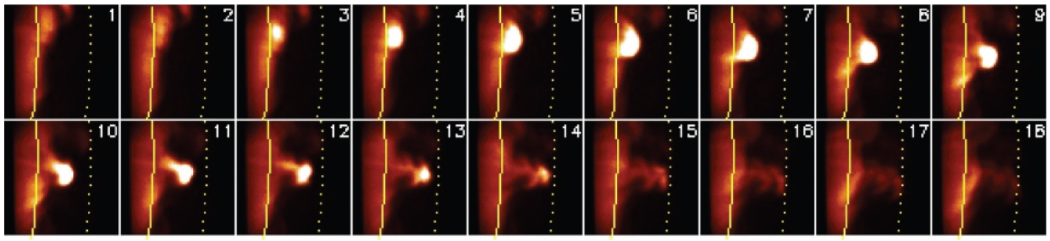


Figure 3.2: Gass-puff imaging of turbulence structure propagation located at outboard midplane of NSTX tokamak in H-mode. Time delay between frames is 7.5$\mu$s, size of each frame is 24 × 24 cm. The image represents part of radial-poloidal plane, white vertical lines show position of the LCFS. Reproduced from [97].

SOL in L-mode (see Chap. 2.4) is typically observed in range $0.3 - 0.6$, increasing with distance from LCFS and often reaching values $\sigma_n/\langle n\rangle \approx 1$ at the most outward positions [26, 56, 18, 74]. These fluctuations are highly correlated with radial velocity $v_r$ and probability distribution function (PDF) of radial particle flux $\Gamma_n = nv_r$ is not Gaussian, exhibiting long intermittent tail as shown in Fig. 3.3. It shows that in the SOL, large fraction of the total radial plasma outflux is caused by small fraction of transport events. The long-tailed shape of PDF of density fluctuations is surprisingly universal for different magnetic confinement devices [31] indicating robust mechanism of radial plasma losses. Fluctuations of floating potential are observed with comparable amplitude and approximately $\pi/2$ phase shift against density fluctuations [33]. If the temperature fluctuations are neglected, this can be interpreted as a source of radial transport of density by $E_p \times B$ drift with flux

$$\Gamma_n = -\tilde{n}\frac{1}{B}\frac{\partial}{\partial p}\tilde{V}_{fl}. \tag{3.21}$$

Here coordinate $p$ means poloidal direction and tilde denotes fluctuation of the quantity. The error made by using $V_{fl}$ instead of $\phi$ is proportional to the term $\tilde{n}\partial\tilde{T}/\partial p$ that depends on spatial correlations between density and temperature. We note that when $\tilde{n}$ and $\tilde{T}$ are out of phase, the term can be negligible even in cases when $V_{fl}$ itself is significantly influenced by local temperature. While mean profiles of density and temperature are routinely measured, relation between fluctuations of density and temperature is not fully clear. While modelling and simple theory of interchange motions predict high spatial correlation of $\tilde{n}$ and $\tilde{T}$ [44], there are some new experimental measurements that put this relation into question [74]. Generally, the measured relative level of fluctuations is lower for temperature than for density, estimated as $\sigma_T/\langle T\rangle \approx (0.2 - 0.4)\sigma_n/\langle n\rangle$ in [18, 74].

In the measurements with imaging techniques like fast cameras, gas-puff imaging or 2D-arrays of Langmuir probes, high-density coherent structures (blobs) are observed in the SOL (see Fig. 3.2). They appear intermittently in time with non-Gaussian distribution of amplitude of associated particle flux and they are generally responsible for the long-tailed PDF of $\Gamma_n$ shown in Fig. 3.3. These structures are typically $\approx 0.5 - 4$ cm in size with radial velocity $\approx (0.5 - 4) \times 10^3$ m $\cdot$ s$^{-1}$ and relative density $\tilde{n}/\langle n\rangle \approx 1$ [93, 31]. In one-point measurements by Langmuir probes, techniques of conditional averaging (CA) or computing of auto-correlation (cross-correlation) functions are often used to visualise average wave-form of de-

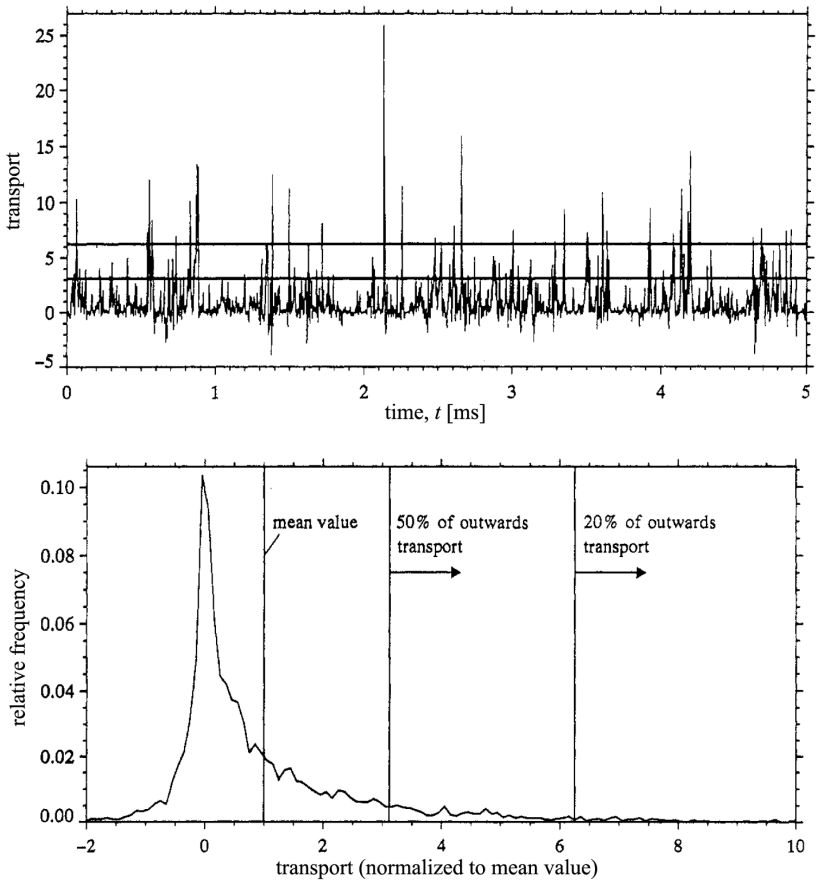


Figure 3.3: *Top:* Time signal of radial particle flux $\Gamma_n/\langle Gamma_n\rangle$ measured at midplane of ASDEX in the SOL at position $r-r_{LCFS} \approx 1-2$ cm. *Bottom:* Probability distribution function of $\Gamma_n$ signal shown upwards. Both figures reproduced from [33].

tected structures.

In the CA method, mean value $\langle g\rangle$ and standard deviation $\sigma_g$ of time-trace of triggering quantity $g$ (usually density) measured at fixed point is computed. Then, times $t_i$ of all local maxima of the signal fulfilling the condition $g(t_i) \geq \langle g\rangle + g_{thr}\sigma_q$ are detected and the signal of second quantity $h$ is averaged in the surroundings of each $t_i$ in window of size $2\delta_t$,

$$h_{CA,g}(t) = \frac{1}{N}\sum_{i=1..N} h(t_i + t);\ -\delta_t \leq t \leq \delta_t. \tag{3.22}$$

Due to large fluctuations carried by blobs, compared to the background, and its intermittent character, value of the averaging threshold $g_{thr}$ is usually chosen around 2. Note that both quantities, the trigger $g$ and averaged quantity $h$, can be (and often are) the same. An example of conditionally-averaged blob wave-form for one-point and 2D Langmuir probe measurements is shown in Fig. 3.4, demonstrating that the CA technique can be also used in 2D case to obtain typical radial-poloidal form of the blobs. The 1D profiles exhibit very sharp density growth in the front of the blob and slow decay in its trailing wake with exponential growth and decay rates independent on amplitude of density perturbation [50]. Simultaneous measurement of potential together with density reveals bipolar character of blobs with

poloidally separated potential hill and valley that are located on blob's sides and with zero potential at the position of density maximum [58]. The radial $E \times B$ movement (see Sec. 4.1.3) of the blob is then driven by potential difference between the potential valley and hill.

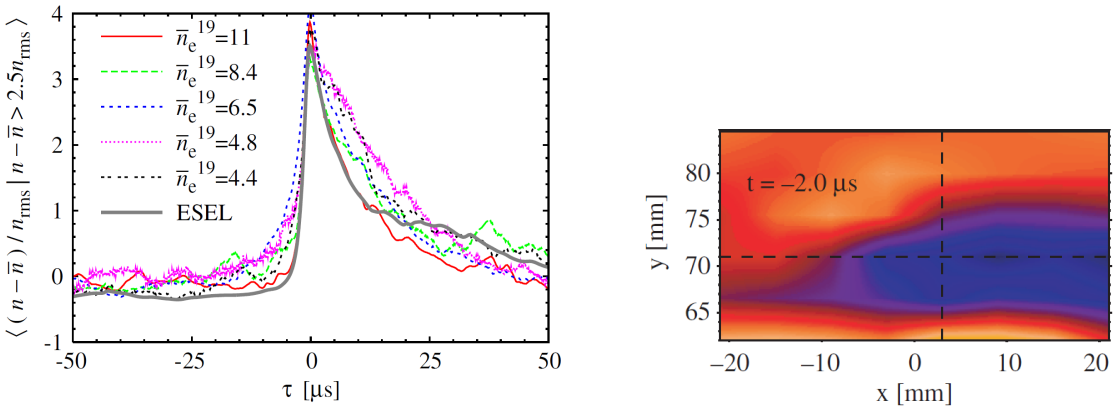


Figure 3.4: *Left:* TCV tokamak - conditional average of density at level $n_{thr} = 2.5$ for several discharges with different line-averaged density $\bar{n}_e$. Symbol $n_{rms}$ denotes root mean square of density fluctuations and $\bar{n}$ is mean density at the point of measurement. Gray line shows results of numerical model of interchange turbulence ESEL (see Sec. 5). Reproduced from [50]. *Right:* CASTOR - 2D image of negative conditionally averaged $V_{fl}$ structure with CA triggering threshold $V_{fl,thr} = -1.5$. Reproduced from [98].

There is still an ongoing discussion on the question how strongly is the edge turbulence linked with electromagnetic effects (see e.g. Section 5 in [28] and references therein). Generally, it is expected that the turbulence should be mainly electrostatic in the conditions with low $\beta$ ($\equiv p/(2B/\mu_0)$ in the plasma with pressure $p$, magnetic field $B$ and vacuum permeability $\mu_0$) while the electromagnetic effects may play a role in high-$\beta$ conditions. Recent experimental observations show that the level of magnetic fluctuations $\tilde{B}/B$ and associated current $\tilde{J}_{\|}$ carried by turbulent structures differ between L-mode turbulence and H-mode ELMs. This is being explained by the fact that ELMs are larger transport events that carry generally much higher pressure perturbation then L-mode turbulence. In [99] an order of magnitude difference between fluctuations of current carried by L-mode structures and H-mode ELMs was found. Typically, the L-mode turbulence is considered electrostatic while the current carried by ELMs is non-negligible [150, 99] and for correct description of the ELM cycle (still an open issue) the description should be fully electromagnetic and global [113].

In the last two decades understanding of plasma transport in tokamak edge changed from classical model describing competition of (anomalous) diffusive radial transport with parallel losses [145] to more complicated picture consisting of transport dominated by convection of plasma by long-living coherent turbulent structures (blobs) [88]. Even though large level of fluctuations (that are associated with the presence of the coherent structures) was observed from the beginning, it was assumed in the classical picture that the decrease of radial density and heat profiles is dominated by parallel losses and effect of turbulent fluctuations was described only by effective (anomalous) diffusion coefficient [88]. The new paradigm was motivated by observations of edge plasma by fast visible cameras (one

of the first in [55]), 2D arrays of Langmuir probes and other imaging diagnostics that revealed intermittent presence of long-lived radially moving structures in SOL carrying large amount of the particle flux. However, even though these observations has been long known, radial plasma transport by blobs was not recognized as significant (and often dominant) transport mechanism in the SOL until measurements on Alcator C-Mod [149]. On Alcator C-Mod there were for the first time observed similar magnitudes of fluxes passing through LCFS and those hitting first tokamak wall, which demonstrated that parallel losses were very small compared to radial transport.

In the last ten years several numerical and analytical models that discussed properties of plasma transport induced by blob presence in SOL appeared and they are summarized e.g. in [88, 31]. Advances in edge plasma diagnostics now allow direct comparison between statistical features of the models with experimental measurements and we recommend review paper [31] that summarizes the work made in experiment-theory comparison.

## 3.4 Drift waves

In tokamak edge, it is radial pressure gradient that provides dominant source of free energy for turbulence drive. Several modes are unstable in these conditions [27] and in this section and in the following one we will briefly describe the two most relevant - interchange and drift modes.

Electrostatic modes called drift waves appear in low-$\beta$ plasmas (typical situation in tokamaks) in which pressure gradient perpendicular to $B$ is present. Dynamics of the drift waves and the drift-wave turbulence is a result of balance between parallel electron currents (governed by generalized Ohm's law (4.79)) and E×B drift dynamics in drift plane locally perpendicular to magnetic field. In isothermal case (bearing in mind that inhomogeneous temperature does not principally change the drift wave dynamics [128]) any perturbation of density $\tilde{n}$, that locally appears at a field line, gives rise to parallel electron current that changes plasma potential $\phi$ and that tries to establish Boltzmann relation $\tilde{\phi}/T_e \approx \tilde{n}/n$. In case of zero parallel resistivity $\tilde{n}$ and $\tilde{\phi}$ are in phase and the resulting E×B drift is out of phase from $\tilde{n}$ by $\pi/2$. Then, harmonic perturbation along direction $\vec{n}_y = (\vec{b} \times \vec{n}_{\nabla n})$ moves in this direction with electron diamagnetic velocity $v_{De}$, but there is no net transport $\Gamma_n$ in direction of the density gradient, only oscillations [30]. In case of finite resistivity (the waves are often called resistive drift waves) the response of parallel current is delayed, perturbations $\tilde{n}$ and $\tilde{\phi}$ are slightly out of phase, and net flux $\Gamma_n$ in direction $\vec{n}_{\nabla n}$ appears. An example of $\tilde{\phi}$ and $\tilde{n}$ fields taken from our simulation of Hasegawa-Wakatani model of drift waves (see Sec. 7.6) is shown in Fig. 3.5.

The resistive drift waves have small but nonzero parallel wave number which fulfils relation $k_\parallel \ll k_y$ [30]. Since drift-waves require presence of nonzero perturbation along the field line, $k_\parallel \neq 0$, it is often assumed that their effect in the SOL, where all parallel perturbations quickly expand towards material targets, is limited. Instead, only flute-like perturbations ($k_\parallel = 0$) of interchange type discussed in the next section are often considered in modelling and analysis of turbulent transport in the SOL region [85, 43, 88, 53, 31]. Indeed, discussion on this topic is far from being closed and recent studies show that drift-waves can significantly

influence plasma transport in SOL when convective rate of interchange structures is on the order of drift-wave growth rates [3, 4]. On the other hand, in the region of closed field lines the finite $k_{\parallel}$ cannot vanish [127] and drift-waves dominate over interchange modes for typical edge plasma parameters [130].

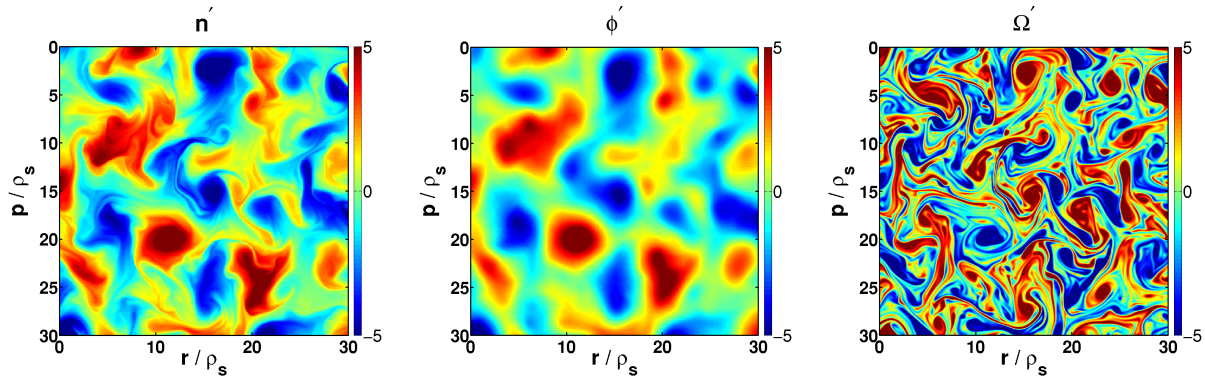


Figure 3.5: Snapshot of density fluctuation, $n'$, potential fluctuation, $\phi'$ and vorticity, $\Omega$, fields from our code modelling Hasegawa-Wakatani equations (Sec. 7.6). All fields are normalized according to 7.47.

## 3.5 Interchange instability

Another mode crucial for understanding of turbulent transport in tokamak edge is an interchange mode, often called Rayleigh-Taylor. The nature of interchange mode in plasma is similar to the behaviour of inversely stratified fluid in classical hydrodynamics [49]. The interchange instability in tokamaks appears due to presence of inhomogeneous magnetic and pressure fields and its mechanism is nicely discussed e.g. in [42]. In fluid description (see Sec. 4.3) the mechanism can be described as follows. When small pressure perturbation locally appears, diamagnetic drift (corresponding to charge-dependent curvature, grad-B and magnetization single-particle drifts) is compressible at the sides of the perturbation (transverse to direction of magnetic field gradient) and leads to separation of charge. This creates potential perturbation that is by $\pi/2$ out of phase from the pressure perturbation and the resulting E×B drift moves the initial pressure perturbation. At the same time there is a (weaker) electric field between regions of separated charge and surrounding neutral plasma. This electric field moves the surrounding plasma in the opposite direction, along the sides of main pressure perturbation. The whole situation is schematically illustrated in Fig. 3.6.

If gradient of the global pressure equilibrium $\nabla p$ is present, relative amplitude of the initial perturbation $\delta p$ either grows with the E×B movement or decreases, depending on the direction of the movement relative to the direction of the background pressure gradient (illustrated in Fig. 3.7). In tokamaks, the interchange mode is unstable on the low-field side where $\nabla p \cdot \nabla B > 0$ and $\delta p$ grows during its movement, while it is stabilized on the high-field side where $\nabla p \cdot \nabla B < 0$. This leads to so called ballooning nature of the transport that refers to the fact that majority of the flux through LCFS is observed at the 30° angle around outer midplane [59]. In this region the hot and dense confined plasma is interchanged with

relatively cold and sparse plasma from SOL in form of convective cells called blobs (hot and dense) and holes (relatively cold and sparse). An illustrative example of growth of interchange structure can be found also in Fig. 7.20.

From the point of view of a single field line located in the SOL, ballooning nature of the interchange transport causes perturbations of pressure and energy to appear approximately in the middle of the field line length (depending on symmetry of divertor legs, limiter position, etc.). These perturbations then quickly expand along the field line towards its ends. Time scale of the plasma expansion along the field line and time scale of cross-field interchange motions are comparable and the interplay between the two processes may become non-Markovian (with memory) and non-linear (see discussion in Sec. 5.7.1)

Experimental measurements of plasma fluctuations in SOL have been compared with predictions of the interchange model for several times, finding good agreement. Large part of the work on this experiment-theory comparison is summarized in recent review paper [31].

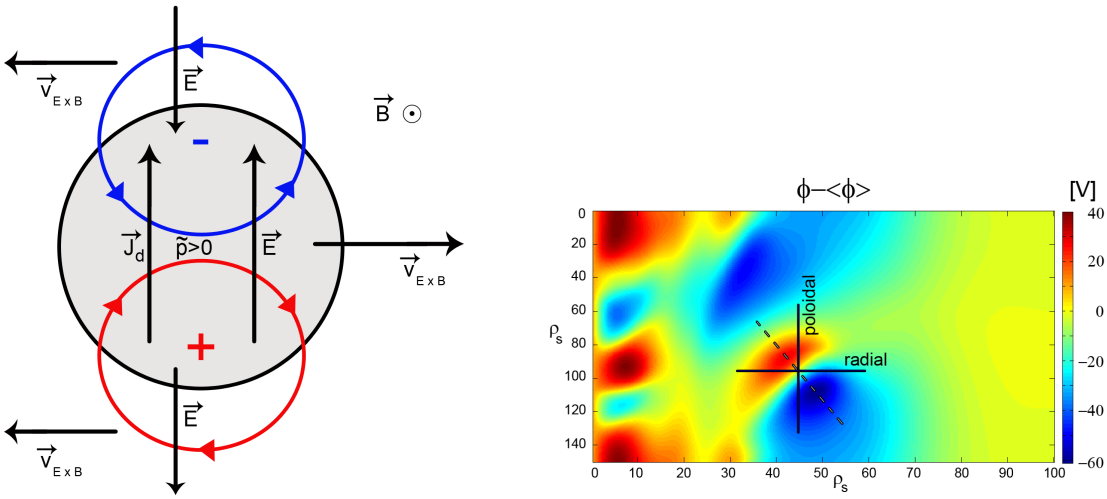


Figure 3.6: *Left :* Schematic illustration of interchange structure (blob) moving radially outwards due to radial electric field $E_r$ created by charge polarization. Two holes moving inwards at the edges of the main blob are illustrated as well. Blue and red circles represent areas of opposite charge and oposit sign of vorticity. [132] *Right :* Snapshot of turbulent potential in ESEL model of interchange turbulence (see Chap. 5) showing tilted bipolar blob structure [132].

## 3.6 Zonal flows

Magnitude of turbulence fluctuations in tokamak plasma is often regulated by layers exhibiting large radial shear of poloidal E×B velocity. Such layers that can be observed as large poloidally and toroidally symmetrical potential ($\phi$) structures are called zonal flows [32]. If the shearing rate

$$\omega_{E\times B} = 1/\tau_{shear} \equiv \partial v_p/\partial r = -\frac{1}{B}\frac{\partial^2\phi}{\partial r^2} \tag{3.23}$$

becomes comparable with inverse of autocorrelation time ($1/\tau_{ac}$) of individual turbulence structures then the shear layer is able to destroy their coherence and limit

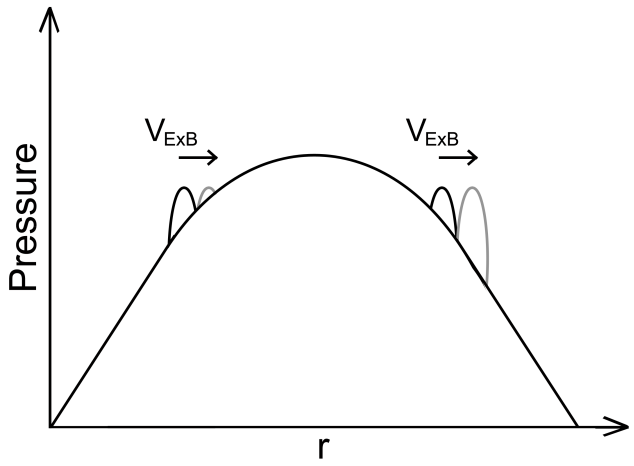


Figure 3.7: Illustration of mechanism leading to growth of interchange structures at outer side of tokamak and their suppression at the inner side.

turbulent transport [32, 45]. This mechanism called shear decorrelation is schematically illustrated in Fig. 3.8.

One of the processes contributing to generation of the sheared flows is the turbulence itself through mechanism called Reynolds stress [10, 110]. When the advective term $\vec{v} \cdot \vec{\nabla} \vec{v}$ appearing e.g. in Navier-Stokes [17] or fluid equations (see Eq. 4.45) is averaged over time, it gives two different contributions. One is given by mean velocity $\langle \vec{v} \rangle$ and the second one by time average of their fluctuation parts $\langle \tilde{v}_i \tilde{v}_j \rangle$ [10, 17],

$$\langle \vec{v} \cdot \vec{\nabla} \vec{v} \rangle = \langle \vec{v} \rangle \cdot \vec{\nabla} \langle \vec{v} \rangle + \overleftrightarrow{R} \text{ where } R_{ij} = \langle \tilde{v}_i \tilde{v}_j \rangle. \tag{3.24}$$

$\overleftrightarrow{R}$ is Reynolds stress tensor that couples energy in the turbulent velocity fluctuations (i.e. fluctuations of electric field when E×B drift is dominant) and mean plasma flows. The dynamics of turbulence together with poloidal flows can be described as predator-prey model [49, 96, 13, 34]. High level of turbulence generates strong and sheared poloidal flows that in turn start to decorrelate and suppress the turbulence when the condition $\tau_{shear} \approx \tau_{ac}$ is fulfilled. Without the turbulence drive the flows dissipate and as the shear decorrelation mechanism weakens, the turbulence structures appear again. Such system can be found in the state close to marginal stability $\tau_{shear} \approx \tau_{ac}$ [69]. Nice illustration of this interplay between interchange instability and self-generated poloidal flows is shown in Fig. 3.9.

The self-regulation of turbulence by zonal flow generation is important for both, drift as well as interchange modes [82]. In the literature term transport barrier is often used and it describes regions of reduced radial turbulent transport, usually due to shear decorrelation.

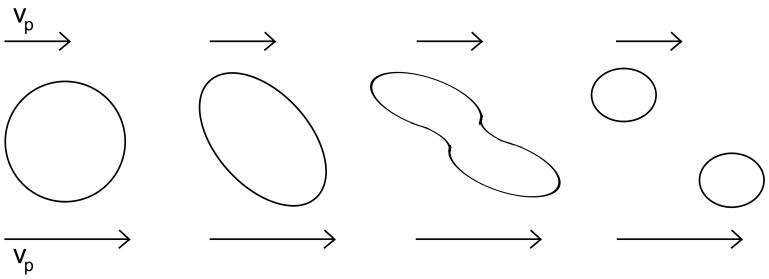


Figure 3.8: Illustration of mechanism decorrelating turbulent structures by radial shear of poloidal velocity $\partial v_p/\partial r$.

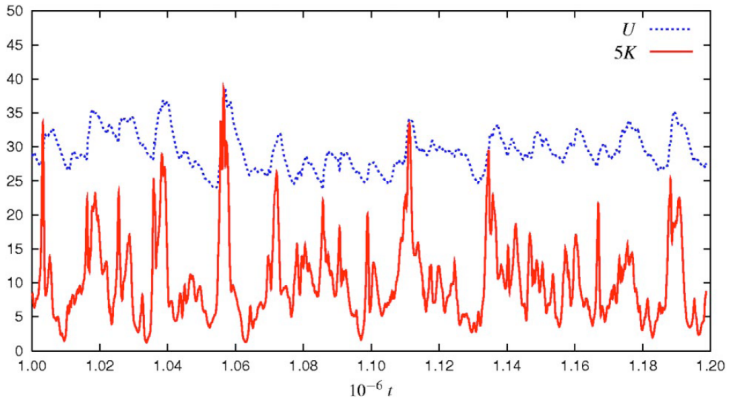


Figure 3.9: Kinetic energy in the turbulent fluctuations, K, and sheared poloidal flows, U, in ESEL model [44]. Time $t$ is normalized to $\omega_{ci}$. Reproduced from [44].

# 4. Guiding center drifts and fluid description of plasma turbulence

Plasma behaviour and its transport properties are significantly influenced by presence of electromagnetic fields. In tokamak these fields are of two types - externally imposed and those created self-consistently by collective motions of plasma particles. Especially the latter is very important for generation of tokamak edge turbulence and for understanding its enhanced transport properties.

In the following section 4.1 we will recall basic theory of motion of charged particle in an electromagnetic field. This one-particle Lagrangian description will be then used in Sec. 4.3 to interpret collective plasma motion in fluid approximation and set of fluid equations describing basic properties of edge plasma turbulence will be derived and discussed.

## 4.1 Single particle drifts in guiding center approximation

### 4.1.1 Cyclotron gyration of particle in constant magnetic field

Motion of particle with charge $q$ and mass $m$ in magnetic $\vec{B}(\vec{x},t)$ and electric $\vec{E}(\vec{x},t)$ fields is given by Lorentz force [30]

$$\frac{\mathrm{d}\vec{v}}{\mathrm{d}t} = \frac{q}{m}\left(\vec{E} + \vec{v}\times\vec{B}\right). \tag{4.1}$$

The simplest case is a motion of particle in homogeneous purely magnetic field $\vec{B}_0 = B_0\vec{b}, \vec{E} = 0$, where $\vec{b}$ represents unit vector in direction of the field. In this case the equation (4.1) reads

$$\frac{\mathrm{d}\vec{v}_\perp}{\mathrm{d}t} + \frac{\mathrm{d}\vec{v}_\parallel}{\mathrm{d}t} = \frac{q}{m}\vec{v}_\perp\times\vec{B}_0 \tag{4.2}$$

where $\vec{v}_\parallel = (\vec{v}\cdot\vec{b})\vec{b} = v_\parallel\vec{b}$ is field-aligned part of the velocity ($\vec{v}_\parallel\times\vec{b} = 0$) and $\vec{v}_\perp = \vec{v} - \vec{v}_\parallel$ is its cross-field part ($\vec{v}_\perp\cdot\vec{b} = 0$). By scalar multiplication of (4.2) with $\vec{b}$ we readily see that $v_\parallel$ is constant, given by initial conditions. Solving remaining two coupled differential equations reveals that in the plane perpendicular to $\vec{b}$ particle position $\vec{x}$ undergoes cyclotron gyration around center $\vec{x}_c$ (that moves itself with $\vec{v}_\parallel$),

$$\vec{x} - \vec{x}_c = r_L(\sin(\omega_c t + \phi_0), \cos(\omega_c t + \phi_0), 0) \tag{4.3}$$

with initial phase $\phi_0$, constant cyclotron frequency $\omega_c$ and radius (Larmor radius) $r_L$

$$\omega_c = \frac{qB_0}{m}, \quad r_L = \frac{mv_\perp}{|q|B_0}. \tag{4.4}$$

Velocity of such cyclotron motion $\vec{v}_{gyr}$ is in the plane perpendicular to $\vec{b}$ described by relations [42]

$$\frac{\mathrm{d}\vec{v}_{gyr}}{\mathrm{d}t} = \omega_c \vec{v}_{gyr} \times \vec{b}, \tag{4.5}$$

$$\vec{v}_{gyr} = \omega_c (\vec{x} - \vec{x}_c) \times \vec{b}. \tag{4.6}$$

### 4.1.2 Guiding center approximation

If any additional term (force) $\vec{F}(\vec{x}, t)$ arises in equation of motion,

$$\frac{\mathrm{d}\vec{v}}{\mathrm{d}t} = \frac{q}{m}\vec{v} \times \vec{B}_0 + \frac{1}{m}\vec{F}, \tag{4.7}$$

its effect can be described by motion of the gyration center with velocity $\vec{u}(\vec{x}, t)$.

Separating motion of guiding center $\vec{u}$ and gyromotion $\vec{v}_{gyr}$ in (4.1), $\vec{v} = \vec{u} + \vec{v}_{gyr}$, and reminding (4.5), Eq. (4.7) transforms to

$$\frac{\mathrm{d}\vec{u}}{\mathrm{d}t} = \frac{q}{m}\vec{u} \times \vec{B}_0 + \frac{1}{m}\vec{F}. \tag{4.8}$$

An additional assumption can be often placed on $\vec{u}$,

$$\mathrm{d}\vec{u}/\mathrm{d}t \ll \vec{u}. \tag{4.9}$$

This allows to evaluate $\vec{u}$ iteratively. After dividing $\vec{u}$ into field-aligned part $\vec{u}_\parallel = u_\parallel \vec{b}$ and cross-field part $\vec{u}_\perp = \vec{u} - \vec{u}_\parallel$ we can rewrite previous equation as

$$\vec{u}_\perp = \frac{1}{m\omega_c}\vec{F} \times \vec{b} - \frac{1}{\omega_c}\frac{\mathrm{d}\vec{u}}{\mathrm{d}t} \times \vec{b} \tag{4.10}$$

$$\vec{u}_\parallel = \frac{1}{m}\int \left[\vec{F} \cdot \vec{b} - \vec{b} \cdot \frac{\mathrm{d}\vec{u}_\perp}{\mathrm{d}t}\right] \mathrm{d}t. \tag{4.11}$$

Generally, the perturbation force $F$ may be dependent on phase of the gyromotion or explicitly on time or particle position. Then, also the guiding center drift would have explicit temporal or spatial dependency. If the strength of the perturbation is low and the dependency is approximately periodic, $\vec{u}$ is usually time-averaged over one gyroperiod, as we will show in the following chapter 4.1.3, giving the averaged gyrocenter drift $\langle\vec{u}\rangle$.

In most cases, velocity and/or direction of the guiding center drift differ for different plasma species. Then, there is a current density associated to the drift,

$$\vec{j} = \sum_k n_k q_k \vec{u}_k \tag{4.12}$$

where $k$ goes through all relevant plasma species, $n_k$ is their density, $q_k$ charge and $u_k$ corresponding guiding center drift.

### 4.1.3 Static electromagnetic field

If constant electric field $\vec{E}$ is present together with the constant magnetic field, the force acting on particle is $\vec{F}_E = q\vec{E}$ (see Eq. 4.1). Then, according to (4.11), its parallel component uniformly accelerates the particle along magnetic field lines. The cross-field electric field causes $E \times B$ drift of the center of cyclotron gyration as described by Eq. (4.10),

$$\vec{u}_E = \frac{\vec{E} \times \vec{b}}{B_0}. \tag{4.13}$$

The total velocity is thus given as sum of all three parts, $\vec{v} = (v_{\parallel,0} + u_\parallel)\vec{b} + \vec{u}_E + \vec{v}_{gyr}$ where $v_{\parallel,0}$ is initial parallel velocity of the particle. It is important to note, that $\vec{u}_E$ is not dependent neither on charge nor mass and therefore any plasma species moves due to $E \times B$ drift with the same velocity in the same direction and for quasineutral plasma no net current is generated, $\vec{j}_E = 0$.

In a weakly inhomogeneous magnetic field, series expansion of the field in the position of gyration center $\vec{x}_c(t)$ can be made to describe effects of the inhomogeneity on the motion of $\vec{x}_c$. In the first order of expansion the magnetic field is

$$\vec{B}(\vec{x}) = \vec{B}(\vec{x}_c) + ((\vec{x} - \vec{x}_c) \cdot \vec{\nabla})\vec{B}(\vec{x}_c). \tag{4.14}$$

The error made by this approximation is in the order of $\mathcal{O}(\frac{(\vec{x}-\vec{x}_c)^2}{l^2}) \approx \mathcal{O}(\frac{r_L^2}{l^2})$, where $l$ is the spatial scale of the inhomogeneity. This means that the scale of the inhomogeneity must be significantly larger than $r_L$, $l \gg r_L$, otherwise higher-order terms of the expansion should be taken into account.

To the first order we can assume that the cyclotron trajectory is not perturbed, i.e. that the velocity on the right hand side of (4.1) is $\vec{v} \approx \vec{v}_{gyr}$. Substituting expansion of $\vec{B}$ (4.14) into Lorentz force (4.1), comparing with (4.7) and averaging over one gyroperiod, mean force due to the gradient of the magnetic field is

$$\langle \vec{F}_{\nabla B} \rangle \equiv q\omega_c \int_0^{\omega_c^{-1}} \vec{v}_{gyr} \times \left( \vec{b}((\vec{x} - \vec{x}_c) \cdot \vec{\nabla})B(\vec{x}_c) \right) \mathrm{d}t \tag{4.15}$$

where we have used the fact that particle gyrates in plane perpendicular to $\vec{b}$, $(\vec{x} - \vec{x}_c) \cdot \vec{b} = 0$. After substitution of trajectory of unperturbed cyclotron orbit (4.3) and its velocity (4.6) and performing the integration, one gets the mean force

$$\langle \vec{F}_{\nabla B} \rangle = -\frac{q\omega_c r_L^2}{2} \vec{\nabla} B \tag{4.16}$$

and the corresponding guiding center drift (4.10)

$$\vec{u}_{\nabla B} = \frac{v_\perp^2}{2\omega_c} \vec{b} \times \vec{\nabla} \ln B. \tag{4.17}$$

During derivation of $\nabla B$-drift we have assumed that the direction of the magnetic field does not change in the cross-field plane, $\vec{\nabla}_\perp \vec{b} = 0$. However, also curvature of the field lines $\vec{\nabla}_\parallel \vec{b} \neq 0$ must be taken into account. The local change of magnetic field as particle moves along the field line is

$$\frac{\mathrm{d}\vec{b}}{\mathrm{d}t} = (\vec{v} \cdot \vec{\nabla})\vec{b} = v_\parallel (\vec{b} \cdot \vec{\nabla})\vec{b}. \tag{4.18}$$

The additional term arising from the fact that $\mathrm{d}\vec{v}_\parallel/\mathrm{d}t = \mathrm{d}v_\parallel/\mathrm{d}t \cdot \vec{b} + v_\parallel \mathrm{d}\vec{b}/\mathrm{d}t$ is

$$\vec{F}_{curv} = -mv_\parallel \frac{\mathrm{d}\vec{b}}{\mathrm{d}t} = -mv_\parallel^2 (\vec{b}\cdot\vec{\nabla})\vec{b}. \tag{4.19}$$

This is usually interpreted as centrifugal force acting on a particle and bending its trajectory to move along the curved field line [42, 30]. The guiding center drift (4.10) resulting from the centrifugal force is (using vector calculus identity $(\vec{b}\cdot\vec{\nabla})\vec{b} = -\vec{b}\times(\vec{\nabla}\times\vec{b}) + \frac{1}{2}\vec{\nabla}(\vec{b}\cdot\vec{b})$)

$$\vec{u}_{curv} = \frac{v_\parallel^2}{\omega_c}\vec{\nabla}\times\vec{b}. \tag{4.20}$$

When the volume currents can be neglected, the Maxwell equation $\vec{\nabla}\times\vec{B} = 0$ implies that $\vec{\nabla}\times\vec{b} = \vec{b}\times\vec{\nabla}\ln B$ and both, curvature and grad-B drifts, can be written together as

$$\vec{u}_{\nabla B+curv} = \frac{1}{\omega_c}\vec{b}\times\vec{\nabla}\ln B(\frac{1}{2}v_\perp^2 + v_\parallel^2). \tag{4.21}$$

Note that regardless of particle energy, the direction of the combined drift in toroidal tokamak geometry with magnetic field described in Eq. (2.4) will be always outwards. The drift (4.21) is charge dependent which may give rise to current associated with inhomogeneities of magnetic field. Since the drift depends on particle velocity, we will anticipate results of Sec. 4.2 and write the current $\vec{J}_{\nabla B+curv}$ due to inhomogeneous curved magnetic field as

$$\vec{J}_{\nabla B+curv} = \frac{1}{B}(p_\perp + p_\parallel)\vec{b}\times\vec{\nabla}\ln B \tag{4.22}$$

where pressure $p = nT$ is in both directions summed over pressure of all species.

Similar expansion can be made for the case of inhomogeneous electrostatic field,

$$\vec{E}(\vec{x}) = \vec{E}(\vec{x}_c) + ((\vec{x}-\vec{x}_c)\cdot\vec{\nabla})\vec{E}(\vec{x_c}) + \frac{1}{2}((\vec{x}-\vec{x}_c)^2\vec{\nabla}^2)\vec{E}(\vec{x_c}). \tag{4.23}$$

Note that the expansion is made up to the factor $\mathcal{O}(\frac{r_L^3}{k^3})$, where $k$ is spatial scale of the inhomogeneity in the electrical field, i.e. one order more than for magnetic field. The reason is that gyro-averaging of the first order term gives zero and the first non-zero term is the second-order correction. Performing averaging over an unperturbed cyclotron orbit gives second-order correction to the $E\times B$ drift

$$\vec{u}_{E+\nabla E} = \vec{u}_E + \vec{u}_{\nabla E} = (1 + \frac{1}{4}r_L^2\vec{\nabla}^2)\frac{\vec{E}\times\vec{b}}{B_0}. \tag{4.24}$$

Larmor radius $r_L$ is significantly different for electrons and ions and therefore $\vec{u}_{\nabla E}$ drift has an associated current (in contrast to the basic $E\times B$ drift (4.13)) and may lead to charge separation.

### 4.1.4 Inertia drift

Inertia drift (often called polarization drift) of the guiding center appears in presence of time-dependent electric field $\vec{E}(t)$. Then the time derivative of $\vec{u}$ in (4.10) cannot be neglected and besides the usual $E \times B$ drift $\vec{u}_E$ we get a new term, polarization drift $\vec{u}_P$. To be able to solve Eq. (4.10) iteratively, the term $(1/\omega_c)\mathrm{d}\vec{u}/\mathrm{d}t \times \vec{b}$ must be a second order correction i.e., the characteristic rate of change of the electric field $\omega_E$ must be much smaller then the cyclotron frequency $\omega_c$,

$$\omega_E \ll \omega_c. \tag{4.25}$$

In such slowly varying electric field the polarization drift is

$$\vec{u}_P = \frac{1}{\omega_c B} \frac{\mathrm{d}\vec{E}_\perp}{\mathrm{d}t}. \tag{4.26}$$

Note that the time derivative of electric field has a form of convective derivative, not partial, and therefore it has to be evaluated along particle trajectory. In the lowest order, performing gyro-averaging replaces the full velocity in the convective derivative by perpendicular $E \times B$ drift $\vec{u}_E$. Since $\vec{E}_\perp$ may change along field line, parallel velocity $\vec{u}_\parallel$ (4.11) should be also taken into account.

Inertia drift is charge and mass dependent and hence gives rise to a polarization current

$$\vec{J_p} = \sum_k \frac{n_k m_k}{B^2} \frac{\mathrm{d}\vec{E}_\perp}{\mathrm{d}t} = \sum_k \frac{n_k m_k}{B^2} \left( \frac{\partial}{\partial t} + \vec{u} \cdot \vec{\nabla} \right) \vec{E}_\perp \tag{4.27}$$

where we sum over electron and ion species. The current is called polarization current because compressibility of the partial derivative of $\vec{E}_\perp$ in (4.27) gives rise to bound charge, similar to the bound charge in dielectric medium. For slow changes of $\vec{E}$ and small variation of $E_\parallel$ the bound charge increases relative permittivity in the plasma by factor inversely proportional to the second power of $B$,

$$\epsilon_r = 1 + \sum_i \frac{n_i m_i}{\epsilon_0 B^2}. \tag{4.28}$$

Value of $\epsilon_r$ is typically very large, with values in typical tokamak edge plasma in the order of $\epsilon_r \approx 10^3$.

## 4.2 Velocity averaged single particle drifts

Particle velocity distribution in tokamak plasma is often considered as approximately Maxwellian [154], especially in the edge where the collisionality is relatively large. Distribution function of particle momentum $p$ in such case is

$$f(\vec{p}) = \frac{n}{(2\pi m k T_\perp)\sqrt{2\pi m k T_\parallel}} \exp\left( -\frac{(\vec{p}_\perp - m\vec{v}_{\perp,0})^2}{2mkT_\perp} - \frac{(\vec{p}_\parallel - m\vec{v}_{\parallel,0})^2}{2mkT_\parallel} \right), \tag{4.29}$$

where $n$ is local plasma density, $T_\perp$ and $T_\parallel$ local temperature perpendicular and parallel to magnetic field, respectively, $m$ is particle mass, $\vec{p} = \vec{p}_\perp + \vec{p}_\parallel = m\vec{v}$ particle momentum, $\vec{v}_0 = \vec{v}_{\perp,0} + \vec{v}_{\parallel,0}$ mean velocity of the plasma at given point and $k$ is Boltzman constant. Since some of the single-particle velocities derived in

Sec. 4.1 are dependent on the velocity of the particle, one should take into account the momentum distribution function and derive their averaged form.

First, we will discuss the cyclotron motion itself. If the particle density and temperature as well as the magnetic field are all homogeneous, there is no net drift of particles due to their cyclotron motion and no net current. However, if at least one of the three quantities is inhomogeneous in space, the local current exists. This can be described as magnetization current $\vec{J}_\mu = \int \vec{\nabla} \times (n\vec{\mu}(v_\perp)) f(\vec{v}_\perp) \mathrm{d}\vec{v}_\perp$, where $\vec{\mu} = -(mv_{gyr}^2/(2B))\vec{b}$ is magnetic moment of current loop created by cyclotron orbit of single particle (4.3). After performing the integration we find average velocity of plasma element $\vec{u}_\mu = \vec{j}/(nq)$ as [42]

$$\langle \vec{u}_\mu \rangle = \frac{1}{qnB} \left[ \vec{b} \times \vec{\nabla}(nT_\perp) - (nT_\perp) \left( \vec{b} \times \vec{\nabla} \ln B + \vec{\nabla} \times \vec{b} \right) \right]. \tag{4.30}$$

$E \times B$ drift (4.13) is not velocity dependent and after averaging it remains in the same form. The velocity averaging of grad-B drift (4.17) and curvature (4.20) drift gives

$$\langle \vec{u}_{\nabla B + curv} \rangle = \frac{1}{qB} \left( T_\perp \vec{b} \times \vec{\nabla} \ln B + T_\parallel \vec{\nabla} \times \vec{b} \right). \tag{4.31}$$

In vacuum field we get this drift in somewhat simpler form, obtained from Eq. (4.21),

$$\langle \vec{u}_{\nabla B + curv} \rangle = \frac{T_\perp + T_\parallel}{qB} \vec{b} \times \vec{\nabla} \ln B. \tag{4.32}$$

## 4.3 Fluid approximation

Reducing complicated particle motion in plasmas to guiding center drifts makes the description of plasma transport significantly easier, however it is still necessary to handle large number of particles, trace their trajectory and self-consistently evaluate time dependent electric fields. Due to large number of particles typically present in plasmas, all of this may be very time consuming. This task may be further simplified when the plasma is treated as a fluid and described using local macroscopic quantities such as particle density $n$, mass density $\rho$, momentum density $\vec{\pi}$, pressure tensor $\overleftrightarrow{\tau}$ and others. This represents transition from Lagrangian to Eulerian formulation of plasma movement, which is often easier to handle. The macroscopic quantities are defined as moments of particle distribution function $f(\vec{x}, \vec{p}, t)$,

$$n \equiv \langle f \rangle, \tag{4.33}$$

$$\rho \equiv nm, \tag{4.34}$$

$$\vec{\pi} \equiv \langle \vec{p} f \rangle = mn\vec{v} = \rho\vec{v}, \tag{4.35}$$

$$\overleftrightarrow{T} \equiv \frac{1}{m} \langle \vec{p}\vec{p} f \rangle = mn\vec{v}\vec{v} + \overleftrightarrow{\tau} = \rho\vec{v}\vec{v} + \overleftrightarrow{\tau}. \tag{4.36}$$

Here $\langle \cdot \rangle$ means averaging over momentum space. Note that $\overleftrightarrow{T}$ and $\overleftrightarrow{\tau}$ are by the definition symmetric with only 6 independent components. The pressure tensor is often divided into scalar pressure $p$ and viscous stress tensor $\overleftrightarrow{\Pi}$, [54] $\overleftrightarrow{\tau} = \overleftrightarrow{I}\, p + \overleftrightarrow{\Pi}$. Particle mobility along and across magnetic field lines may differ, which

is reflected in direction dependence of temperature in (4.29) and pressure $p_\perp \neq p_\parallel$. In such case we will denote by $\overleftrightarrow{\Pi}$ the difference of $\overleftrightarrow{\tau}$ from gyrotropic pressure tensor,

$$\overleftrightarrow{\tau} = (\overleftrightarrow{I} - \vec{b}\vec{b})p_\perp + \vec{b}\vec{b}p_\parallel + \overleftrightarrow{\Pi}. \tag{4.37}$$

Kinetic energy $\epsilon = \langle p^2/2m \rangle$ and heat energy $\epsilon_0$ of the element are given by the trace of $\overleftrightarrow{\tau}$ and $\overleftrightarrow{T}$ as

$$\epsilon_0 \equiv \frac{1}{2}\mathrm{Tr}(\overleftrightarrow{\tau}) \tag{4.38}$$

$$\epsilon \equiv \frac{1}{2}\mathrm{Tr}(\overleftrightarrow{T}) = \frac{1}{2}\rho v^2 + \epsilon_0. \tag{4.39}$$

The kinetic energy is a sum of two components, representing energy of the mean flow of particles in the fluid element and energy $\epsilon_0$ of their random motion. If we assume Maxwellian distribution function (4.29), it allows for explicit integration of the moments and we can write the form of $\overleftrightarrow{\tau}$ and $\epsilon_0$ using perpendicular $p_\perp = nkT_\perp$ and parallel $p_\parallel = nkT_\parallel$ pressure, obtaining gyrotropic pressure tensor

$$\overleftrightarrow{\tau} = p_\perp(\overleftrightarrow{I} - \vec{b}\vec{b}) + p_\parallel \vec{b}\vec{b} \tag{4.40}$$

and

$$\epsilon_0 = p_\perp + \frac{1}{2}p_\parallel \tag{4.41}$$

The components of 3rd-order momentum of $f$ correspond to heat flux $Q^{ijk}$

$$Q^{ijk} = \frac{1}{m^2}\langle p^i p^j p^k f \rangle = \rho v^i v^j v^k + v^i \tau^{jk} + v^j \tau^{ik} + v^k \tau^{ij} + q^{ijk} \tag{4.42}$$

where $q^{ijk}$ is heat flux in the frame of reference co-moving with the fluid element. For better readability, we will write more complicated expressions in components (using Einstein summation law) whenever needed. Due to symmetry, there are only 10 independent components of $Q^{ijk}$.

All the defined macroscopic quantities are space and time dependent and their time evolution is governed by time evolution of the underlying distribution function $f$. Boltzmann equation describing time evolution of distribution function $f(\vec{x}, \vec{p}, t)$ of particles with charge $q$ and mass $m$ under influence of electric field with potential $\phi$ and magnetic field $\vec{B}$ is [154]

$$\frac{\partial f}{\partial t} + \frac{\vec{p}}{m} \cdot \frac{\partial f}{\partial \vec{x}} + q[-\vec{\nabla}\phi + (\vec{v} \times \vec{B})] \cdot \frac{\partial f}{\partial \vec{p}} = \left(\frac{\delta f}{\delta t}\right)_c \tag{4.43}$$

where $\vec{x}$ and $\vec{p}$ are position and momentum, respectively, and $\left(\frac{\delta f}{\delta t}\right)_c$ is change of the distribution function due to collisions.If any other effects that change $f$ (like recombination, ionisation, chemical reactions, etc.) should be taken into account, they would modify the Boltzmann equation similarly to the collisional term.

Computing moments of (4.43) in momentum space gives equations for time evolution of the moments of the distribution function (4.33-4.36) and (4.42). These equations then form a hierarchy where time evolution of the $n$-th order moment is dependent also on the moment of the order $n + 1$. In the following sections we will explicitly write these evolution equations for the first three moments and use closure that will allow to cut of all moments of order higher then 3. In order to perform the integration $\langle \cdot \rangle \equiv \int \mathrm{d}^3 p$ we will assume boundary conditions such that boundary terms in per-partes method will become zero.

### 4.3.1 Momentum equation

The first moment of Boltzman equation (4.43), $\int \vec{p}\mathrm{d}^3p)$, gives time evolution of the momentum $\vec{\pi}$ or velocity $\vec{v}$.

$$\frac{\partial}{\partial t}\vec{\pi} + \vec{\nabla}\cdot\overleftrightarrow{T} - nq[-\vec{\nabla}\phi + (\vec{v}\times\vec{B})] = \left(\frac{\delta\vec{\pi}}{\delta t}\right)_c \tag{4.44}$$

$$mn(\frac{\partial}{\partial t} + \vec{v}\cdot\vec{\nabla})\vec{v} + \vec{\nabla}\cdot\overleftrightarrow{\tau} - nq[-\vec{\nabla}\phi + (\vec{v}\times\vec{B})] = \left(\frac{\delta\vec{\pi}}{\delta t}\right)_c - \vec{v}m\left(\frac{\delta n}{\delta t}\right)_c \tag{4.45}$$

Note that to come from (4.44) to (4.45) we have anticipated the result of the next section, the continuity equation (4.53).

Since character of particle motion perpendicular to the magnetic field is significantly different than the motion along magnetic field lines, we will separate the perpendicular dynamics in (4.45) by vector multiplication with term $\vec{b}/(qnB)$, which gives

$$\begin{aligned}\vec{v}_\perp = \vec{v}_E + \vec{v}_D + \vec{v}_P + \vec{v}_C = {} & \frac{1}{B}\vec{b}\times\vec{\nabla}\phi + \frac{1}{qnB}\vec{b}\times\vec{\nabla}\cdot\overleftrightarrow{\tau} + \\ & + \frac{m}{qB}\vec{b}\times(\frac{\partial}{\partial t} + \vec{v}\cdot\vec{\nabla})\vec{v} + \frac{1}{qnB}\vec{b}\times\left[\left(\frac{\delta\vec{\pi}}{\delta t}\right)_c - \vec{v}m\left(\frac{\delta n}{\delta t}\right)_c\right].\end{aligned} \tag{4.46}$$

Here we have defined electrical, or $E\times B$, drift $\vec{v}_E$, diamagnetic drift $\vec{v}_D$, polarization drift $\vec{v}_P$ and drift due to collisions $\vec{v}_C$. The two terms on the right still keep dependency on the total velocity $\vec{v}$, however when $\mathrm{D}/\mathrm{d}t \ll qB/m$ and collisional frequency $\nu \ll qB/m$, the problem can be treated iteratively [139, 41] substituting $\vec{v}_E$.

There exists direct correspondence between fluid and gyrocenter drifts which is very illustratively explained in [42]. The correspondence between $E\times B$ drift in fluid (4.13) and gyrocenter (4.46) approximation can be readily seen. When the distribution function $f$ is Maxwell-Boltzmann, the pressure tensor is gyrotropic, given by (4.41), and form of diamagnetic drift becomes similar to the sum of velocity averaged single particle $\nabla B$ and curvature drifts (4.32) and magnetization drift (4.30) [42]:

$$\vec{v}_D = \frac{1}{qnB}\vec{b}\times\vec{\nabla}(p_\perp) + \frac{p_\parallel - p_\perp}{qnB}\vec{\nabla}\times\vec{b}. \tag{4.47}$$

Therefore, the diamagnetic drift covers real movement of particle gyrocenters (grad-B and curvature drifts) together with magnetization effects. In typical edge plasma parameters the $E\times B$ drift is dominant and correspondence of $v_P$ with $u_P$ in (4.26) can be acquired substituting $\vec{E}_\perp = \vec{B}\times\vec{v}_E$. Through the outlined links, motion of the fluid can be understood in terms of motion of its individual particles.

In the homogeneous magnetic field $\vec{v}_E$ would be incompressible, $\vec{\nabla}\cdot\vec{v}_E = 0$. This, however, does not hold for a magnetic field in tokamak toroidal geometry (2.4) and all drifts from 4.46 become compressible. For the case of gyrotropic

pressure tensor (4.41) and lowest order iteration $\vec{v} \approx \vec{v}_E$ it is

$$\vec{\nabla} \cdot \vec{v}_E = \mathcal{C}(\phi) \tag{4.48}$$

$$\vec{\nabla} \cdot \vec{v}_D = \frac{1}{qn}\mathcal{C}(p_\perp) + \frac{1}{qnB}(\vec{\nabla} \times \vec{b}) \cdot (\vec{\nabla}\delta p - \delta p \vec{\nabla} \ln B) - \vec{v}_D \cdot \frac{\vec{\nabla} n}{n} \tag{4.49}$$

$$\vec{\nabla} \cdot \vec{v}_P = \frac{m}{q}\vec{\mathcal{K}} \cdot \frac{\mathrm{d}\vec{v}_E}{\mathrm{d}t} - \frac{m}{qB}\vec{b} \cdot \left(\vec{\nabla} \times \frac{\mathrm{d}\vec{v}_E}{\mathrm{d}t}\right) \approx -\frac{m}{qB}\vec{b} \cdot \left(\vec{\nabla} \times \frac{\mathrm{d}\vec{v}_E}{\mathrm{d}t}\right) \tag{4.50}$$

where $\mathcal{C}$ is curvature operator

$$\mathcal{C} = \frac{1}{B}[\vec{\nabla} \times \vec{b} + \vec{b} \times \vec{\nabla} \ln B] \cdot \vec{\nabla} = \vec{\mathcal{K}} \cdot \vec{\nabla} \tag{4.51}$$

and $\delta p = p_\parallel - p_\perp$. Note, that even though $\vec{v}_P$ itself is typically small (it is a second-order drift) and we have neglected all terms directly proportional to $\mathrm{d}\vec{v}_E/\mathrm{d}t$, its divergence may become not negligible due to the remaining (rightmost) term in (4.50). As will be described in Sec. 4.3.6, it is the divergence of polarization current that controls the evolution of plasma vorticity and gives rise to turbulent convective structures. Amper's law ($\vec{\nabla} \times \vec{B} = \mu_0 \vec{J}$) shows that both terms in the first equality in curvature operator (4.51) differ by term proportional to plasma current $\vec{J}$. For low-$\beta$ tokamak plasmas the current can be neglected and both terms considered equal [44].

### 4.3.2 Continuity equation

The zeroth moment of Boltzman equation (4.43), the continuity equation, can be obtained by integration of (4.43) over momentum space:

$$\frac{\partial n}{\partial t} + \frac{1}{m}\vec{\nabla} \cdot \vec{\pi} = \left(\frac{\delta n}{\delta t}\right)_c \tag{4.52}$$

$$\frac{\partial n}{\partial t} + \vec{\nabla} \cdot (n\vec{v}) = \left(\frac{\delta n}{\delta t}\right)_c \tag{4.53}$$

Evolution of the velocity $\vec{v}$ can be either solved together with full momentum equation (4.45) or reduced to the algebraic equation (4.46), separating motion parallel and perpendicular to magnetic field lines. Since the latter will be used in two models of edge tokamak plasma that we will present later, we will further discuss mainly the reduced approach.

Assuming low-frequency variations, in the lowest order we will neglect flux due to polarization drift, which is of the second order, and rewrite continuity equation (4.53) using (4.46) and (4.48-4.49) into form

$$\begin{aligned}(\frac{\partial}{\partial t} + \vec{v}_E \cdot \vec{\nabla})n &+ n\mathcal{C}(\phi) + \frac{1}{q}\mathcal{C}(p) + \frac{1}{qB}(\vec{\nabla} \times \vec{b}) \cdot (\vec{\nabla}\delta p - \delta p \vec{\nabla} \ln B) = \\ &= -\vec{\nabla} \cdot (n\vec{v}_C) - \vec{\nabla} \cdot (n\vec{v}_\parallel) + \left(\frac{\delta n}{\delta t}\right)_c \end{aligned} \tag{4.54}$$

where we have split the total velocity into its perpendicular and parallel component, $\vec{v} = \vec{v}_\perp + \vec{v}_\parallel$. The first term on the left-hand side shows that the density is advected purely by $E \times B$ drift (with some possible corrections due to $\vec{v}_C$) and

expected advection by diamagnetic drift is cancelled by the terms coming from the compressibility of $\vec{v}_D$. We can see this more explicitly in Eq. (4.49) that shows that $n\vec{\nabla}\cdot\vec{v}_D$ contains term $-\vec{v}_D\cdot\vec{\nabla}n$ that cancels the advection. This is called effect of *diamagnetic cancellation* and will be present in the energy equation (Sec. 4.3.3) as well. Due to similar mechanism the diamagnetic drift does not contribute to the advective nonlinearity in the polarization drift [44]. From the point of view of movement of individual particles, we may understand the diamagnetic cancellation in terms of magnetization drift discussed in Sec. 4.2 that shows nonzero average velocity of particles at given point even when the magnetic field is homogeneous (i.e. no curvature and grad-B drifts) and gyration center of all particles is fixed (there is no advection of local $n$ or $T$).

### 4.3.3 Energy equation

Similarly to continuity and momentum equation, the equation for pressure tensor is obtained by integration of (4.43) multiplied by $p^i p^j$. For better readability, we will present it in components (with summation over similar indexes) and get back to vector notation in energy equation.

$$\frac{\partial T^{jk}}{\partial t} + \frac{\partial Q^{ijk}}{\partial x^i} - \frac{q}{m}(\pi^j E^k + \pi^k E^j + \epsilon^{jlm}T^{kl}B^m + \epsilon^{klm}T^{jl}B^m) = \left(\frac{\delta T^{jk}}{\delta t}\right)_c \tag{4.55}$$

$$\begin{aligned}\frac{\partial \tau^{jk}}{\partial t} + \frac{\partial q^{ijk}}{\partial x^i} + \frac{\partial (v^i\tau^{jk})}{\partial x^i} + \tau^{ki}\frac{\partial v^j}{\partial x^i} + \tau^{ji}\frac{\partial v^k}{\partial x^i} - \frac{q}{m}(\epsilon^{jlm}\tau^{kl}B^m + \epsilon^{klm}\tau^{jl}B^m) = \\ = \left(\frac{\delta T^{jk}}{\delta t}\right)_c + mv^j v^k\left(\frac{\delta n}{\delta t}\right)_c - v^j\left(\frac{\delta \pi^k}{\delta t}\right)_c - v^k\left(\frac{\delta \pi^j}{\delta t}\right)_c\end{aligned} \tag{4.56}$$

Energy of fluid element is given by trace of the $\overleftrightarrow{\tau}$ or $\overleftrightarrow{T}$ in (4.38) or (4.39), respectively. By making contraction of (4.55) and (4.56) we get energy equations

$$\frac{\partial \epsilon}{\partial t} + \vec{\nabla}\cdot\vec{Q} - qn\vec{v}\cdot\vec{E} = \left(\frac{\delta \epsilon}{\delta t}\right)_c \tag{4.57}$$

$$\frac{\partial \epsilon_0}{\partial t} + \vec{\nabla}\cdot\vec{q} + \vec{\nabla}\cdot(\vec{v}\epsilon_0) + \overleftrightarrow{\tau} : \vec{\nabla}\vec{v} = \left(\frac{\delta \epsilon}{\delta t}\right)_c + \frac{mv^2}{2}\left(\frac{\delta n}{\delta t}\right)_c - \vec{v}\cdot\left(\frac{\partial \vec{\pi}}{\delta t}\right)_c \tag{4.58}$$

where

$$Q^i = \frac{1}{2}Q^{ikk};\quad q^i = \frac{1}{2}q^{ikk} \tag{4.59}$$

Rewriting the energy equations in terms of (4.37), (4.41) and separating terms involving perpendicular velocity and viscosity (blue, two indexes $\perp$), parallel terms (red, index $\parallel$) and mixed terms (magenta) will allow us to see structure of the

energy equations in more detail.

$$\frac{\partial}{\partial t}\left(\frac{1}{2}nT_{\parallel}+\frac{1}{2}mnv_{\parallel}^{2}\right)+\frac{\partial}{\partial t}\left(nT_{\perp}+\frac{1}{2}mnv_{\perp}^{2}\right)+ \tag{4.60}$$
$$\frac{\partial}{\partial x^{\parallel}}\left(v^{\parallel}(\frac{3}{2}nT_{\parallel}+nT_{\perp})+\frac{1}{2}mnv^{\parallel}v_{\parallel}^{2}+v^{\parallel}\Pi_{\parallel}^{\parallel}\right)+\frac{\partial}{\partial x^{\parallel}}\left(\frac{1}{2}mnv^{\parallel}v_{\perp}^{2}+v^{\perp_{\alpha}}\Pi_{\perp_{\alpha}}^{\parallel}+v^{\parallel}\Pi_{\perp_{\alpha}}^{\perp_{\alpha}}\right)+$$
$$\frac{\partial}{\partial x^{\perp_{\alpha}}}\left(v^{\perp_{\alpha}}(2nT_{\perp}+\frac{1}{2}nT_{\parallel})+\frac{1}{2}mnv^{\perp_{\alpha}}v_{\perp}^{2}+v^{\perp_{\beta}}\Pi_{\perp_{\beta}}^{\perp_{\alpha}}+v^{\perp_{\alpha}}\Pi_{\perp_{\beta}}^{\perp_{\beta}}\right)+$$
$$\frac{\partial}{\partial x^{\perp_{\alpha}}}\left(\frac{1}{2}mnv^{\perp_{\alpha}}v_{\parallel}^{2}+v^{\parallel}\Pi_{\parallel}^{\perp_{\alpha}}+v^{\perp_{\alpha}}\Pi_{\parallel}^{\parallel}\right)+$$
$$+\frac{\partial q^{\parallel}}{\partial x^{\parallel}}+\frac{\partial q^{\perp_{\alpha}}}{\partial x_{\alpha}^{\perp}}-qnv^{\parallel}E^{\parallel}-qnv^{\perp_{\alpha}}E^{\perp_{\alpha}}=\left(\frac{\delta\epsilon}{\delta t}\right)_{c}$$

$$\frac{1}{2}n\left(\frac{\partial}{\partial t}+v^{\parallel}\frac{\partial}{\partial x^{\parallel}}\right)T_{\parallel}+nT_{\parallel}\frac{\partial v^{\parallel}}{\partial x^{\parallel}}+\frac{\partial q^{\parallel}}{\partial x^{\parallel}}+\Pi_{\parallel}^{\parallel}\frac{\partial v^{\parallel}}{\partial x^{\parallel}}+\Pi_{\parallel}^{\perp_{\alpha}}\frac{\partial v^{\perp_{\alpha}}}{\partial x^{\parallel}} \tag{4.61}$$
$$n\left(\frac{\partial}{\partial t}+v^{\perp_{\alpha}}\frac{\partial}{\partial x^{\perp_{\alpha}}}\right)T_{\perp}+nT_{\perp_{\alpha}}\frac{\partial v^{\perp_{\alpha}}}{\partial x^{\perp_{\alpha}}}+\frac{\partial q^{\perp_{\alpha}}}{\partial x^{\perp_{\alpha}}}+\Pi_{\perp_{\beta}}^{\perp_{\alpha}}\frac{\partial v^{\perp_{\beta}}}{\partial x_{\alpha}^{\perp}}+\Pi_{\perp_{\alpha}}^{\parallel}\frac{\partial v^{\parallel}}{\partial x^{\perp_{\alpha}}}=$$
$$\left(\frac{\delta\epsilon}{\delta t}\right)_{c}+\left(\frac{1}{2}mv^{2}-\frac{1}{2}T_{\parallel}-T_{\perp}\right)\left(\frac{\delta n}{\delta t}\right)_{c}-v^{\perp_{\alpha}}\left(\frac{\delta\pi^{\perp_{\alpha}}}{\delta t}\right)_{c}-v^{\parallel}\left(\frac{\delta\pi^{\parallel}}{\delta t}\right)_{c}$$

Here we used $p_k = nT_k$ and assumed that viscous forces vary in time slowly such that terms $\partial \overleftrightarrow{\Pi}/\partial t$ can be neglected.

### 4.3.4 Effects of collisions

Evolution of heat flux $\vec{q}$ and viscous terms $\overleftrightarrow{\Pi}$ can be described by their own moments of Boltzmann equation, however at this point the hierarchy of moment equations is often closed by assuming an explicit form of both terms. Including effects of collisions with assumption of highly magnetized plasmas ($\omega_{c,j}/\nu_{ji} \gg 1$ where $\nu_{ji}$ represents frequency of collisions of species $j$), isotropic pressure $p_{\parallel} = p_{\perp} = p$ and quasineutrality, $n_e \approx n_i \approx n$, the remaining terms can be written in following form [54, 154, 76].

Momentum transfer due to collisions is the same, but with opposite sign, for electrons and ions $\left(\frac{\delta\vec{\pi}_e}{\delta c}\right)_c = -\left(\frac{\delta\vec{\pi}_i}{\delta c}\right)_c = \vec{R}$ and has two components, $\vec{R} = \vec{R}_u + \vec{R}_T$, frictional force $\vec{R}_u$ due to plasma resistivity and thermal force $\vec{R}_T$.

$$\vec{R}_u = 0.51\frac{m_e\nu_{ei}}{e}\vec{j}_{\parallel} \tag{4.62}$$
$$\vec{R}_T = -0.71n\nabla_{\parallel}T_e - \frac{3}{2}\frac{n\nu_{ei}}{\omega_{c,e}}\vec{b}\times\nabla_{\perp}T_e \tag{4.63}$$

The collisional heating is, again, of the same magnitude but opposite sign for electrons and ions, $\left(\frac{\delta\epsilon_e}{\delta c}\right)_c = -\left(\frac{\delta\epsilon_i}{\delta c}\right)_c = Q$.

$$Q = 3\frac{m_e}{m_i}n\nu_{ei}(T_i - T_e) \tag{4.64}$$

Further, change of $\left(\frac{\delta n}{\delta c}\right)_c$, $\left(\frac{\delta\vec{\pi}}{\delta c}\right)_c$ and $\left(\frac{\delta\epsilon}{\delta c}\right)_c$ due to ionisation, recombination and charge exchange can be taken into account.

Closure of the heat flux $\vec{q}$ has form

$$\vec{q}_j^T = \frac{nT_j}{m_j\omega_{c,j}}\left(-\frac{\omega_{c,j}}{\nu_{ji}}\kappa_\parallel^{j1}\nabla_\parallel T_j - \frac{\nu_{ji}}{\omega_{c,j}}\kappa_\perp^{j2}\nabla_\perp T_j + \frac{5}{2}\vec{b}\times\nabla_\perp T_j\right) \tag{4.65}$$

$$\vec{q}_v = 0.71nT_e v_\parallel + \frac{3nT_e\nu_{ei}}{2\omega_{ce}} \tag{4.66}$$

$$\vec{q}_i = \vec{q}_i^T;\ \ \vec{q}_e = \vec{q}_e^T + \vec{q}_v \tag{4.67}$$

where $j$ is index of plasma species ($i$ or $e$), $\vec{q}_j^T$ is thermal gradient heat flux, $\vec{q}_v$ frictional heat flux and $\kappa^{e1} = 3.2$, $\kappa^{i1} = 3.9$, $\kappa^{e2} = 4.7$ and $\kappa^{i2} = 2$. The term

$$\vec{q}_\perp^D = \frac{5}{2}\frac{nkT_\perp}{qB}\vec{b}\times\vec{\nabla}T \tag{4.68}$$

is not of collisional origin but it represents cross-field diamagnetic heat flux. The net heat flux comes from the difference in energies of particles having their guiding center in the regions with different temperatures. It is charge dependent and electron and ion contribution can cancel. Since the flux heads along isotemperature lines, it does not change temperature of the plasma. Similarly to the situation with diamagnetic cancellation in continuity equation, the compressibility of diamagnetic heat flux $\vec{\nabla}\cdot\vec{q}_\perp^D$ together with compressibility of diamagnetic velocity $T\vec{\nabla}\cdot\vec{v}_D$ cancel the advective contribution of diamagnetic velocity $\vec{v}_D\cdot\vec{\nabla}T$ and the temperature field is advected across magnetic field by $E\times B$ drift only [44].

Closure of $\overleftrightarrow{\Pi}$ is rather complicated and since it will not be directly involved in any physics discussed later we refer reader to its explicit form that can be found e.g. at p. 38 in [76].

### 4.3.5 Vorticity relation to plasma potential

In the tokamak edge, cross-field fluid velocity is in the lowest order given by $\vec{v}_E$. Vorticity of such flow, given by curl of velocity field, is

$$\vec{\Omega} = \vec{\nabla}\times\vec{v}_E = \vec{\nabla}\times\left(\frac{1}{B}\vec{b}\times\vec{\nabla}\phi\right). \tag{4.69}$$

After some algebra (see e.g. Appendix of [72]) this can be rewritten for vacuum field ($\vec{\nabla}\cdot B = 0$) to the form

$$\vec{\Omega} = \frac{1}{B}\left[\vec{b}(\vec{\nabla}_\perp^2\phi) - (\vec{b}\cdot\vec{\nabla})\vec{\nabla}_\perp\phi + (\vec{\nabla}_\perp\phi\cdot\vec{\nabla})\vec{b} - (\vec{\nabla}\ln B\cdot\vec{\nabla}_\perp\phi)\vec{b}\right]. \tag{4.70}$$

Because turbulent potential structures in the edge are much smaller compared to $\nabla\ln B \sim 1/R$, i.e. $k_\perp R \gg 1$, magnetic field variation in the third and fourth term on right-hand side of (4.70) can be neglected. The second term vanishes for perturbations with $k_\parallel \ll k_\perp$. Then the vorticity has only one nonzero component

$$\Omega = \Omega_\parallel = \frac{1}{B}\vec{\nabla}_\perp^2\phi. \tag{4.71}$$

Comparing this expression with Gauss's law

$$\nabla^2\phi = \nabla_\perp^2\phi + \nabla_\parallel^2\phi = -\frac{\rho_q}{\epsilon_0} \tag{4.72}$$

shows that when $k_\perp \gg k_\parallel$, the vorticity $\Omega$ represents (is proportional to) local charge density. This has consequences for the derivation of vorticity equation as will be shown in the next section.

### 4.3.6 Quasineutrality and vorticity equation

To describe behaviour of the electric field, we will first subtract continuity equation (4.53) for electron and ions to obtain conservation of charge density $\rho_q = e(n_e - n_i)$ (asumming $Z_i = 1$)

$$\frac{\partial \rho_q}{\partial t} + \vec{\nabla} \cdot (\rho_q(\vec{v}_E + \vec{v}_\parallel)) + \vec{\nabla} \cdot \vec{J} = \left(\frac{\delta \rho_q}{\delta t}\right)_c . \tag{4.73}$$

The local charge density can be changed in three ways. Either by compressibility of flux $\rho_q(\vec{v}_E + \vec{v}_\parallel)$ maintained by $E \times B$ and parallel drifts that advect both plasma species similarly, by compressibility of current density $\vec{J}$ given by polarization or diamagnetic current, or by other processes such as collisions. When the terms describing advection of charge density by $\vec{v}_E$ are expanded using Gauss's law (4.72),

$$\frac{\partial \rho_q}{\partial t} + \vec{v}_E \cdot \vec{\nabla} \rho_q \to \epsilon_0 \left(\frac{\partial}{\partial t} + \vec{v}_E \cdot \vec{\nabla}\right) \vec{\nabla}^2 \phi \tag{4.74}$$

are compared with compressibility of polarization current $\vec{J_p} = m_i q_i v_{p,i} + m_e q_e v_{p,e}$ in the lowest order,

$$\vec{J_p} = \frac{(n_i m_i + n_e m_e)}{B} \vec{b} \times \left(\frac{\partial}{\partial t} + \vec{v}_E \cdot \vec{\nabla}\right) \vec{v}_E \approx \frac{n m_i}{B} \vec{b} \times \left(\frac{\partial}{\partial t} + \vec{v}_E \cdot \vec{\nabla}\right) \vec{v}_E \tag{4.75}$$

$$\vec{\nabla} \cdot \vec{J_p} \approx -\frac{n m_i}{B} \left(\frac{\partial}{\partial t} + \vec{v}_E \cdot \vec{\nabla}\right) \vec{\nabla} \times \vec{v}_E \approx -\frac{n m_i}{B^2} \left(\frac{\partial}{\partial t} + \vec{v}_E \cdot \vec{\nabla}\right) \vec{\nabla}_\perp^2 \phi \tag{4.76}$$

we find that dominant terms describing compressibility of polarization drift (4.76) are similar to the advection by $\vec{v}_E$ (4.74), but larger by factor $n_i m_i/(\epsilon_0 B^2)$ [44] where $\epsilon_0$ is vacuum permittivity and $m_i$ and $m_e$ ion and electron mass, respectively. The factor is large in typical tokamak plasma, for $B \approx 1$ T and $n \approx 1 \times 10^{19}$ m$^{-3}$ we get $n m_i/(\epsilon_0 B^2) \approx 10^3$. The extra parallel derivative of potential in (4.74) compared to (4.76) does not overweight this factor, because parallel wavenumber of potential structures is usually significantly smaller than the perpendicular one. Then, neglecting also $(\delta \rho_q/\delta t)_c$ term in (4.73) and parallel advection of both charges, we can write quasineutrality equation in the common form

$$\vec{\nabla} \cdot \vec{J} = 0. \tag{4.77}$$

By making curl of momentum equation (4.45) and neglecting collisional terms, equation describing time evolution of vorticity $\vec{\Omega}$ can be obtained. Its field-aligned (parallel) component has form similar to the quasineutrality equation (4.77) [47],

$$-\frac{n m_i}{B} \left(\frac{\partial}{\partial t} + (\vec{v}_E + \vec{v}_\parallel) \cdot \vec{\nabla}\right) \Omega + \mathcal{C}(p) = -\vec{\nabla} \cdot \vec{J}_\parallel, \tag{4.78}$$

and numerical tracking of evolution of vorticity (charge density) in form of Eq. (4.78) is more precise than solution of continuity equations (4.53) separately for electrons and ions and their subsequent subtraction. The first term on the left hand side of (4.78) describes compressiblity of $J_p$ together with parallel advection of vorticity and the second term is just compressiblity of diamagnetic current for

isotroppic pressure. The form of parallel current $\vec{J}_\parallel$ will be discussed in Secs. 4.4.2-4.4.8. It has high impact on the process of turbulent generation and transport and we will devote Secs. 5.5 and 5.6 to modelling of two different assumptions on $\vec{\nabla}\cdot\vec{J}_d$.

We end this section with remark on Eq. (4.78) in which we have neglected, among others, terms of the form $\vec{J}_p\cdot\vec{\nabla}\ln n$. This is called *Boussinesq approximation* and it is usually introduced since it allows computationally much less demanding solver for Eq. 4.78. However, the term may have non-negligible values when density gradients are large, which is often the case in SOL. In [157] it is demonstrated that relaxing the Boussinesq approximation can change dynamics of turbulent structures, especially in later stages of their development, and increase their radial speed.

### 4.3.7 Generalized Ohm's law

In previous chapters, perpendicular drifts and associated perpendicular currents were discussed. To describe form of parallel current $J_\parallel = e(n_i v_{i,\parallel} - n_e v_{e,\parallel}) \approx en(v_{i,\parallel} - v_{e,\parallel})$ (with $Z_i = 1$), one can subtract momentum equations (4.45) for electrons and ions and after neglecting terms with factor $m_e/m_i$, small quadratic terms of the form $(\vec{v}\cdot\vec{\nabla})\vec{v}$, assuming slow variations such that $\partial/\partial t$ terms can be neglected and using collisional terms (4.62) and (4.63) he gets [54]

$$\eta_\parallel J_\parallel = -\nabla_\parallel\phi + \frac{1}{en}\nabla_\parallel p + \frac{1}{e}0.71\nabla_\parallel T_e. \tag{4.79}$$

This equation is referred as generalized Ohm's law and it describes response of the parallel current to parallel electric field and pressure and temperature gradients.

As already discussed in Sec. 3.4, two basic types of low frequency modes can be distinguished - drift modes and interchange/MHD-type modes [153]. Drift modes have high parallel electron mobility with near-Boltzman electron distribution and non-negligible $k_\parallel$ which plays important role in the dynamics through the gradients in (4.79). In the MHD-type modes parallel electric field is close to zero and in electrostatic case $k_\parallel$ is small such that time scale of parallel advection due to parallel gradients is smaller than growth-rate of relevant modes ($k_\parallel v_{th,e} \ll \omega$) [153]. Then, the gradients in (4.79) can be neglected in the first order and the transport is ambipolar with no net parallel current. These two modes can be found in different regions of tokamak edge plasmas. In the region inside LCFS, where magnetic field-lines are closed, $k_\parallel \neq 0$ can be easily established and the parallel dynamics is dominated by drift-type modes. In case of open field lines outside LCFS, any perturbation with $k_\parallel \neq 0$ quickly expands to the targets. Then, $k_\parallel$ can be considered very small (ideally flute mode with $k_\parallel = 0$) and dynamics of pressure-driven MHD modes becomes important. Mutual coupling of both types of dynamics in its nonlinear phase may become complicated, with growth of MHD modes later surpassed by drift dynamics [130], and it is still subject of a current research.

## 4.4 2D model of turbulence in tokamak geometry

Fluid modelling of edge plasma needs to resolve turbulence on temporal scales of ion cyclotron frequency $\omega_{ci} \approx 10^7$ Hz and spatial scales of the order of hybrid

gyroradius $\rho_s \approx 10^{-3}$ m in direction perpendicular to the magnetic field and scale of parallel gradients ($\approx 1$ m) in parallel direction. 3D modelling of the whole tokamak edge (edge thickness $\approx 10^{-2}$ m, perimeter $\approx 1$ m, connection length $\approx 10$ m) for a period sufficient to obtain reasonable turbulent statistics (tens of ms) is very demanding even for computational resources of current computers. Therefore, reduction of the problem from 3D to 2D is still often used. In this approach, dynamics parallel to the field lines is decoupled and reduced to simple analytical expressions (e.g. [63, 39, 87, 83]) dependent on quantities known in the 2D cross-field plane. Indeed, such description cannot cover gradients of magnetic field along field line and associated change of dynamics (e.g. stabilization of interchange modes on the inner midplane) nor effects of magnetic shear or nonlinear interaction of different parallel modes. Therefore, the parallel transport terms are fully localized to a certain parallel position, averaged over the whole field line or only some characteristic value is considered.

### 4.4.1 Slab coordinates

Reduced 2D equations are often described in Cartesian slab coordinates $x$,$y$, where $x-y$ plane is perpendicular to the magnetic field, which itself goes along third coordinate $s$. This largely simplifies terms in the fluid equations for computational use.

For all the terms except curvature operator, we will neglect toroidicity and use cylindrical coordinates. If characteristic size of the modelled problem (perpendicular size of turbulent structures $\delta$) is much smaller then tokamak minor radius, $\delta \ll r$, cylindrical coordinates can be expanded in the vicinity of reference radius $r = a$ and the slab coordinates are defined as [126]

$$x = r - a \tag{4.80}$$

$$y = a(\theta - \frac{\xi}{q}) \tag{4.81}$$

$$s = R\xi \tag{4.82}$$

where

$$q = \frac{\mathrm{d}\xi}{\mathrm{d}\theta} = \frac{rB}{RB_p} \tag{4.83}$$

is safety factor describing field line pitch, $\theta$ and $\xi$ are poloidal and toroidal angle, respectively, and $B_p$ is poloidal component of magnetic field. $x$ coordinate then represents radial coordinate and $y$ represents poloidal coordinate with correction to toroidal position that ensures that both coordinates are perpendicular to $\vec{b}$ and $s$, respectively. Moving in toroidal direction, poloidal position of a field line changes with rate (4.83). Term $-\xi/q$ then shifts $y$ to compensate this field line rotation:

$$\vec{b}\cdot\vec{\nabla}x = \vec{b}\cdot\vec{\nabla}r = 0 \tag{4.84}$$

$$\vec{b}\cdot\vec{\nabla}y = a\left(\vec{b}\cdot\vec{\nabla}\theta - \frac{1}{q}\vec{b}\cdot\vec{\nabla}\xi + \frac{\xi}{q^2}\frac{\partial q}{\partial r}\vec{b}\cdot\vec{\nabla}r\right) = \vec{b}\cdot(\vec{\nabla}\theta - \frac{1}{q}\vec{\nabla}\xi) = 0 \tag{4.85}$$

$$\vec{b}\cdot\vec{\nabla}s = R\vec{b}\cdot\vec{\nabla}\xi = R\frac{1}{R} = 1. \tag{4.86}$$

Note that the coordinates are not orthogonal if magnetic shear is present. When $\partial q(r)/\partial r \neq 0$, $y$ coordinate changes with radius $r$ and

$$\vec{\nabla}x \cdot \vec{\nabla}y = a(\vec{\nabla}r \cdot \vec{\nabla}\theta - \frac{1}{q}\vec{\nabla}r \cdot \vec{\nabla}\xi + \frac{\xi}{q^2}\frac{\partial q}{\partial r}\vec{\nabla}r \cdot \vec{\nabla}r) = \frac{as}{Rq^2}\frac{\partial q}{\partial r} = S \neq 0 \quad (4.87)$$

Metric tensor in such situation is [126]

$$g^{ij} = \begin{pmatrix} 1 & S & 0 \\ S & 1+S^2 & 0 \\ 0 & 0 & 1 \end{pmatrix} \quad (4.88)$$

and

$$\vec{\nabla}_\perp^2 = \left(\frac{\partial}{\partial x} + S\frac{\partial}{\partial y}\right)^2 + \frac{\partial^2}{\partial^2 y}. \quad (4.89)$$

The dissipative terms then depend on toroidal position and act on structures differently on different positions along field line [126]. In the following chapters, we will neglect the role of the shear ($S \approx 0$) and use fully orthogonal slab coordinates $p$ and $r$.

Advection of quantity $g$ by drift of the form $v \sim \vec{b} \times \vec{\nabla} f$ that appears in fluid equations is proportional to the expression $\vec{b} \times \vec{\nabla} f \cdot \vec{\nabla} g = \vec{b} \cdot \vec{\nabla} f \times \vec{\nabla} g$. For perturbations with $k_\parallel \ll k_\perp$, parallel derivation $\partial/\partial s$ can be neglected and after some algebra we find that [126]

$$\vec{b} \times \vec{\nabla} f \cdot \vec{\nabla} g = \left(\frac{\partial f}{\partial x}\frac{\partial g}{\partial y} - \frac{\partial g}{\partial x}\frac{\partial g}{\partial y}\right) + \mathcal{O}\left(\frac{k_\parallel}{k_\perp}\right) = [f, g] + \mathcal{O}\left(\frac{k_\parallel}{k_\perp}\right). \quad (4.90)$$

The square brackets $[,]$ stand for Poisson brackets.

Magnetic curvature is another toroidal effect that needs to be discussed. As was shown in Sec. 4.3.1, presence of the curvature gives rise to compressibility of $v_E$ (Eq. (4.48)) and $v_D$ (Eq. (4.48)). These terms drive the vorticity equation (4.78) and it is therefore crucial to keep them even in 2D slab coordinates. To do this, first-order toroidicity correction in form of inhomogeneous magnetic field (2.4) must be included. Curvature operator reduces in low-$\beta$ limit by $\vec{\nabla} \times \vec{b}$ term in (4.51) to

$$\mathcal{C} \approx \frac{1}{B}\vec{b} \times \vec{\nabla} \ln B \cdot \vec{\nabla}. \quad (4.91)$$

To obtain curvature operator in slab coordinates we will substitute magnetic field (2.4) into (4.91), neglect dependence $\partial\theta/\partial s \approx 0$ and get

$$\mathcal{C} = -\frac{1}{R}\left[\sin\theta\frac{\partial}{\partial x} + (\cos\theta + S\sin\theta)\frac{\partial}{\partial y}\right]. \quad (4.92)$$

If the region is located at the outer midplane ($\theta = 0$) with magnetic field without shear ($S = 0$), curvature operator acting on any plasma quantity $q$ reduces to simple derivative

$$\mathcal{C}(q) = -\frac{1}{R}\frac{\partial}{\partial y}q = [\frac{1}{B(x)}, q]. \quad (4.93)$$

Discussion of coordinates used for 3D models can be found e.g. in [131]

### 4.4.2 Closed field lines and Hasegawa-Wakatani model of parallel transport

In the region of closed field lines, parallel gradients of plasma quantities do not vanish [127]. Famous Hasegawa-Wakatani (H-W) model [63] describes behaviour of a single parallel mode (4.79) in these conditions. If collisional damping is stronger then Landau damping, isothermal approximation $\nabla_\parallel T_e \approx 0$ may be introduced [63]. Then (4.79) can be rewritten in the form

$$\nabla_\parallel J_\parallel = -\frac{T_e}{\eta_\parallel e}\nabla_\parallel^2 \left( \frac{e\phi}{T_e} - \ln n \right). \tag{4.94}$$

Next, fluctuations are separated from profiles, $\tilde{q} = q - \langle q \rangle$ for all plasma quantities $q$. Second derivation of the profiles vanishes $\nabla_\parallel^2 \langle q \rangle = 0$. If the parallel structure of fluctuations is dominated by single parallel mode $k_\parallel$, we may replace $\nabla_\parallel^2 q \to -k_\parallel^2 \tilde{q}$ and write (4.94) as

$$\nabla_\parallel J_\parallel \approx \frac{T_e k_\parallel^2}{\eta_\parallel e} \left( \frac{e\tilde{\phi}}{T_e} - \widetilde{\ln n} \right). \tag{4.95}$$

Note, that $\widetilde{\ln n}$ denotes fluctuation of the density logarithm and for small fluctuations it is often linearised by $\widetilde{\ln n} \approx \tilde{n}/\langle n \rangle$.

Classical Hasegawa-Wakatani approach treats only single parallel mode and neglects its interaction with other modes. This largely simplifies the problem and allows its modelling in 2D. More complex 3D models, however, exist, including electromagnetic effects, interaction of different parallel modes and gyro-effects (e.g. [129]). In this thesis we will focus on the 2D case and simulations of drift waves will be presented in Sec. 7.6.1.

Generalization of (4.95) for the non-isothermal case was derived in [83]. It does not neglect collisional term $\frac{1}{e}0.71\nabla_\parallel T_e$ in (4.79) which modifies (4.95) for small perturbations to

$$\nabla_\parallel J_\parallel \approx \frac{\langle T_e \rangle k_\parallel^2}{\eta_\parallel e} \left( \frac{e\tilde{\phi}}{\langle T_e \rangle} - \frac{\tilde{n}}{\langle n \rangle} - 1.71\frac{\tilde{T}_e}{\langle T_e \rangle} \right). \tag{4.96}$$

### 4.4.3 Equivalent electric circuit

To illustrate behaviour of parallel currents in SOL, useful idea of equivalent electric circuit was introduced in [88]. It is schematically illustrated in Fig. 4.1. Basic property of blobs in SOL is their dipole structure that creates poloidal electric field responsible for radial $E \times B$ motion of the structure. This charge polarization can be conceived as a current source $I$ that generates dipole structure of parallel currents. There are different possible ways how the current paths close the electric circuit, such as by the contact with material surface, due to collisional dissipation or perpendicular polarization currents. Most relevant closures will be discussed in the following sections.

### 4.4.4 Turbulent structures in touch with material surface

If plasma in SOL follows magnetic field lines that intersect material surfaces, simplified model of $\vec{b} \cdot \nabla J_\parallel$ can be derived from the properties of the sheath layer that

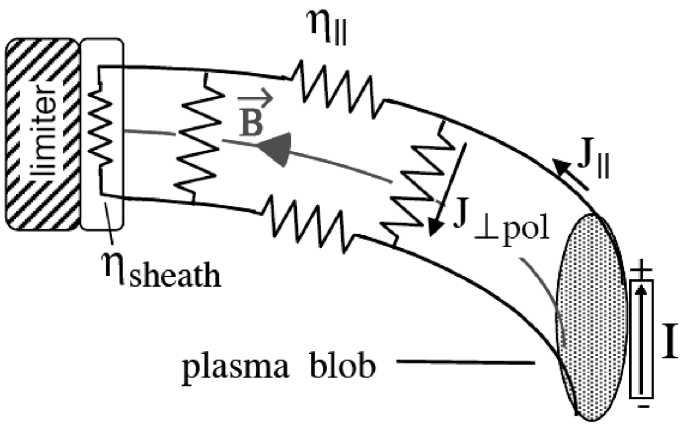


Figure 4.1: Equivalent electric circuit and illustration of possible current paths. Dipole structure of the blob (grey area) acts as a current source $I$. Closure of parallel current $J_{\parallel}$ on material surface and by perpendicular polarization current $J_{\perp pol}$ is illustrated. Reproduced from [88].

forms close to the surfaces [47]. Parallel mobility of electrons is higher then that of ions and more electrons then ions are lost to the wall. This leaves plasma with positive potential compared to the wall. Due to Debye shielding in the plasma, the potential drop is restricted to the distance of several Debye lengths from the wall, to the layer referred as sheath. Bohm sheath criterion formulates condition necessary for the sheath to establish - ions must enter the layer with their prallel velocity $v_{i,\parallel}$ higher then the ion sound speed [146, 30],

$$v_{i,\parallel} > c_s = \sqrt{\frac{kT_e}{m_i}}. \tag{4.97}$$

This condition guarantees, that there will be always more ions in the sheath than electrons and the potential of plasma will remain positive compared to the wall. In order to describe influence of the material surface in the fluid model, simple model is often used. Assuming that the electron distribution is Boltzmann, $v_{i_\parallel} = c_s$ and the surface is electrically floating, the parallel electric current at the boundary is [47]

$$J_{\parallel} = -enc_s \left(1 - \exp\left(-\frac{e\delta\phi}{T_e}\right)\right) \vec{n} \cdot \vec{b} \tag{4.98}$$

where $\delta\phi$ is deviation of the plasma potential with respect to the surface potential $\phi_s = 2.8T_e/e$ and $\vec{n}$ is the surface unit normal vector. $\nabla_{\parallel} J_{\parallel}$ needed in the vorticity equation (4.78) is then taken as an average value of its divergence along the whole field line (neglecting plasma resistivity) and therefore it is given by difference of the currents $J_{\parallel}$ at both field line ends. Since the current has opposite direction at both ends, the closure is

$$\langle \vec{\nabla} \cdot \vec{J}_{\parallel} \rangle \approx \langle \vec{b} \cdot \nabla J_{\parallel} \rangle = \frac{enc_s}{L_{\parallel}} \left(1 - \exp\left(-\frac{e\delta\phi}{T_e}\right)\right) \tag{4.99}$$

where $L_{\parallel}$ is connection length from the midplane to the target or half of the connection length from target to target in asymmetric case.

### 4.4.5 Subsonic advection along open field lines

In case that the particles' mean free path in parallel direction is small compared to the connection length $L_\parallel$, one may assume that $\nabla_\parallel J_\parallel$ given by the sheath boundary condition are located near the field line ends and uncorrelated with its value at the outer midplane (location of the turbulent drive). Then, $(\nabla_\parallel J_\parallel)|_{midplane} \approx 0$. Then, subsonic advection of vorticity is the dominant mechanism of parallel vorticity losses in (4.78). Such losses may be described by term [39]

$$\left(\frac{\partial \Omega}{\partial t}\right)_\parallel \approx -v_\parallel \nabla_\parallel \Omega \approx -\frac{c_s M_\parallel}{L}\Omega = -\tau_\Omega^{-1}\Omega \tag{4.100}$$

where $M_\parallel$ is parallel Mach number, in SOL of TCV experimentally determined as $M_\parallel \approx 0.5$, and $\tau_\Omega$ is characteristic time of parallel vorticity losses. $L$ is characteristic parallel length scale of the structures, taken as connection length from midplane to divertor target in [39]. We have shown in [65] that due to ballooning nature of the interchange turbulence that localized mainly around outer midplane, $L$ should be rather related to the length of the field line inside the unstable region, roughly estimated as $2\pi R q_{95}/6$ with factor 1/6 describing extent of the ballooning region.

In some cases, the $\nabla_\parallel J$ is completely neglected and vorticity advection is not taken into account. This is called as inertial, hydrodynamic or Rayleigh-Taylor limit and is discussed e.g. in [88].

Simulations show that sheath-connected structures tend to form radially elongated 'fingers' (see e.g. [125]), while sheath-disconnected structures are more rounded and drop-like (see e.g. [47, 48]). This can be understood as a consequence of difference in parallel damping terms in vorticity equation (4.78). When collisional dissipation and curvature drive are neglected and Fourier transform of potential is made ($\phi \to \tilde{\phi}_k$, $\Omega \to k^2\tilde{\phi}_k$), vorticity equation reveals that [39]

$$\frac{\mathrm{d}\ln\tilde{\phi}_k}{\mathrm{d}t} \approx \tau_\Omega^{-1} \tag{4.101}$$

for sheath-disconnected structures described by damping (4.100) and

$$\frac{\mathrm{d}\ln\tilde{\phi}_k}{\mathrm{d}t} \approx \tau_\phi^{-1}k^{-2} \tag{4.102}$$

for sheath-connected structures described by damping (4.99). Large structures in sheath-connected regime are apparently quickly suppressed with damping rate proportional to the square of their size.

### 4.4.6 Parallel currents in the X-point region

As blobs expand toroidally along magnetic field lines, their wave-form in poloidal plane deforms due to magnetic shear. When the magnetic shear is high, the relevant flux tube is stretched [35] as illustrated in Fig. 4.2(right). This situation is most relevant for the X-point region, where poloidal magnetic field component is very small and the local magnetic shear very large.

When the flux tube thickness drops below certain threshold, bipolar structure of parallel currents can be effectively short-circuited by cross-field currents. Namely the role of ion polarization currents and electron collisional terms has been studied

(see [87] and references therein). Note, that stretching the flux tube enhances processes that contain $\vec{\nabla}_\perp$ terms, such as cross-field polarization currents ($\sim \vec{\nabla}_\perp^2 \phi$) or magnetic diffusion ($\sim \eta_\parallel \vec{\nabla}_\perp^2 A_\parallel$) [88]. In the X-point, (4.79) can be simplified to

$$\nabla_\parallel J_\parallel \approx \frac{-ik_\parallel}{L_\parallel \eta_\parallel} \phi \tag{4.103}$$

In the electrostatic limit [105], where the spatial scales are given by dispersion relation $k_\parallel^2 \sigma_\parallel = -k_\perp^2 \sigma_\perp$ (with $\sigma = 1/\eta$ denoting plasma conductivity), one gets closure for vorticity equation due to X-point influence

$$\nabla_\parallel J_\parallel \approx \frac{\sqrt{\sigma_\parallel \sigma_\perp}}{L_\parallel \delta_b} \phi \tag{4.104}$$

where $\sigma_\perp$ is cross-field plasma conductivity given by the ion polarization current or by the electron collisional process. $\delta_b \approx 1/k_\perp$ is perpendicular size of the blob. The transition of X-point closure (4.104) to the sheath-connected limit (4.99) was studied in [106] using two coupled 2D simulations in the midplane and X-point region. They show that X-point closure is relevant when ellipticity of flux tube deformation in the X-point region $\epsilon \approx k_{\perp_x}/k_{\perp_y}$ is

$$\epsilon > \sqrt{\frac{L_\parallel^2}{\rho_s R}} \left( \frac{\rho_s}{\delta_b} \right)^{5/2} \tag{4.105}$$

where $R$ is tokamak major radius and $\rho_s$ hybrid ion gyroradius (5.7).

### 4.4.7 Parallel currents in the large-$\beta$ case

In case plasma pressure $p$ inside turbulent structure is large compared to magnetic pressure $p_M = B^2/(2\mu_0)$, i.e. value of blob's $\beta$

$$\beta_b = \frac{2nT\mu_0}{B^2} \tag{4.106}$$

is large, magnetic field may be dragged by radially moving turbulent structures. This situation is illustrated in Fig. 4.2. Magnetic field lines bended by moving blobs may touch material surface at midplane even without touching divertor targets. The 2D description of these 3D magnetic effects was originally developed in the study of material ablation from pellets [124, 118]. As the bending (originally localized only at outer midplane due to ballooning) spreads along the field line, parallel current associated with Alfven waves is emitted at its ends. In order to maintain quasineutrality, this current is compensated by current flowing along field lines,

$$J_\parallel = -\frac{1}{\mu_0} \vec{\nabla}_\perp^2 A_\parallel \tag{4.107}$$

where $A_\parallel$ is parallel part of vector magnetic potential. Parallel electric field remains negligible

$$E_\parallel = -ik_\parallel \phi + i\omega A_\parallel \approx 0 \tag{4.108}$$

with $k_\parallel$ and $\omega$ given by dispersion relation of Alfvén waves,

$$\frac{\omega}{k_\parallel} = v_A = \frac{B}{\sqrt{\mu_0 mn}}. \tag{4.109}$$

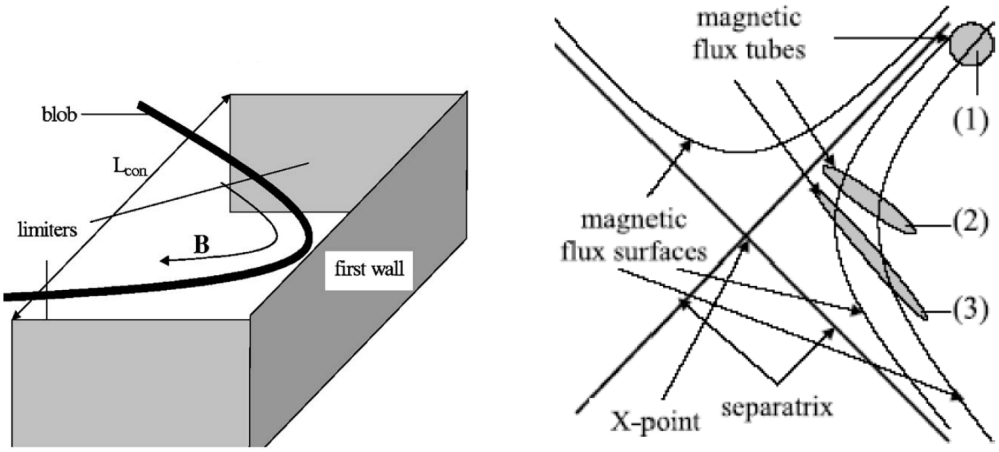


Figure 4.2: Left: Illustration of bending of magnetic field line dragged by high-$\beta$ blob. Reproduced from [157]. Right: Illustration of flux tube deformation close to the X-point. Points (1),(2) and (3) represent flux tube at different toroidal positions. Reproduced from [88].

Similarly to the already discussed case of sheath-connected blobs, the $\nabla_\parallel J_\parallel$ term is approximated as an average value over the length of the magnetic field perturbation $L_b$, i.e. given by (4.107) at the ends of perturbation. If symmetry of the problem is assumed, currents at both ends are the same, but with opposite direction, which gives factor 2. After substitution of 4.108 into 4.107 and averaging one finds that [87]

$$\nabla_\parallel J_\parallel \approx -\frac{2}{\mu_0 v_A L_b}\vec{\nabla}_\perp^2\phi = -\frac{2B}{\mu_0 v_A L_b}\Omega. \tag{4.110}$$

The $v_A$ is evaluated at the end point of spreading magnetic perturbation i.e., with background density $\langle n\rangle$. Writing this expression in dimensionless form, with vorticity normalized by $\omega_{ci}$, $\Omega \to \omega_{ci}\Omega'$, we get

$$\nabla_\parallel J'_\parallel = -\frac{2v_A}{L_b}q\langle n\rangle\Omega'. \tag{4.111}$$

Then, the term $\frac{1}{qn}\nabla_\parallel J'_\parallel$ is similar to advective term (4.100) up to the factor given by ratio of $v_A$ and $c_s$. For SOL plasma, this ratio is typically very large and loss of vorticity by Alfvén waves (4.111) should dominate if the $\beta$ is sufficiently large to allow perturbations of magnetic field induced by turbulent structures.

### 4.4.8 Dissipative closure

In this closure, collisional dissipation of vorticity $\mu_\Omega$ (3.12) is taken into account, effectively giving [88]

$$\nabla J_\parallel \approx \mu_\Omega \vec{\nabla}_\perp^4\phi. \tag{4.112}$$

Although the collisional diffusion coefficient $\mu_\Omega$ is quite small, it is important to keep numerical simulations stable by suppressing numerical noise and structures with spatial scales below resolution of the simulation. Especially when the ion polarization current is dominant, vorticity quickly cascades to small scales [88].

Therefore, the diffusion term (4.112) is often added to the simulations with ad hoc value in order to cut-off the vorticity cascade.

# 5. Modelling of interchange turbulence in SOL

## 5.1 ESEL model

ESEL [43, 44, 48] is 2D electrostatic model of interchange turbulence in tokamak edge developed at Technical University of Denmark. Presently, we use and further develop this model for simulations of edge turbulence in tokamaks ASDEX, JET, TCV and COMPASS. Some of the simulations will be presented in this chapter.

ESEL consists of three fluid equations for time evolution of plasma vorticity $\Omega$ (Eq. (4.78)), density $n$ (Eq. (4.54)), electron temperature $T_e$ (blue terms in (4.61)) in the drift plane perpendicular to magnetic field and of additional equation for calculation of plasma potential $\phi$ from the vorticity field (Eq. (4.71)). Plasma momentum equation (4.45) is reduced to the algebraic expression for cross-field drifts (4.46) - $E \times B$, diamagnetic and polarization drift,

$$\vec{v}_\perp = \vec{v}_E + \vec{v}_D + \vec{v}_P. \tag{5.1}$$

The polarization drift is neglected in the temperature and density equation. Compressiblity of polarization current, however, gives rise to the vorticity equation in form

$$\left(\frac{\partial}{\partial t} + \frac{1}{B}\vec{b} \times \vec{\nabla}\phi \cdot \vec{\nabla}\right) \Omega - \mathcal{C}(nT_e) = \Lambda_\Omega \tag{5.2}$$

where $\Lambda_\Omega$ describes collisional dissipation and parallel losses and $\mathcal{C}$ represents curvature operator (4.51).

The continuity and temperature equations have form

$$\left(\frac{\partial}{\partial t} + \frac{1}{B}\vec{b} \times \vec{\nabla}\phi \cdot \vec{\nabla}\right) n + \qquad n\mathcal{C}(\phi) - \mathcal{C}(nT_e) \qquad = \Lambda_n, \tag{5.3}$$

$$\left(\frac{\partial}{\partial t} + \frac{1}{B}\vec{b} \times \vec{\nabla}\phi \cdot \vec{\nabla}\right) T_e + \quad \tfrac{2}{3}T_e\mathcal{C}(\phi) - \tfrac{7}{3}T_e\mathcal{C}(T_e) - \tfrac{2}{3}\tfrac{T_e^2}{n}\mathcal{C}(n) \quad = \Lambda_{T_e}. \tag{5.4}$$

Advection of all three quantities in (5.2)-(5.4) is due to $E \times B$ drift only and generated structures fulfil $k_\perp \gg k_\parallel$. Therefore, one may utilize assumptions from Sec. 4.3.5 and relate plasma potential to the vorticity as

$$\Omega = \nabla_\perp^2 \phi. \tag{5.5}$$

In this chapter all quantities are dimensionless (unless otherwise specified) with Bohm normalization

$$\vec{x}/\rho_s \to \vec{x}\ ;\ t\omega_{ci} \to t\ ;\ B/B_0 \to B\ ;\ n/n_0 \to n\ ;\ T_e/T_{e,0} \to T\ ;\ e\phi/T_{e,0} \to \phi \tag{5.6}$$

with ion sound speed $c_s$, hybrid gyroradius $\rho_s$ (Larmor radius evaluated at ion mass and electron temperature) and ion cyclotron frequency $\omega_{ci}$ evaluated at $T_{e,0}$,$n_0$ and $B_0$,

$$\rho_s = \frac{\sqrt{eT_{e,0}m_i}}{q_iB_0};\ \ \omega_{ci} = \frac{q_iB_0}{m_i};\ \ c_s = \rho_s\omega_{ci}. \tag{5.7}$$

Normalization of density, $n_0$, temperature, $T_0$, and magnetic field, $B_0$, is typically chosen as values at the position of LCFS.

Sink terms $\Lambda_n$, $\Lambda_T$, $\Lambda_\Omega$ describe collisional dissipation and parallel losses,

$$\Lambda_n = D_n \nabla_\perp^2 n + \left(\frac{\partial n}{\partial t}\right)_\parallel, \tag{5.8}$$

$$\Lambda_\Omega = D_\Omega \nabla_\perp^2 \Omega + \left(\frac{\partial \Omega}{\partial t}\right)_\parallel, \tag{5.9}$$

$$\Lambda_T = D_T \nabla_\perp^2 T + \left(\frac{\partial T}{\partial t}\right)_\parallel. \tag{5.10}$$

The dissipative term represents neoclassical collisional diffusion (3.11)-(3.14) and parallel losses estimated from 0D analytical model are considered as advective for density and vorticity and diffusive for temperature, with characteristic time scales of parallel transport $\tau_n$, $\tau_\Omega$ and $\tau_T$ [39],

$$\left(\frac{\partial n}{\partial t}\right)_\parallel = \frac{n}{\tau_n} = -\frac{n v_\parallel}{L_{\parallel,n}}, \tag{5.11}$$

$$\left(\frac{\partial \Omega}{\partial t}\right)_\parallel = \frac{\Omega}{\tau_\Omega} = -\frac{\Omega v_\parallel}{L_{\parallel,\Omega}}, \tag{5.12}$$

$$\left(\frac{\partial T}{\partial t}\right)_\parallel = \frac{T}{\tau_T} = -\frac{2}{3}\frac{T \chi_{\parallel e}}{L_{\parallel,T}^2}. \tag{5.13}$$

Term $D_T$ covers both electron and ion energy dissipation, $D_{\chi,e}$ and $D_{\chi,i}$, respectively,

$$D_T = D_{\chi,e} + \Theta_{i,e} D_{\chi,i} \tag{5.14}$$

where the coupling term $\Theta_{i,e}$ ranges from 0 to 1 and describes coupling between electron and ion energy channels [39]. Speed of parallel advection $v_\parallel = M_\parallel c_S$ is chosen according to experiments [72, 39] that show Mach number of parallel fluxes in the SOL, $M_\parallel \approx 0.5$. The characteristic parallel length of the parallel transport processes is in the lowest approximation (assuming simple SOL conditions) taken as the connection length $L_\parallel$ from midplane to the solid target. Electron heat diffusivity is approximated by Spitzer-Harm expression $\chi_{\parallel e} \approx \chi_{\parallel e}^{SH} = 3.2 v_{T,e}^2 / \nu_{ee}$ given by electron thermal velocity $v_{T,e}$ and electron-electron collisional frequency $\nu_{ee}$.

ESEL uses Cartesian slab coordinates with simulation region located at the outer midplane (Fig. 5.1). In these coordinates curvature operator and convective derivative may be simplified to a form of Poisson bracket - Eqs. (4.90) and (4.93). To compute the Poisson bracket, Arakawa scheme [5] is used. This conserves mean square vorticity and mean kinetic energy of the flow, preventing computational instability that might otherwise arise from the nonlinear terms. The equations are advanced in time by a 3rd order explicit linear multistep method (7.55).

### 5.1.1 Edge, SOL and wall shadow regions

As an analogue to typical dependency of $L_\parallel$ in tokamak edge on radial coordinate, the simulation region in ESEL is divided into three parts as illustrated in Fig. 5.1.

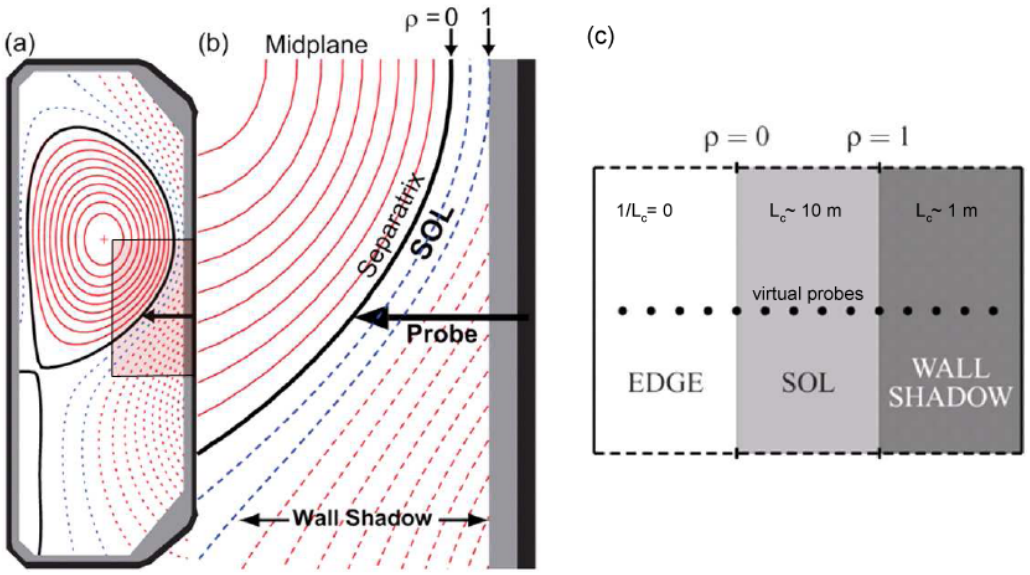


Figure 5.1: Sketch of tokamak edge geometry (a) with black rectangle zoomed in (b). ESEL simulation region (c) approximates geometry of the tokamak edge.

The innermost part represents edge region inside LCFS with $L_\parallel \to \infty$, effectively setting parallel sinks to zero. In the edge region nonzero value of $k_\parallel$ is predicted [127] and parallel sinks should be represented by drift wave terms (e.g. (4.95) in H-W closure). These drift waves effects are, however, neglected in the ESEL model. It is argued that turbulent transport in SOL is dominated by convective structures of interchange nature that are born in the vicinity of LCFS and in the first approximation, their properties are decoupled from the properties of drift waves that may create their initial perturbation. Validity of this assumption is still under investigation. While some simulations show that drift wave nonlinearity may outweigh the interchange drive [130, 3], comparison with experimental measurements on TCV [39, 46, 50] and JET [39] shows reasonable agreement between some properties of the turbulence generated by ESEL model and those measured by reciprocating probes.

Second region, with $L_\parallel \approx 10$ m, represents the SOL itself. Continual outflow of plasma along field lines to divertor creates large radial pressure gradient on the inner boundary of the region (there are no parallel sinks in the edge region) i.e. around LCFS. Since $(\partial p/\partial r) \cdot (\partial B/\partial r) > 0$, convective structures grow by interchange instability and propagate radially into the SOL. Radial density profiles typically flatten in the outter part of the SOL and sometimes designations 'near SOL' (steep density gradient close to the LCFS) and 'far SOL' (flatter density gradient, outward part of SOL) is used.

In the outermost part of the simulation, called wall shadow, $L_\parallel \approx 1$ m. Wall shadow represents region slightly below the tokamak midplane, where the field lines hit tokamak wall on one end and divertor target on the other. Due to close distance to the wall ($\approx 1\ m$) plasma losses significantly increase compared to the SOL and blobs quickly loose their density and energy. At the inner boundary of the region, pressure gradient increases similarly to the edge-SOL boundary and

new vorticity may be generated by interchange drive.

To describe radial variations of processes in SOL for different discharges, it is convenient to introduce dimensionless coordinate $\rho$ as

$$\rho = \frac{r - r_{LCFS}}{\Delta_{SOL}} \tag{5.15}$$

where $r_{LCFS}$ is radial position of the LCFS and $\Delta_{SOL}$ is SOL width. In the following we will use symbol $\rho$ in this sense, instead of $\rho$ as mass density as introduced in the theoretical chapter 4.

### 5.1.2 Boundary conditions

ESEL simulation region is located at the outboard tokamak midplane. Neglecting ballooning nature of interchange turbulence, i.e. assuming that $B$ in slab coordinates is independent on poloidal coordinate $p$, periodicity of the simulation in poloidal direction in all four quantities $(n, T, \Omega, \phi)$ can be used. Indeed, this brings additional requirement that size of the simulation domain must be larger than poloidal size of blobs. This condition has to be verified a posteriori and prevents mutual interaction of different parts of the same blob.

In order to maintain large radial gradients observed in experiment, either Dirichlet or Neumann boundary conditions (BC) are used. Dirichlet BCs placed at inner boundary

$$n(r = r_{min}) = n_{BC} \; ; \; T(r = r_{min}) = T_{BC} \; ; \; \Omega(r = r_{min}) = 0 \; ; \; \phi(r = r_{min}) = \phi_{IN} \tag{5.16}$$

maintain influx of density and temperature into the simulation by diffusive flux driven by local radial gradients,

$$\Gamma_{n,BC} = -D_n \frac{n(r_{min} + \delta_r) - n_{BC}}{\delta_r} \; ; \; \Gamma_{T,BC} = -D_T \frac{T(r_{min} + \delta_r) - T_{BC}}{\delta_r}. \tag{5.17}$$

Dirichlet conditions on $\Omega$ and $\phi$, that implicate their zero poloidal derivatives on the boundary, then guarantee that there will be no $E \times B$ radial motion through the boundary. Indeed, presence of the boundary inside the edge region is not physical, but it helps to maintain profiles of $n$ and $T$ by balancing parallel losses in SOL by the diffusive influx. Moreover, shear of poloidal velocity $v_p$ at the boundary of edge and SOL region is assumed to decorrelate fluctuations from both regions, thus efficiently decoupling turbulence in SOL from direct influence of the inner boundary.

At the outer boundary, Neumann BCs used for density and temperature

$$\frac{\partial n}{\partial r}(r = r_{max}) = \frac{\partial T}{\partial r}(r = r_{max}) = 0 \tag{5.18}$$

allow large relative density fluctuations caused by intermittent presence of blobs. On the other hand, it does not restrict $n$ and $T$ values from bellow and since ESEL does not incorporate any atomic processes or neutral recycling that would keep $n$ and $T$ at some minimal level, the values at the outermost part of the wall shadow region may drop below realistic levels. Vorticity at the outer boundary is again kept at zero level by Dirichlet condition

$$\Omega(r = r_{max}) = 0. \tag{5.19}$$

There are two different outer BC typically used for $\phi$ [72] - either the value of $\phi$ is set to zero,

$$\phi(r = r_{max}) = 0, \tag{5.20}$$

or zero poloidal velocity is assumed

$$\frac{\partial \phi}{\partial r}(r = r_{max}) = 0. \tag{5.21}$$

Both BC conditions are not fully equivalent, they, however, produce very similar turbulent statistics in SOL. This is due to the fact that Eqs. (5.2)-(5.4) are dependent only on spatial derivatives of $\phi$ and not on the absolute value of $\phi$ itself. If potential field $\phi(p, r)$ is obtained by solving Eq. (5.2), potential field $\phi'(p, r)$

$$\phi'(p, r) = \phi(p, r) + A_r r + A_p p + B, \tag{5.22}$$

where $A_r$, $A_p$ and $B$ are constants, is solution of Eq. (5.2) as well. Indeed, due to poloidal periodicity we require $A_p = 0$. Analysis of ESEL equations shows that using $\phi'$ instead of $\phi$ does not change turbulent dynamics, changing only mean poloidal rotation of the plasma:

$$v'_p(p, r) = v_p(p, r) + A_r. \tag{5.23}$$

Therefore, for the case of BC (5.20) such $A_r$ and $B$ may be found that $\langle \partial \phi'(p, r = r_{max})/\partial r \rangle_p = \phi_{IN}$ and $\phi'(p, r = r_{min}) = 0$, getting $\phi'$ very close to the solution of Eq. (5.2) with Neumann BC (5.21). Here $< \cdot >_p$ means averaging over poloidal direction.

Note that this degree of freedom in $\phi$ (and $v_p$) may implicate some problems during comparison with experiment, because change $v_p \to v'_p$ naturally changes time scales on all virtual probes in simulation (fixed in space) where $v_p \neq 0$.

Discussion in previous paragraphs was based on assumption that there is no term in Eqs. (5.2)-(5.4) that depends on absolute value of $\phi$. However, if assumption of sheath connected blobs is used (see Sec. 4.4.4) instead of sheath-disconnected blobs with vorticity sink dominated by subsonic advection (4.100), dependence of parallel vorticity damping on $\phi$ arises as a consequence of Bohm's sheath criterion. Then transformation to $\phi'$ (5.22) would lead to different vorticity damping than the $\phi$ itself. In such case it is natural to prefer Dirichlet condition (5.20) at the outer boundary because it will keep value of $\phi$ fixed (corresponding to fixed value of sheath potential), whereas Neumann condition (5.21) would allow large fluctuations of $\phi$ leading to large fluctuations of the vorticity damping term (4.99). Reasonable radial profile of $v_p$ will be maintained by the sheath dissipation term itself, because for slow fluctuations it tends to minimize parallel damping, keeping mean potential near the level $< \phi > \approx \alpha < T_e >$. More on this topic will be discussed in Sec. 5.6.

### 5.1.3 Previous comparison of ESEL with experimental measurements

In the past six years results of ESEL have been compared with experimentally measured data on several tokamaks. Most often data from reciprocating Langmuir probes have been used, since it is most suitable diagnostics to measure fluctuations

of SOL plasma on short time and spatial scales that are needed to resolve turbulent structures. To allow such comparison, there is a a set of virtual probes implemented in the ESEL (illustrated in right part of Fig. 5.1). The virtual probes are located poloidally in the center of the simulation region and have some small radial distance (typically $1-4$ mm) in order to cover and reproduce the whole radial profile. These probes do not perturb the plasma, just output time trace of all quantities needed for comparison. In order to take into account dimensions of real probe pins, each quantity is averaged in space over area corresponding to the size of the pin. If there is more than one probe pin on the real probe head, ESEL uses more virtual probes on each radius in correspondence with geometry of the probe head. If not stated otherwise, we will use probe head geometry from [72] in which there are three virtual probes on each radius separated by poloidal distance 0.5 mm and one additional probe shifted 1.5 mm inwards from the central probe. This allows more realistic estimation of radial and poloidal derivatives as seen by the probe.

The most extensive comparison was done for parameters of TCV tokamak [72, 46, 50, 39, 51]. For TCV case a surprisingly good agreement was found in radial density profiles, density fluctuations as well as in conditionally averaged profile of turbulent structures [50] (see Fig. 5.2). This comparison provides strong support for a model of interchange plasma transport in SOL. The agreement was, however, achieved only for a limited range of plasma parameters and the results of ESEL do not follow experimentally observed scaling of density profiles with parallel plasma collisionality

$$\nu^*_{ei} = L_{||}/\lambda_{ei}. \tag{5.24}$$

Here $\lambda_{ei}$ is mean free path for ion-electron collisions. With decreasing collisionality the e-folding length of radial density profile $\langle n \rangle$

$$\lambda_n = \left( \frac{\partial \ln \langle n \rangle}{\partial r} \right)^{-1} \tag{5.25}$$

increases more rapidly in experiment than in the ESEL model. The disagreement in $\lambda_n$ was found mainly for JET [39] and ASDEX [152] cases in which the collisionality was generally lower than for TCV. Interestingly, much lower discrepancy was found in scaling of the e-folding length $\lambda_T$ of radial electron temperature profiles. The discrepancy in $\lambda_n$ may have several reasons, the main of which are [39]:

- The simple analytical estimates for parallel losses in (5.11)-(5.13) do not take into account ballooning nature of interchange transport i.e., the observation that radial influx into SOL is located about 30° around outer midplane [59]). This increases parallel gradients and effectively shortens parallel gradient length $L_{||}$ in (5.11)-(5.13). Our preliminary study ([65], see Sec. 5.7.1) shows that this effect can increase parallel losses of density by an order of magnitude while estimate of parallel losses of energy in (5.13) stays in the same order.

- With decreasing parallel collisionality $\nu^*$, the subsonic vorticity advection (4.100) may be no longer dominant and sheath dissipation term (4.99) should be included in the model. The sheath-dissipative regime decelerates radial blob motion [14] which in turn influences mean radial profiles. This topic will be discussed in Sec. 5.6.

- Radial electric field around LCFS, $E_r(r_{LCFS})$ may be influenced by other processes than only by turbulent Reynolds stress, that is main source of $E_r(r_{LCFS})$ in standard ESEL version, e.g. by presence of drift waves or ion orbit losses [78]. Change of radial electric field in the vicinity of LCFS then changes properties of blobs that survive shear decorrelation and penetrate into the SOL. As a result, $\lambda_n$ scales with $E_r(r_{LCFS})$. We show this process in Sec. 5.6.

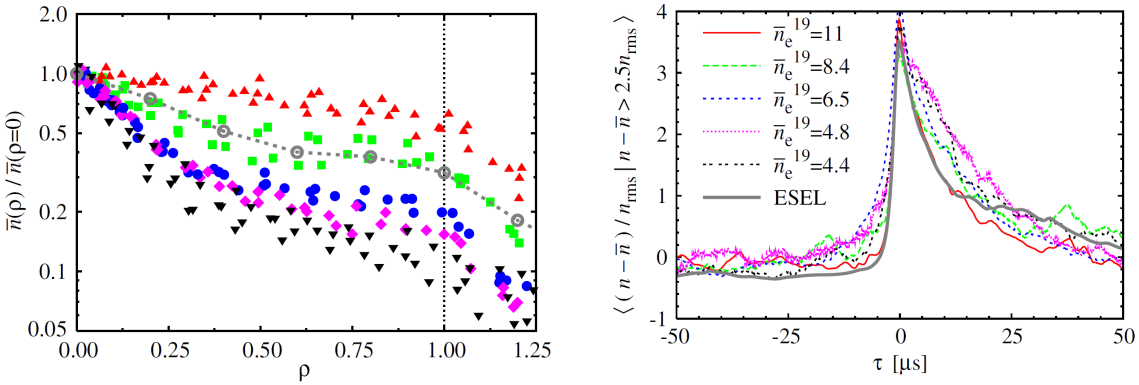


Figure 5.2: Comparison of radial density profile (left) and conditionally averaged profile of density fluctuation $(n-\bar{n})$ (right) in ESEL (gray) with profiles measured by reciprocating Langmuir probe in several discharges on TCV (colors) at radial position $\rho = 1$. Color coding is the same in both figures. Reproduced from [50].

## 5.2 Treatment of dissipative terms in ESEL and OpenMP paralelization

Dissipative terms present in Eqs. (5.2)-(5.4) through (5.8)-(5.10) constitute a stiff problem [79] and time integration scheme must be chosen properly. In ESEL the dissipative terms are included implicitly by solving Helmholtz equation. For simplicity we will illustrate the method on case of simple Euler scheme for time integration, but it can be appropriately generalized also for 3rd order explicit linear multistep method described later in Eq. (7.55) that is actually used.

After time discretisation with constant time step $\Delta t$, each of the Eqs. (5.2)-(5.4) can be written in form

$$\frac{q(t^i,p,r) - q(t^{i-1},p,r)}{\Delta t} - f(t^{i-1},p,r) = D_q \vec{\nabla}^2_\perp q(t^i,p,r) \tag{5.26}$$

where $q$ stands for $n$, $T$ or $\Omega$ and $t^i$ is time of $i$-th time step. $f$ includes all terms except the dissipative one and the dissipation is included implicitly. Poloidal periodicity allows Fourier transform in poloidal direction $(p \to k_p; q \to \tilde{q})$, giving Helmhotz equation for $\tilde{q}(t^i, k_p, r)$

$$\left[(k_p^2 - \frac{\partial^2}{\partial r^2}) + \frac{1}{D_q \Delta t}\right] \tilde{q}(t^i,k_p,r) = \frac{1}{D_q \Delta t}(\tilde{q}(t^{i-1},k_p,r) + \tilde{f}(t^{i-1},k_p,r)\Delta t). \tag{5.27}$$

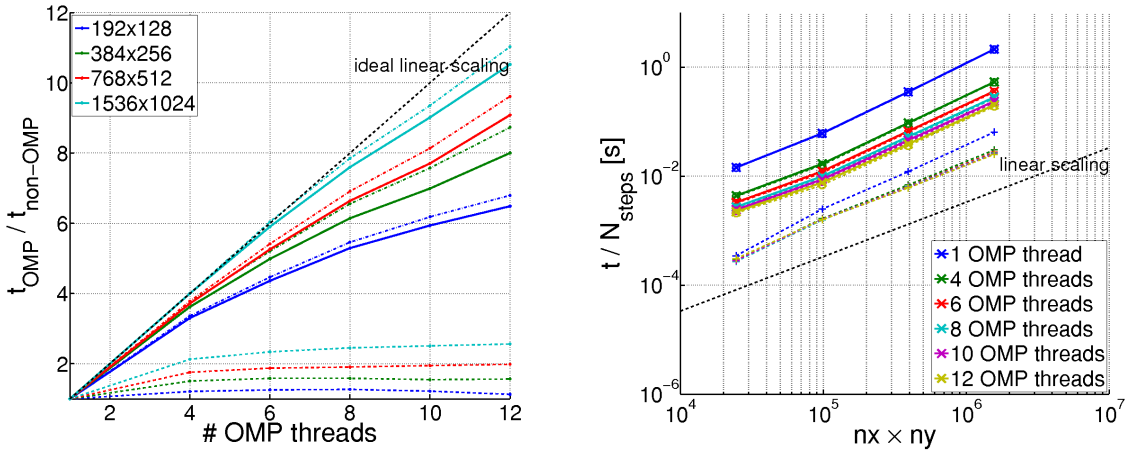


Figure 5.3: *Left:* Scaling of running time of ESEL (solid lines), its computational part (dash-dotted lines) and its output part (dashed lines) for several grid resolutions. Ideal linear scaling is plotted as black dashed line. *Right:* Average running time of a time step as a function of number of grid points $n_x \times n_y$. Ratio $n_x = 1.5n_y$ was used in all cases. The total time (solid line, crosses), time of computational part (dash-dotted line, circles) and time of file outputs (dashed line, plus signs) are plotted. In most of the cases the dash-dotted line is almost identical to the solid line. Black dashed line illustrates slope of linear scaling.

After space discretisation (regular grid and central differences are used) this equation can be solved for each $k_p$ separately. For given $k_p$, operator standing on the left hand size of (5.27) before $\tilde{q}(t^i)$ has a form of tridiagonal matrix of size $n_r \times n_r$ where $n_r$ is number of grid points in radial direction. Such matrix can be easily solved in linear time [79]. The Helmohltz equation is solved for $n_p$ distinct values of $k_p$ where $n_p$ is number of grid points in poloidal direction. Note that similar approach using Fourier transform in poloidal direction can be used also for radially varying diffusion coefficient $D_q(r)$, but not if the diffusion coefficient is poloidally dependent, $D_q(p, r)$. In case of $D_q(p, r)$ the poloidal Fourier transform of $D_q(t^i, p, r)\vec{\nabla}^2_\perp q(t^i, p, r)$ would result in convolution of both fields and operator applied on $q(t^i, k_p, r)$ on the left-hand side of (5.27) would have more complicated structure, not solvable in linear time.

Since modelling of low-collisional plasmas with small diffusivities requires very refined spatial grid, the ESEL simulation may become very slow. Therefore, we have performed shared-memory parallelization of the original code using OpenMP library[1]. All the terms in Eqs. (5.2)-(5.4) that are covered by term $f(t^{i-1}, k_p, r)$ in Eq. (5.26) are local in space and their parallelization is straightforward. The spatial grid is divided into $N$ domains, where $N$ is number of available threads, and each thread computes $f(t^{i-1}, k_p, r)$ on a single domain. Parallelization of Helmholtz solver is allowed by the fact that the fast Fourier transform (FFT) is made for each radius separately and it is independent on data located on different radial positions. This allows to compute several forward and/or backward FFTs by different threads at the same time. Consequently, also Eq. (5.27) can be solved for each $k_p$ separately. Tested on server with four quad-core CPUs AMD Opteron 8356 2.3 GHz with 2MB

[1] http://www.openmp.org

L2 cache, usage of 12 OpenMP threads provides for grid of $1024 \times 1536$ points $11\times$ shorter running time of the main part of the code that advances fluid Eqs. (5.2)-(5.4) in time, compared to a single-threaded application. Such acceleration of our code is sufficient for our current purposes, however, the scaling of performance gain with respect to number of used threads is sublinear (see Fig. 5.3) and further rearrangement of the code and data memory layout is planned in order to optimize access of threads to a relatively slow main memory and hence achieve better scaling. The scaling improves with finer grid resolution as the computational complexity of local (cached) operations rises more quickly then the amount of data that need to be transferred. The file output consumes approx. 10% of the running time and scales very weekly, with maximum performance gain of factor 2.5.

In Sec. 5.7 we present first results of coupling of ESEL code with code SOLF1D that computes transport along field lines, replacing analytical estimates (5.11)-(5.13). In typical situation the SOLF1D part is several times slower then ESEL and therefore most of the available CPU cores/threads is used by SOLF1D. The SOLF1D part constitutes the main bottleneck and performance of the ESEL OMP parallelization (typically 1-2 OMP threads used) was sufficient in all tested cases.

## 5.3 Overview of performed ESEL simulations

In the frame of this work we have made several ESEL simulations for parameters of edge plasma in tokamaks TCV and ASDEX. The basic parameters of these simulations are summarized in Tab. 5.1. There are two sets of simulations for the TCV case that differ in the values of diffusion coefficients and estimation of parallel losses. The run referred as #116 uses ad hoc values of the diffusivities and constant values of characteristic parallel loss times that were used in the original papers [72, 46], while the second TCV run is based on neoclassical collisional diffusivities and parallel losses derived in [39] and presented in this work as Eqs. (5.8)-(5.10). The potential boundary conditions were set as $\phi(r_{max}) = 0$, $\langle \partial\phi/\partial r \rangle(r_{max}) = 0$ and $(\partial\phi/\partial p)(r_{min}) = 0$ where the brackets $\langle\cdot\rangle$ denote averaging over poloidal extent of the simulation. These boundary conditions are different from that used in the original ESEL simulations [72] and their purpose is to improve behaviour of plasma potential and its fluctuations. The boundary conditions set the potential and mean poloidal $E \times B$ velocity to zero at the position of outer wall, which agrees with experimental observations [74].

Both TCV simulations were at first made with resistive closure $\nabla J_{\|} \approx 0$ and vorticity sink described only by subsonic advection (4.100), that is routinely used in ESEL. These simulations later served as a basis for set of simulations with altered $\nabla J_{\|}$ term. The simulation #116 was used in Sec. 5.5 for assessment of impact of parallel vorticity losses by Alfvén speed. the TCV simulation with neoclassical diffusivities provided base for set of simulations in Sec. 5.6 investigating role of sheath dissipation and radial electric field in the edge region on blob transport in the SOL. The run #116 was also used in Sec. 5.4.2 for tracking of blob trajectories and in Chap. 6 where several aspects of electrostatic probe measurements in turbulent environment are discussed.

The last simulation, made for parameters of ASDEX Upgrade, should be considered as preliminary. The parallel collisionality in this case is lower than in the TCV case and thus sheath dissipation is expected to play more significant role

than for parameters of TCV plasmas. Since sheath dissipation wass neglected in the performed simulation, this manifests itself in significantly flatter radial profiles of density than those observed in experiment on ASDEX Upgrade while at the same time there is an agreement in radial profiles of electron temperature (see Sec. 6.2). This behaviour of ESEL model was already reported for JET case in [39]. Based on the results of Secs. 5.6 and 5.7.1 we believe that the disagreement may be caused by non-negligible role of the sheath dissipation together with underestimated parallel losses of density. New simulations with improvements concerning these mechanisms are in preparation.

| | TCV #116 [72, 46] | TCV | ASDEX [74] |
|---|---|---|---|
| $n_{LCFS}$ [$10^{19}$ m$^{-3}$] | 2 | 2 | 1.1 |
| $T_{LCFS}$ [eV] | 20 | 20 | 65 |
| $B_0$ [T] | 1.4 | 1.4 | 2.34 |
| $q_{95}$ | 3.0 | 3.0 | 4.5 |
| $L_{1,\parallel}$ ($L_{2,\parallel}$) [m] | 15 | 10 | $\approx 10$ (40) |
| $L_{w.s.,\parallel}$ [m] | 1 | 1 | 1 |
| $\nu_e^*$ | 66 | 66 | $2.5 - 5.5$ |
| $\rho_{s,LCFS}$ [$10^{-3}$ m] | 0.46 | 0.46 | 0.5 |
| $c_{s,LCFS}\vert_{T_i=0}$ [$10^3$ m $\cdot$ s$^{-1}$] | 31 | 31 | 56 |
| $\omega_{ci}$ [$10^6$ s$^{-1}$] | 67 | 67 | 112 |
| width of SOL region [$10^{-3}$ m] | 25 | 25 | 52 |
| $D_{\perp,n,LCFS}/D_{b,LCFS}$ | $4.5 \times 10^{-3}$ | $8.5 \times 10^{-4}$ | $1.2 \times 10^{-4}$ |
| $D_{\perp,\Omega,LCFS}/D_{b,LCFS}$ | $2.5 \times 10^{-2}$ | $1.7 \times 10^{-2}$ | $2.3 \times 10^{-3}$ |
| $D_{\perp,T,LCFS}/D_{b,LCFS}$ | $1.0 \times 10^{-2}$ | $1.6 \times 10^{-2}$ | $2.5 \times 10^{-4}$ |
| $1/(\tau_{n,0}\omega_{ci})$ | $3.1 \times 10^{-5}$ | $3.3 \times 10^{-5}$ | $3.5 \times 10^{-5}$ |
| $1/(\tau_{\Omega,0}\omega_{ci})$ | $3.1 \times 10^{-5}$ | $3.3 \times 10^{-5}$ | $3.5 \times 10^{-5}$ |
| $1/(\tau_{T,0}\omega_{ci})$ | $1.9 \times 10^{-4}$ | $1.8 \times 10^{-4}$ | $1.4 \times 10^{-3}$ |
| $D$ =const. | YES | NO | NO |
| $\tau$ =const. | YES | NO | NO |
| spatial resolution | $256 \times 512$ | $512 \times 768$ | $1024 \times 1536$ |
| time step [$1/\omega_{ci}$] | 0.5 | 0.15 | 0.1 |
| run time [$1/\omega_{ci}$] | $10^6$ | $10^6$ | $10^6$ |

Table 5.1: Basic edge plasma parameters and derived transport coefficients for performed simulations. Values of characteristic parallel damping times $\tau$ and diffusivities $D_\perp$ for middle and right case are computed from $n$ and $T$ values on LCFS. In the left case, ad hoc values of $\tau$ and $D_\perp$ adopted from original ESEL simulation [46] are used. If the connection length $L_{1,\parallel}$ in the SOL is asymmetric, both values, $L_{1,\parallel}$ and $L_{2,\parallel}$, are presented in the table. The parallel losses in the simulation are, however, computed from the shorter one only. Connection length to the nearest wall in wall shadow region was in all cases estimated as $L_{w.s.,\parallel} = 1$ m. $D$ =const. distinguishes whether diffusion coefficients are kept spatially constant or whether they are dependent on poloidally averaged (at each time) values of density and temperature according to (3.11)-(3.14). $\tau$ =const. distinguishes between constant values of characteristic parallel loss times and values dependent on local $n$ and $T$. Normalization constant $D_b = \rho_s^2/\omega_{ci} \sim T_{e,0}/B_0$. All values are computed for deuterium plasma.

## 5.4 2D blob detection and tracking

In order to determine properties and statistics of individual bobs and holes in the simulation, we developed a blob tracking routine and used it together with ESEL code. The algorithm is based on conditional averaging approach used for blob detection by Langmuir probes (see Sec. 3.3).

First, it is necessary to let the simulation evolve into a state of saturated turbulence, where the time-averaged radial density profile $\bar{n}(r)$ becomes stable. Then, in every algorithm time step, field of density fluctuations $\tilde{n}(r,p)$ is obtained by subtracting mean radial density profile $\langle n \rangle(r)$ from instantaneous density field $n(r,p)$,

$$\tilde{n}(r,p) = n(r,p) - \langle n \rangle(r). \tag{5.28}$$

For a given threshold $\tilde{n}_{th}$, all areas with

$$\pm\, \tilde{n} \geq \tilde{n}_{th}\sigma_n \tag{5.29}$$

are detected, with + sign for blobs, − sign for holes and $\sigma_n$ being standard deviation of density fluctuations at given radius. Each detected area $S_i$ is considered a single structure. Every structure is characterized by its center of mass (CMS)

$$\vec{x}_{i,CMS} = \int_{S_i} \vec{x}(r,p)\tilde{n}(r,p)\mathrm{d}r\mathrm{d}p, \tag{5.30}$$

geometrical center

$$\vec{x}_{i,center} = \int_{S_i} \vec{x}(r,p)\mathrm{d}r\mathrm{d}p, \tag{5.31}$$

maximum relative amplitude

$$\tilde{n}_{i,max} = \max_{S_i} \tilde{n}(r,p) \tag{5.32}$$

and location of the maximum $\vec{x}_{i,max}$.

In order to get more detailed information on properties of blobs and to detect their possible merging or splitting, $\tilde{n}_{th}$ does not have a single value, but covers the range from 1 upto some maximum value chosen separately for every particular simulation (according to the level of fluctuations in the simulation). Then, if two structures detected at higher threshold are contained inside a single structure detected at lower threshold, it is a signal of process of merging or splitting of two different structures.

The trajectory and velocity of every blob is determined by comparing position of its center of mass $\vec{x}_{i,CMS}$ and/or position of the maximum density $\vec{x}_{i,max}$ with $\vec{x}_{j,CMS}$ and/or $\vec{x}_{j,max}$ of all blobs found in previous detection time step. The condition to identify two structures in two consequent times as the same, but translated blob is set as $|\delta\vec{x}| < \Delta x$ , where $\Delta x$ is chosen constant and $\delta\vec{x}$ is either difference in positions of center of mass or of density maxima of two structures detected in consequent times. Testing shows that tracking structures according to their center of mass gives better results than tracking of the point of maximum relative density inside the structure. The later may fail when secondary maximum rises over the primary one. In such case the tracking point can jump over distance that may be larger then $\Delta x$. If the algorithm time step is $\Delta t$, two distinct blobs will be

identified as the same when their mutual distance $\delta\vec{x}$ and relative speed $\delta\vec{v}$ fulfil $|\delta\vec{x}\Delta t - \delta\vec{v}| > \Delta x\Delta t$. On the other hand, single blob may be identified as two blobs when its velocity $|\vec{v}| > \Delta x/\Delta t$. These two conditions set natural constraints on the choice of $\Delta x$ and $\Delta t$.

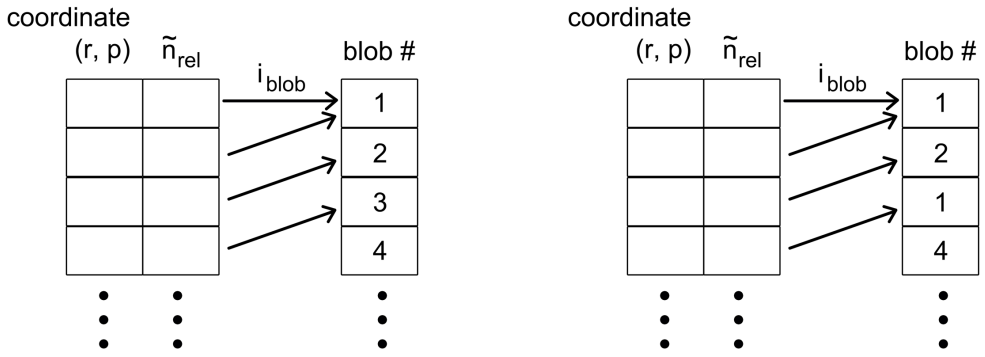


Figure 5.4: Illustration of merging two already detected areas into one blob by renumbering elements in array 'blob #'. Before (left) and after (right).

For each structure $S_i(t)$ successfully matched to structure $S_j(t - \Delta t)$ from previous time, intersection $S_i(t) \cap S_j(t - \Delta t)$ is computed. We assume that change of structure area in time $\Delta t$ can be neglected and set $\Delta t$ and $\Delta x$ such that ratio $(S_i(t) \cap S_j(t - \Delta t))/S_i(t) > 0.9$. This helps to reduce false alarm ratio (when two different structures are detected as one) caused by $\Delta t$ and $\Delta x$ being too large.

The detection of area of all structures with density fluctuation above certain threshold is done by modification of algorithm of connected component labelling. The algorithm proceeds in the following way:

1. Array of all data points $\tilde{n}_{rel}(r, p)$ together with pointers to their neighbours is created and sorted according to amplitude of $\tilde{n}_{rel}(r, p)$. Each array element contains also an additional integer $i_{blob}$ that will store pointer to second array containing blob numbers. The sorting is computationally most demanding part, since the algorithm sorting $N$ data points is, contrary to the following steps, always slower then $\mathcal{O}(N)$. The benefit of computing list of points sorted according to their $\tilde{n}_{rel}$ value comes when blob detection is made at several different threshold values for single image. Then, it is not necessary to go repeatedly through all the points in the frame, but information obtained during detection with higher threshold $\tilde{n}_{th,high}$ can be easily reused also for the lower threshold $\tilde{n}_{th,low}$. Then only points with their value in range $\tilde{n}_{th,low} \leq \tilde{n}_{rel}(r, p) \leq \tilde{n}_{th,high}$ are processed and 'glued' to already detected blobs.

2. Starting with the largest value of the threshold $\tilde{n}_{th}$, index $i_{th}$ of the last data point with value above $\tilde{n}_{th}$ is found, dividing the array to the data points inside and outside detected structures.

3. Going through the array from the first element (with largest $\tilde{n}_{rel}$) without any blob assigned:

- The lowest number of already detected blob in element neighbourhood is found and assigned to the element by setting its $i_{blob}$. If neighbouring points do not have any blob number assigned, a new unique value of $i_{blob}$ is added to the element and new entry in the array containing blob numbers is created. To prevent situations where a thin part of a blob is divided into several pieces as shown in Fig. 5.5, we use the whole 8-point neighbourhood instead of 4-point one.
- If there is more than one distinct blob number found in the element neighbourhood, all points in the image with these blob numbers are merged into one blob. This is done by renumbering entries in the array containing blob numbers, keeping pointers $i_{blob}$ of all points intact as illustrated in Fig. 5.4. Merging blobs is then made in time proportional to number of already detected structures.

4. When all data elements before index $i_{th}$ are processed, position, size and all other needed properties are computed for every detected structure.

5. Lower threshold value $\tilde{n}_{th}$ is taken, new $i_{th}$ found and the algorithm continues with step 3.

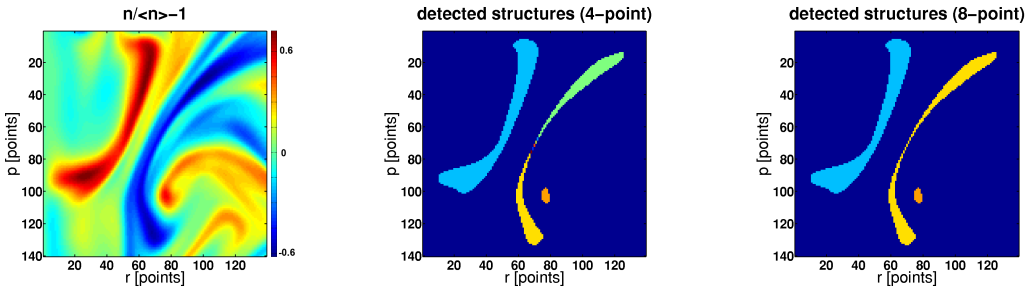


Figure 5.5: Example of field of relative density fluctuations in the edge region of ESEL simulation (left) and results of turbulent structure detection with 4-point (middle) and 8-point (right) neighbourhood. Different structures are distinguished by different colors. 4-point detection algorithm breaks single structure into several pieces when a narrow part is present, while 8-point algorithm detects structures correctly.

### 5.4.1 Estimation of blob size and tilting

Information obtained during blob detection may be used to estimate spatial characteristics of detected structures. In the first approximation we will assume that boundary of structure can be described in slab radial and poloidal coordinates $\tilde{r}$ and $\tilde{p}$ shifted to the center of the blob by an ellipse of size $\delta_r$, $delta_p$, rotated by angle $\xi$:

$$\left(\frac{\cos^2\xi}{\delta_r^2}+\frac{\sin^2\xi}{\delta_p^2}\right)\tilde{r}^2-\sin(2\xi)\left(\frac{1}{\delta_r^2}-\frac{1}{\delta_p^2}\right)\tilde{p}\tilde{r}+\left(\frac{\cos^2\xi}{\delta_p^2}+\frac{\sin^2\xi}{\delta_r^2}\right)\tilde{p}^2=1. \quad (5.33)$$

Computing integral of $\tilde{r}^2$, $\tilde{p}^2$ and $\tilde{r}\tilde{p}$ over area $S$ of the ellipse (5.33) gives set of three equations

$$\int_S \tilde{r}^2 \mathrm{d}r\mathrm{d}p = \langle \tilde{r}^2 \rangle = \frac{\pi \delta_r \delta_p}{4} (\delta_p^2 \cos^2 \xi + \delta_r^2 \sin^2 \xi) \tag{5.34}$$

$$\int_S \tilde{p}^2 \mathrm{d}r\mathrm{d}p = \langle \tilde{p}^2 \rangle = \frac{\pi \delta_r \delta_p}{4} (\delta_r^2 \cos^2 \xi + \delta_p^2 \sin^2 \xi) \tag{5.35}$$

$$\int_S \tilde{r}\tilde{p} \mathrm{d}r\mathrm{d}p = \langle \tilde{r}\tilde{p} \rangle = \frac{\pi \delta_r \delta_p}{8} (\delta_p^2 - \delta_r^2)(\delta_p^2 \cos^2 \xi + \delta_r^2 \sin^2 \xi) \times \times \sin \xi \cos \xi. \tag{5.36}$$

Since area of each blob is detected during blob tracking, terms $\langle \tilde{r}^2 \rangle \equiv \langle (r - \langle r \rangle_{blob})^2 \rangle_{blob}$, $\langle \tilde{p}^2 \rangle \equiv \langle (p - \langle p \rangle_{blob})^2 \rangle_{blob}$, $\langle \tilde{r}\tilde{p} \rangle \equiv \langle (r - \langle r \rangle_{blob})(p - \langle p \rangle_{blob}) \rangle_{blob}$ can be computed in the simulation and shape of the blob approximated by equivalent ellipse whose properties $\delta_r$, $\delta_p$ and $\xi$ are obtained by solving Eqs. (5.34)-(5.36). The fact that shape of the structures can be approximated by ellipse (5.33) is verified a posteriori as shown in Fig. 5.6.

Typical interchange structure in highly-collisional regime evolve from ellipsoidal shape to banana shape (can be seen in Fig. 5.6), as its center moves with higher radial velocity than the edges. In cases with low collisionality, this behaviour is even more pronounced. Therefore, even though in most cases we find reasonable agreement with ellipsoidal blob shape, we plan to generalize the method to include also this bending of blob shape. Several snapshots of density field in the simulation are presented in Fig. 5.6 where the algorithm successfully detects all regions with relative density perturbation $\tilde{n}/\langle n \rangle > 2\sigma_n$ (marked by white line) and approximates them by ellipsoidal shapes. The black line shows trajectory of the center of the ellipse for each blob, starting from the time of the first snapshot shown or from the time of first blob detection, depending on what was first. The trajectory is smooth, which allows good estimation of blob velocity as difference of position of blob center divided by time step of the detection algorithm. Note that the detected center of the blob (ellipse) is not equivalent to the position of its maximum density, which is located at the steep front of the blob. In times 29.8 $\mu$s and 44.7 $\mu$s we can observe two typical cases of blob disintegration. When smaller blobs lose their radial momentum, they not only stop their radial movement, but they are often influenced by potential of the surrounding plasma that can reverse the radial movement for a short while until they completely disappear. This can be observed also in Fig. 5.7 that shows bundle of different blob trajectories. Spatially larger blobs tend to break up into two separate pieces created by their two lobes. This happens when potential hill and valley (that create poloidal electric that moves the blob radially) become too separated in space or amplitude of at least one of them too weak. In such case the local $E \times B$ drift is influenced by potential difference between the lobe and surrounding plasma (either background plasma or lobe of another blob). This happens especially when strongly tilted blob enters wall shadow region. In such case potential of the more outward lobe is quickly lost due to increased vorticity losses in the wall shadow and electric field driving the blob as a coherent structure disappears.

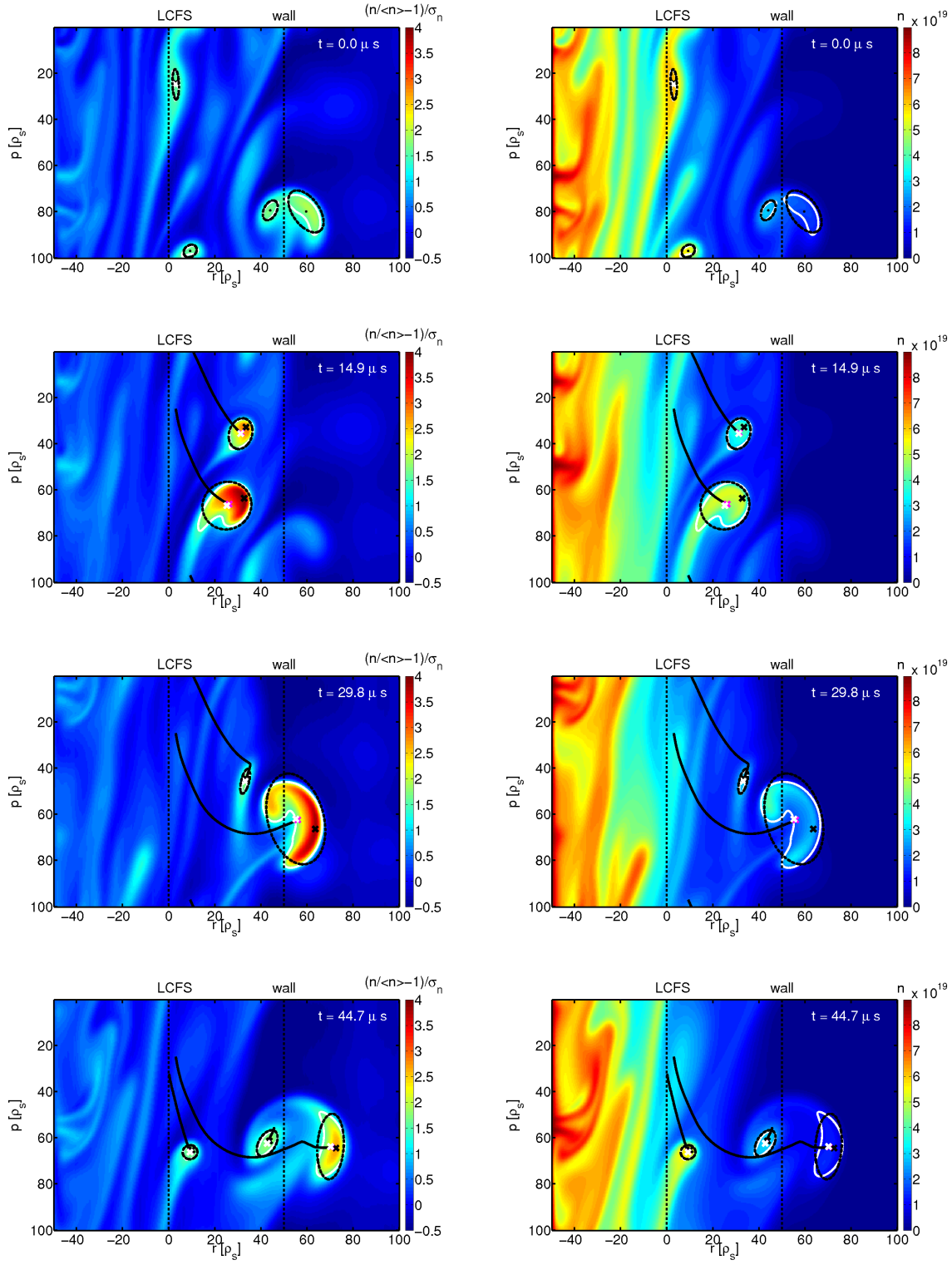


Figure 5.6: Snapshots of field of relative density normalized to standard deviation of local density fluctuations $\sigma_n$ (left) and snapshot of density field (right) in ESEL simulation #116. Regions with $\tilde{n}/\langle n\rangle > 2\sigma_n$ are bordered by white line and approximated by black dashed ellipse. Trajectory of center of the ellipse beginning at time of the first plotted snapshot or at time of first detection of the blob is marked by black solid line. Black cross marks position of maximum of $\tilde{n}/\langle n\rangle$, white cross geometrical center and magenta cross center of mass of each detected blob.

### 5.4.2 Properties of blobs in SOL

Investigation of properties of blob trajectory, size and tilting in the SOL can provide information on mechanisms that form or dissipate blob's bipolar structure, thus regulating its internal electric field and associated $E \times B$ velocity. In several works (e.g. [47, 108]) the topic of impact of $\nabla J_{\parallel}$ closure on movement of single Gaussian blob imposed over some fixed background was studied. The main disadvantage of these 'seeded blob' studies is, however, the fact that they neglect interaction with inhomogeneous background plasma and its poloidal flows. These effects can disturb idealised (and often symmetric) evolution of the seeded blob and bring more complicated blob dynamics. Our blob-tracking algorithm brings the advantage of studying blob properties in an environment of fully developed self-regulated turbulence. This provides more realistic statistics of initial blob perturbations and of influence of non-uniform background on the blob motion than the case of single seeded blob imposed on fixed background. In this section, properties of blob movement and deformation will be characterized for the standard ESEL simulation #116, with parallel vorticity losses described by subsonic advection, that was previously successfully compared with radial experimental profiles. Analogous study is currently being prepared for the case of $\nabla J_{\parallel}$ closure describing sheath dissipation, which should allow more detailed comparison of properties of both modes.

The blob tracking algorithm presented in Secs. 5.4 and 5.4.1 allows visualisation of trajectories of individual blobs in ESEL simulation together with estimation of blob's spatial extent and associated density or temperature fluctuations. In Fig. 5.7 we plot trajectories of several randomly chosen blobs detected at LCFS. Poloidal periodicity of the simulation allowed to shift all trajectories to a single poloidal location at LCFS. Each trajectory is plotted in color that corresponds either to maximum relative density fluctuation inside the tracked blob $(n - \langle n \rangle)/\sigma_n$ (left part) or to poloidal size of the blob $\delta_p$ (right part). These trajectories reveal that blobs carrying less density as well as poloidally smaller blobs (both cases plotted by dark blue color) feel poloidal plasma flow stronger than blobs with higher poloidal extent or higher density amplitude. Many of the small blobs do not even reach outer part of SOL and they are dissipated in the middle of SOL. And, vice versa, only the largest blobs (in the sense of their spatial extent as well as of their relative density fluctuation) are able to penetrate into the wall shadow region and hit the outer wall. As parallel losses of density, energy and vorticity dissipate the blobs, number of detected structures decreases with radius (Fig. 5.8(left)). Large blobs move faster in the radial direction (Fig. 5.9(left)) and therefore fraction of large blobs compared to the small ones increases in the far SOL (Fig. 5.8(left)).

Radial profile of blobs' mean radial ($v_r$) and poloidal ($v_p$) velocity is plotted in Fig. 5.9. The poloidal velocity of blobs in the SOL is almost independent on their density amplitude and it is different from the mean poloidal plasma flow. This indicates that rotation (tilt) of blobs is such that it just compensates differencies in the total blob velocity and all blobs have (on average) the same poloidal velocity component $v_p$ regardless of their amplitude. Fig. 5.10(right) confirms that stronger/larger blobs are less tilted (their tilt angle $\alpha$ is closer to zero). As a consequence, the differences in inner electric field of blobs, that drives their motion, is projected mainly to the radial velocity component, which is larger for blobs carrying larger density perturbation. Therefore, even though large blobs move poloidally with the same speed as the small ones, the difference in $v_r$ is responsible for the

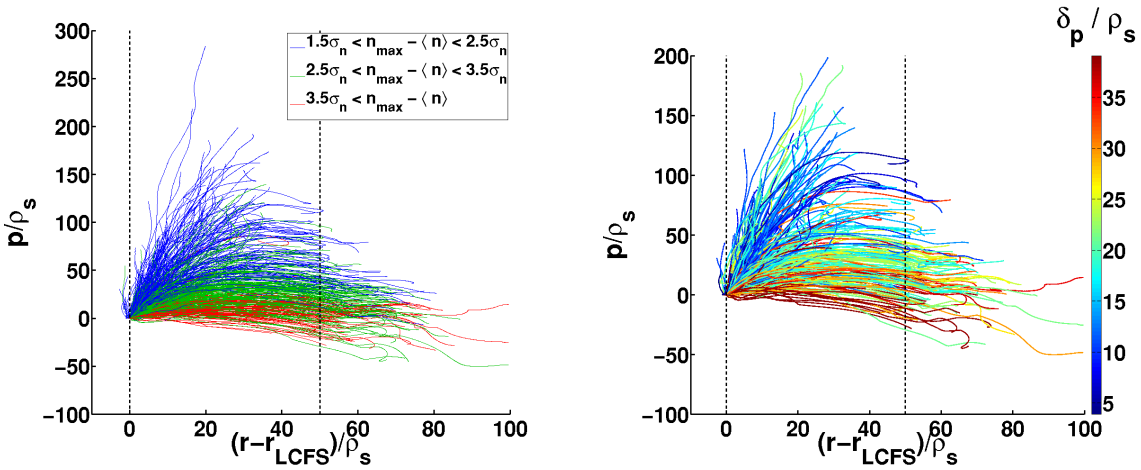


Figure 5.7: Trajectories of randomly chosen blobs detected at position of LCFS in ESEL simulation #116. The color coding distinguishes blobs according to their maximum relative density fluctuation (left) and estimated poloidal size (right) at the position of LCFS. LCFS and end of SOL are marked by vertical dashed lines.

final shape of their trajectory. Large blobs move almost radially, their time spent in the SOL is short and, therefore, they are able to reach the wall shadow before being dissipated by parallel plasma losses. Generaly, poloidal velocity of the blobs consists of two components. Mean poloidal plasma flow dragging the blobs and movement of the blob generated by its internal electrical field. The latter produces radially almost constant offset ($\approx 0.02 c_{s_0}$) of blob poloidal velocity from the mean poloidal plasma flow (Fig. 5.9(right)).

Measurement of average poloidal ($\delta_p$) and radial ($\delta_r$) sizes of blobs in SOL can be achieved with reciprocating probe diagnostics. In [155] it was shown that blob structures on JET are poloidally elongated in the vicinity of LCFS, $\delta_p/\delta_r \approx 2-3$, transforming to a circular shape in the far SOL, $\delta_p/\delta_r \approx 1$. Using the blob-tracking we estimated the ratio $\delta_p/\delta_r$ from the simulation as shown in Fig. 5.8. The results show good agreement with the experimentally measured behaviour, which further supports validity of ESEL simulations for modelling scrape-off layer transport. The shape of the blobs can be visualised using 2D conditional average that is shown in Fig. 5.16(left) and in 5.15 the radial and poloidal sizes of blobs are compared between two different $\nabla J_{\|}$ closures.

The blobs entering the wall shadow are often tilted (Fig. 5.10) and one of the lobes enters the region earlier than the other one. Since vorticity losses increase with decreased connection length in this region, the vorticity of this lobe gets weaker then vorticity of the other lobe. This asymmetry causes rotation of the whole structure and its possible disintegration (see Fig. 5.6 as an example). This can be observed in profile of poloidal velocity of blobs (Fig. 5.9(right)) where a small wave generated by disintegrating blobs can be observed at the boundary of far SOL and wall shadow regions. The rotation is visible also in histogram of tilting angles in Fig. 5.10(left) where large number of the rotated blobs is discontinued at the boundary of SOL and wall shadow. Only small number of blobs or their fragments with minor axis oriented in the radial direction ($\xi \approx 0$) penetrate into the wall shadow. Note that since large blobs are much less tilted, their dissintegration

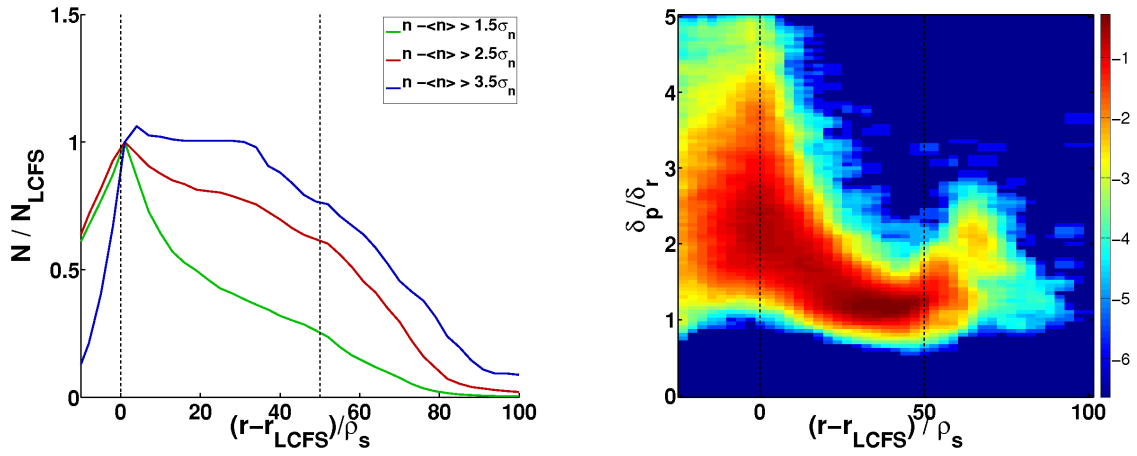


Figure 5.8: *Left:* Radial decay of number of blobs detected at LCFS with three different thresholds of relative density fluctuation, normalized to their number at LCFS. All blobs detected with given thresholds at radius $0 \geq (r - r_{LCFS})/\rho_s < 5$ were taken into account which results in artificial increase of the blue curve above 1 at position $(r - r_{LCFS})/\rho_s = 5$. LCFS and end of SOL are marked by vertical dashed lines. *Right:* Logarithm of histogram of ratio $\delta_p/\delta_r$ for blobs detected at LCFS with $n - \langle n \rangle > 1.5\sigma_n$. The histogram was divided by number of all blobs detected with given condition at LCFS and by verticle size of the bins, $\Delta(\delta_p/\delta_r) = 0.05$.

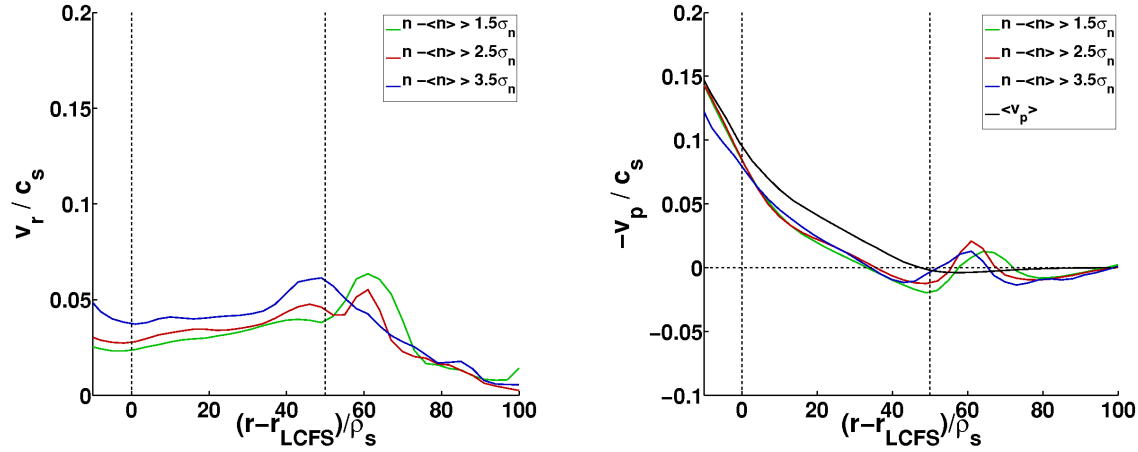


Figure 5.9: Mean radial (left) and poloidal (right) velocity of blobs tracked in ESEL simulation #116 for different values of blobs' relative density fluctuation. Only blobs with specified relative density fluctuation at LCFS (see legend) were taken into account. Mean poloidal velocity of plasma in the simulation is plotted by black line. LCFS and end of SOL are marked by vertical dashed lines.

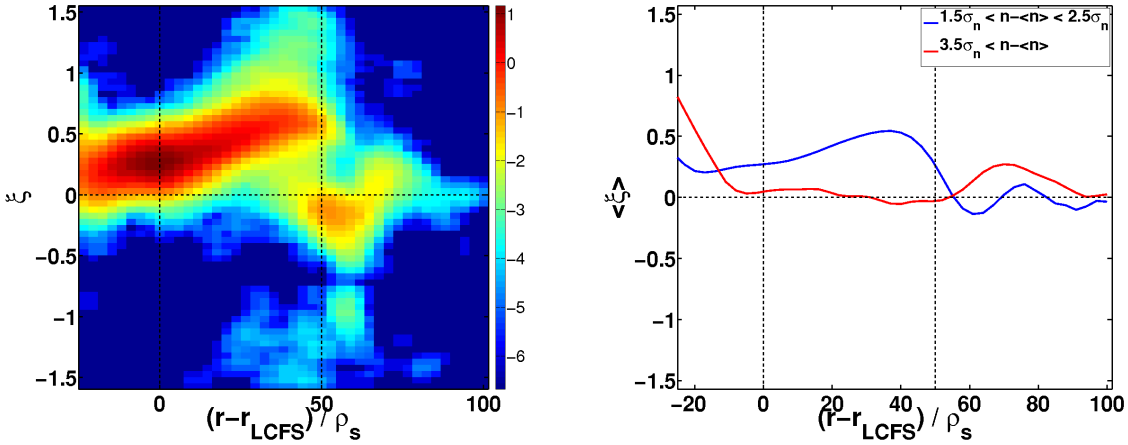


Figure 5.10: *Left :* Logarithm of histogram of blob tilting angles $\xi$ for blobs with amplitude at LCFS $1.5\sigma_n < n - \langle n \rangle < 2.5\sigma_n$. The histogram was divided by number of all blobs detected with given condition at LCFS and by verticle size of the bins, $\Delta\xi = 0.05$. *Right :* Mean tilting angle $\langle\xi\rangle$ as a function of radius for blobs with two different amplitude ranges. In both figures the black horizontal dashed line indicates tilting angle $\xi = 0$ in which case the blob axes are aligned with radial and poloidal directions. LCFS and end of SOL are marked by vertical dashed lines.

at this boundary is less probable.

In this section, we have discussed properties of blobs present in SOL when subsonic vorticity advection is dominant and similar analysis is prepared also for regime with sheath dissipation included. In principle, all the results allow verification by measurement made either by set of radially and poloidally separated Langmuir or ball-pen probes (the spatial separation is needed to measure electric fields and/or blob dimensions) or by gass-puff imagining (GPI) that can visualise blob shape in 2D and allows estimation of their dimensions and velocities. On COMPASS tokamak, the former diagnostics is already available and installation of the GPI is considered. Using both diagnostics for comparison with the presented results is envisaged as a part of effort for characterisation of SOL in this newly installed machine.

## 5.5 Vorticity damping by emitted Alfvén waves

Resistive closure $\nabla J_\parallel \approx 0$ used in standard ESEL model is not the only one possible. Some authors suggest [157, 87] that in case that the $\beta$ of blobs is relatively large, closure (4.111) describing parallel current associated with field line bending by blobs and generation of Alfvén waves should be included in 2D models. In analogy with modelling of drift turbulence, where coupling of drift waves with Alfvén waves is an important process influencing plasma dynamics, the Alfvén closure was proposed by B. Scott [112] to be used also in ESEL model. So far, properties of blob transport in SOL influenced by vorticity drain by emitted Alfvén waves was studied mostly analytically or numerically for the case of individual seeded blobs [157, 87, 88]. In this section we show the way how the term (4.111) influences dynamics in the situation of fully developed turbulence.

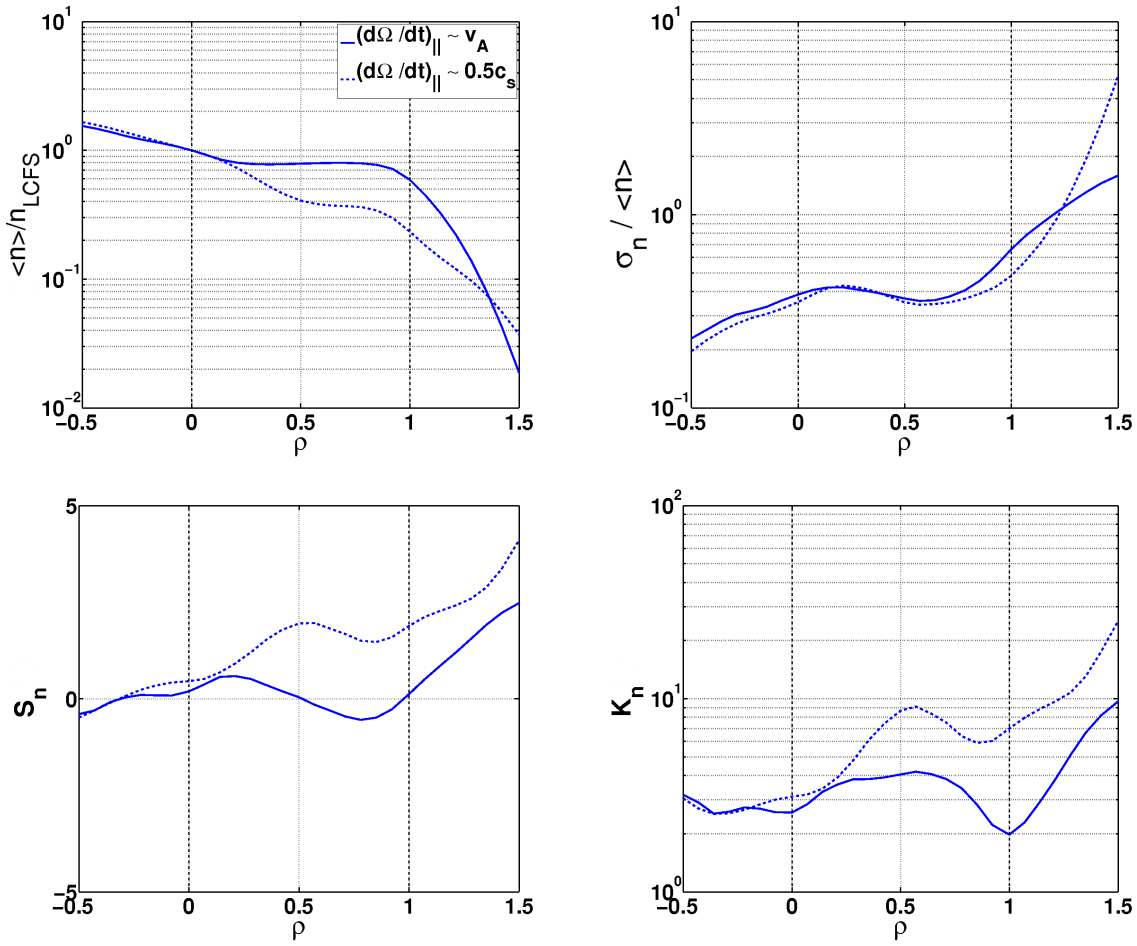


Figure 5.11: Mean value $\langle n \rangle$, relative fluctuation level $\sigma_n/\langle n \rangle$, skewness $S_n$ and kurtosis $K_n$ of density fluctuations in ESEL simulation for TCV parameters with subsonic parallel vorticity advection (dashed line) and Alfvénic closure of $\nabla J_{\|}$ (solid line).

In order to compare with standard case of subsonic parallel vorticity advection, the simulation with Alfvénic vorticity damping was made for similar parameters of TCV plasma as simulation #116, differing only in the vorticity parallel loss term. Both loss terms, subsonic (4.100) and Alfvénic (4.111), have similar structure with linear dependency on local vorticity $(\partial\Omega/\partial t)_{\|} = f(n,T)\Omega$. In Alfvénic case $f \sim v_A$ while in the subsonic case $f \sim c_s$ due to subsonic advection. For typical parameters of TCV plasmas ($n \approx 2\cdot 10^{19}$ m$^{-3}$, $T_e \approx 20$ eV) the ion sound speed $c_s \approx 40$ km$\cdot$s$^{-1}$ is much smaller than Alfvén velocity $v_A \approx 3500$ km$\cdot$s$^{-1}$. Their ratio is $v_A/c_s \approx 90$ and since the #116 simulation uses constant characteristic times for description of parallel losses (i.e. $\tau_{\Omega,\#116}$ =const.), the $\tau_{\Omega,\#116}$ was divided by this factor,

$$\tau_{\Omega,v_A} \approx \tau_{\Omega,\#116}/90. \tag{5.37}$$

Indeed, the Alfvénic damping causes very strong vorticity losses. Such large drain of vorticity influences potential structure of blobs, the corresponding electric field and consequently also their radial velocity. This, in turn, has an effect on radial profiles and fluctuation statistics in SOL as presented in Figs. 5.11-5.16.

Fig. 5.11 shows that fluctuation statistics inside the LCFS is almost the same for

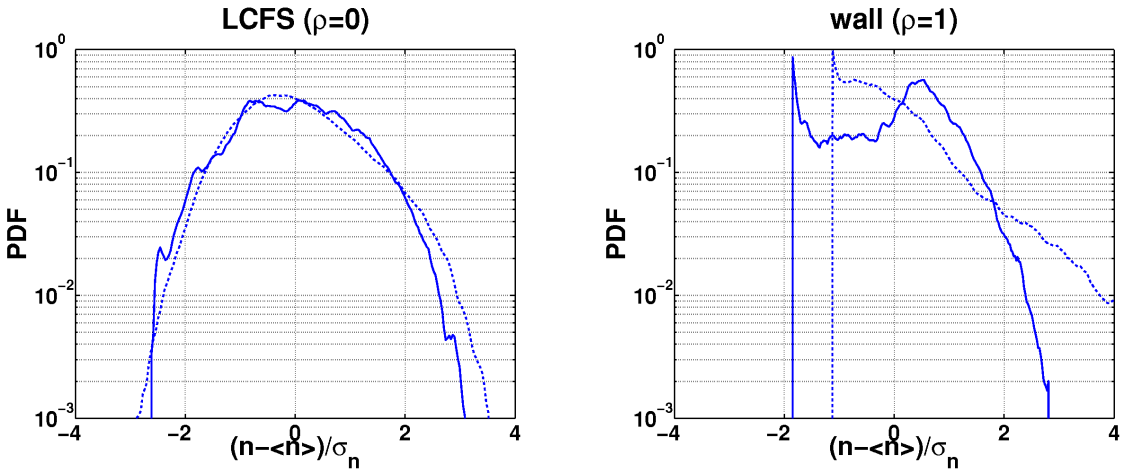


Figure 5.12: PDF of density fluctuations at position of LCFS (left) and SOL/wall-shadow boundary (right). ESEL simulation for TCV parameters with subsonic parallel vorticity advection (dashed line) and Alfvénic closure of $\nabla J_{||}$ (solid line).

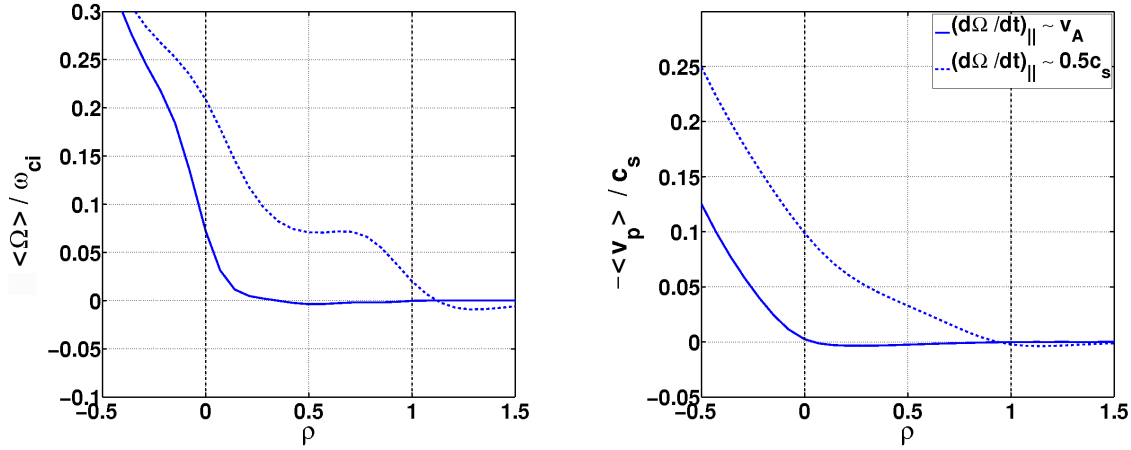


Figure 5.13: Radial profile of mean vorticity (left) and mean poloidal velocity (right) in ESEL simulation for TCV parameters with subsonic parallel vorticity advection (dashed line) and Alfvénic closure of $\nabla J_{||}$ (solid line).

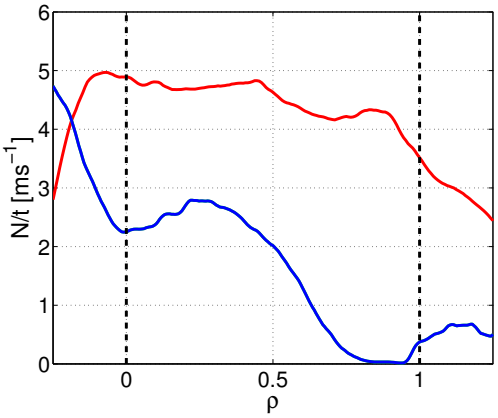


Figure 5.14: Number of blobs per millisecond detected at level $3\sigma_n$ in simulation with subsonic parallel vorticity advection (red) and with parallel vorticity losses given by Alfvén speed (blue).

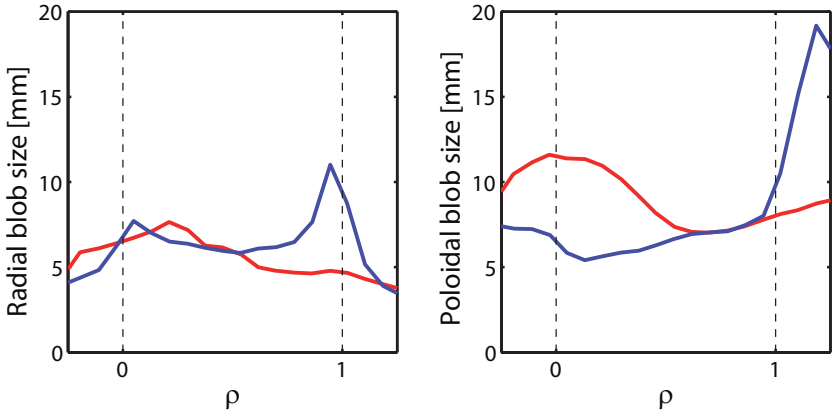


Figure 5.15: Radial (left) and poloidal (right) size of blobs detected with threshold $2\sigma_n$ in simulations with subsonic (red) and Alfvénic (blue) vorticity losses.

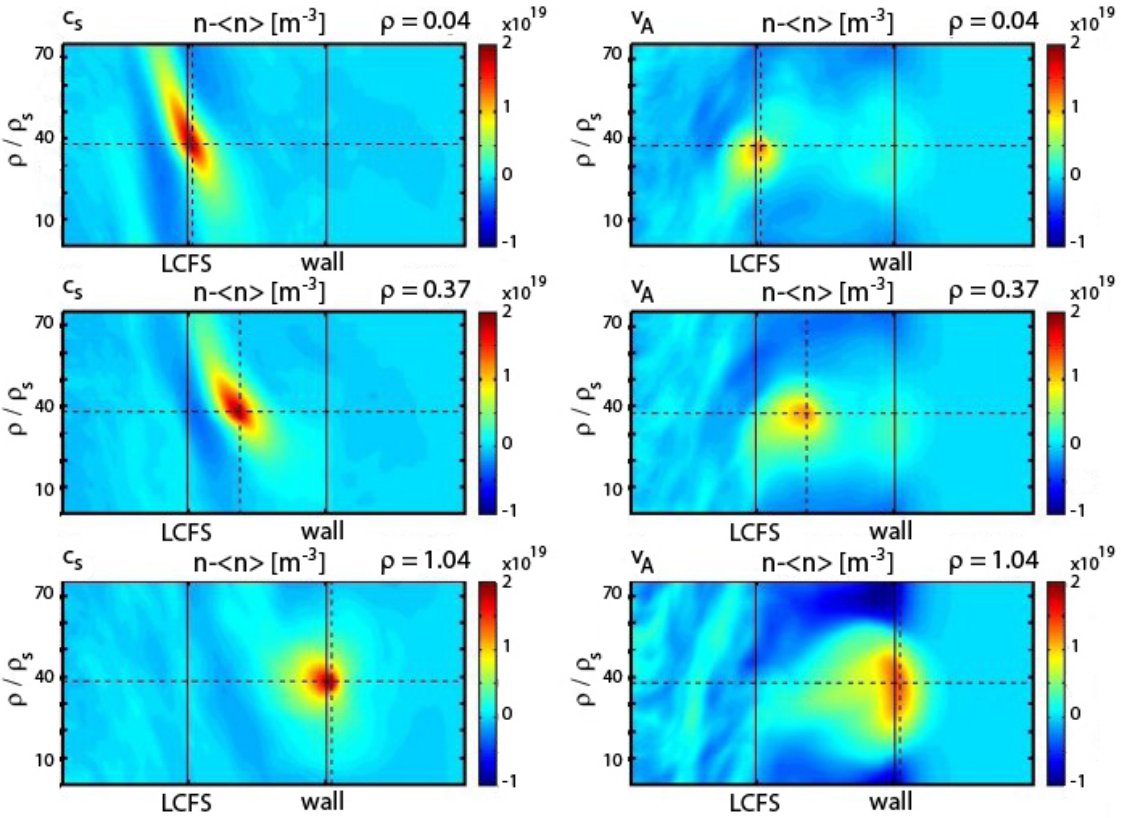


Figure 5.16: Conditional average of relative density field at threshold $2\sigma_n$ in ESEL simulation for TCV parameters [112]. Difference in blob shape for subsonic parallel vorticity advection (left) and Alfvénic closure of $\nabla J_{\|}$ term (right) is shown. Crossection of thin black dashed lines marks position of the CA trigger that was radially located at $\rho = 0.04$ (top), $\rho = 0.37$ (middle) and $\rho = 1.04$ (bottom).

both cases. The same observation holds for temperature, vorticity and potential fields and their mutual phase shifts. Therefore, in both simulations the initial perturbations that give rise to blobs observed in SOL have similar characteristics. Also characteristics of blobs that penetrate LCFS are similar. This is supported by the left part of Fig. 5.12 that compares PDF of density fluctuations at LCFS.

In the SOL the fluctuation statistics clearly differs between the cases. While the mean value $\langle n \rangle$ in the subsonic case drops down with radius in very good agreement with experimentally measured profile as shown in [72, 50], it is almost constant in the Alfvénic case. We explain that as follows. Drain of vorticity due to generation of Alfvén waves significantly slows the blobs down. Therefore, on a fixed probe the fraction of signal in which the blobs are present increases, which in turn increases the mean value of density. Large number of blobs lose all their vorticity inside the SOL, stops and does not even reach far SOL or wall shadow region (Fig. 5.14). This further increases the mean density as the only way how the material (and energy) brought by the destroyed blob can be removed is by the parallel losses whose characteristic time ($\tau_{\parallel,n} \approx 3 \times 10^4/\omega_{ci}$) is much larger then characteristic time of the cross-field transport in the subsonic case ($\tau_\perp \approx \delta/v_\perp \approx (20\rho_s)/(0.1c_s) \approx 2 \times 10^2/\omega_{ci}$, where $\delta$ stands for blob size and $v_\perp$ is cross-field blob velocity). The presence of slow or destroyed blobs deforms the PDF of density fluctuations in the far SOL (Fig. 5.12(right)), changing higher statistical moments (for skewness and kurtosis see Fig. 5.11). In the subsonic case the PDF of density fluctuations in the far SOL is well-described by Gamma distribution which, again, agrees well with the experiment [50].

The excessive vorticity drain can be well demonstrated on radial profiles of vorticity and poloidal velocity - Fig. 5.13. The Alfvénic term quickly damps vorticity profile towards zero. Averaging relation (5.5) over poloidal direction and substituting $v_p = (\partial\phi/\partial r)/B$, the vorticity profile close to zero implies missing radial shear of poloidal velocity in the SOL, $\partial\langle v_p \rangle/\partial r \sim \langle \Omega \rangle$. The radial shear of $v_p$ is responsible for blob tilting and elongated blob shape in the subsonic case and as there is almost no shear in the Alfvénic case the blobs are less tilted as shown in Fig. 5.16.

In addition to the basic fluctuation statistics, in Fig. 5.16 we have computed conditionally averaged 2D density fields. First, radii $r^j_{CA}$ on which the conditional averaging will be performed were defined. All blobs with $\tilde{n}_{i,max}/\langle n \rangle > 2\sigma_n$ were tracked and whenever position of blob's density maximum $\vec{x}_{i,max}$ crossed radius $r^j_{CA}$ for the first time, the whole 2D field of relative density $n(p,r) - \langle n \rangle(r)$ was added to the average. Blobs crossing each of the radii $r^j_{CA}$ where averaged separately. Before the averaging, each 2D field was poloidally rotated such that poloidal coordinate of blob's density maximum $p_{i,max}$ was the same in all averaged cases, $p_{i,max} = 38\rho_s$. This is allowed by poloidal periodicity of the simulation and it ensures that the result is not distorted by different poloidal positions of individual blobs. The relative density field $\tilde{n}^j_{CA}$ conditionally averaged with condition placed at radius $r^j_{CA}$ can be written as

$$\tilde{n}^j_{CA}(r,p) = \frac{1}{N^j} \sum_{t^i_j} \tilde{n}(t^i_j, r, (p - p_{i,max} + 38\rho_s) \bmod l_p) \tag{5.38}$$

where $l_p$ is poloidal extent of the simulation region, $t^i_j$ is time of detection of density maxima of i-th blob at radius $r^j_{CA}$ and $N^j$ is number of averaged blobs. Difference

between the two studied cases, subsonic advection and Alfvénic vorticity damping, is presented in Fig. 5.16. While in the subsonic case the blobs are elongated poloidally in the near SOL (with factor $\delta_p/\delta_r \approx 2$) and transform to the circular shape in the far SOL, the behaviour for Alfvénic case is just the opposite (see also estimated blob sizes in Fig. 5.15). In the near SOL the blobs are almost circular (due to low shear of $v_p$) with $\delta_p/\delta_r \approx 1$, and they elongate poloidally as they slow down. The ratio of radial $\delta_r$ and poloidal $\delta_p$ blob size was measured on JET [155], giving $\delta_p/\delta_r \approx 2-3$ at LCFS and $\delta_p/\delta_r \approx 1$ in the far SOL. This, together with difference in statistical moments of density fluctuations and missing shear of poloidal velocity in the SOL, discussed in previous paragraphs, leads us to the conclusion that Alfvénic closure of $\nabla J_\parallel$ term is not appropriate for 2D modelling of fully developed interchange turbulence in the TCV and JET conditions [112].

## 5.6 Effect of electric connection of blobs to material surface

In the literature it is often assumed that the turbulence in SOL is electrically connected to material targets located at field line ends (typically limiter or divertor) and closure of $\nabla J_\parallel$ (4.99) that describes sheath dissipation is used either in full (e.g. [15, 16]) or linearised (e.g. [125, 107, 87]) form. The ESEL model was originally developed for the case of high parallel electron collisionality $\nu_e^* > 10$ and the main arguments why influence of the sheaths is neglected in the model and only subsonic vorticity advection is used are summarized in [39]. It is mainly the argument that the sheath-limited approach may not be suitable for conduction-limited regime where the parallel transport is driven by local parallel gradients. Moreover, the term (4.99) represents field line average, which may not be appropriate if the averaged terms are strongly non-linear. In this chapter we will analyse influence of the sheath dissipation on turbulence generated in ESEL (keeping plasma parameters such that $\nu_e^* > 10$) and its relation to the experiment will be discussed.

First, before we discuss results of our simulations, we have to point out that when the sheath dissipation term is used as a parallel vorticity sink, the simulation is no longer independent on radial boundary conditions (BC) placed on potential field and it gets an additional degree of freedom. The reason was already discussed in Sec. 5.1.2. This dependency was not fully realized at the beginning and first results of our simulations with the sheath dissipation included and with Dirichlet BC ($\phi_{IN} = \phi_{OUT} = 0$) [114] produced turbulence with very weak shear of $v_p$ around LCFS (fluctuation statistics of this simulation is shown as cyan line in Figs. 5.17, 5.18, 5.20, 5.21 and 5.23). In such case the potential structure representing sheared poloidal $E \times B$ drift is quickly damped to the sheath potential $\approx 2.8T_e$ and since boundary condition $\phi_{OUT} = 0$ limits radial electric field in the edge region, the weakened transport barrier is not able to stop even the weakest turbulence structures.

In the following set of simulations we add the sheath dissipation $\nabla J_\parallel$ closure (4.99) on top of the standard advective loss term (4.100). Similarly to all other parallel loss terms, the sheath dissipation is used in SOL and wall shadows regions but not in the edge region. The boundary conditions on $\phi$ are placed such that $\phi_{OUT} \equiv \phi(r = r_{max}) = 0$ and we make a scan over different values of $\phi_{IN} \equiv$

$\phi(r = r_{min})$. The value of outer BC $\phi_{OUT} = 0$ is chosen to correspond to the value of plasma potential measured in experiment in the wall shadow [74]. The scan over $\phi_{IN}$ represents scan over mean radial electric field in the edge region and consequently also scan over strength of the poloidal velocity shear layer. The mechanism of regulating the shear layer by $\phi_{IN}$ is based on the fact that the sheath dissipation term (4.99) quickly pushes local potential (in SOL and wall shadow where the sheath dissipation is used) to the level $\phi \approx 2.8T_e$ and thus the mean radial electric field inside LCFS (which implicates rotation inside LCFS) is given as

$$\langle \bar{E}_r \rangle_{edge} \approx -\frac{\bar{\phi}(r = r_{LCFS}) - \phi_{IN}}{r_{LCFS} - r_{min}} \approx -\frac{2.8\bar{T}_e(r = r_{LCFS}) - \phi_{IN}}{r_{LCFS} - r_{min}}. \tag{5.39}$$

Here the brackets $\langle \cdot \rangle_{edge}$ denote averaging over radial extent of the edge region and the bar represents poloidally and time averaged quantity. By keeping $\bar{T}_e(r = r_{LCFS})$, $r_{LCFS}$ and $r_{min}$ the same in all simulations and changing $\phi_{IN}$, we regulate mean poloidal velocity in the edge region $\langle \bar{v}_p \rangle_{edge} \sim \langle \bar{E}_r \rangle_{edge}$. When the sheath dissipation is strong, the mean poloidal velocity in the near SOL can be approximated as $\bar{v}_p(r) \sim \partial\bar{\phi}(r)/\partial r \approx 2.8\partial\bar{T}_e(r)/\partial r$. The difference between the poloidal velocity in the edge and near SOL regions implicates presence of shear layer that limits plasma transport from the edge to the SOL. Term $\langle \bar{v}_p \rangle_{edge}$ represents mean value over the whole edge region and we note that the effect on local poloidal velocity in the edge and its local shear may not scale fully linearly with $\phi_{IN}$.

### 5.6.1 Radial profiles of potential and poloidal velocity

Scaling of the poloidal velocity and properties of the velocity shear layer for different values of $\phi_{IN}$ are shown in Fig. 5.17. It reveals that the shear layer consists of two parts, one with positive shear in the outer vicinity of the LCFS and one with negative shear inside the LCFS. This property is clearly introduced by the sheath dissipation term (through the mechanism outlined in previous paragraph) since the shear in the standard advective case is always positive. Qualitative comparison of the shear layer structure with measurements of radial electric field made by reciprocating ball-pen probe on ASDEX [104] shows that similar double structure of the shear layer is observed also in the real tokamak plasmas. Zero radial electric field (i.e. zero poloidal $E \times B$ drift) was measured at LCFS, which agrees with the case modelled by the sheath dissipation (Fig. 5.17(right)). Similar experimental data from TCV were, however, not available and similar set of simulations with sheath dissipation term is being prepared for parameters of ASDEX Upgrade (Tab. 5.1) to allow direct comparison with $\langle v_p \rangle$ profiles measured by ball-pen probe technique in [74].

The shape of $v_p$ profile is directly derived from the profile of plasma potential, $\langle v_p \rangle = (\partial\langle\phi\rangle/\partial r)/B$, shown in Fig. 5.18. Influence of the introduced sheath dissipation term can be directly seen on the radial dependency of ratio $\langle\phi\rangle/\langle T_e\rangle$. The interaction with the divertor sheaths causes that the parallel vorticity sink

$$\left(\frac{\partial\vec{\nabla}_\perp^2\phi}{\partial t}\right)_\parallel = \left(\frac{\partial\Omega}{\partial t}\right)_\parallel \approx \frac{1}{n}\nabla J_\parallel \approx \frac{c_s}{L_\parallel}(2.8 - \frac{\phi}{T_e}) \tag{5.40}$$

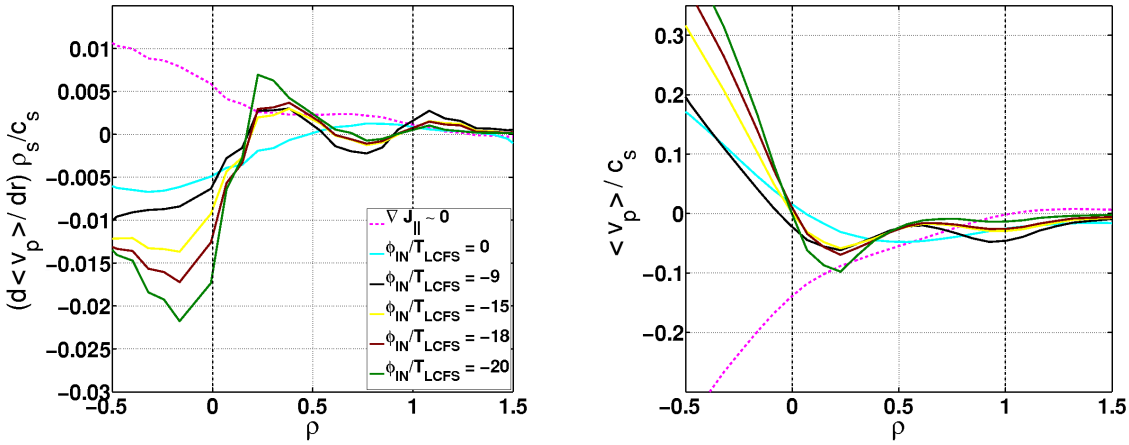


Figure 5.17: Radial profile of poloidal velocity (right) and its radial shear (left) in ESEL simulation for TCV parameters with subsonic vorticity advection (magenta dashed line) and sheath (solid lines) closure of $\nabla J_{\|}$. Different values of $\phi_{IN}$ are plotted with different colors.

minimizes difference $(2.8 - \phi/T_e)$ and the radial profile of plasma potential (and poloidal flows) is primarily determined by the temperature profile $\langle\phi\rangle \approx 2.8\langle T_e\rangle$. In the case of subsonic vorticity advection both quantities $\phi$ and $T_e$ are generally independent and their ratio sharply increases towards the LCFS. Here we should note that the electron temperature in the sheath dissipation term should be taken at the position of the sheaths, i.e. at field line ends. This information is, however, not available in 2D model and for simplicity it is substituted by the electron temperature at the midplane, assuming flat temperature profiles along field lines.

More illustrative point of view to the relation between $T_e$ and $\phi$ in the simulations is provided by Fig. 5.19 where scatter plot of their instantaneous values on different positions (distinguished by different colors) is shown. In the sheath dissipated case any perturbation of potential from the value $\phi \approx 2.8T_e$ results in quick change of parallel current pushing potential back to its equilibrium value. Due to this mechanism the potential fluctuation level is by factor of $2-3$ reduced compared to the case of subsonic vorticity advection as seen also in Fig. 5.18(top left) (except the case $\phi_{IN} = 0$ where the transport barrier around the LCFS is weakened and not able to hold plasma confined inside the LCFS). The reduction of fluctuations of plasma (5.18(top right)) and floating (Fig. 5.18(bottom right)) potential is favourable - the simulations with sheath dissipation show good agreement with experimental data on fluctuation level of floating potential $V_{fl}$ (bottom right in Fig. 5.18) which indicates that the sheath dissipation is present even in conditions with high parallel collisionality.

Based on our analysis of the influence of the sheath dissipation term on the interchange turbulence and on properties of the radial potential and velocity profiles, Dr. A.H. Nielsen from Technical University of Denmark made a preliminary simulation for ASDEX Upgrade parameters with the sheath dissipation term included. In [152] the simulation was compared with reciprocating probe measurements and surprisingly good agreement was found in radial profiles of plasma potential and associated poloidal velocity. Moreover, improvement in previously (with subsonic

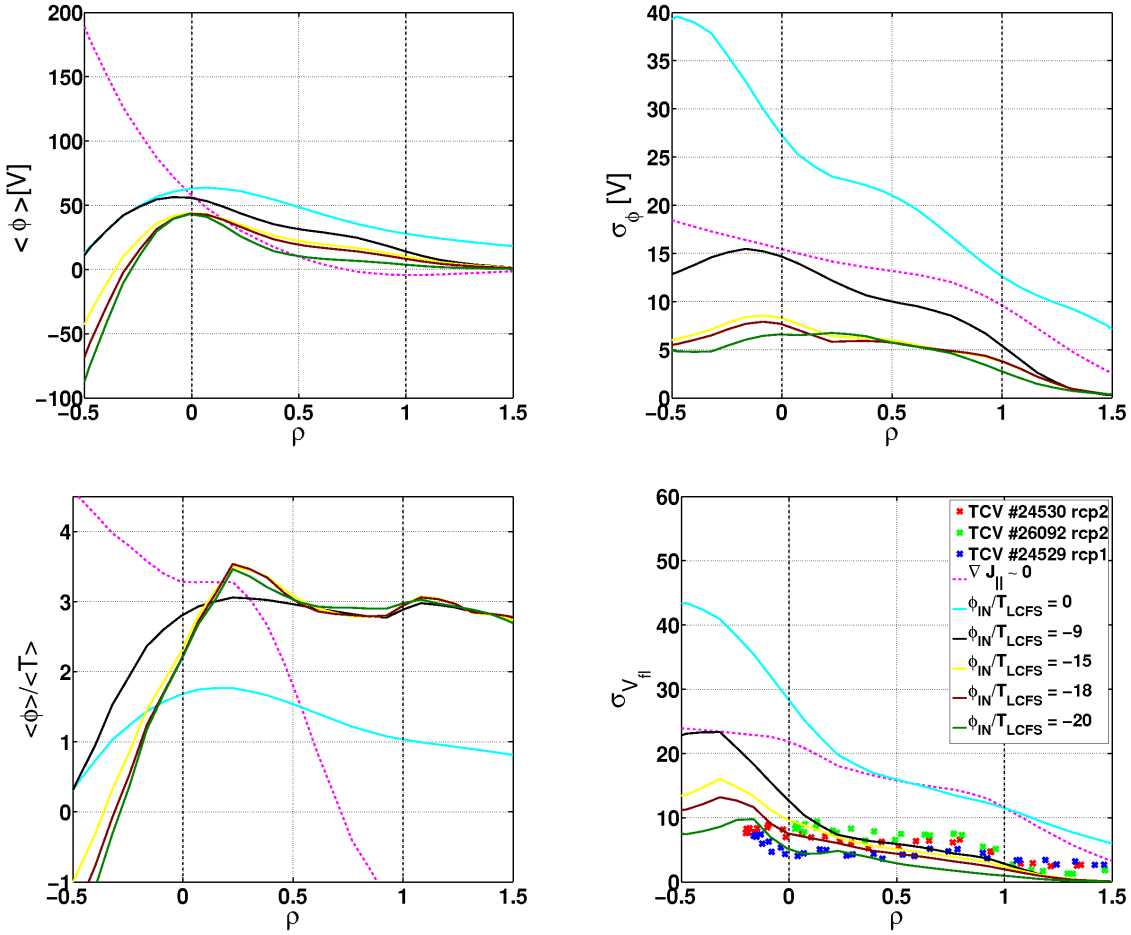


Figure 5.18: Radial profile of plasma potential $\phi$ (top left) and its fluctuation level (top right) for different values of parameter $\phi_{IN}$. Radial profile of ratio of mean potential and temperature (bottom left) and of floating potential fluctuation level $\sigma_{V_{fl}}$ (bottom right). The experimental data from reciprocating probe measurements (crosses, [72]) for discharges with different line-averaged density are plotted for comparison: discharge #24530 (red), discharge #26092 (green) and discharge #24529 (blue). Solid lines represent simulations with sheath dissipation, reference simulation with subsonic vorticity advection is plotted by dashed magenta line.

parallel vorticity advection) found discrepancy in density e-folding length $\lambda_n$ was achieved. The success in the comparison of $\phi$ and $v_p$ is strong indication that effects of electrical connection of blobs to the sheath play a role in the real plasmas and should be taken into account. This first simulation, however, used different set of inner boundary conditions which were, in our opinion, the cause of unrealistically high fluctuations of all quantities in the SOL ($\sigma_\phi/\langle T_e\rangle \approx 3$). The situation is, to some extent, probably similar to the $\phi_{IN} = 0$ case in our analysis where high level of potential fluctuations (Fig. 5.18(top right)) is observed as well. Therefore, full scan over degree of freedom given by inner potential BC $\phi_{IN}$ made also for ASDEX parameters is needed and it is already in preparation. Nevertheless, we note that it was the first time when good agreement of plasma potential profile was obtained in direct comparison between ESEL simulation and experiment.

### 5.6.2 Time scale of $\phi - T_e$ coupling

The interaction with the sheaths not only changes the relation of the mean profiles of $\phi$ and $T_e$ and lowers the fluctuation level of $\phi$, but it also couples their fluctuations on a fast scale. This can be seen in the insets of Fig. 5.19 where the PDF of fast fluctuations (below 15 $\mu s$) is plotted. Comparing both cases reveals that independent (or slightly anticorrelated) fluctuations of $\phi$ and $T_e$ in the case of subsonic vorticity advection become coupled when the sheath dissipation term is introduced and the main axis of the PDF is rotated towards line $\phi = 2.8T_e$.

Even though local and instantaneous values of $\phi$ and $T_e$ are usually used when modelling sheath dissipation, the reaction of the sheath dissipation term on potential perturbations carried by blobs cannot be instantaneous [39]. Some time is needed to carry the information from the midplane to the sheath were the equivalent electric circuit is closed. This time may be comparable to or even larger than the time of radial blob transit over single field line [39]. In such case, the response of parallel currents on given field line would be delayed after turbulent fluctuations passing over the field line and the effect of the sheath dissipation term (4.99) would effectively average in time. In such situation the sheath dissipation acts on mean potential and vorticity profiles but not on fast perturbations associated with blobs. In such case the radial profiles of mean $\phi$ and $T_e$ would be highly correlated (due to sheath dissipation) while there would be no (or only weak) correlation between the fluctuations (fast vorticity fluctuations damped by subsonic advection). Therefore, we suggest to use form of the sheath dissipation term (4.99) time-averaged over characteristic parallel time $\tau_\parallel$,

$$\vec{\nabla}\cdot\vec{J}_\parallel \approx \langle \frac{enc_s}{L_\parallel}\left(1-\exp\left(-\frac{e\delta\phi}{T_e}\right)\right)\rangle_{\tau_\parallel} \approx \langle \frac{enc_s}{L_\parallel}\frac{e\delta\phi}{T_e}\rangle_{\tau_\parallel}. \tag{5.41}$$

The characteristic time scale of the $\phi$ and $T_e$ coupling, $\tau_\parallel$, could be determined by the rate of rotation of the PDF with respect to the time scale of the studied fluctuations (the high-pass filtering threshold). This type of analysis used on experimental data should determine character and reaction rate of the parallel currents that couple midplane turbulence to the divertor sheaths. Currently, we have available $T_e$ and $\phi$ data measured by reciprocating ball-pen probe on ASDEX Upgrade ([74]) and preliminary analysis revealed picture very similar to that shown in bottom part of Fig. 5.19 i.e., it strongly favours the sheath dissipation regime. We

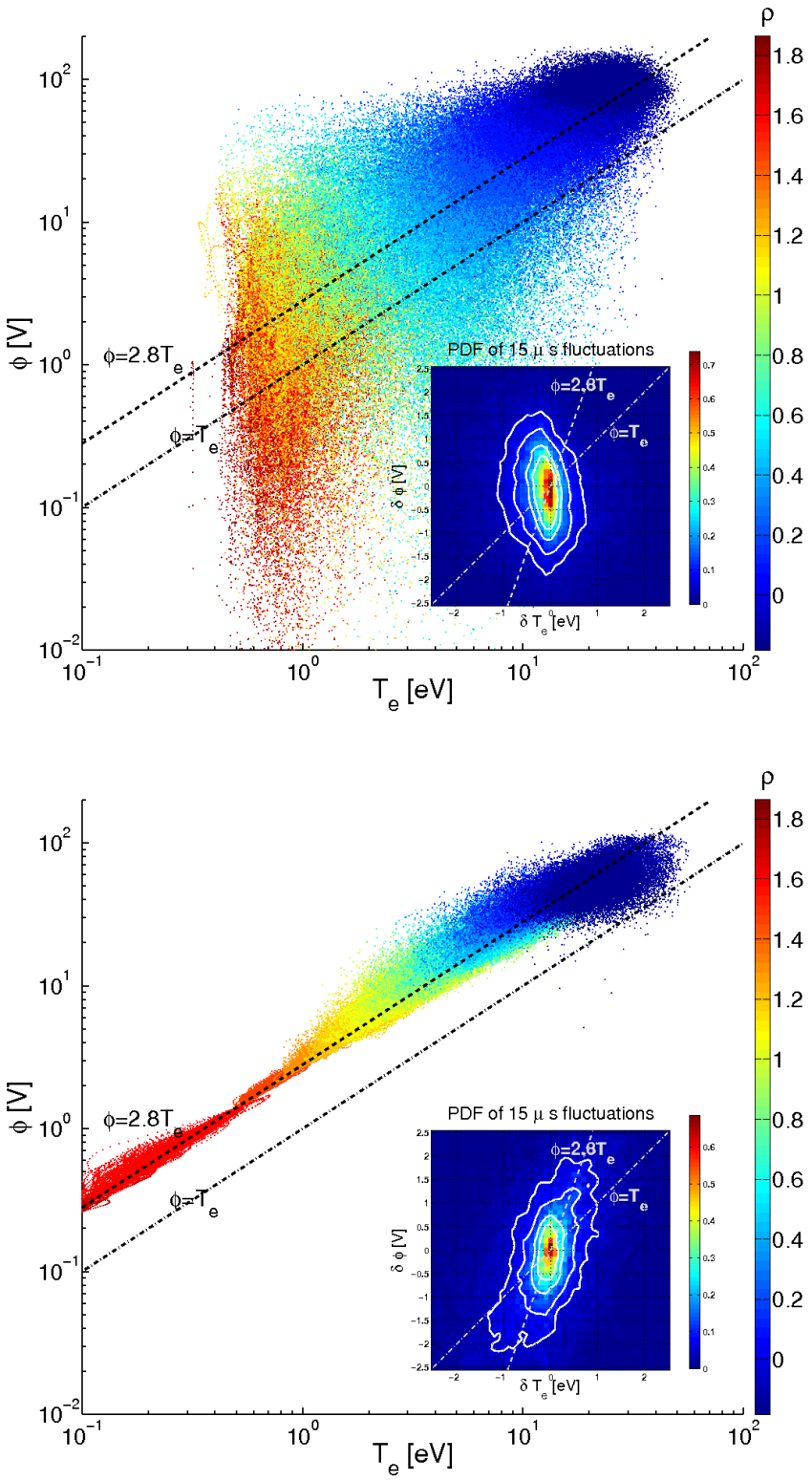


Figure 5.19: Scatter plot of instantaneous values of plasma potential $\phi$ vs. electron temperature $T_e$ for subsonic vorticity advection (top) and case with sheath dissipation included and $\phi_{IN}/T_{LCFS} = -15$ (bottom). Different colors distinguish radial positions. Inset figure shows 2D probability distribution function of potential and temperature fluctuations at all radii, i.e. PDF of high-pass filtered signals with filtering threshold 15 $\mu s$. Contours at levels 0.05, 0.1, 0.2 and 0.3 are plotted in white.

expect that confirmation or rejection of the hypothesis (5.41) will be brought by detailed analysis of experimental data. Moreover, more information on this topic will be brought by planned extension of SOLF1D model [65] with solver of generalized Ohm's law (4.79), replacing currently used assumption ($\nabla J_{\parallel} \approx 0$). SOLF1D computes transport along field lines and it was recently fully coupled with the ESEL code (see Sec. 5.7). When augmented with full Ohm's law, the coupled code will allow to model behaviour of the $\nabla J_{\parallel}$ term in a highly fluctuating (turbulent) environment and test our hypothesis (5.41).

### 5.6.3 Scaling of density and temperature

In Fig. 5.17 we have shown that change of $\phi_{IN}$ regulates strength of radial shear of poloidal plasma velocity. This represents regulation of transport barrier around LCFS and this mechanism influences blob penetration into SOL and has significant impact on radial density and temperature profiles as shown in Figs. 5.20 and 5.21. With increasing amplitude of the shear layer (decreasing $\phi_{IN}$) the steepness of density profile quickly rises as can be seen also on scaling of (minimal) radial density and temperature e-folding lengths ($\lambda_n = 1/(\partial \ln n/\partial r)$ and similarly for $\lambda_T$) in the near SOL shown in Fig. 5.22. By making fit to the data we find relations (for $\phi_{IN} < \phi(r = r_{LCFS})$)

$$\lambda_n \approx 117 \cdot \exp\left(0.14 \frac{\phi_{IN}}{T_{e,LCFS}}\right) \approx 172 \cdot \exp\left(4.2 \times 10^{-3} \cdot \frac{\langle \bar{E}_r \rangle_{edge}}{T_{e,LCFS}}\right) \quad (5.42)$$

$$\lambda_T \approx 36 \cdot \exp\left(0.08 \frac{\phi_{IN}}{T_{e,LCFS}}\right) \approx 44 \cdot \exp\left(2.4 \times 10^{-3} \cdot \frac{\langle \bar{E}_r \rangle_{edge}}{T_{e,LCFS}}\right) \quad (5.43)$$

where we have substituted $\phi_{IN} \approx 2.8 T_{e,LCFS} + \delta r \langle \bar{E}_r \rangle_{edge}$ from (5.39), $T_{e,LCFS} \equiv \bar{T}_e(r = r_{LCFS})$ and $\delta r = 3 \times 10^{-2}$ m is radial width of edge region in the simulation. Here $\phi_{IN}$ is given in $V$, $T_e$ in $eV$, $E_r$ in $V/m$ and $\lambda$ in $mm$. This dependency is, in principle, experimentally verifiable when $T_{e,LCFS}$ and $\langle \bar{E}_r \rangle_{edge}$ are measured, however, we note that the coefficients are relevant for the modelled TCV case only. Since the coefficients may differ for other tokamaks, new set of simulations would be needed.

In the case of weak radial electric field $E_r$ in the edge region (e.g. $\phi_{IN} = 0$) almost all perturbations can penetrate through the transport barrier and this penetration happens very often. On the other hand, probability of blob penetrating the transport barrier formed with large $E_r$ in the edge is small and such event happens rarely. This is documented in Fig. 5.23(left) where number of events with relative fluctuation threshold above $2\sigma_n$ is plotted for different values of $\phi_{IN}$. With decreasing $\phi_{IN}$ (increasing $v_p$ shear) the number of blobs ejected from edge into SOL decreases. Conditional average of radial particle flux carried by these blobs in the near SOL region (Fig. 5.23(right)) reveals that the flux decreases with decreasing $\phi_{IN}$, which results in further steepening of the density profile. At the same time, the PDF of relative density fluctuations in Fig. 5.20(bottom) remains more or less similar for all the studied cases,which agrees with observation made in experimental data sets [50].

In Fig. 5.20 experimental data from TCV obtained from discharges with different line-averaged density are plotted for comparison. In the simulation, values of $\phi_{IN}$ can be found such that the radial density profile in all three discharges is

reasonably reproduced. This indicates that the radial electric field around LCFS was different between the discharges, however, this could not be verified since experimental data on $E_r$ inside LCFS of TCV were not available. While profiles of the mean values are matched well in all of the cases except $\phi_{IN} = 0$, comparison of fluctuation level $\sigma_n$ shows larger differences, but not more than by factor of 2 (again, except case $\phi_{IN} = 0$) and typically deeper in the SOL. The fluctuation level grows as the profile steepens and best agreement with experimental values is found approximately in the range $-19 \leq \phi_{IN}/T_{LCFS} \leq -15$. The different level of fluctuations in the other cases may be influenced by several factors. In our opinion, the two most important are: (i) The analytical approximation of parallel sink terms (Eqs. (5.11)-(5.13)) may not be fully appropriate [65] and incorrectly determined density losses distort level of density fluctuations; (ii) The instantaneous form of the sheath dissipation term (4.99) is appropriate only for conditions with lower parallel collisionality (which is correlated with presence of steep gradients of density profile [52]) where interaction with the sheath takes place on fast time scales. Otherwise, its time averaged form (5.41) should be used, restricting sheath dissipation to time-averaged potential and velocity profiles only, keeping fast fluctuations free, damped by subsonic advection only. Both topics will be examined in our next works.

Radial profile of electron temperature scales similarly to the profile of density, again showing reasonable agreement (except case $\phi_{IN}/T_{LCFS} = -20$) with experimentally measured profiles in the SOL (Fig. 5.20(left)). The disagreement in temperature profiles in the wall shadow region is probably caused by inability of the diagnostics to measure low temperatures. This topic will be discussed in more details in Sec. 6.2. The temperature profile was measured by swept probe that does not provide data on fast fluctuations. Instead, fast fluctuations of floating potential were measured by nearby located probe. In [74] we have shown on data measured at ASDEX Upgrade that fluctuation level of floating potential $\sigma_{V_{fl}}$ is dominated by temperature fluctuations and it corresponds to approximately $\sigma_{V_{fl}} \approx 2.8\sigma_T$. Since $\sigma_{V_{fl}}$ in the TCV simulations with sheath dissipation is comparable to experimentally measured values (Fig. 5.18(bottom right)), it indicates that also fluctuation level of temperature is in the simulation in correct order. Nevertheless, we note that the temperature fluctuations are above interval $\sigma_T/\langle T\rangle \approx (0.2 - 0.4)\sigma_n/\langle n\rangle$ reported in the literature [18, 74].

### 5.6.4 Conclusions

After comparing behaviour of sheath dissipated turbulence in SOL with experimental findings, we must pronounce that mechanism of sheath dissipation brings improvements against case taking into account subsonic vorticity advection only. Even though arguments about very high parallel collisionality $\nu_e^* \approx 60$ in the studied cases, that could decouple midplane turbulence from the influence of divertor targets, may be risen, the comparison of floating potential fluctuations with experimental values indicates that connection to the sheath plays a role even in these conditions. To join both arguments, we propose model (5.41) of sheath dissipation term averaged over characteristic time scale of parallel transport $\tau_\parallel$. With increasing $\tau_\parallel$, this model should exhibit smooth transition between sheath-dissipative and purely advective case and the corresponding time scale can be principally ob-

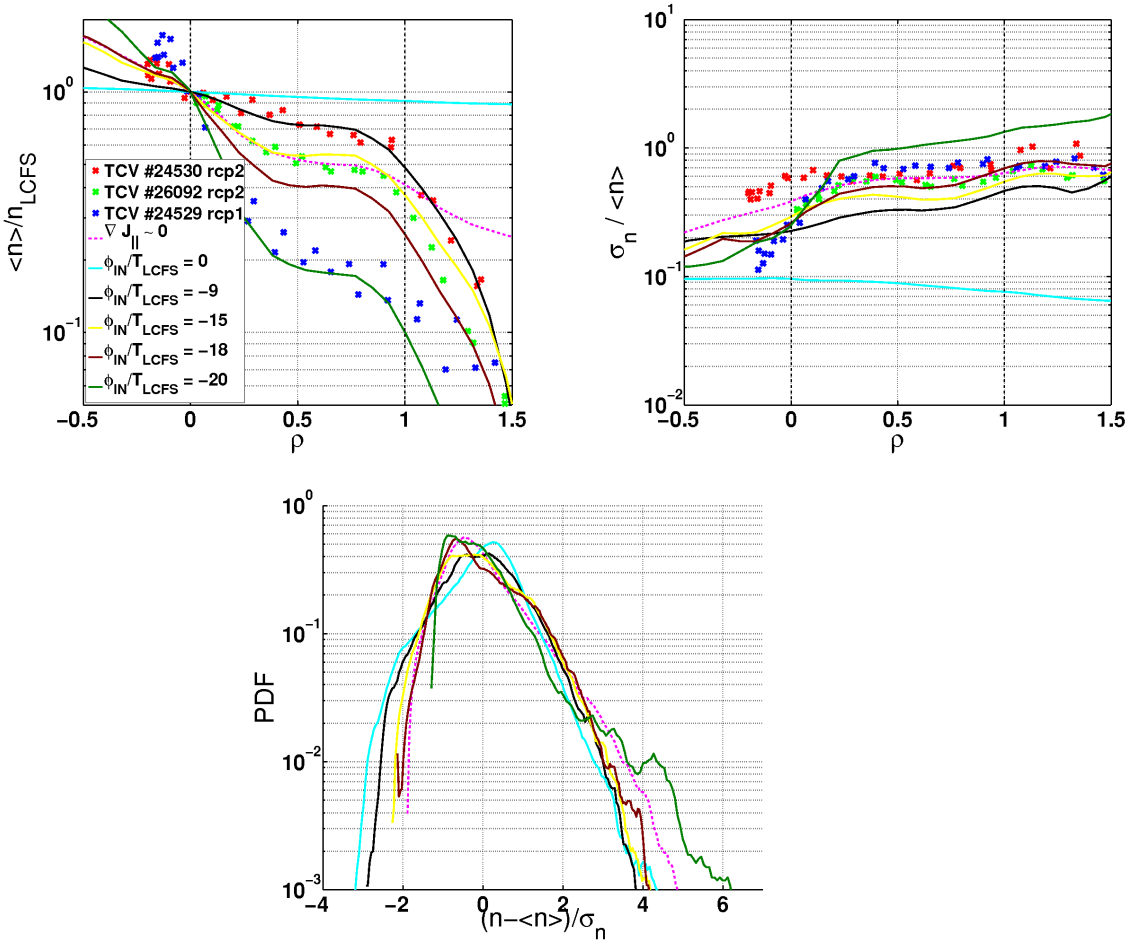


Figure 5.20: Radial profile of mean density (top left), relative density fluctuation level (top right) and PDF of density fluctuations at $\rho = 0.3$ (bottom) in ESEL simulation for TCV parameters with subsonic vorticity advection (magenta dashed line) and sheath dissipation (solid lines). The experimental data from reciprocating probe measurements (crosses, [72]) are plotted for comparison.

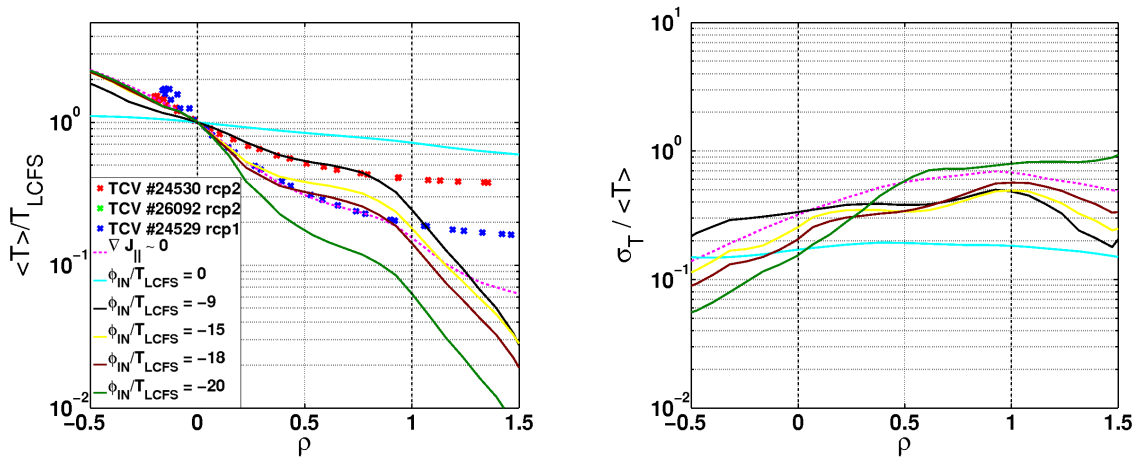


Figure 5.21: Radial profile of mean temperature (left) and relative temperature fluctuation level (right) in ESEL simulations for TCV parameters with subsonic vorticity advection (magenta dashed line) and sheath dissipation (solid lines).

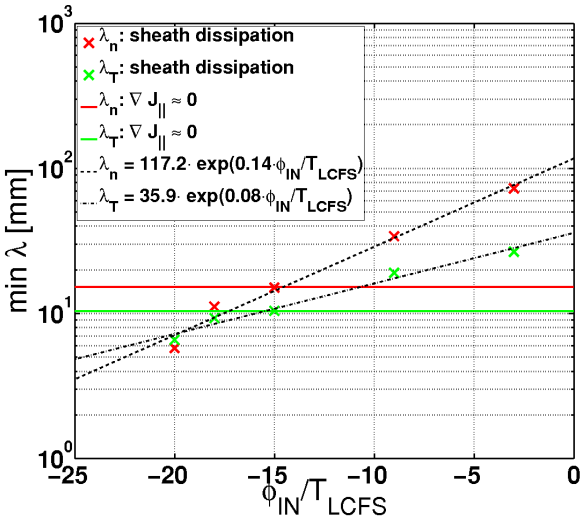


Figure 5.22: Scaling of minimum density (red) and temperature (green) e-folding length $\lambda_n$ and $\lambda_T$, respectively, in the near SOL with boundary condition $\phi_{IN}$ in ESEL simulations (TCV parameters) with sheath dissipation term (crosses). Values obtained in case of subsonic vorticity advection are plotted by horizontal lines.

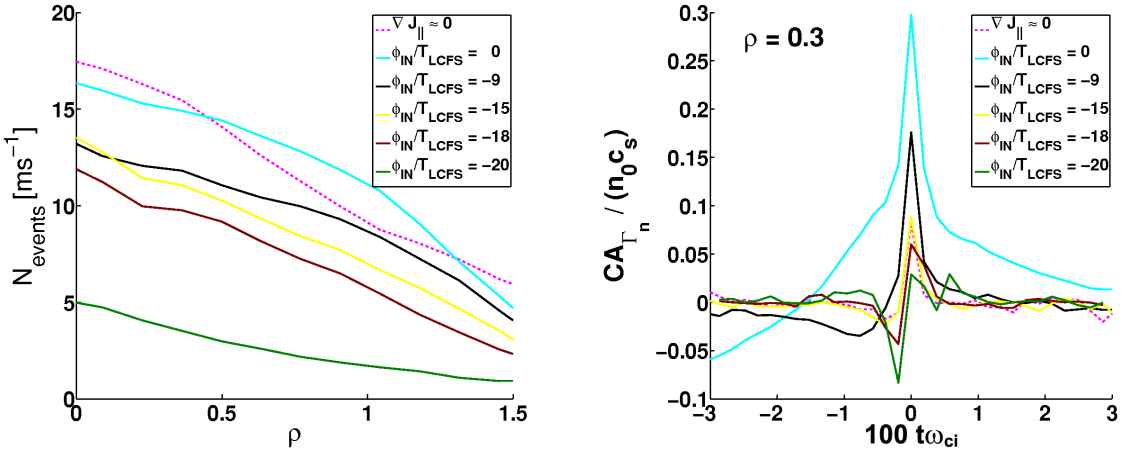


Figure 5.23: *Left:* Number of blobs per millisecond whose peak amplitude of density fluctuation is above level $2\sigma_n$. Scan over simulations with sheath dissipation included and with different BC $\phi_{IN}$ is plotted with solid lines, standard case of subsonic vorticity advection is plotted with dashed line. *Right:* Conditionally averaged profile of radial particle flux $\Gamma_n$ in the near SOL ($\rho = 0.3$). The CA trigger was set on density signal at level $2\sigma_n$.

tained from simultaneous experimental measurement of $\phi$ and $T_e$ signals. This is one of the goals of our future work.

At the same time, simulations including sheath dissipation are able to cover much broader range of density and temperature e-folding lengths than the simulation with subsonic vorticity advection. The density and temperature profiles scale with free parameter of the model, $\phi_{IN}$, that changes mean radial electric field in the edge region. Indeed, the relation (5.39) approximating radial electric field in the edge by linear relationship between $T_e(r = LCFS)$ and $\phi_{IN}$ is of the lowest order only and either physical processes contributing in this region to generation of $E_r$ should be included in the model or the value of $E_r$ should be matched with experimentally measured value. At present time, our work is focused on the latter as there are data of $E_r$ obtained from two independent diagnostics available for ASDEX Upgrade [104]. Nevertheless, scaling of the density and temperature profiles with $\phi_{IN}$ shows good agreement with experimental profiles in the case of TCV at the cost of somewhat lower density fluctuation level when values of higher $\phi_{IN}$ are used. We note, that the fluctuation statistics may be influenced by the way how plasma is lost along field lines (Eqs. (5.11)-(5.13)). In [65] we have shown that these analytical estimations of parallel losses may misinterpret the actual level of parallel transport and in future we aim to clarify the effect of parallel density and temperature sinks by coupling ESEL and SOLF1D codes (see Sec. 5.7).

## 5.7 Coupling of ESEL and SOLF1D codes and estimation of parallel losses

Closely connected with the topic of parallel dissipation of vorticity discussed in previous sections is the issue of estimation of parallel losses of density and tempe-

rature. Standard ESEL version uses analytical expressions (5.11)-(5.13) derived in [39], that assume subsonic parallel advection of density and vorticity and Spitzer-Harm diffusion of energy in conditions of simple SOL. These expressions are based on two main assumptions. First, that the characteristic gradient of the quantities along each field line is related to the connection length from midplane (where blobs are generated) to the material targets. And second, that parallel losses are independent on history of fluctuations on the field line. The first assumption, however, neglects ballooning nature of interchange transport due to which blobs appear on a field line as perturbations localised around midplane.

In order to assess validity of both assumptions we have, in cooperation with Dr. Eva Havlíčková from Culham Centre for Fusion Energy, performed coupling of the ESEL code with code SOLF1D. SOLF1D [64, 65] is a 1D fluid code solving Branginskii equations of plasma transport along field line, thus allowing to replace analytical expressions for parallel losses in ESEL (5.11)-(5.13) by a more realistic model. The equations solved by SOLF1D consist of parallel parts of: continuity equation (4.53) assuming $n_e \approx n_i \approx n$, ion momentum equation (4.45) and energy equation (4.60) for both plasma species. Parallel momentum of electrons is neglected. Presently, the generalised Ohm's law is simplified assuming ambipolar diffusion $v_e^{\parallel} = v_i^{\parallel} = v^{\parallel}$ and neglecting parallel currents $J_{\parallel} = 0$, but relaxing of these assumptions in upcoming version is considered. The final set of equations solved by SOLF1D is [64, 65]:

$$\frac{\partial n}{\partial t} + \frac{\partial}{\partial x^{\parallel}}(nv^{\parallel}) = S_i^n + S_{\perp}^n, \tag{5.44}$$

$$\frac{\partial}{\partial t}(m_i n v^{\parallel}) + \frac{\partial}{\partial x^{\parallel}}(m_i n v_{\parallel}^2 + \Pi^{\parallel\parallel}) = -\frac{\partial}{\partial x^{\parallel}}(n(T_i + T_e)) + m_i S_i^v + m_i S_{\perp}^v, \tag{5.45}$$

$$\frac{\partial}{\partial t}(\frac{3}{2}nT_e) + \frac{\partial}{\partial x^{\parallel}}(\frac{5}{2}v^{\parallel}nT_e + q_e^{\parallel}) = v^{\parallel}\frac{\partial}{\partial x^{\parallel}}(nT_e) - Q + S_e^E + S_{e,\perp}^E, \tag{5.46}$$

$$\frac{\partial}{\partial t}(\frac{3}{2}nT_i + \frac{1}{2}mnv_{\parallel}^2) + \frac{\partial}{\partial x^{\parallel}}(\frac{5}{2}v^{\parallel}nT_i + q_i^{\parallel} + \frac{1}{2}m_i n v^{\parallel}v_{\parallel}^2 + v^{\parallel}\Pi_{\parallel}^{\parallel}) = v^{\parallel}\frac{\partial}{\partial x^{\parallel}}(nT_e) + Q + S_i^E + S_{i,\perp}^E. \tag{5.47}$$

Terms $S_i^n, S_i^v, S_e^E, S_i^E$ describe changes due to atomic processes (ionization, charge exchange, recombination and excitation) and perpendicular sources $S_{\perp}^n, S_{\perp}^v, S_{e,\perp}^E, S_{i,\perp}^E$ represent effect of cross-field plasma motions that are computed and provided to SOLF1D by ESEL. Since ESEL model does not include ion temperature, some assumption has to be made on the form of $S_{i,\perp}^E$ that is typically taken as some multiple (1 or 2) of $S_{e,\perp}^E$. $Q$ is collisional heating (4.64). Optionally, effect of neutral particles that are localized near divertor targets can be included by solving their continuity and momentum equations.

Schematic illustration of coupling scheme of the codes is shown in Fig. 5.24. Each spatial point in ESEL has an associated instance of SOLF1D code that receives cross-field fluxes in form of perpendicular sources $S_{\perp}$, advances Eqs. (5.44)-(5.47) in time and returns parallel sinks to be substituted in ESEL for the rightmost terms in (5.8)-(5.10). In SOLF1D, Gaussian profile of the cross-field sources along field line is used,

$$S_{\perp}(x^{\parallel}) = S_{\perp,ESEL} e^{-(x^{\parallel} - x^{\parallel}_{midplane})^2/\Delta^2_{ballooning}}, \tag{5.48}$$

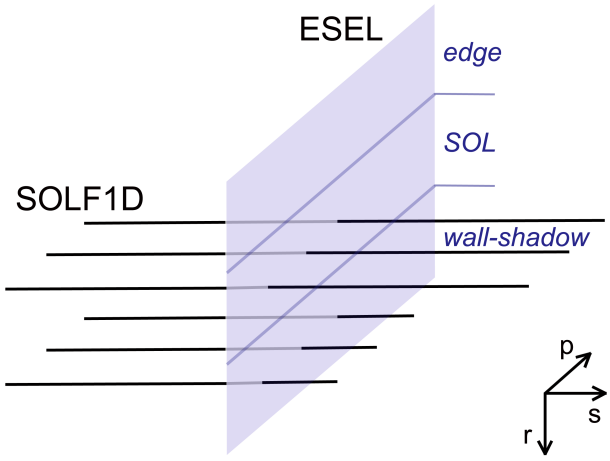


Figure 5.24: Schematic illustration of geometry of ESEL-SOLF1D coupling. Field lines in the wall shadow region are asymmetric, reflecting different connection length from midplane to divertor (left side) and from midplane to the first wall (right side).

representing ballooning nature of the turbulent transport. Maximum of the sources is located at position of the midplane $x^{\parallel}_{midplane}$ and width $\Delta_{balloning}$ of the Gaussian represents width of the ballooning region. Difference in local density and temperature values between ESEL and corresponding SOLF1D instance is checked and if needed, small artificial cross-field source is added on the input of SOLF1D to ensure consistency of both solutions. The artificial source is, however, needed very rarely and does not influence the final results. The coupled code neglects mixed parallel-perpendicular transport terms in the energy equation (violet terms in (4.60)) as well as in the momentum equation.

The parallelization of the coupled code has been made using Message Passing Interface (MPI) library such that the ESEL code constitutes the root MPI thread and SOLF1D instances are homogeneously distributed between the rest of available MPI threads. First performance tests made with ESEL run with spatial resolution $256 \times 384$ points show that during computation of one ESEL time on a single CPU core time step of approximately 115 SOLF1D instances (each with 100 points in parallel direction) can be computed on equivalent CPU core. To speed up the computation, the code allows reduction of number of SOLF1D instances by computing parallel transport with SOLF1D on sparser grid than is spatial grid used in ESEL. Then, the parallel sinks computed by SOLF1D instances are in ESEL interpolated in space. The impact of the interpolation on the results has, however, yet to be assessed.

### 5.7.1 Transport of turbulent fluctuations along field lines

In the first phase of the coupling we have used data from our ESEL simulation #116 as a source of fluctuations and provided them to Dr. Eva Havlíčková, author of the SOLF1D code, as an input to standalone SOLF1D code [64, 65, 66]. The simulation verified stability of the SOLF1D under strong forcing and provided some insight into spreading of turbulent fluctuations along magnetic field lines.

There are several observations that could be made prior to the full coupling

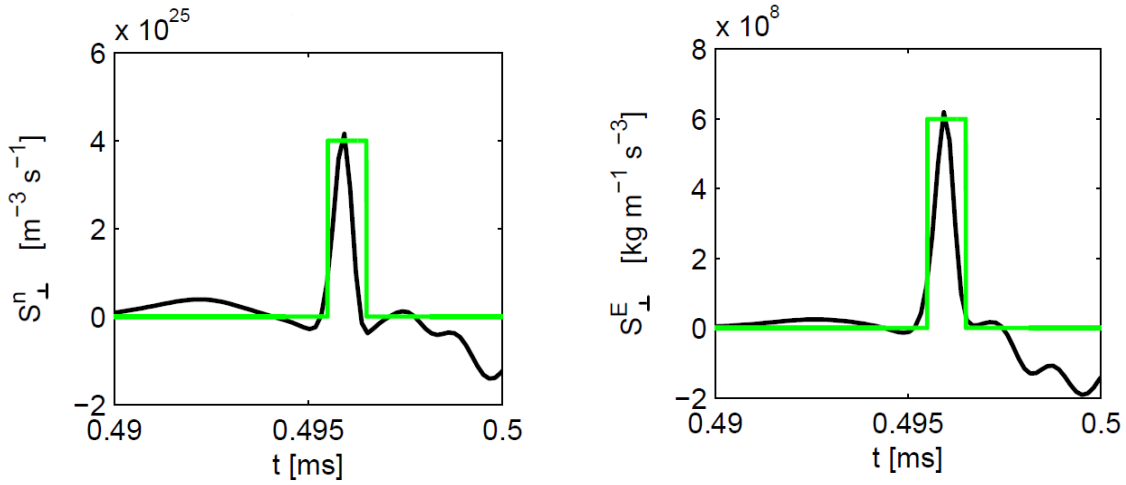


Figure 5.25: Trace of cross-field sources $S_\perp^n$ (left) and $S_\perp^E$ (right) at fixed point in ESEL simulation #116 during blob transit (black) and its approximation by step function used as an input for SOLF1D (green). [64].

of the codes. First, we have approximated cross-field sources associated with blob moving over SOLF1D field line by a step function [64, 65]. 1 $\mu$s duration of the event and amplitudes $S_\perp^n = 4 \cdot 10^{25}$ m$^{-3} \cdot$ s$^{-1}$, $S_{e,\perp}^E = S_{i,\perp}^E = 6 \cdot 10^8$ kg $\cdot$ m$^{-1} \cdot s^{-3}$ were used as values representing typical transient event in the ESEL simulation (see Fig. 5.25). The transient cross-field sources were applied on top of SOLF1D steady-state solution with neutrals at time $t = 30$ $\mu$s. In order to model ballooning nature of the interchange transport, Gaussian profile of the sources along field line (5.48) was used. Width of the profile corresponded to the width of the ballooning region for modelled parameters of TCV. Spreading of the event along field line is shown in Fig. 5.26 where profile of plasma density, temperature and parallel velocity are plotted at three different times: $t = 25$ $\mu$s - the steady state; $t = 31$ $\mu s$ - maximum of density at midplane; $t = 75$ $\mu$s - relaxation back to the steady state. Apparently, local density gradients are not given by connection length between midplane (center of the field line) and divertor targets, $L_\parallel = 15$ m, as is assumed in the approximation of parallel density losses (5.11) used in ESEL. Instead, the perturbation splits into two separate halves that move in opposite directions with Mach number $M_\parallel = 0.5$. As a result, parallel losses estimated by analytical expression (5.11) are underestimated by a factor $\approx 2-10$ [65]. Therefore, we argue that the connection length $L_\parallel$ should be in approximation of parallel density losses (5.11) replaced by length of the ballooning region, $L_\parallel \to L_b \approx L_\parallel/6$. On the other hand, the temperature profile quickly spreads over the field line and approximation of parallel gradients by connection length $L_\parallel$ is reasonable except the short time when the transient cross-field sources are present.

Both observations made for the case of step transient event are consistent with results of ESEL modelling of JET [39] and ASDEX [152] cases, where comparison with experiment founds density profiles being too flat in the simulation (i.e. parallel losses are underestimated) while at the same time the temperature profiles are in a reasonable agreement. The aim to improve this discrepancy provides one of the

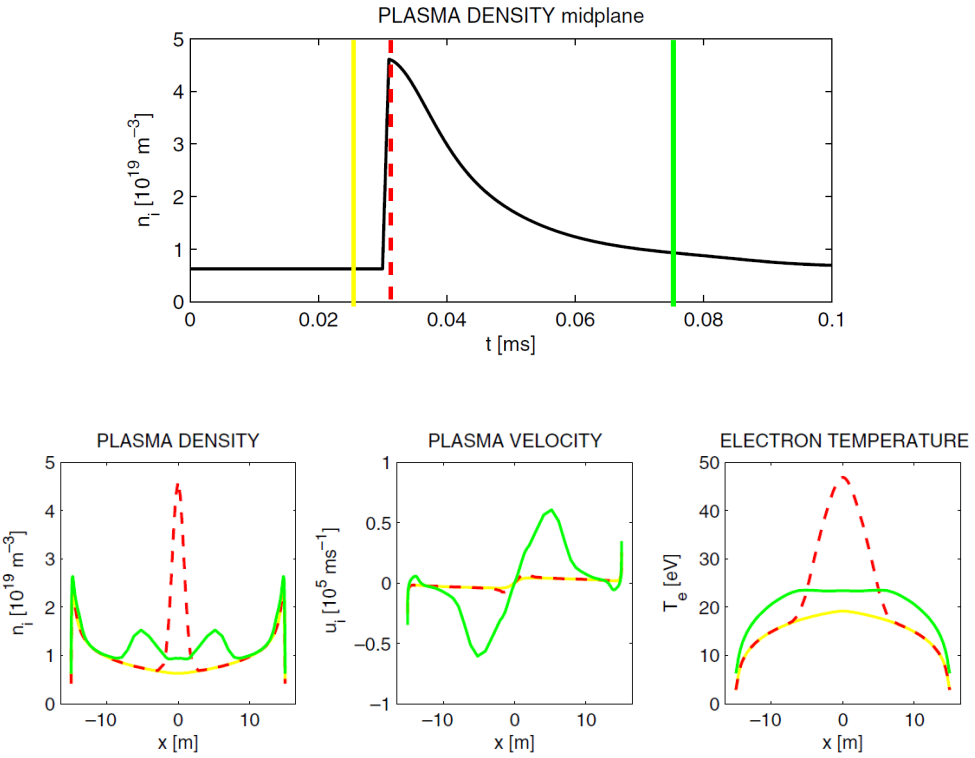


Figure 5.26: Time evolution of midplane density (top) and parallel profiles of density (bottom left), parallel velocity (bottom midle) and temperature (bootom right) in SOLF1D simulation with transient cross-field sources in form of step function with duration 1 $\mu$s. The profiles are shown in three different times: original steady-state profile (yellow), time of maximum midplane density (red) and relaxation back to steady-state (green). The transient event started at time $t = 30$ $\mu$s. [65].

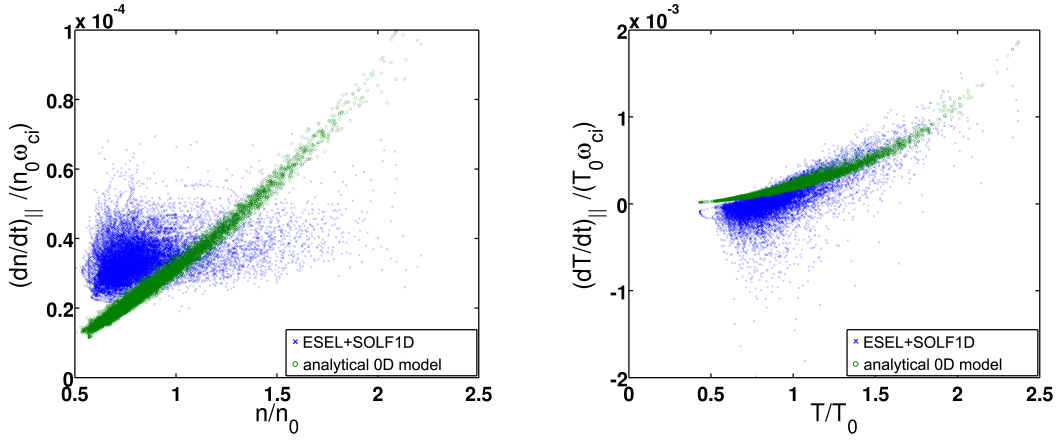


Figure 5.27: Parallel sink terms of density (left) and electron temperature (right) as a function of local density (left) and electron temperature (right) in fully coupled ESEL+SOLF1D code at radial position $\rho = 0.2$. SOLF1D version without neutrals was used. Prediction of 0D analytical model (5.11)-(5.13) is plotted by green circles, results of SOLF1D by blue crosses.

main motivations for the full coupling of both codes.

The second motivation for the full coupling is illustrated in Fig. 5.27. The density, temperature and velocity profiles along each field line keep memory of previous fluctuations and the whole system becomes, from the point of view of ESEL, non-Markovian. As a result, the response of midplane parallel losses on the same transient event is dependent on the history of fluctuations imposed on the field line and it cannot be easily parametrised in terms of midplane density and temperature as was done in Eqs. (5.11)-(5.13). Especially parallel losses of density (Fig. 5.27(left)) behave differently from the analytical 0D estimation and do not show any convincing dependence on local density and temperature in ESEL. Therefore, the fully coupled code is necessary for correct evaluation of parallel plasma losses from ESEL. The plotted data were taken from one of the first simulations made with the fully coupled code for parameters of TCV and they confirm previous estimations made by standalone SOLF1D version with ESEL forcing [65]. We note, that the coupled code should not be considered as 3D, since it does not include cross-field motions elsewhere, but in a single plane where the field lines cut outer midplane. This, indeed, neglects possibly important effects such as stabilisation of interchange modes at the inner midplane (illustrated in Fig.3.7) or vortex stretching in the vicinity of X-point (illustrated in Fig. 4.2(right)).

Example of behaviour of parallel losses in the coupled code is presented in Fig. 5.28. It shows that while peak values of temperature losses are comparable with the analytical model, density losses in the analytical model are most of the time underestimated by a factor of 2. In quiescent phases, when there are temporarily no turbulent structures crossing the field line, all density perturbations slowly expand towards field line ends, characteristic parallel length scale becomes comparable to the connection length and rate of density losses modelled by SOLF1D drops to the level comparable to the analytical model. On the simplified case of a step-like transient event we have shown that maximum of parallel density losses is delayed behind maximum of local density [65] and the same behaviour is present in Fig.

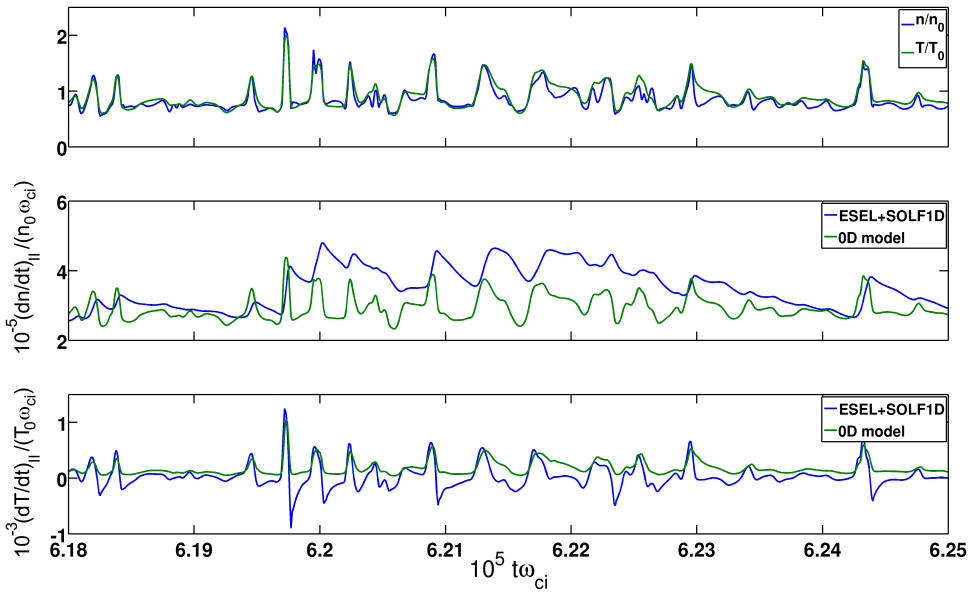


Figure 5.28: Time trace of local temperature and density (top) in coupled ESEL+SOLF1D simulation and corresponding parallel losses of density (middle) and temperature (bottom) predicted by 0D analytical model (5.11)-(5.13) (green) and modelled by SOLF1D without neutrals (blue).

5.28(middle). After blob transits over the field line, the temperature damping is negative and energy, that was spread along the field line when high-temperature blob was present, flows back to the middle of the field line that, after the blob was exchanged with background plasma by cross-field motion, became cooler than the field line ends.

The full coupling of both codes has been performed very recently. Stability and performance of the code were already successfully tested and relevant physical results from the fully coupled code will be available soon. In the future, the code will offer opportunity to compare modelled interplay between cross-field and parallel turbulent motions with fairly unique diagnostic installed on tokamak COMPASS - set of two reciprocating probes, one moving horizontally at the position of outer midplane, one moving vertically down from the top of tokamak vessel. The toroidal location of both reciprocating manipulators is such that approximate magnetic connection of the probes, and thus observation of parallel spreading of individual blobs, should be possible.

### 5.7.2 Averaging of transport coefficients

Radial profiles of mean density, temperature or pressure result from an interplay between plasma transport perpendicular and parallel to magnetic field lines. Even though the perpendicular transport is highly intermittent and plasma-surface interaction non-linear, effective transport coefficients computed from mean values of relevant thermodynamic quantity are often used in steady-state transport codes such as EDGE2D and SOLPS. This may be one of the sources of disagreement observed between result of the code and experiment [29]. Indeed, computing nonlinear

| radial position | $\rho = 0.0$ | $\rho = 0.0$ | $\rho = 0.0$ | $\rho = 0.2$ | $\rho = 0.4$ | $\rho = 0.6$ |
|---|---|---|---|---|---|---|
| parallel position [m] | x=0 | x=10 | x=15 | x=0 | x=0 | x=0 |
| $\langle n \rangle$ [$10^{19}$ m$^{-3}$] | 2.05 | 2.40 | 1.35 | 1.53 | 1.05 | 0.83 |
| $\sigma_n / \langle n \rangle$ | 0.37 | 0.08 | 0.18 | 0.49 | 0.64 | 0.76 |
| $\langle T_e \rangle$ [eV] | 20.99 | 20.33 | 3.52 | 12.33 | 6.68 | 4.23 |
| $\sigma_{T_e} / \langle T_e \rangle$ | 0.50 | 0.11 | 0.29 | 0.72 | 1.06 | 1.39 |
| $\langle n T_e \rangle / \langle n \rangle \langle T_e \rangle$ | 1.18 | 1.17 | 3.03 | 1.33 | 1.64 | 1.96 |
| $\langle n T_e^{3/2} \rangle / \langle n \rangle \langle T_e \rangle^{3/2}$ | 1.37 | 1.31 | 4.30 | 1.75 | 2.68 | 3.81 |
| $\langle T_e^{5/2} \rangle / \langle T_e \rangle^{5/2}$ | 1.49 | 1.71 | 5.29 | 2.10 | 3.77 | 6.31 |
| $\langle T_e^{7/2} \rangle / \langle T_e \rangle^{7/2}$ | 2.33 | 2.16 | 12.30 | 4.73 | 14.83 | 36.69 |

Table 5.2: Error made by fluctuation averaging for several non-linear functions of density $n$ and electron temperature $T_e$ evaluated at several radial points in ESEL simulation (x = 0 m) and along field line computed by SOLF1D that was located in the vicinity of LCFS ($\rho = 0$). x = 0 m is position of midplane at the center of the field line, x = 15 m is position of divertor target. [66].

function using average instead of fluctuating values in such intermittent environment as SOL may result in a significant error, with $\langle f(n, T_e) \rangle \neq f(\langle n \rangle, \langle T_e \rangle)$. The size of the error depends on fluctuation statistics, correlations between $n$ and $T_e$ and nonlinearity of the considered term. Another example can be found when lower hybrid wave propagation through edge plasma is studied [37, 38]. Then, presence of fluctuations may lead to intermittent damping of the wave on blobs.

In order to estimate the error made by using averaged values in non-linear function instead of averaging the whole function, we have used time trace of $n$ and $T_e$ fluctuations from different positions in ESEL run #116 and at the same time the data were provided as a forcing for standalone SOLF1D code to Dr. Eva Havlíčková [66]. Note that parallel losses computed by SOLF1D were not transferred back to ESEL and constant characteristic loss times from Tab. 5.1 were used instead. Also different potential boundary conditions in ESEL, $\phi(r = r_{min}) = 0$ and $(\partial\phi/\partial r)(r = r_{max}) = 0$, were used in order to fully reproduce the original run from [46].

The error due to non-linear nature of several considered terms is summarized in Tab. 5.2. The error is smallest near the LCFS at midplane and grows as the relative fluctuations increase and become more intermittent i.e., towards the far SOL and divertor targets. The biggest impact of the fluctuation averaging can be seen on strong functions of temperature such as parallel heat conductivity ($\sim T_e^{5/2}$) or thermal heat flux ($\sim T_e^{7/2}$). Generally, the transport coefficients may have very different dependency on $n$ and $T_e$ and therefore, in Fig. 5.29 we visualise ratio $\langle f(n, T_e) \rangle / f(\langle n \rangle, \langle T_e \rangle)$ at the midplane for the whole set of functions having form $f \approx n^{\alpha_n} T^{\alpha_T}$.

We should note that due to lack of experimental data we cannot verify level of $T_e$ fluctuations in the simulation and since experimentally measured level indicates rather lower level of fluctuations of $T_e$ [18, 74] than observed in ESEL, the values presented in Fig. 5.29 and Tab. 5.2 should be understood as an upper estimate. Moreover, these results will be verified when the full coupling of both codes is used, which may change amplitude of temperature and density fluctuations. Nevertheless, the observed impact of neglected fluctuations on value of transport

coefficients is non-negligible and the approach of fluctuation averaging may bring significant errors, especially in the boundaries of tokamak plasmas (outer wall, divertor targets).

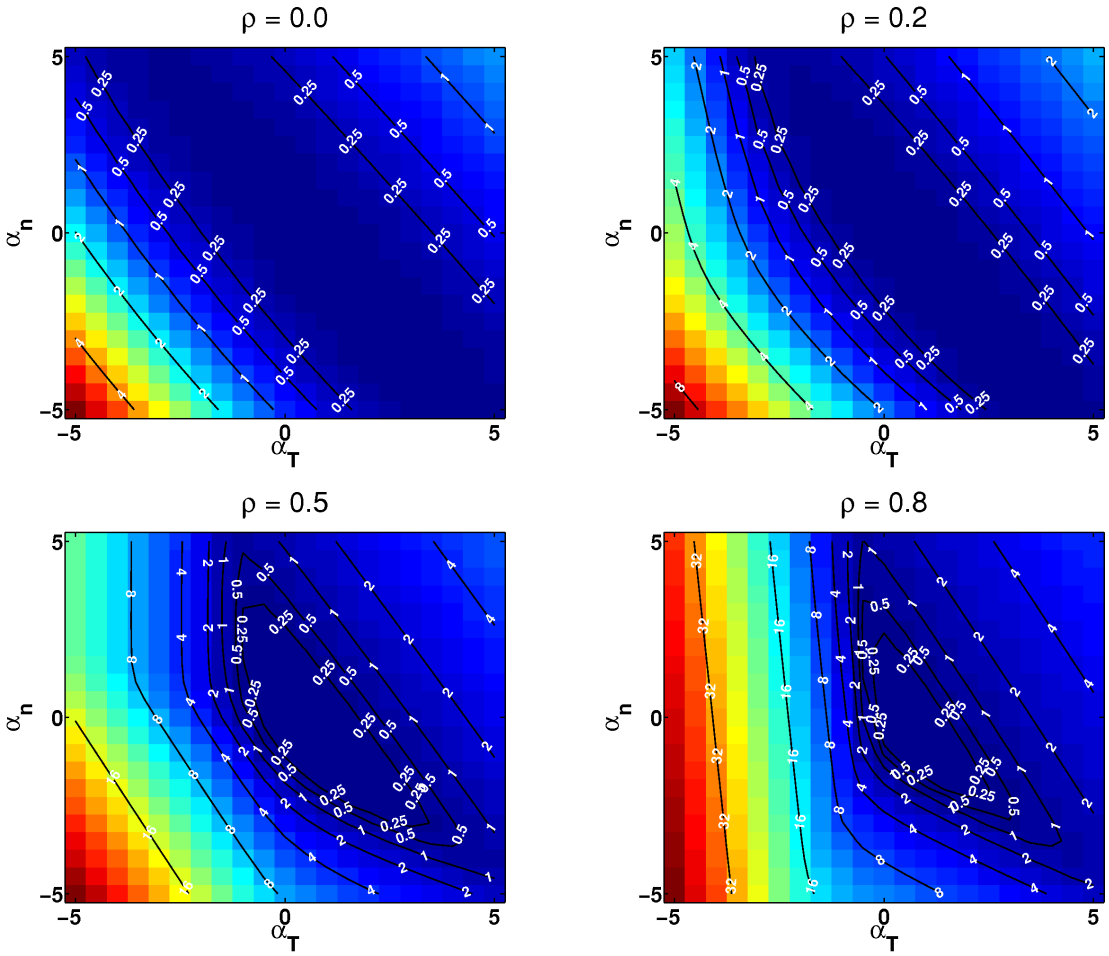


Figure 5.29: Error made by fluctuation averaging of functions of the form $f = n^{\alpha_n} T_e^{\alpha_T}$ estimated for different radial positions in ESEL #116 simulation. Decimal logarithm of the error i.e. function $\log_{10}\left(\frac{\langle f(n,T_e)\rangle}{f(\langle n\rangle,\langle T_e\rangle)}\right)$ is plotted.

# 6. Interpretation of probe measurements based on turbulence modelling

Electric probes are widely used diagnostics of tokamak edge plasma. The main advantage is their high spatial and temporal resolution. Besides basic Langmuir probes discussed in Sec. 3.2, combinations of several probe pins on a single probe head are often used, allowing measurement of gradients and correlation analysis. There also exist several advanced probe concepts specialized on measurements of quantities hardly obtainable from the basic Langmuir probes (see e.g. [100, 147]). There are two basic plasma parameters, electron temperature and plasma potential, that can be determined with swept Langmuir probes by measuring the I-V characteristic (3.15), however time resolution of such data is usually insufficient to correctly resolve individual structures on time scale of SOL turbulence. Some attempts were made to increase the sweeping frequency to $\approx$ 100 kHz - 1 MHz, however this approach brings additional problems such as hysteresis of the measured I-V characteristics caused by capacitive effects [73] and interpretation of the data may become very problematic.

In the next three sections we will use turbulence simulations presented in chapter 5 to discuss some aspects of measurement using concept of ball-pen probe (BPP) i.e., probe designed to allow fast and direct measurement of plasma potential and electron temperature. Then, in the last two sections of this chapter, correlation technique for measurement of poloidal plasma velocity and U-probe concept for determination of plasma vorticity will be discussed.

## 6.1 Ball-pen probe

Influence of local electron temperature $T_e$ on floating potential $V_{fl}$ (3.19) is given by factor $\alpha$, whose value is in typical SOL $\alpha \approx 2.5 - 3$. Since mean values as well as standard deviation of $T_e$ and $\phi$ fluctuations are comparable in the SOL [74], the term $\alpha T_e$ may cause significant differencies of floating and plasma potential. The basic idea of concepts of direct plasma potential measurement by emissive probe and ball-pen probe (BPP) is to reduce the value of $\alpha$, thus reducing also parasitic influence of $T_e$ in the measured potential [147].

Well-known emissive probes achieve this by heating the probe (either directly or indirectly by laser beam), which gives rise to electron emission current $I_{ee}$. $\alpha$ is then given as $\alpha = \ln(I_{sat}^{-}/(I_{sat}^{+} + I_{ee}))$. When the ratio of currents is adjusted near 1, $\alpha \approx 0$ [147].

Alternative concept of BPP uses geometrical means to reduce $I_{sat}^{-}$ by reducing the number of electrons hitting the collector. Ball-pen probe utilizes the fact that in strongly magnetized plasma Larmor radii of electrons and ions significantly differ. The collector is therefore hidden inside insulating shielding, as shown in Fig. 6.1. This allows ions with large Larmor radius to reach the collector, while majority of the electrons is removed by the shielding. The collector is left electrically floating and therefore no potential sweeping is necessary for potential measurement and

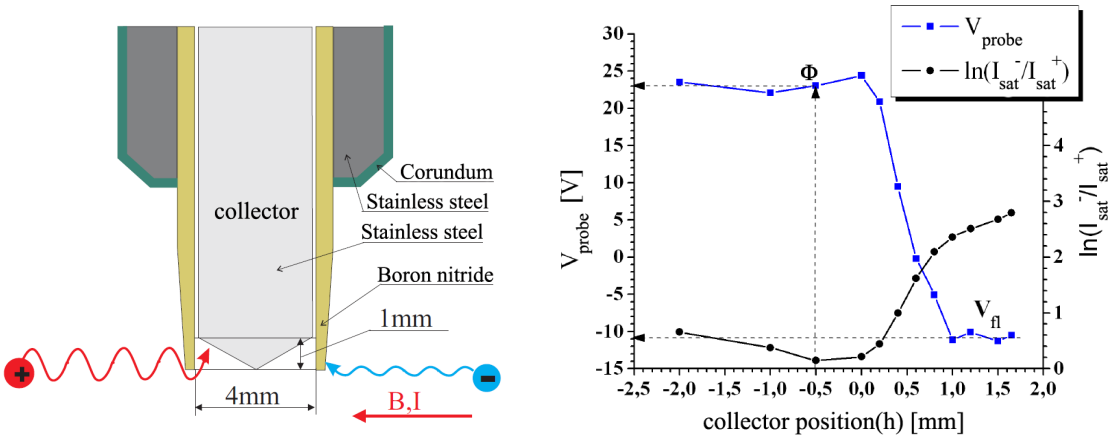


Figure 6.1: *Left*: Illustration of ball-pen probe principle - ions with larger Larmor radius reach the collector while electrons are removed by the shielding. *Right*: Change of measured potential $V_{probe}$ and factor $\alpha = \ln(I^-_{sat}/I^+_{sat})$ with position of the collector (negative position means collector retracted inside the shielding). Reproduced from [147].

high temporal resolution of the measurement ($\mu s$ time scale) is possible.

The collector is usually made movable and the influence of collector position on ratio of $I^-_{sat}/I^+_{sat}$ was investigated in [147]. The result reproduced in Fig. 6.1 (right) shows that measured potential sharply changes its value from $V_{fl}$ in Langmuir-probe mode to some new value, as the collector is retracted inside shielding. At the same time the ratio of saturation currents drops approximately to $I^-_{sat}/I^+_{sat} \approx 1.1$ which means that BPP with retracted collector measures potential very close to plasma potential with $\alpha \approx 0.6 \pm 0.3$ [2]. The reason why electrons are always present inside the shielding and $\alpha$ does not drop to zero even for deeply retracted collector, as expected from the simple geometrical arguments, is still not clear. Recent particle-in-cell simulations of similar ion sensitive probe indicate that self-consistently established electrical field in the entrance of the shielding may play an important role in transport of the electrons into the shielded tube [80, 81].

## 6.2 Overestimation of electron temperature in the wall shadow region by swept Langmuir probes

Previous comparison of ESEL simulations with Langmuir probe measurements on TCV tokamak have shown disagreement in the value of electron temperature $T_e$ in the wall shadow region [72]. While the measured radial profile is very flat in this region with temperature almost constant ($T_e \approx 5$ eV), ESEL predicts strong drop in the temperature profile as shown e.g. in Fig. 5.21(left). The drop in the model is present due to rapid increase of parallel energy transport rate (5.13) as a consequence of shortening of connection length to the nearest wall, $L_{\parallel,SOL} \approx 10$ m becomes $L_{\parallel,w.s.} \approx 1$ m ([72]). The discrepancy may be related to the known issue reported e.g. in [103], that Langmuir probes in the divertor region in high recycling and detached regime measure higher temperature than other diagnostics. There were some attempts to explain the discrepancy (e.g. by probe sensitivity to high-energy electrons reaching the probe due to strong $T_e$ gradient along magnetic field

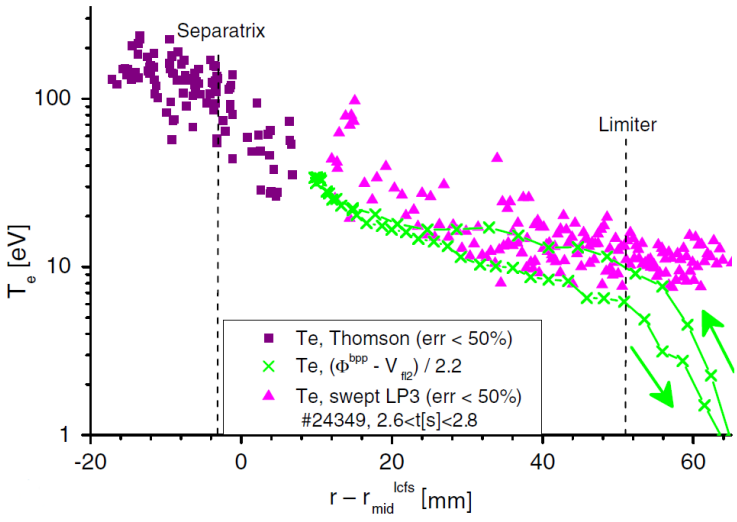


Figure 6.2: Radial profile of electron temperature in ASDEX Upgrade measured in [74] by swept Langmuir probe (triangles), ball-pen probe technique (crosses) and by Thomson scattering (squares). Estimated e-folding length of $T_e$ profiles is $3 \times 10^{-2}$ m in SOL and $5 \times 10^{-3}$ m in wall shadow region. [74].

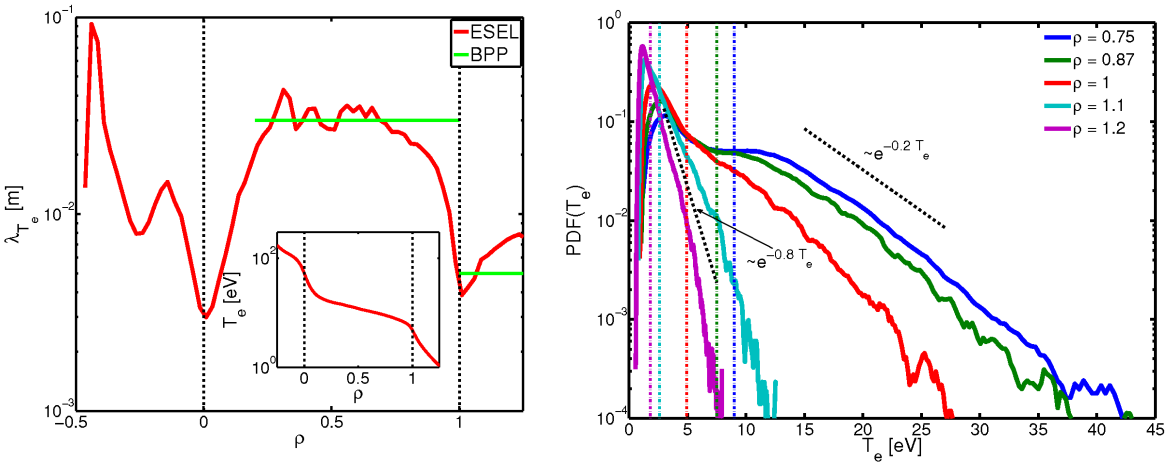


Figure 6.3: *Left:* Temperature e-folding length $\lambda_T$ from ESEL simulation for parameters of ASDEX Upgrade (red) compared with values $\lambda_{T_e,SOL} = 3 \times 10^{-2}$ m and $\lambda_{T_e,w.s.} = 5 \times 10^{-3}$ m estimated from the experimental BPP measurements (green) shown in Fig. 6.2. *Right:* Change of temperature PDF in the ESEL simulation in vicinity of far SOL and wall shadow boundary.

lines [71]), however its origin is still not fully understood.

Based on the capability of newly developed ball-pen probe to measure potential close to the plasma potential, a method for fast electron temperature measurements was proposed [2]. By subtracting floating potential $V_{fl}$ measured by floating Langmuir probe and potential $\phi_{BPP}$ from a ball-pen probe located nearby, electron temperature can be determined from (3.19) as

$$T_e = \frac{\phi_{BPP} - V_{fl}}{\alpha_{V_{fl}} - \alpha_{BPP}}. \tag{6.1}$$

Difference of factors $\alpha$ for cold Langmuir probe, $\alpha_{V_{fl}}$, and for BPP, $\alpha_{BPP}$, gives $\delta\alpha = 2.8 - 0.6 = 2.2$.

Simultaneous temperature measurement in SOL of ASDEX-Upgrade by method (6.1) and by swept Langmuir probe was carried out in [2, 74]. Comparison of both methods (Fig. 6.2) shows similar difference in radial gradient of temperature profile in wall shadow region as previously found in comparison of ESEL and swept Langmuir probe measurement on TCV (Fig. 5.21(left), [72]). This indicates that problems of swept Langmuir probe method in this region are responsible for the discrepancy in temperature profile between ESEL model and experiment found in [72], rather than incorrect physics in ESEL model. To strengthen the argument, we have made ESEL simulation for relevant parameters of the ASDEX Upgrade plasma (Tab. 5.1). The e-folding length of $T_e$ profile from the simulation is shown in Fig. 6.3(left) and compared with values obtained by the ball-pen probe technique. In SOL, the e-folding length is around value $\lambda_{T_e,SOL} \approx 3 \times 10^{-2}$ m for both cases and drops to $\lambda_{T_e,w.s.} \approx 5 - 6 \times 10^{-3}$ m in wall shadow. Fig. 6.2 shows that on the contrary to $T_{e,BPP}$ and $T_{e,ESEL}$, profile of $T_e$ measured by Langmuir probes remains flat in the wall shadow.

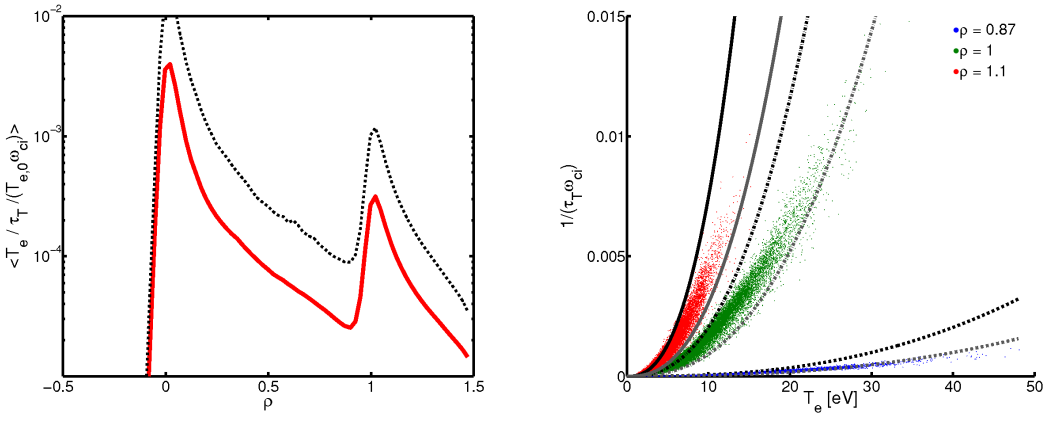


Figure 6.4: *Left*: Dependency of average rate of parallel losses $\langle T/\tau_T \rangle$ (red) together with interval of one standard deviation (black dashed) in ESEL simulation for parameters of ASDEX Upgrade. *Right*: Scatter plot of rate of parallel temperature losses in the simulation in many randomly chosen times at far SOL (blue), in wall shadow (red) and on the boundary of both regions (green). $1/(\tau_T\omega_{ci})$ estimated by Eq. 5.13 from local mean temperature and mean density at LCFS (grey) or local mean density (black) is plotted for parallel connection lengths at given radius - $L_\parallel = 10$ m (dashed), $L_\parallel = 0.55$ m (dash-dotted) and $L_\parallel = 1$ m (solid). Note that $1/(\tau_T\omega_{ci}) \sim 1/L_\parallel^2$.

The parallel connection length changes its value between SOL and wall shadow region in the considered ASDEX Upgrade discharge by factor $L_{\parallel,SOL}/L_{\parallel,w.s.} \approx 10$ [74]. For blobs with velocity $v_r$ and temperature $T$ moving over background plasma with small constant temperature $T_{bg}$, the e-folding length can be estimated as

$$\lambda_T \approx \langle T + T_{bg} \rangle \langle \left( \frac{\mathrm{d}T}{\mathrm{d}r} \right)_{\parallel}^{-1} \rangle = \frac{\langle T + T_{bg} \rangle}{v_r} \langle \left( \frac{\mathrm{d}T}{\mathrm{d}t} \right)_{\parallel}^{-1} \rangle. \tag{6.2}$$

Then, from expression (5.13) for characteristic energy parallel loss time, $\tau_T \sim 1/L^2$, one could expect that shortening of connection length $L^2_{\parallel,SOL}/L^2_{\parallel,w.s.} \approx 100$ will change radial e-folding length $\lambda_T$ in the ESEL model by similar factor, $\lambda_{T,SOL}/\lambda_{T,w.s.} \approx 100$. However, the parallel losses are of diffusive nature and thus strongly nonlinear function of temperature $\tau_T \sim T^{5/2}/n$. As a consequence, large temperature fluctuations are quickly damped, while rate of change of background (as well as mean) plasma temperature is slower. After shortening of $L_{\parallel}$, blobs are rapidly cooled down by parallel losses as can be seen in Fig. 6.3(right) and in right part of Fig. 6.4. This creates the largest drop in $\lambda_T$ in Fig. 6.3(left) observed at position $\rho \approx 1$. After that, the parallel temperature losses drop down faster then $T_e$ and $\lambda_T$ slowly increases. Fig. 6.4(left) shows that due to nonlinear nature of $\tau_T$ the average change of temperature in time by parallel losses, $\langle (\mathrm{d}T/\mathrm{d}t)_{\parallel} \rangle = -\langle T/\tau_T \rangle$, increases only by factor of 10 between far SOL and wall shadow (left part of the figure), while for fixed temperature the damping term $1/\tau_T$ increases as $L^2_{\parallel,SOL}/L^2_{\parallel,w.s.}$ by factor of 100 (right part of the figure where black and gray lines scale with connection length as $1/L^2_{\parallel}$). Then, the change of $\langle (\mathrm{d}T/\mathrm{d}t)_{\parallel} \rangle$ by factor of 10 explains similar change of $\lambda_T$. Note that data in Fig. 6.4 include also decrease of density by its parallel outflow, that further increases $\tau_T$.

There are several factors that may further influence the found agreement of $\lambda_T$ between simulation and BPP measurement in the wall shadow region, such as more complicated geometry of plasma facing components than modelled by constant connection length, atomic processes missing in the model may play significant role at the low temperatures, the diffusive model of parallel energy transport may not be fully appropriate near the wall or the probes may be affected by proximity to the wall along magnetic field lines. Nevertheless, our simulation shows that increased temperature gradient should be present at the boundary of far SOL and wall shadow region and in this sense the model clearly prefers the experimental results obtained by technique based on utilization of ball-pen probe over temperature obtained from swept I-V characteristics.

Method similar to Eq. (6.1) was previously used for evaluation of electron temperature $T_{e,emiss.}$ by difference of potentials of floating Langmuir probe and emissive probe. The results were compared with temperature obtained from swept Langmuir probe technique $T_{e,swept}$ [94] and the paper shows that the measurement may be influenced by secondary processes (such as secondary electron emission or difference in probe collecting areas of electron and ions) that change the value of $\alpha_{V_{fl}}$ and result in constant ratio $T_{e,swept}/T_{e,emiss} \approx 1.5 - 2$ [94, 141]. Similar effects may also influence the value of temperature computed from Eq. (6.1), however experimental measurement of (6.1) on ASDEX Upgrade is supported by the fact, that it follows temperature profile obtained by Thomson scattering diagnostic (Fig. 6.2) reasonably well. Moreover, [94] shows that radial gradient remains the same for

$T_{e,swept}$ and $T_{e,emiss}$ and therefore these effects probably do not explain discrepancy observed in wall shadow of ASDEX Upgrade between temperature measured by ball-pen probe and swept Langmuir probe methods (Fig. 6.2).

To conclude this section, we have shown that measurement of radial temperature profile in SOL of ASDEX Upgrade by combination of BPP and floating Langmuir probe is well consistent with ESEL modelling and with analytical estimation (5.13) describing diffusive energy transport along field lines. Reasons, why swept Langmuir probe technique overestimates temperature in the wall shadow is not yet clear. Our hypothesis is that possible source of error may come from the fact that the temperature is not constant during sweeping period and, moreover, PDF of its fluctuations exhibits long tail (Fig. 6.3(right)). Therefore, if the sweeping is slower than time scale of the fluctuations, the distribution of electron energies effectively seen by the probe during sweeping is distorted and it appears non-Maxwellian, which is in contradiction with assumption of Maxwellian distribution used in the standard method for temperature estimation from I-V characteristics. This would be somewhat similar to the case presented in [121] where it is shown that if electron energy distribution is bi-Maxwellian with two different temperatures, the standard method for temperature estimation from I-V characteristics returns the higher temperature only, even if density of the high-temperature electrons is an order of magnitude lower than density of the main low-temperature part. Then, if high-temperature blob shortly appears during sweeping period, the fitting of I-V characteristic will tend to return temperature of the blob and not average temperature during the whole sweeping period. If our hypothesis is correct and temperature obtained by fitting of I-V characteristics is overestimated due to intermittent temperature fluctuations, the result should be dependent on frequency of the sweeping. This can be experimentally tested.

## 6.3 Difference in plasma potential and floating potential power spectra

Langmuir probes routinely used for measurement of edge plasma properties do not allow direct fast measurement of plasma potential. Instead, its combination with temperature, the floating potential $V_{fl}$ (3.19), is typically measured and used instead of plasma potential (e.g. [33]). However, in general case one must be very careful when substituting plasma potential by $V_{fl}$. The different nature of both potential types can be demonstrated by comparing their power spectral density (PSD) - Fig. 6.5. This can be naturally measured by BPP diagnostics. When collector of the probe is pulled up, floating potential is obtained. Due to basic theory of BPP, retracting the collector inside the shielding should reduce coefficient $\alpha$ and thus reduce the influence of temperature fluctuations on the result. PSD for different positions of the collector was measured in [20] and is reprinted in Fig. 6.5(left). As the collector was retracted, the amplitude of PSD of the measured potential strongly dropped down. Moreover, an unexplained peak appeared in the PSD for the most retracted position of the collector (Fig. 6.5(right), [1, 2]). Since measurement of the potential using BPP is a novel technique, there appeared doubts whether these two properties of the PSD are physical or whether they are a consequence of the BPP filtering high frequencies due to geometrical effects when

the collector is retracted bellow surface of the probe.

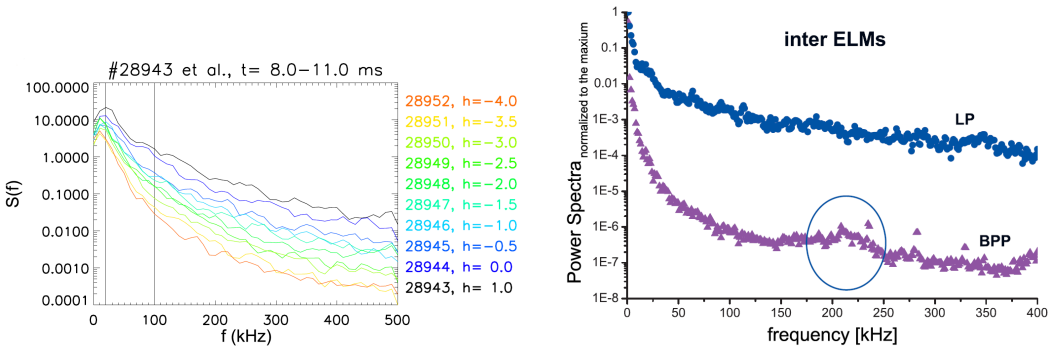


Figure 6.5: Power spectra $S(f)$ of the potential measured by BPP on the tokamak CASTOR [20] (left) and ASDEX Upgrade [2] (right). Position of the collector tip is denoted by $h$, with negative values under the surface level of the probe. On the data from ASDEX Upgrade a peak in PSD of the potential measured with fully retracted collector (denoted by label BPP) can be clearly identified while in the case of $h > 0$ (denoted by label LP) it is not present. In the BPP regime the probe measures potential close to the plasma potential $\phi$ while in the LP regime the floating potential $V_{fl}$ is measured. Reproduced from [20] and [2].

We have made numerical experiment and compared PSD of the two types of potential, $\phi$ and $V_{fl}$, measured in one point in space in ESEL simulation. We aim just at the qualitative comparison and thus even though the experimental data were obtained on ASDEX Upgrade tokamak, in the simulation we have used parameters of the TCV edge plasma. This is because properties of such simulation are much better understood and under control than properties of a new simulation with ASDEX parameters that we would otherwise use. Moreover, we argue by universality of basic edge turbulence properties among many tokamaks [31]. All PSD in this chapter were computed using Welch method [148] that splits the signal into several overlapping intervals, applies Hamming windowing function, computes PSD from each interval and averages the results.

The results of the simulation shown in Fig. 6.6(left) are very similar to those obtained by BPP measurement [1, 2]. The PSD of plasma potential drops with frequency significantly faster then PSD of the floating potential. Moreover, PSD of the floating potential is almost identical with PSD of temperature fluctuations, which shows that PSD of the floating potential is dominated by fluctuations of temperature and not by fluctuations of the plasma potential. Note that similar problem of parasitic influence of temperature on floating potential will appear again in Sec. 6.5 dealing with measurement of vorticity using grid of Langmuir probes.

Since $(\frac{\partial^2}{\partial r^2} + \frac{\partial^2}{\partial p^2})\phi \sim \Omega$, potential structures are generally smoother than those of vorticity, density and temperature - the spatial spectrum $\tilde{\phi}(k_r, k_p)$ quickly decays as $\sim -\tilde{\Omega}(k_r, k_p)/(k_r^2 + k_p^2)$. When poloidal velocity is dominant and turbulence does not evolve on time scales of its transit over the probe, the poloidal wave number $k_p$ is transformed to time frequency, $k_p \sim f/v_p$, as turbulent structures pass over the fixed probe. Then, the observed difference in PSD of temperature (or vorticity) and of plasma potential measured by fixed probe reflects differences in their poloidal

spectra.

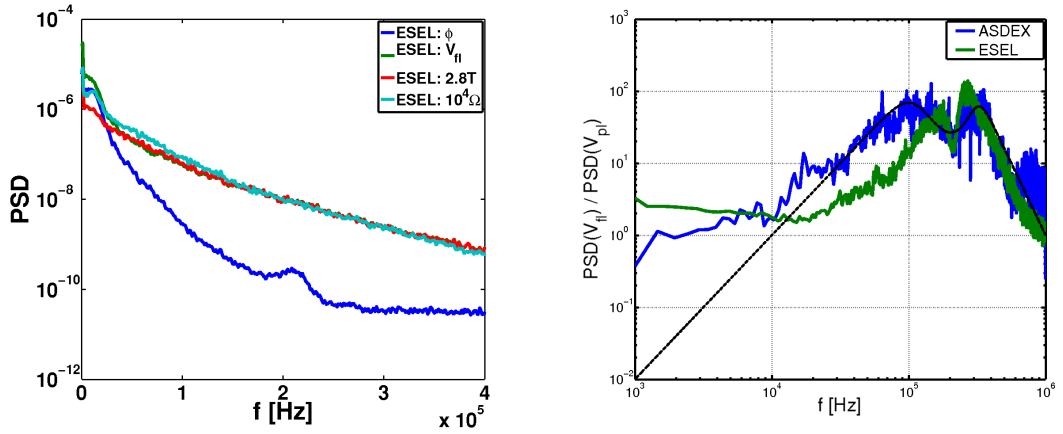


Figure 6.6: *Left*: PSD of point measurements inside ESEL simulation #116. PSD of floating potential is clearly dominated by temperature fluctuations (red line is plotted over the green one) and cannot be directly related to the PSD of plasma potential. Vorticity and temperature spectra exhibit similar decay with $f$. *Right*: Ratio of power spectral density of floating and plasma potentials measured by BPP on ASDEX Upgrade during H-mode in inter-ELM periods (blue line) and modelled using ESEL code for parameters of TCV (green line) [2]. Result of fit of analytical model (6.5) with $\delta_t = 0$ and $k_{p,\phi}\Delta = 2$ is plotted by black line.

PSD of plasma potential obtained from the numerical simulation shown in Fig. 6.6(left) exhibits similar peak around 220 kHz as the PSD measured by BPP (right part of Fig. 6.5). To compare the results, we compute ratio of amplitudes of floating and plasma potential PSDs, $\mathrm{PSD}(V_{fl})/\mathrm{PSD}(\phi)$ for both cases. Since the experimental measurement is naturally burdened by some level of noise, white noise is added to the simulation data with amplitude at the level of saturation of experimental plasma potential power spectrum (at frequency $5 \cdot 10^5$ Hz and above). Both results are qualitatively in agreement as shown in right part of Fig. 6.6 i.e., location of the peaks in PSD (drops in the figure) is similar and both have similar amplitude [1, 2]. We did not compare the plasma potential PSD directly because its shape, influenced by behavior of the background plasma, may differ between simulation and the experiment even though both exhibit comparable convective structures and similar differencies between floating and plasma potential fluctuations.

Appearance of the peak in $\mathrm{PSD}(\phi)$ can be explained by the following analytical model. Conditionally averaged profile of plasma potential in the blob (Fig. 6.7) measured by virtual probe at fixed position in the simulation shows that its shape is approximately sinusoidal. This indicates that poloidal velocity $v_p$ is larger than radial $E \times B$ velocity $v_r$ of the structure, otherwise the signal would not see both poles of the blob's bipolar structure. Based on the conditionally averaged profile, we make assumption that each blob appears in the signal of the probe in a form of sinusoid damped at its edges to zero,

$$\phi_{blob}(t) = \phi_0 \sin\left(\frac{t - t_i}{\Delta_{t,\phi}}\right) e^{-\frac{(t-t_i-\delta_t)^2}{2\Delta_t^2}} \tag{6.3}$$

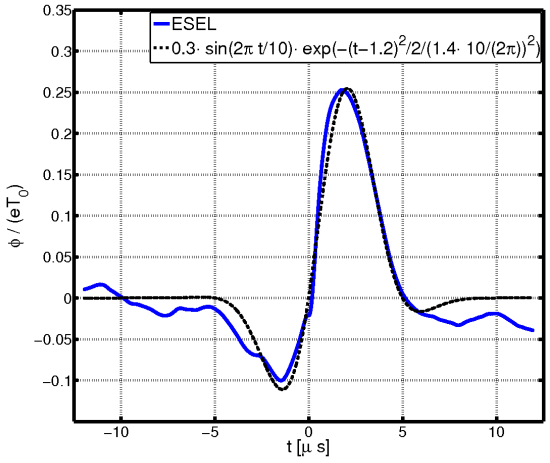


Figure 6.7: Conditionally averaged profile of plasma potential from ESEL simulation (TCV parameters) with the condition set on temperature, $\tilde{T} \geq 2\sigma_T$ (blue line). $t = 0$ corresponds to the time of maximal temperature. Black dashed line shows fit of function (6.3).

where $t_i$ is time of appearance of the blob, $t$ is time from the beginning of the measurement, $\Delta_{t,\phi}$ is temporal scale of the signal which is related to the poloidal wavenumber of the potential $k_{p,\phi}$ as $\Delta_{t,\phi} = (k_{p,\phi} v_p)^{-1}$. Shift of the envelope $\delta_t$ models potential asymmetry that is present due to tilt of the blob (one potential lobe is stronger than the other, as experimentally measured also in [74]). Fig. 6.7 confirms that the model (6.3) agrees with average blob potential in the simulation. The exponential form of the envelope was chosen arbitrarily with the advantage that simple analytical expression for Fourier transform ($\phi \to \tilde{\phi}, t \to \omega$) of (6.3) exists,

$$\tilde{\phi}_{blob}(\omega) = -i\sqrt{2\pi}\phi_0 \Delta_t \sinh\left(\frac{\omega\Delta_t^2 + i\delta_t}{\Delta_{t,\phi}}\right) e^{-\frac{1}{2}\frac{\Delta_t^2}{\Delta_{t,\phi}^2}(1+\omega^2\Delta_{t,\phi}^2) - i\omega(t_i+\delta_t)}. \tag{6.4}$$

Expressing squared amplitude of (6.4) in terms of $k_{p,\phi}$, $v_p$ and spatial scale of the envelope $\Delta = v_p\Delta_t$ gives

$$(\tilde{\phi}_{blob} \cdot \overline{\tilde{\phi}}_{blob})(\omega) = \phi_0^2 2\pi \frac{\Delta^2}{v_p^2}\left(\sin^2(\delta_t k_{p,\phi} v_p) + \sinh^2\left(\frac{\omega\Delta^2 k_{p,\phi}}{v_p}\right)\right) e^{-\Delta^2 k_{p,\phi}^2 (1+\frac{\omega^2}{k_{p,\phi}^2 v_p^2})}. \tag{6.5}$$

Here the bar means complex conjugation. Indeed, the result is not dependent on the time $t_i$ when the blob appears and contributions to the PSD from all individual blobs sum up. Eq. (6.4) has local maximum at $\omega = c v_p k_{p,\phi}$, where $c$ is coefficient depending on the chosen values of product $k_{p,\phi}\Delta$ and $\sin(\delta_t k_{p,\phi} v_p)$. For symmetric case with $\delta_t = 0$, $k_{p,\phi}\Delta = 1$ gives $c \approx 1.2$ and $k_{p,\phi}\Delta \geq 2$ gives $c \approx 1$. Therefore, maximum of the measured peak should be found around frequency $f = \omega/(2\pi)$

$$f_{peak} \approx \frac{k_{p,\phi} v_p}{2\pi} = \frac{v_p}{L_{p,\phi}}. \tag{6.6}$$

Typical poloidal velocity in the SOL is in the order $v_p \approx 10^3$ m $\cdot$ s$^{-1}$ and size of the blob $L_{p,\phi} = (2\pi)/k_{p,\phi} \approx 10^{-2}$ m, which gives estimate $f_{peak} \approx 10^5$ Hz that is

in agreement with the experimental observation $f_{peak,exp.} = 2.2 \times 10^5$ Hz. In our simulation as well as in the BPP measurement the ratio $v_p/L_{p,\phi}$ was approximately the same, which results in good agreement of position of the drop observed in right part of Fig. 6.6, even though both cases bind to edge plasma of different tokamaks.

Assuming that background fluctuations of temperature scale as $\approx f^{-\gamma_T}$, differently from background fluctuations of plasma potential $\approx f^{-\gamma_\phi}$ where $\gamma_\phi > \gamma_T$, the analytical model is able to reproduce also the shape of measured ratio of temperature and potential PSD (right part of Fig. 6.6). As ESEL model shows, the temperature is highly correlated with density and its structures have exponential shape that does not generate any significant peak in the PSD. Therefore we use following forms of PSDs:

$$\begin{aligned} \mathrm{PSD}(\phi) &\approx c_{blobs}\left(\sin^2\left(\delta_t k_{p,\phi} v_p\right) + \sinh^2\left(\frac{\omega \Delta^2 k_{p,\phi}}{v_p}\right)\right) e^{-\Delta^2 k_{p,\phi}^2 (1+\frac{\omega^2}{k_{p,\phi}^2 v_p^2})} + \\ &\quad + c_\phi f^{-\gamma_\phi} + c_{noise}, \qquad (6.7) \\ \mathrm{PSD}(T_e) &\approx c_T f^{-\gamma_T}, \qquad (6.8) \\ \mathrm{PSD}(V_{fl}) &\approx \mathrm{PSD}(\phi) + 2.8\mathrm{PSD}(T_e). \qquad (6.9) \end{aligned}$$

Fit of the $\mathrm{PSD}(V_{fl})/\mathrm{PSD}(\phi)$ ratio described by these relations to the experimental data is plotted in Fig. 6.6(right). The slope of the curve is in its left part dependent on difference of both exponents and our fit gives $\gamma_T - \gamma_\phi \approx 1.3$. If the noise is present, PSD of the plasma potential saturates for higher frequencies at the noise level and the slope of the PSD ratio in the high-frequency range is given by $-\gamma_T$. The width of the drop (or peak) agrees well with the experimental data, but it is wider in the analytical model than in the numerical simulation. This is consequence of simplified form of the typical blob potential (6.3). More accurate form of potential profiles of individual blobs could be used, together with PDF describing variation of the potential amplitude and width among different blobs, to obtain better agreement with ESEL data. However we consider the presented model sufficient to explain origin of the peak in the experimentally observed spectra of the plasma potential.

Both, experiment and simulation, have comparable slope of the ratio $PSD(V_{fl})/PSD(\phi)$ for frequencies in the range $10^4 - 10^5$Hz, but with smaller values for the simulation. This means that difference $\gamma_T - \gamma_\phi$ is similar for both cases, but they differ by multiplicative constant $c \approx 2.8 c_T/c_\phi$ in

$$\mathrm{PSD}(V_{fl})/\mathrm{PSD}(\phi) \approx c f^{\gamma_\phi - \gamma_T}. \qquad (6.10)$$

This disagreement is a topic of our further study and is probably related to different parallel collisionality between the real and modelled case and to the choice of $\nabla J_\parallel$ closure in the turbulence model.

To conclude this section, we have shown in support of correctness of ball-pen probe measurement, that in the plasma interchange turbulence the PSD of floating potential is dominated by temperature fluctuations. For higher frequencies the PSD of plasma potential is significantly smaller with respect to the PSD of floating potential and temperature. Experimentally observed peak in the potential spectra measured by BPP was reproduced in the numerical simulation and explained by model assuming bipolar character of blobs with some characteristic size and by domination of poloidal component of its velocity over radial.

## 6.4 Estimation of poloidal phase velocity

When two poloidally spaced Langmuir probes, both in the same regime ($I_{sat}$ or floating) are used in the experiment, poloidal phase velocity can be estimated using cross-correlation technique [21, 22, 151]. First, cross-correlation of the signal from the probes is computed. Position of its maximum $t_{cc,max}$ then corresponds to average time interval in which plasma structures travel from one probe to another. Average poloidal velocity $v_{p,cc}$ can be estimated using mutual distance of the probes $d$ as

$$v_{p,cc} = \frac{d}{t_{cc,max}}. \tag{6.11}$$

The distance of the probes is a key issue for this technique. The probes have to be close enough to measure similar signal, as will be discussed later, and at the same time their mutual distance is limited by frequency of data acquisition. E.g., to be able to measure velocities up to $5 \times 10^3$ ms$^{-1}$ with sampling frequency $10^6$ Hz, their distance must be at least $5 \times 10^3/10^6 = 5 \times 10^{-3}$ m. In principle, $v_{p,cc}$ estimates velocity of coherent structures only, but measurements in [137] as well as our simulations (see Fig. 6.9) indicate that this velocity is reasonably close to the total $E \times B$ velocity of the plasma.

The cross-correlation technique is based on the assumption that poloidal velocity of blobs $v_p$ is much larger then their radial velocity $v_r$, $|v_p| \gg |v_r|$. If this condition is not fulfilled, both poloidally spaced probes get different signal and the position of the maximum cross-correlation $t_{cc,max}$ can be significantly influenced by spatial correlations inside turbulent structures. While $|v_p| \gg |v_r|$ is usually fulfilled in the middle of SOL, the condition may break in two cases: near the wall where poloidal velocity is small and in the vicinity of LCFS where the velocity shear layer (VSL) forms transport barrier and the poloidal velocity usually changes sign (see e.g. [137]). To describe the influence of finite $v_r$, we will consider turbulent structure of Gaussian shape (in $I_{sat}$) passing over the probe. Each probe then measures signal

$$I_{sat} = I_{sat,0} \exp\left( - \left( \frac{r_i - v_r t}{\Delta_r} \right)^2 - \left( \frac{p_i - v_p t}{\Delta_p} \right)^2 \right) \tag{6.12}$$

where $\Delta_r$ and $\Delta_p$ is radial and poloidal size of the blob and $r_i$ and $p_i$ is radial and poloidal position of the $i$-th probe. After some algebra, we find that cross-correlation

$$C(I_1, I_2) = \int_{-\infty}^{\infty} I_1(t) I_2(t+\tau) \mathrm{d}\tau \tag{6.13}$$

of signal of two probes separated purely poloidally, $r_1 = r_2$ and $p_2 = p_1 + d$, has maximum in a time

$$t_{cc,max} = \frac{v_p d}{v_p^2 + v_r^2 \left( \frac{\Delta_p}{\Delta_r} \right)^2}. \tag{6.14}$$

This expression is independent on mutual position of the pair of probes and the structure, and thus structures with the same velocity but different position will give the same time $t_{cc,max}$. The ratio of $v_{p,cc}$ estimated from (6.11) and of the real poloidal velocity $v_p$ of the structure is

$$\frac{v_{p,cc}}{v_p} = 1 + \left( \frac{v_r}{v_p} \frac{\Delta_p}{\Delta_r} \right)^2. \tag{6.15}$$

This relation shows that when $|v_p\Delta_r| \gg |v_r\Delta_p|$, simple cross-correlation method in Eq. (6.11) gives correct results. This is more precise version of the originally introduced assumption $|v_p| \gg |v_r|$ (note that typically $\Delta_p/\Delta_r \approx 1-2$ in SOL). For other cases, the difference between real and estimated velocity is shown in left part of Fig. 6.8. Eq. (6.15) shows that the absolute value of estimated velocity $v_{p,cc}$ cannot be less then $|v_r\Delta_p/\Delta_r|$ and every curve in Fig. 6.8(left) has two branches i.e., two real poloidal velocities, $v_{p,1} > v_r$ and $v_{p,2} < v_r$, are projected on a single estimated velocity $v_{p,cc}$. One must be especially careful when interpreting estimation $v_{p,cc}$ in the vicinity of LCFS because, as Fig. 6.8(left) shows, for $v_p$ close to zero the estimated velocity diverges. This could be incorrectly interpreted as an increased velocity shear inside VSL.

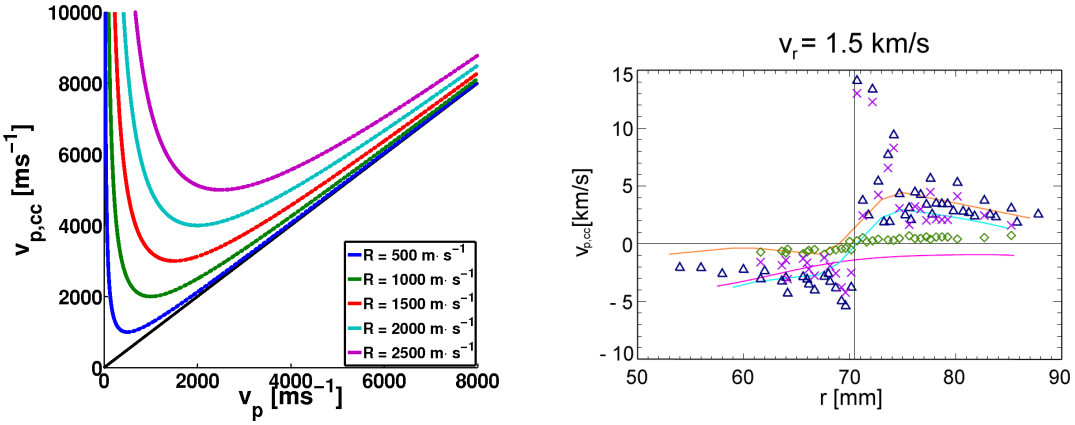


Figure 6.8: *Left*: Dependence of poloidal velocity $v_{p,cc}$ estimated by relation (6.11) on the real velocity $v_p$ for several values of product $R = v_r\Delta_p/\Delta_r$. Black line shows ideal situation $v_{p,cc} = v_p$. *Right*: Velocities $v_{p,cc}$ estimated by cross-correlation technique applied on $I_{sat}$ data from double rake probe measurements on tokamak CASTOR [22] (blue triangles) and correction using relation (6.15): high-velocity branch is plotted with magenta crosses and low-velocity branch with green diamonds. $E \times B$ velocity estimated from radial electric field (orange line), electron part of diamagnetic velocity (violet line) and their sum (cyan line) are shown for comparison. Black vertical line at $r = 70.5$ mm marks position of LCFS.

The situation is demonstrated in right part of Fig. 6.8 on data measured in CASTOR tokamak using double rake probe [22]. Estimation of poloidal velocity using relation (6.11) clearly diverges in the region where $v_p \approx 0$ ($r = 70.5$ mm). Comparison with the discussed model (6.15) for estimated value $R = v_r\Delta_p/\Delta_r \approx 1.5 \times 10^3$ m $\cdot$ s$^{-1}$ shows that near the velocity shear layer the low-velocity branch is meaningful while deeper in the SOL the high-velocity branch should be used. Scattering of the data near the VSL comes from insufficient temporal resolution of the diagnostics with poloidal distance of probes $d = 2.5$ mm and sampling frequency 1 MHz. To allow measurement of $v_{p,cc}$ up to 15 km $\cdot$ s$^{-1}$ the cross-correlation data had to be interpolated (see [22, 23] for more details).

Data from numerical simulation using ESEL code with TCV parameters are plotted in Fig. 6.9. Different potential boudary conditions than described in Sec. 5.3 were used, $\phi(r = r_{max}) = -4; \phi(r = r_{min}) = 0$. This change does not affect dynamics of turbulent structures, but shifts mean poloidal velocity such that it

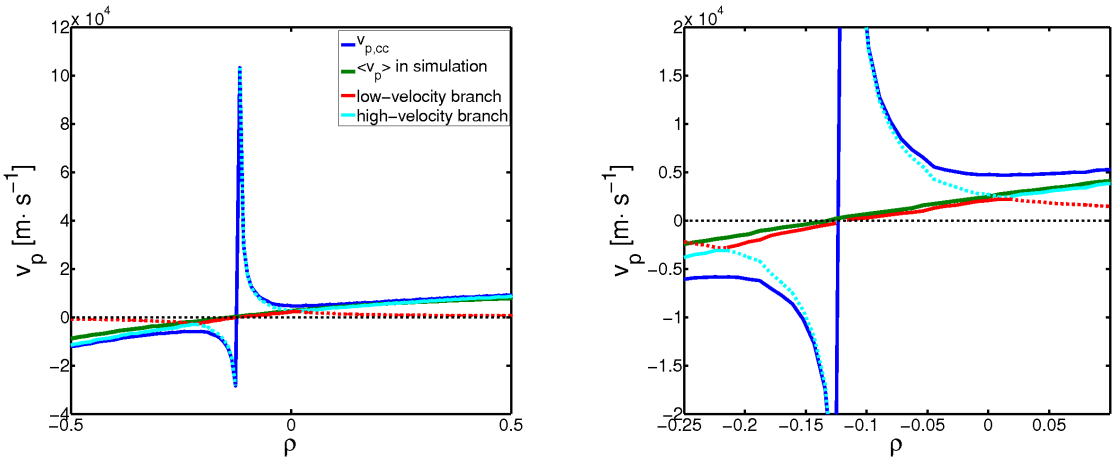


Figure 6.9: *Left*: Radial profile of $\langle v_p \rangle$ from ESEL simulation #116 (green) with double Dirichlet boundary conditions imposed on potential, $\phi(r = r_{max}) = -4; \phi(r = r_{min}) = 0$. Its estimation (6.11) from cross-correlation of two virtual probes in poloidal distance $d_p = 5$ mm (blue) diverges at $\rho = -0.095$ where $\langle v_p \rangle \approx 0$. Correction of $v_{p,cc}$ by (6.15) is shown in cyan (high-velocity branch) and red (low-velocity branch). Resulting corrected profile of poloidal velocity is given by solid parts of cyan and red lines. Value of parameter $R$ ($R_{right} = 2.33 \times 10^3$ m $\cdot$ s$^{-1}$ outwards from the VSL and $R_{left} = 2.9 \times 10^3$ m $\cdot$ s$^{-1}$ inwards from the VSL) was determined by condition of continuity of the $v_p$ profile. *Right*: Zoom of the left figure.

changes sign near the LCFS as is typically observed in experiment. Comparison of the mean poloidal velocity (that is known in the simulation) with its estimate from the cross-correlation technique shows that the correction (6.15) can successfully reconstruct $v_p$ profile even in the VSL region. The difference in probe signals located in the simulation in poloidal distance $d = 5$ mm is plotted in Fig. 6.10. While probe signals for $|v_p| \approx 4$ km$\cdot$s$^{-1}$ are highly correlated but shifted, signal for $|v_p| \approx 0.1$ km $\cdot$ s$^{-1}$ is influenced by spatial correlations inside turbulent structures, resulting in drop of maximum of the cross-correlation and the time lag $t_{cc,max} \approx 0$ (Fig. 6.11).

The main limitation of the method for a case of two-point measurements is the product $R = v_r \Delta_p / \Delta_r$ which is unknown and may vary radially inside the shear layer. To determine the value of $R$ we use the fact that the velocity profile is continuous. Then the value of $R$ can be estimated from the condition that high-velocity and low-velocity branches must touch each other as implemented in Fig. 6.9. The estimated value of $R$ can be different on the outward and inward side of the VSL because the velocity shear changes properties of turbulent structures passing through it.

Third probe placed in small radial distance cannot provide additional information if the whole signal is taken into account, because it will register both blobs moving outwards ($t_{cc,max,rad} > 0$) as well as holes moving inwards ($t_{cc,max,rad} < 0$) and the total estimated time shift of cross-correlation maxima of two radially separated probes, $t_{cc,max,rad}$, will therefore be close to zero. This is principally different from the discussed case of two probes separated poloidally because $v_p$ of both blob and holes has the same sign (while the sign of their $v_r$ is opposite). This problem

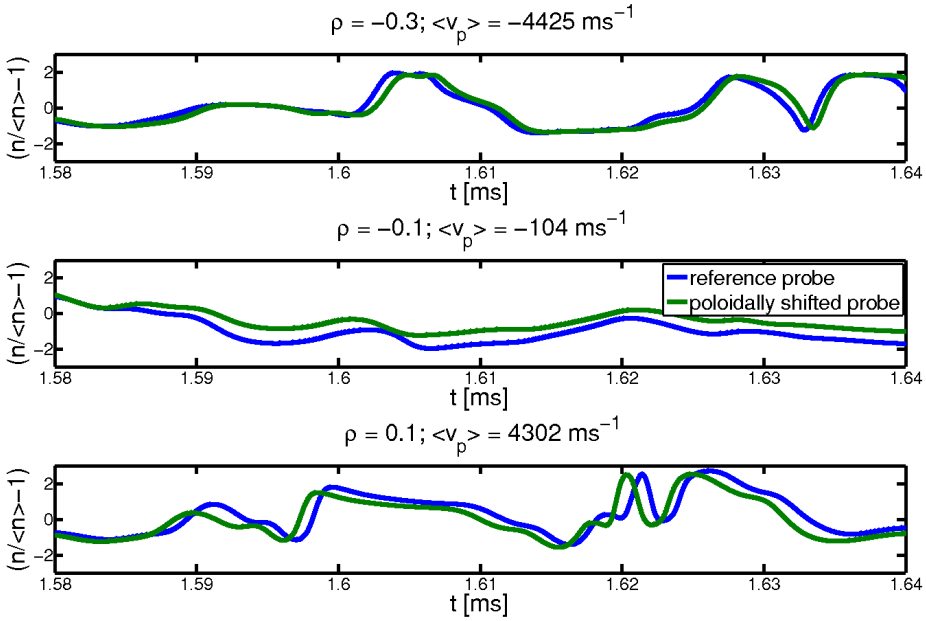


Figure 6.10: Time trace of two virtual probes in poloidal distance $d_p = 5$ mm in ESEL TCV simulation. Position inward from the VSL (top), in the VSL (middle) and outward from the VSL (bottom) is shown.

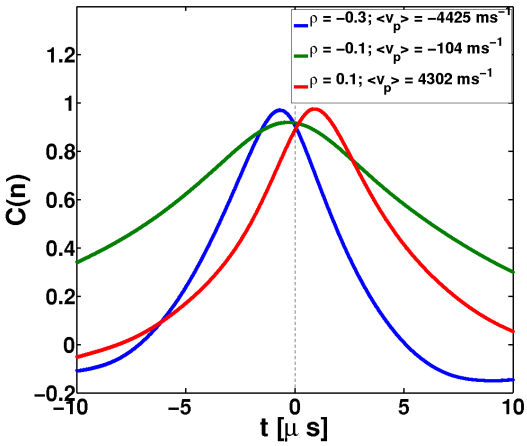


Figure 6.11: Cross-correlation of two probes placed poloidally in distance $d_p = 5$ mm in three positions around VSL.

can be avoided by separating positive perturbations (moving outwards due to their interchange nature) by conditionally averaging the signal. Then, the conditional average consists of signal of same type of structures moving in the same radial direction. Equations that could be used to obtain blob velocity and size from signal of more then two probes are derived in Appendix A.

We propose to use the fact that estimate $v_{p,cc}$ diverges in the region where $v_p \approx 0$ as a basis of algorithm for detection of the VSL. It is clearly seen on data from ESEL simulation in Fig. 6.9(left) that for $t_{cc,max}$ computed for several probe pairs on different radii (or from different time-intervals of signal from reciprocating probe), the quantity $1/t_{cc,max} \sim v_{p,cc}$ shows sharp transition in the VSL region. On tokamak COMPASS, measurements with reciprocating probe entering H-mode pedestal are envisaged [75]. Detection of the VSL location may during such experiments provide important information concerning propagation of turbulent structures through the transport barrier.

## 6.5 U-probe

Recently, complex probe called U-probe designed for measurement of electromagnetic properties of plasma filaments in SOL was developed on reversed field pinch RFX [143, 144, 99]. To our best knowledge, it is the first time when an attempt to experimentally determine vorticity structure of edge turbulent structures was made. U-probe consists of two spatially separated 2D arrays of Langmuir probes with each row of the arrays allowing to simultaneously measure density, electron temperature and floating potential at the same radial position [144]. This allows to determine electron pressure, temperature, density, floating potential and $E \times B$ velocity simultaneously. The authors of [144] use measured floating potential $V_{fl}$ as an approximation for plasma potential $\phi$ and estimate plasma vorticity as

$$\Omega = \frac{1}{B}\vec{\nabla}_\perp^2 \phi \approx \frac{1}{B}\vec{\nabla}_\perp^2 V_{fl}. \tag{6.16}$$

Measured pressure and vorticity waveforms of the conditionally averaged blob are shown in Fig. 6.12(left). Maximum values of both, pressure as well as of vorticity, are located very close to each other at the center of the blob and perturbations of pressure and (floating) potential are found to be in phase [99]. The authors use this fact, among others, to support their conclusion that observed turbulence is of drift-Alfvén type. However, in this chapter we will show that the zero phase shift between derived vorticity and pressure cannot be unambiguously assigned to the drift-type turbulence. When floating potential is used instead of plasma potential, similar relations between the floating potential, derived vorticity and pressure (or density), are observed in simulation also for interchange turbulence, whose structures clearly possess $\pi/2$ shift between both quantities (see Fig. 6.7).

Presently, new U-probe is being developed for tokamak COMPASS [84]. Its schematic design is shown in Fig. 6.13. It consists of two identical towers with 3D magnetic coils inside. Each tower has three Langmuir probes on top and radial row of Langmuir probes on its side. The U-probe is planned to be used for measurement of electromagnetic features of turbulent structures in the SOL, where interchange turbulence is expected to be dominant. One of the goals of the new probe originally was to carry on similar measurements of vorticity as were made on RFX. In order

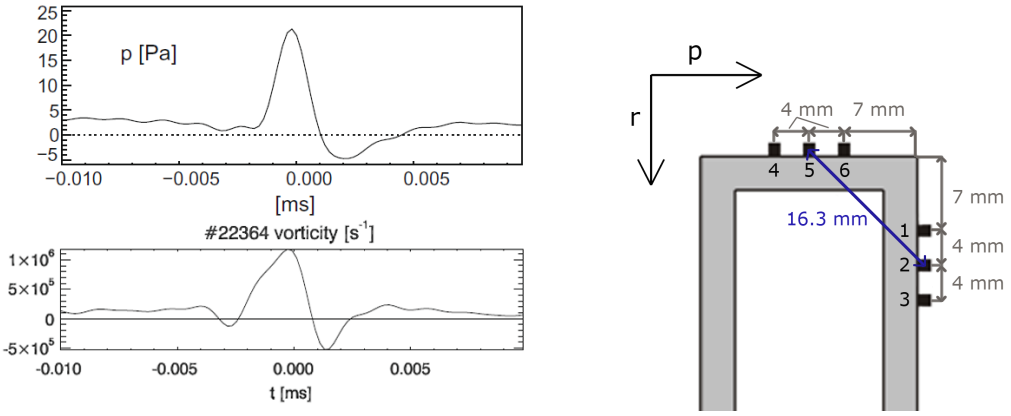


Figure 6.12: *Left:* Profile of pressure and estimated vorticity in an average filament on RFX. Time $t = 0$ corresponds to maximum pressure. Reproduced from [144]. *Right*: U-probe layout in ESEL simulation.

to investigate feasibility of such measurement, we have made numerical simulation of the interchange turbulence with ESEL code and used an array of virtual probes similar to U-probe layout to estimate error made by experimental determination of vorticity from floating potential. Layout of the probes used in the simulation is shown in right part of Fig. 6.12(right). Signal of each probe is averaged over its estimated area projected into the simulation plane ($2 \times 1$ mm). Similarly to the previous chapters, we use ESEL simulation #116 for TCV parameters as the best candidate to obtain realistic blob characteristics. All conditional averages that will be further discussed were obtained with triggering condition $\tilde{n} > 2\sigma_n$ used at position of probe either 2 or 5 (see probe layout in Fig. 6.12(right))

Vorticity is composed from second derivatives of plasma potential in two perpendicular directions,

$$\Omega = \Omega_p + \Omega_r = \frac{1}{B}\left[\frac{\partial^2\phi}{\partial p^2} + \frac{\partial^2\phi}{\partial r^2}\right]. \tag{6.17}$$

The simulation shows that if plasma potential $\phi$ would be measured directly and the CA triggered locally (by density at position of probe 5 for $\Omega_p$ and probe 2 for $\Omega_r$), the proposed distance and size of the probes in the U-probe design allows estimation of local $\Omega_p$ and $\Omega_r$ waveforms with reasonable accuracy (compare green and dark blue lines in Fig. 6.14). One of the weak sides of the U-probe design is, however, that places of measurement of $\Omega_p$ and $\Omega_r$ are not at the same place but in distance of approximately 16 mm, which is comparable to the size of turbulent structures. In order to obtain estimate of conditionally averaged quantity $\Omega = \Omega_p + \Omega_r$, both parts, $\Omega_p$ and $\Omega_r$, have to be averaged at the same time. They are, however, not measured at the same place and at given time they may be located in different parts of blob. Then it is not clear which signal (probe 2 or 5) should be used as a trigger for the determination of the total vorticity $\Omega$. Motivated by this, we investigated the case when the conditional average of $\Omega_p$ or $\Omega_r$ is not triggered locally, as was done in Fig. 6.14, but by the middle probe of the other segment ($\Omega_p$ triggered by probe 2, $\Omega_r$ triggered by probe 5). In such case the nonlocality brings distortion to the resulting estimate of $\Omega_p$ and $\Omega_r$ as shown in

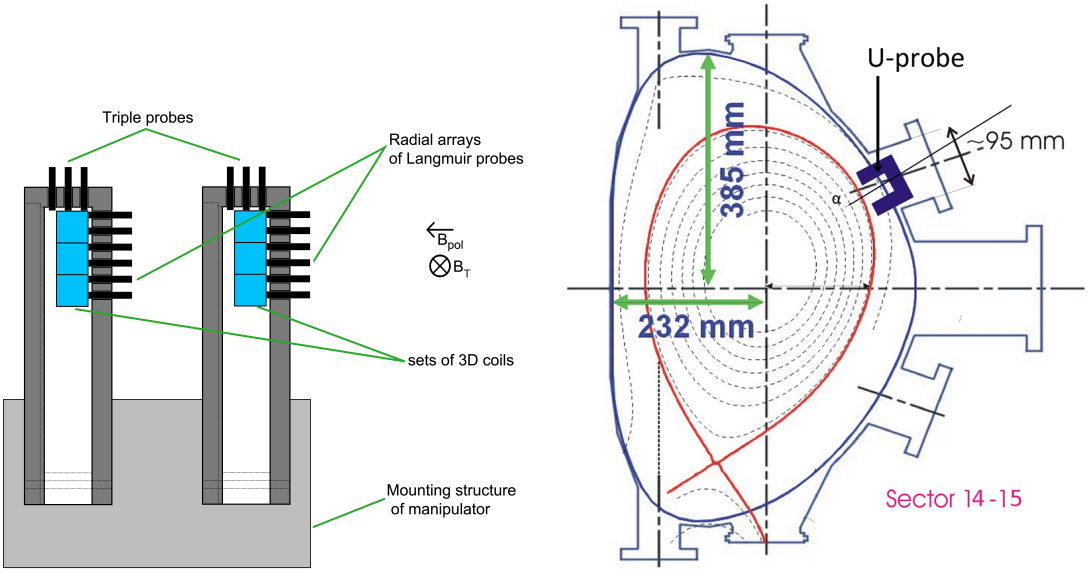


Figure 6.13: Schematic drawing of U-probe design made for COMPASS tokamak and its expected position inside the tokamak [84].

Fig. 6.15(right). This figure shows that smaller error is introduced when the CA of total vorticity $\Omega = \Omega_p + \Omega_r$ is triggered at position of probe 2 (i.e. trigger $\Omega_r$ locally and $\Omega_p$ non-locally) because CA profile of $\Omega_r$ is more sensitive to the problem of non-local triggering and it has also higher amplitude (higher weight in the sum (6.17)).

In cases when the poloidal flow is dominant, $|v_p| \gg |v_r|$, one possible solution could be to use hypothesis of frozen turbulence [36] and replace poloidal derivative $\partial^2/\partial p^2$ in (6.17) by time derivative $(\partial^2/\partial t^2)/v_p^2$ with $E \times B$ drift $v_p$ estimated from difference of $V_{fl}$ measured on neighbouring probes. This method largely depends on accuracy of $v_p$ estimation and detailed error analysis would be necessary for particular SOL conditions.

Another, even more important issue is the parasitic influence of temperature on Langmuir probe measurements. In section 6.3 we have shown that fluctuations of $V_{fl}$ are dominated by fluctuations of $T_e$ instead of fluctuations of $\phi$. In Figs. 6.14, 6.15(left) and 6.16 one can compare estimates of vorticity from the floating potential as used in Eq. 6.16 with its real value. The conditionally averaged waveform of such estimates is clearly dominated by influence of $\vec{\nabla}_\perp^2 T_e$ term that shifts maximum of estimated vorticity to the position of density maximum ($t = 0$). This result is clearly in contradiction with used model of convective interchange structures whose radial motion is dependent on $\pi/2$ phase shift between density and vorticity (or potential) and the vorticity maximum at $t = 0$ could be incorrectly interpreted as an indication of presence of drift-waves. Conditionally averaged waveforms of vorticity obtained from Langmuir probe measurements must be therefore interpreted with extreme caution and observed zero time lag between density and vorticity maximum cannot distinguish between drift-type and interchange-type turbulence by itself. We especially point out surprising similarity between vorticity waveform obtained from the interchange simulation with vorticity estimate based on $V_{fl}$ signal (red line in Fig. 6.15(left)) and that observed in RFX and claimed to be of

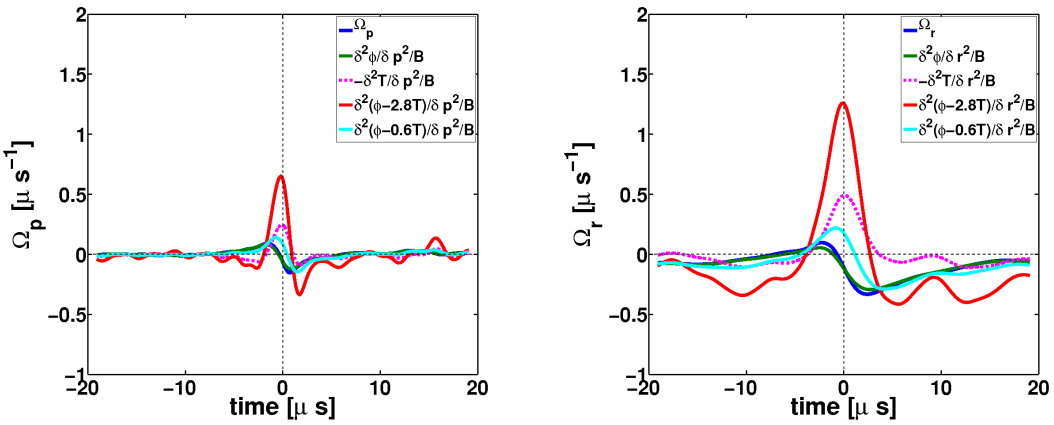


Figure 6.14: Conditionally averaged profile of poloidal (left) and radial (right) contribution to vorticity in ESEL simulation. Condition was set as $\tilde{n} \geq 2\sigma_n$. $\Omega_p = (\partial^2\phi/\partial p^2)/B$ and $\Omega_r = (\partial^2\phi/\partial r^2)/B$ are real local values in the simulation (blue) and $(\delta^2\phi/\delta p^2)/B$ and $(\delta^2\phi/\delta r^2)/B$ is their estimation from plasma potential obtained at the position of probes 4-6 and 1-3 (see Fig. 6.12(right)), respectively (green). Waveforms of $\Omega_p$ and $\Omega_r$ are further compared with their estimation based on floating potential (red) and potential of ball-pen probe (cyan) obtained at probes 4-6 and 1-3. Estimation from floating potential is clearly dominated by parasitic influence of temperature (magenta dashed line) that shifts maximum of the profile to the position of maximum density ($t = 0$).

drift-wave type (Fig. 6.12(left)).

Even in the case that temperature fluctuations would be lower then predicted by ESEL simulation (fluctuations of $T_e$ in ESEL are on the upper boundary of experimentally observed range stated in [18]), spatial structure of temperature will significantly influence the vorticity estimation. This may be seen in Figs. 6.14 and 6.15, where cyan line represents vorticity estimated from simulated BPP signal, i.e. with 4.7× reduced factor $\alpha$ in definition of $V_{fl}$ (3.19).

In this section we have shown that if the temperature fluctuations are not negligible, their parasitic influence in floating potential prevents correct estimation of vorticity for structures of interchange turbulence. Due to this reason, use of ball-pen probes replacing Langmuir probes is considered for the second version of U-probe. Moreover, we recommend to accompany future U-probe vorticity measurements with turbulence simulations focused on the particular SOL conditions. The simulation results could be compared with other diagnostics and should serve as a basis for error estimation for the U-probe vorticity measurement.

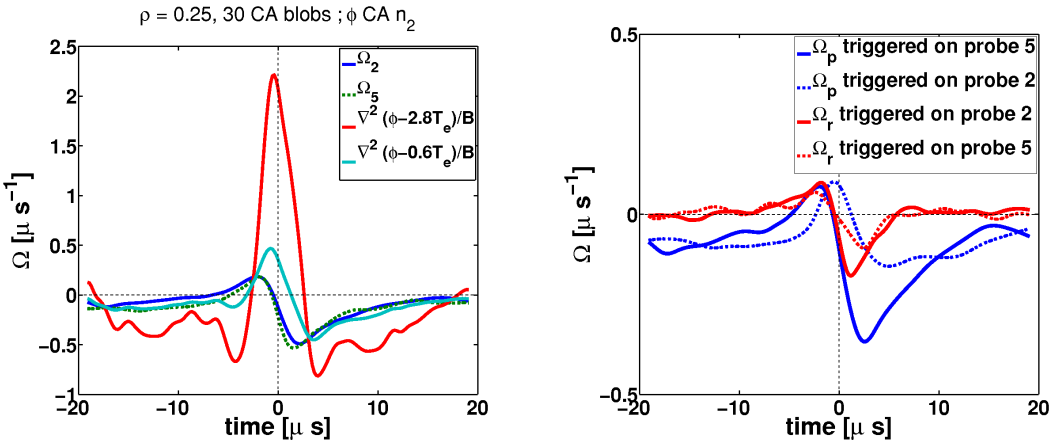


Figure 6.15: *Left:* Conditionally averaged profile of vorticity estimated by relation (6.17). $\Omega_2$ (blue) and $\Omega_5$ (green) show real vorticity in the simulation at position of probe 2 and 5, respectively. Their difference is given by different radial position of the probes. For comparison, estimation of CA vorticity in U-probe geometry (Fig. 6.12(right); triggered by density signal on probe 2) with floating potential (red) and ball-pen probe potential (cyan) substituted in (6.17) instead of $\phi$ is plotted. *Right:* Comparison of CA signal of $\Omega_p$ and $\Omega_r$ trigged locally (solid line) and non-locally from the other segment of probes (dashed line).

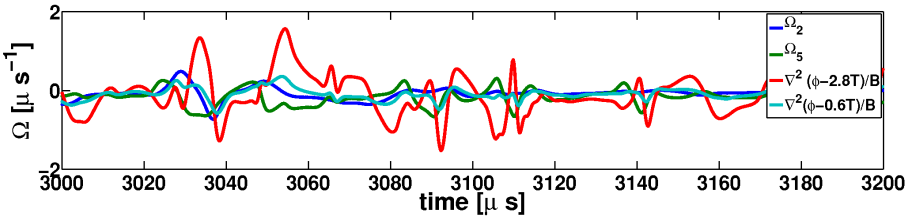


Figure 6.16: Time trace of real vorticity signal at positions of probes nr. 2 (blue) and 5 (green) compared to the signal of vorticity estimated in U-probe geometry (Fig. 6.12(right)) from floating Langmuir probe potential (red) and BPP potential (cyan).

# 7. Statistics of particle transport in turbulent potential

## 7.1 Motivation

Fluid approximation used for modelling of plasma turbulence in Sec. 5 is a fast method how to resolve collective motion of particles under several assumptions used during its derivation. However, not all these assumptions are valid in SOL for all types of particles. Namely, it was assumed that particle undergoing its cyclotron orbit does not feel neither spatial inhomogeneity nor time evolution of the underlying electric field,

$$r_L \ll 1/k_\perp; \;\; \omega_c \gg \omega, \tag{7.1}$$

where $r_L = (mv_\perp)/(qB)$ is Larmor radius of particle with mass $m$, charge $q$ and cross-field velocity $v_\perp$, $\omega_c = (qB)/m$ is cyclotron frequency of the particle and $k_\perp$ and $\omega$ are characteristic spatial and time frequency of the turbulence. If (7.1) does not hold and spatial and temporal scales are comparable, there can arise complicated nonlinear interaction between turbulence and the particle. For typical parameters of SOL turbulence i.e., $B \approx 1$ T, $\omega \approx 10$ MHz and $1/k_\perp \approx 10^{-3} - 10^{-2}$ m, the condition is well satisfied for thermal electrons, $r_{L,e^-}(T = 30 \text{ eV}) \approx 10^{-5}$ m and $\omega_{c,e^-} \approx 105$ MHz. Thermal hydrogen ions are already on the boundary of validity of the fluid approach, $r_{L,H^+}(T = 30 \text{ eV}) \approx 10^{-4}$ m, $\omega_{c,H^+} \approx 10^2$ MHz, and therefore gyrofluid approximation [129] may be needed for edge plasma with hot ions. For plasma impurities with higher $m/q$ ratio assumption (7.1) does not hold at all, e.g. $r_{L,C^+}(T = 30 \text{ eV}) \approx 10^{-3}$ m, $\omega_{c,C^+} \approx 10$ MHz.

When the density $n_{imp}$ of such particles is low compared to the density of main plasma, $n$,

$$n_{imp} \ll n \tag{7.2}$$

a possible approach to estimation of their behaviour in turbulent field is to treat them as test particles that are influenced by the turbulent environment but that do not influence the turbulence back. This approach is valid provided the density of impurities is low enough such that local impurity charge does not enter quasineutrality equation, which translates for edge turbulence as [111],

$$Z_{imp} n_{imp} \ll \frac{\rho_s}{c_s} \vec{\nabla} \cdot \vec{J} \tag{7.3}$$

where $\vec{\nabla} \cdot \vec{J}$ is divergence of plasma currents acting with characteristic time $\rho_s/c_s$. This condition places strict constraints on $n_{imp}$ that are often violated in a real plasma and self-consistent back-reaction of turbulence on presence of impurities becomes non-negligible. Nevertheless, investigation of particle transport in test-particle approach can reveal the most important and still realistic tendencies [111].

## 7.2 Random walk, classical and anomalous diffusion

If trajectory of particle moving in turbulent environment can be divided into series of steps, it is often useful to describe its transport in the frame of theory of random walks. For simplicity, we will now assume that the transport process is one dimensional. If there is a stationary distribution $P_x(\delta_x)$ of lengths $\delta_x$ of statistically independent steps and this distribution conforms with assumptions of central limit theorem (mainly that its variance $\sigma^2$ and mean value $\mu$ are finite), the transport process can be in the limit of large number of steps, $N \gg 1$, described as a diffusive process [25]. Then, the probability $P(\Delta x, N)$ to find particle after $N$ steps in distance $\Delta x$ from its initial position is independent on actual shape of the distribution $P_x$ and it is given solely by its first two moments, $\mu$ and $\sigma^2$, as [25]

$$P(\Delta x, N) = \frac{1}{\sqrt{2\pi\mu^2 N}} e^{-\frac{(\Delta x - N\mu)^2}{2\sigma^2 N}}. \tag{7.4}$$

Definition of the step can vary for different applications and one must be aware that its choice influences subsequent interpretation of the results. One possible approach is to take one component of particle velocity and define each time when it changes its sign as a boundary between two steps as used e.g. in [159, 132, 60].

Typically, there is some characteristic time $t_0$ associated with the steps. Then, the dependence of probability $P$ on time $t$ can be expressed substituting $Nt_0 \to t$:

$$P(\Delta x, t) = \frac{1}{\sqrt{4\pi D t}} e^{-\frac{(\Delta x - \bar{v}t)^2}{4Dt}} \tag{7.5}$$

where diffusion coefficient $D$ and mean velocity $\bar{v}$ are defined as

$$D = \frac{1}{2}\frac{\sigma^2}{t_0}; \quad \bar{v} = \frac{\mu}{t_0}. \tag{7.6}$$

Transport process described by equation (7.5) is reffered as classical diffusion.

There exists second class of diffusive processes that is referred as anomalous diffusion. Note that the word *anomalous* can have different meanings. From the statistical point of view it is 'not covered by classical diffusion' but from the point of view of magnetic plasma confinement (as was used in previous sections) it means 'higher then neoclassical collisional diffusion'. In this chapter these two meanings will be distinguished mainly by their context.

Foundations of the theory of anomalous diffusion were laid in 1920s and 1930s by Paul Lévy who studied summation of random variables with infinite moments ($\sigma^2 = \infty$, or even $\mu = \infty$). He found generalisation of the central limit theorem and the diffusion process for long-tailed distributions,

$$P_x(\delta_x) \sim 1/x^{1+\alpha}, \tag{7.7}$$

such that in the Fourier space ($x \to k$) the probability $P(k, N)$ has form [138, 10]

$$P(k, N) \sim e^{const. \times N|k|^\alpha}; \quad 0 < \alpha \leq 2. \tag{7.8}$$

For simplicity, we present here only two-parameteric ($N$ and $\alpha$) family of symmetric distributions centred around $x = 0$ but they are member of broader

four-parametric class with additional skewness $\beta$ and shift $\mu$ parameters. Random walk with such heavy-tailed step distribution is called Lévy flight. Note that the anomalous diffusion describes classical diffusion as its subclass with $\alpha = 2, \beta = 0$.

In the theory of anomalous diffusion, the concept of diffusion coefficient cannot be used directly since infinite variance of step lengths implicates infinite diffusion coefficient if the definition (7.6) is used. Instead, its dependence on number of steps $N$ (or time $t = Nt_0$) is introduced,

$$D(t) = \frac{1}{2}\frac{(x(t) - x(t=0))^2}{t} \sim t^{\gamma-1}. \tag{7.9}$$

The value of coefficient $\gamma$ then describes character of the transport. The transport is described by classical diffusion when $\gamma = 1$, and it is in superdiffusive regime for $\gamma > 1$ [10]. If duration of the steps is not considered independent on step lengths and infinite variance or mean value of the step duration (or of waiting times between steps) is allowed, third, subdiffusive regime with $\gamma < 1$ can appear [10].

Since variance of the step lengths is infinite, Lévy flights do not posses any characteristic scale and the parameter $\alpha$ describes fractal dimension of set of visited points [138]. A physically motivated example of such process will be shown in Fig. 7.2(right).

In Hamiltonian systems, the presence of long jumps that generate Lévy flights is closely connected with stochastisation of phase space. This can be visualised by Poincare's section that shows intersection of particle orbits in the phase space with its two-dimensional subspace. An example is shown in Fig. 7.1. In this example, three typical structures can be observed. First, the closed lines are created by trapped particles whose motion is regular. Such particles are bound to these orbits and cannot escape. Second, the dotted regions create so called 'stochastic sea' in which the particles are moving freely. The stochastic see is typical for classical diffusion. The last type of structure is called 'cantori' and they are typically present on the boundary between regions of regular motion and the stochastic see. Cantori form layers that form a sort of transport barrier. If some particle appears in between two cantori, probability of its escape back to the stochastic see is very low. The particle is trapped for a long time in this narrow region of phase space and it can exhibit a long spatial jump (or large waiting time) whose length is limited by probability of penetration of the barrier formed by the cantori.

## 7.3 Equations of motion of particle in electrostatic turbulent potential

Movement of charged particle in electromagnetic field given in terms of vector potential $\vec{A}$ and scalar potential $\phi$ as

$$\vec{B} = \vec{\nabla} \times \vec{A} \tag{7.10}$$

$$\vec{E} = -\vec{\nabla}\phi - \frac{\partial \vec{A}}{\partial t} \tag{7.11}$$

can be described in Cartesian coordinates by Hamiltonian

$$H = \frac{1}{2m}\left(\vec{p} - q\vec{A}(\vec{x}, t)\right)^2 + q\phi(\vec{x}, t). \tag{7.12}$$

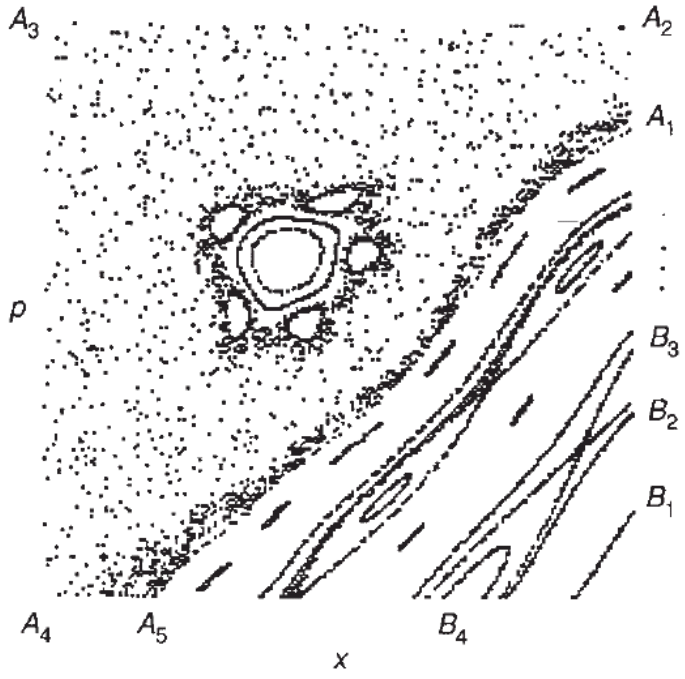


Figure 7.1: Part of Poincare's section of phase space in which three types of motion can be distinguished. Regular quasiperiodic motion along closed curves called islands (B1-B4 and closed curves inside the stochastic see), stochastic see of random motion (dotted area between points A2, A3, A4) and sticky layers (manifesting presence of cantori) on the boundary of stochastic see and islands (e.g. densely populated area between A1-A5). Reproduced from [138].

Here $q$ and $m$ is charge and mass of the particle and $\vec{p}$ is momentum canonically conjugated to the coordinate $\vec{x}$. Components of the equations of motion then have form

$$\frac{dx_j}{dt} = \frac{\partial H}{\partial p_j} = \frac{1}{m}(p_j - qA_j(\vec{x,t})); \quad v_j \equiv \frac{dx_j}{dt}, \tag{7.13}$$

$$\frac{dp_j}{dt} = -\frac{\partial H}{\partial x_j} = \frac{q}{m}\sum_{i\in\{1,2,3\}}\left((p_i - qA_i(\vec{x},t))\frac{\partial A_i(\vec{x},t)}{\partial x_j}\right) - q\frac{\partial\phi(\vec{x},t)}{\partial x_j}. \tag{7.14}$$

In following chapters we will analyse movement of charged particles in turbulent plasma potential that was modelled in 2D slab coordinates (see Sec. 4.4.1). Therefore, we will assume that particle velocity $v_z$ perpendicular to the radial-poloidal plane is in all times small enough such that the particle does not feel potential variations in this direction on time scales of its radial transport. Therefore, on top of standard assumption of drift-interchange turbulence, $k_\parallel \ll k_\perp$, we require also $v_z k_\parallel \ll v_\perp k_\perp$. Similarly in the SOL where the field lines are open with connection length $L_\parallel$ from midplane to target, we must assume that $v_z/L_\parallel \ll v_\perp k_\perp$.

In Hasegawa-Wakatani model of tokamak edge turbulence (see Sec. 7.6.1) the magnetic field strength, $B_0$, is assumed to be constant, heading only in the $z$ direction. Similar assumption will be used in Sec. 7.5 when modelling particle transport in an experimentally measured potential field. With constant magnetic field the magnetic potential can be expressed as $\vec{A} = \frac{1}{2}(-B_0 y, B_0 x, 0)$ and the

Hamiltonian (7.12) becomes

$$H = \frac{1}{2m}(p_x + \frac{qB_0}{2}y)^2 + \frac{1}{2m}(p_y - \frac{qB_0}{2}x)^2 + \frac{1}{2m}p_z^2 + e\phi(x,y,z,t). \tag{7.15}$$

Then the equations of motion (7.13) and (7.14) get form

$$\begin{aligned}
\frac{dx}{dt} &= \frac{1}{m}(p_x + \frac{qB_0}{2}y), & (7.16)\\
\frac{dy}{dt} &= \frac{1}{m}(p_y - \frac{qB_0}{2}x), & (7.17)\\
\frac{dz}{dt} &= \frac{1}{m}p_z, & (7.18)\\
\frac{dp_x}{dt} &= \frac{qB_0}{2m}(p_y - \frac{qB_0}{2}x) - q\frac{\partial\phi(\vec{x},t)}{\partial x}, & (7.19)\\
\frac{dp_y}{dt} &= -\frac{qB_0}{2m}(p_x + \frac{qB_0}{2}y) - q\frac{\partial\phi(\vec{x},t)}{\partial y}, & (7.20)\\
\frac{dp_z}{dt} &= -q\frac{\partial\phi(\vec{x},t)}{\partial z}. & (7.21)
\end{aligned}$$

The potential that we will use is given by numerical modelling that is often made in dimensionless variables ($\phi'$, $x'$, $y'$, $t'$),

$$\phi(x,y,t) = \phi_0\phi'(x/x_0, y/y_0, t/t_0) \tag{7.22}$$

where $\phi_0$, $x_0$, $y_0$, $t_0$ are coefficients of the normalization. We will transform the equations of motion into these dimensionless coordinates and to simplify their form we will use together with previously mentioned

$$x' = \frac{x}{x_0};\;\; y' = \frac{y}{y_0};\;\; t' = \frac{t}{t_0} \tag{7.23}$$

also

$$p_x = \frac{qB_0}{2}y_0p'_x;\; p_y = \frac{qB_0}{2}x_0p'_y. \tag{7.24}$$

Then the equations of motion (7.16), (7.17), (7.19) and (7.20) take simple form

$$\begin{aligned}
\frac{dx'}{dt'} &= T_x(p'_x + y') & (7.25)\\
\frac{dy'}{dt'} &= T_y(p'_y - x') & (7.26)\\
\frac{dp'_x}{dt'} &= T_y(p'_y - x') - R_x\frac{\partial\phi'}{\partial x'}(x',y',t') & (7.27)\\
\frac{dp'_y}{dt'} &= T_x(p'_x + y') - R_y\frac{\partial\phi'}{\partial y'}(x',y',t') & (7.28)
\end{aligned}$$

with four coefficients

$$\begin{aligned}
T_x &= \frac{qB_0}{2m}\frac{t_0y_0}{x_0} = \frac{\omega_c}{2}\frac{t_0y_0}{x_0} & (7.29)\\
T_y &= \frac{qB_0}{2m}\frac{t_0x_0}{y_0} = \frac{\omega_c}{2}\frac{t_0x_0}{y_0} & (7.30)\\
R_x &= \frac{2\phi_0t_0}{B_0x_0^2} & (7.31)\\
R_y &= \frac{2\phi_0t_0}{B_0y_0^2}. & (7.32)
\end{aligned}$$

Often the normalization of spatial scales is the same, $x_0 = y_0$, and then there are only two parameters ($R$, $T$) in the equations of motion,

$$T = t_0 \frac{qB_0}{2m} = t_0 \frac{\omega_c}{2} \tag{7.33}$$

$$R = \frac{2\phi_0 t_0}{B_0 x_0^2}. \tag{7.34}$$

We note that $R$ does not depend on the species of traced particles and changes only with change of normalization of the potential. In addition, if the potential is time-independent, we can choose $t_0$ freely and thus set e.g. $T = 1$. Then there is only single parameter $R|_{t_0=2/\omega_c}$ that fully determines character of the motion. The form of parameters $T$ and $R$ for types of turbulent potential under consideration will be computed in the corresponding sections. We should also note that the parameters $T$ and $R$ are not sufficient for determining trajectory of individual particle. Indeed, the trajectory is dependent also on initial conditions of the particle - its initial position and momentum.

Transport of test particles in a turbulent potential was often studied with particle velocity reduced to basic guiding center drifts (e.g.[95, 109, 11, 111, 60]), eventually with effect of finite Larmor radius described by averaging over the circle of single cyclotron gyration [95, 60]. In [116] trajectories of $C^+$ ions in experimentally measured potential obtained by $E \times B$ drift approximation and by tracing of full particle orbits were compared and difference in transport regime (classical diffusion for $E \times B$ drift and anomalous Lévy walk diffusion for full orbits) was found. In [122, 111] it was shown that ideal tracers moving with $E \times B$ only are insufficient for description for particles with finite mass and also polarization drift should be taken into account. In Secs. 7.6 and 7.7.2 we will show that adding the polarization drift is in some cases still insufficient and results obtained by more precise tracing of full particle orbits described by Eqs. (7.25)-(7.28) differ.

## 7.4 Particle motion in parabolic and egg-crate potential

Turbulent potential structures generated in the edge plasma can have quite complex time-evolving structure, as can be seen in Figs. 3.5 and 7.20. In order to allow analytical investigation of particle transport induced by the structures, one can approximate their form with simple time-independent parabolic shape [12]

$$\phi_{par}(r) = \phi_0 \left(1 - \frac{4k_\perp^2 r^2}{\pi^2}\right) \tag{7.35}$$

or, alternatively, with so called egg-crate potential [89, 90]

$$\phi_{egg}(x, y) = \phi_0 \left(1 + \cos(kx) + \cos(ky)\right). \tag{7.36}$$

Very important property of the parabolic form of potential (7.35) is its azimuthal symmetry, which results in conservation of angular momentum and thus significantly simplifies analysis of particle movement. Writing Hamiltonian of particle in homogeneous magnetic field in polar coordinates $r, \varphi$,

$$H = \frac{1}{m} P_r^2 + \frac{(P_\varphi - \frac{qBr^2}{2})^2}{2mr^2} + q\phi_{par}(r), \tag{7.37}$$

where $P_r$ and $P_\varphi$ are canonical radial and angular momentum, respectively, and reminding that due to symmetry $P_\varphi = \text{const.}$, particle motion can be described as 1D radial motion in one-dimensional effective potential [12]

$$V(r) = \frac{P_\varphi^2}{2mr^2} + \frac{qB^2}{8m} r^2 (1 - \alpha_B \frac{32}{\pi^2}). \tag{7.38}$$

The dimensionless parameter

$$\alpha_B = \frac{m k_\perp^2 \phi_0}{qB^2}. \tag{7.39}$$

determines character of the dynamics. Note, that $\alpha_B$ is exactly the dimensionless parameter $R$ (7.34) with appropriate choice of time normalization $t_0 = 2/\omega_c$ that sets $T = \text{const.}$. When $\alpha_B < \pi^2/32 \approx 0.31$, the effective potential has a minimum, particles are trapped and circumnavigate the potential hill with oscillation in $r$ due to its cyclotron motion. In the other case, when $\alpha_B > \pi^2/32$, the effective potential monotonically decreases and all particles start to descend the potential hill, gaining its energy. We will reffer to this instability as Bellan instability, as was done in [90]. $\alpha_B \sim m/q$ and therefore the character of the dynamics depends on the particle species. Heavy particles with low charge are more likely to get untrapped from the hill and therefore dynamics of the main plasma particles may qualitatively differ from the dynamics of heavier plasma impurities.

Egg-crate potential (7.36) is a step towards somewhat more realistic analytical model of turbulent potential, because it consists of potential hills as well as valleys,resembling potential relief of drift wave turbulence (see Fig. 3.5).In [89, 90], infinite plane of such alternating hills and valleys was used. The results of numerical simulations in these two papers show that results derived for parabolic form of potential hill (7.35) hold similarly for particle behaviour in an infinite egg-crate potential. This comes from the fact, that leading term in Taylor series of (7.36) is quadratic.

Provided that particle Larmor radius is substantially smaller then the wavelength of the potential, $r_L \ll k$, there exist three types of motion (see Fig. 7.2) governed by dimensionless parameter $R \equiv \alpha_B$, now with $k_\perp$ replaced with wavelength $k$. Numerical simulations show [89] that when $R < 0.25$, particles initially positioned on a hill remain trapped, while for $R \geq 0.25$ the previously discussed instability appears and particles descend down the hill. Most of the particles initially positioned in the potential valley remains trapped.

As $R$ grows above $R \geq 0.25$, particle movement in a region adjacent to the potential separatrix ($\phi_{egg} = 1$) becomes stochastized. Particle trajectory is irregular and particle may, with nonzero probability, cross the separatrix and enter neighbouring cell. Particle behaviour in the separatrix region is dependent on the value of $R$. When $0.25 \lesssim R \lesssim 1$, particles crossing the separatrix are trapped by the neighbouring structure and released again after some mean time $\tau$. The whole process repeats and from the statistical point of view it can be described as diffusive or random-walk process with length of the step $l = 1/k$ and diffusion coefficient $D = k^{-2}\tau^{-1}$. When $R$ approaches $R \approx 1$, sticky layer appears in the phase space in the separatrix region [123] and there exists growing number of trajectories that follow the separatrix over multiples of structure length scales before being trapped again. This can be interpreted as a transition from classical diffusion to anomalous Lévy-type diffusion. The study of dependence of the scaling of the variance

of particle position with time, $x^2(t) \sim t^\gamma$, on parameters of the model and initial particle conditions can be found in [90, 117].

The mechanism of generation of long jumps in the egg-crate potential was studied in detail in [123]. When $R$ is sufficiently high, with increasing energy structure of Poincare's section undergoes bifurcations and sticky layer, called also "quasitrap"is formed. The boundary of the layer is formed by a chain of cantori in phase space that form a barrier, strongly reducing probability of particle passing through. The layer is located near potential separatrix and particle that gets into this region can remain trapped for a long time, traveling along the separatrix, before finding its way out through the quasitrap.

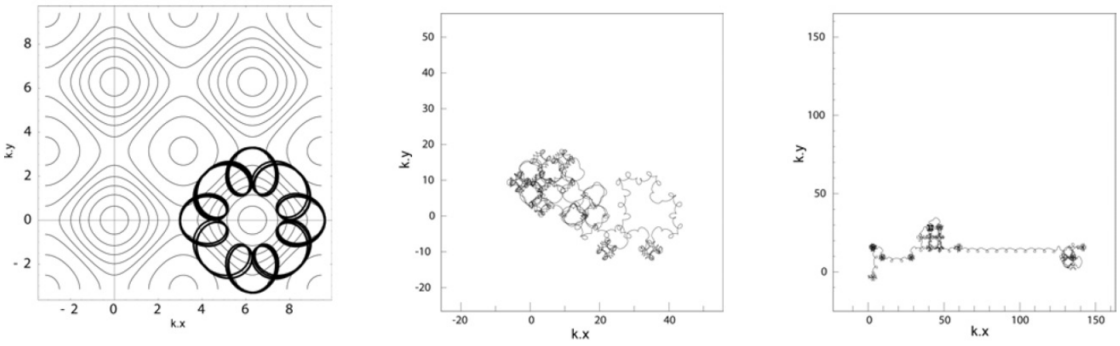


Figure 7.2: Three different types of particle motion in egg-crate potential embedded in a uniform magnetic field. Particles with $R \leq 0.25$ remain trapped with regular motion of their gyrocenter (left). Particles with $0.25 < R < 1$ can escape from potential hill and they have a high probability to be trapped in a neighbouring cell, resulting in classical random-walk (middle). When $R > 1$, particle may intermittently travel long distances along separatrices undergoing Léwy-walk process (right). Figure reproduced from [116].

## 7.5 Particle motion in experimentally measured potential field

In this section, diffusion of particles in a time-evolving experimentally measured turbulent potential will be investigated. We use potential experimentally measured at CASTOR tokamak by two-dimensional array of 8x8 Langmuir probes. CASTOR (now renovated and renamed to GOLEM) was a small tokamak with major radius $R = 0.4$ m, minor radius $a = 0.1$ m and poloidal ring limiter at radius $r = 0.085$ m. Typical toroidal magnetic field was $B = 1$ T. The arrangement of array of probes measuring floating potential $V_{fl}$ is shown in Fig. 7.3. The probes had diameter of 2 mm and their mutual distance was 6 mm in poloidal direction and 4 mm in radial direction, covering total area of $42 \times 31.5$ mm$^2$. The regular grid of the probes can be, if machine curvature is neglected, considered aligned with radial and poloidal direction. The area of the probe system is not negligible compared to the total poloidal section, but it was shown [98] that its perturbing effect is smaller than could be expected and the probe array can even penetrate the separatrix without shifting the plasma column downwards.

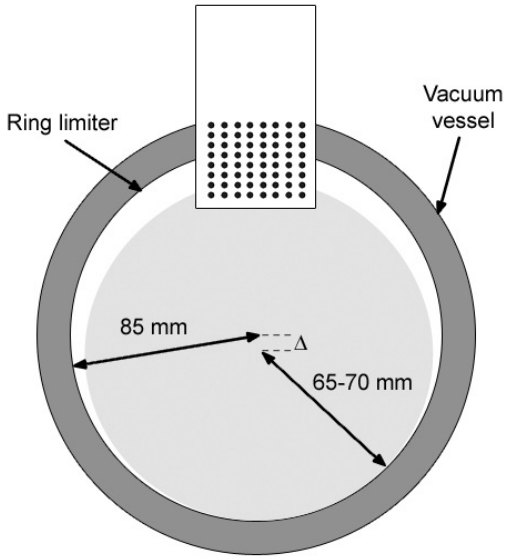


Figure 7.3: Schematic picture of 2D array of Langmuir probes used for measurement of floating potential in CASTOR tokamak. [132]

### 7.5.1 Potential used in the simulation

The characteristics of the measured data are similar to those described in [98]. The potential structures present in the data have average extension about 1-2 cm and move with poloidal velocity 2-5 km·s$^{-1}$. An example of potential landscape is shown in Fig. 7.4(left). Some of the structures can survive several poloidal revolutions with period $\tau \approx 200$ $\mu$s. This is confirmed by autocorrelation function plotted in Fig. 7.4(right) that exhibits secondary maximum at this time shift.

With sampling rate of the original data 1 MHz, time distance between potential samples was larger then time step necessary to precisely resolve cyclotron motion of the particles. Therefore, the data was resampled using sinc-interpolation

$$V'_{fl}(t) = \sum_{n=0}^{N} V_{fl}(nT)\mathrm{sinc}\left[\frac{\pi}{T}(t-nT)\right] \tag{7.40}$$

where $V_{fl}(nT)$ represents original floating potential at time $nT$, $N$ is number of samples and $V'_{fl}(t)$ is interpolated potential at arbitrary time $0 \leq t \leq NT$. The advantage of sinc-interpolation is that it keeps continuous frequency spectra, in contrast to the discrete Fourier interpolation that uses only discrete frequencies. The discrete Fourier interpolation was used for interpolation of data of different probes in space and the potential used in the simulation thus represents 8×8 lowest spatial harmonics of the real potential. In this sense our work extends previous studies of particle movement in egg-crate potential [89, 90, 91], that represents only the single most dominant harmonic.

In the simulation, plasma potential $\phi$ in equations of motion (7.16)-(7.17) and (7.19)-(7.20) was substituted by measured floating potential $V'_{fl}$. The dynamics does not depend on absolute value of the potential used in equations of motion, but on its derivations. Therefore, replacing $\phi$ by $V_{fl}$ is equivalent to introducing isothermal approximation $T_e$ =const. Indeed, turbulent structures carry some perturbation of $T_e$ that is reflected in $V_{fl}$ and increases its gradients. This effect can

lead to overestimation of the overall transport rate, similarly to the estimations made in [133]. As no data on $T_e$ were available, the isothermal approximation, however, cannot be avoided.

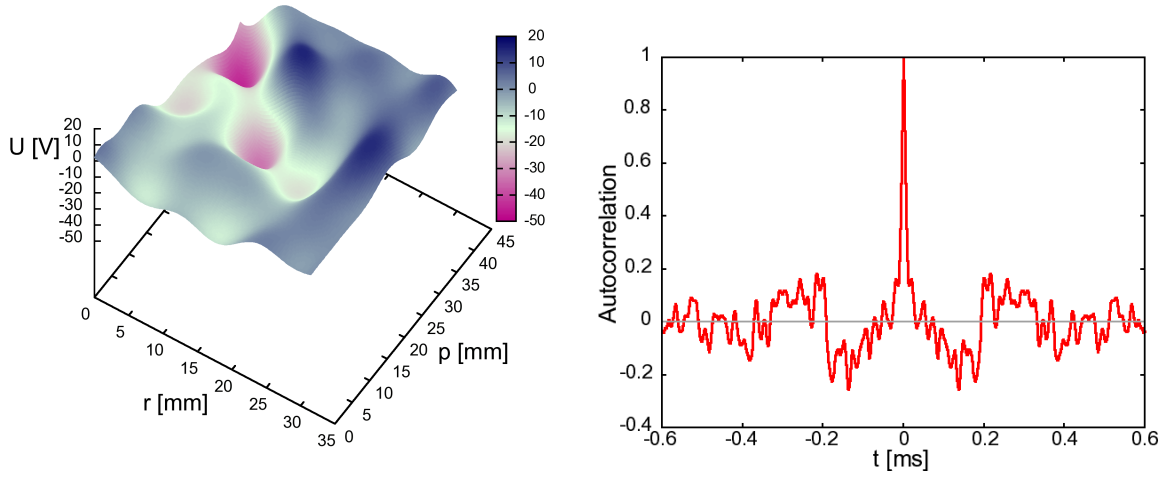


Figure 7.4: *Left:* Example of profile of experimentally measured potential after Fourier interpolation. *Right:* Autocorrelation function of signal measured at the most inserted and most upstream probe. Secondary maxima appear at $t \approx \pm 0.2$ ms.

### 7.5.2 Results of numerical simulations

The experimentally measured approximation of plasma potential field was used as a background for modelling of particle transport in the edge tokamak region. We assumed low density together with low density gradients of the studied particles and treated the particles as passive tracers that are convected by the potential field but do not influence it back.

Full cyclotron gyration of the particles was taken into account and equations of motion (7.16)-(7.17) and (7.19)-(7.20) were advanced in time by explicit fourth-order Runge-Kutta method with time step of 1/1000 of cyclotron period. For each species, $5 \times 10^4$ individual particles were traced which is sufficient to obtain good quality of the statistics. At the beginning of the simulation all particles were distributed randomly in space with zero total velocity $v_0 = 0$ m $\cdot$ s$^{-1}$. This largely simplifies discussion of initial conditions and since the potential is time dependent, the particles get energy from potential fluctuations. After some time, a steady-state is established with almost-Maxwellian distribution of particle velocities (with kurtosis slightly lower - 2.82 instead of expected 3). The temperature of the tracers (28 eV for $C^+$ ions) corresponds well to the ion temperatures ($\approx$ 30 eV) measured in the SOL of CASTOR [147].

The particle dynamics was traced by two types of diffusion coefficient, separately for each direction and each species. The running diffusion coefficient [109] represents long-term overall dynamics of particles and is defined as

$$D_x = \frac{\sigma_x^2}{2t} = \frac{1}{2t} \left\langle [x(t) - x(t=0)]^2 \right\rangle \tag{7.41}$$

where $x$ stands for poloidal ($p$) or radial ($r$) direction, $\sigma_x$ is mean square displacement of particles in this direction and $\langle\cdot\rangle$ averages over all particles of given species. On the other hand, the 'instantaneous' diffusion coefficient

$$D_{i,x} = \frac{\mathrm{d}}{\mathrm{d}t}\frac{\sigma_x^2(t)}{2} = \frac{1}{2}\frac{\mathrm{d}}{\mathrm{d}t}\left\langle [x(t) - x(t=0)]^2 \right\rangle \tag{7.42}$$

represents short-term dynamics of particles affected by actual changes of the background potential.

Time evolution of both types of diffusion coefficient for the case of $C^+$ ions is shown in Fig. 7.5. The sharp initial increase of the diffusion coefficient is given by motion of particles from their initial positions and does not have any further physical meaning. After this initial increase, running radial diffusion coefficient is almost constant, $D_r \approx 1\ \mathrm{m}^2 \cdot \mathrm{s}^{-1}$, which represents regime of classical diffusion. On the other hand, the running version of poloidal diffusion coefficient is slowly growing in time, mainly in short periods of enhanced diffusion accompanied by simultaneous increase of instantaneous diffusion coefficient. The growth of $D_p$ indicates anomalous Lévy-type diffusion. These findings agree with similar results found in [116].

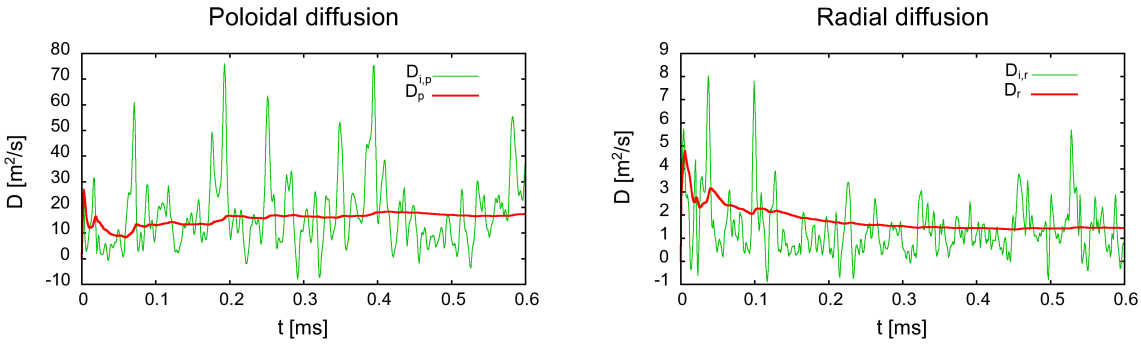


Figure 7.5: Running (red) and instantaneous (green) diffusion coefficient in poloidal (left) and radial (right) direction for $C^+$ ions with zero initial velocities.

The instantaneous diffusion coefficients oscillate most of the time slightly bellow the level of their running counterparts, however short bursts of increased diffusion can be observed. The width of these peaks $\delta t \approx 10 - 18\ \mu$s approximately corresponds to the time $t_{pass}$ necessary for turbulent structures convected by poloidal plasma flow to move from upstream to downstream edge of the measured region. We estimate this transit time from cross-correlation of signal at the middle of the region and middle of the downstream poloidal boundary, $t_{pass} \approx 2t_{corr} = 12\ \mu$s. If this enhanced diffusion is caused by presence of turbulent structures, the instantaneous diffusion coefficient should exhibit increased autocorrelation with shift of $\approx 200\ \mu$s, corresponding to reappearance of the structures after one poloidal revolution. This is confirmed for $D_{p,i}$ in Fig. 7.6(left) where the position of the secondary maxima is similar as for the autocorrelation of the potential signal in Fig. 7.4(right). Autocorrelation of $D_{r,i}$ (Fig. 7.6(right)) does not show such long-time correlation and its oscillations with period 32 $\mu$s are caused by alternating of positive (enhanced diffusion) and negative (suppressed diffusion) parts of potential structures.

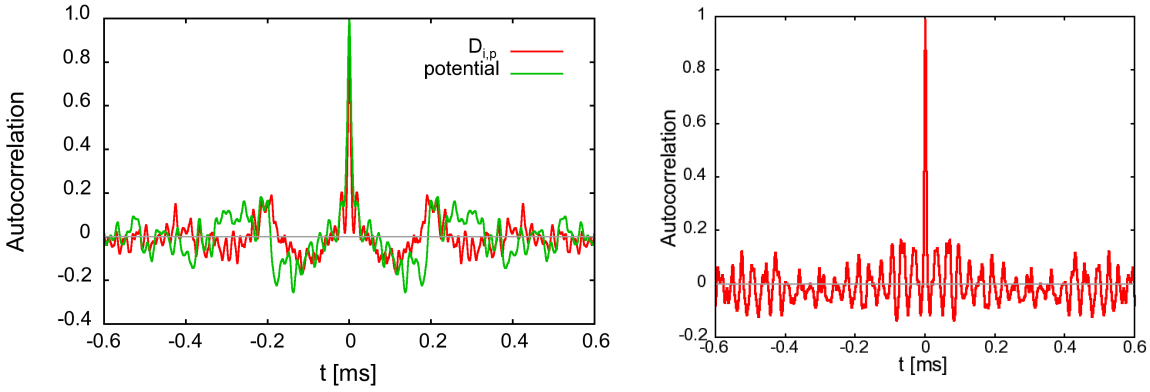


Figure 7.6: Autocorrelation function of instantaneous diffusion coefficient in poloidal ($D_{i,p}$; left) and radial ($D_{i,r}$; right) direction. The autocorrelation of $D_{i,p}$ is compared with autocorrelation of signal received from innermost probe that was shown in Fig. 7.4(right)

In our next set of simulations we have compared diffusion rate for particles with different $m/q$ ratio. We chose the ratio such that it represents some of the more common impurities released by plasma-wall interaction from tokamak material components. Particles of the last category labelled as 'drift' represented the limit $m \to 0$ and their velocity was given by $E \times B$ drift. Time evolution of running diffusion coefficient for all the species is shown in Fig. 7.7. The rate of diffusion is almost the same for the drift particles and $H^+$ ions, decreasing with $m/q$ ratio in poloidal direction and increasing in the radial one. While $D_r$ shows classical behaviour and saturates, $D_p$ is growing in time, showing that the diffusion is of Lévy type for all modelled particle species.

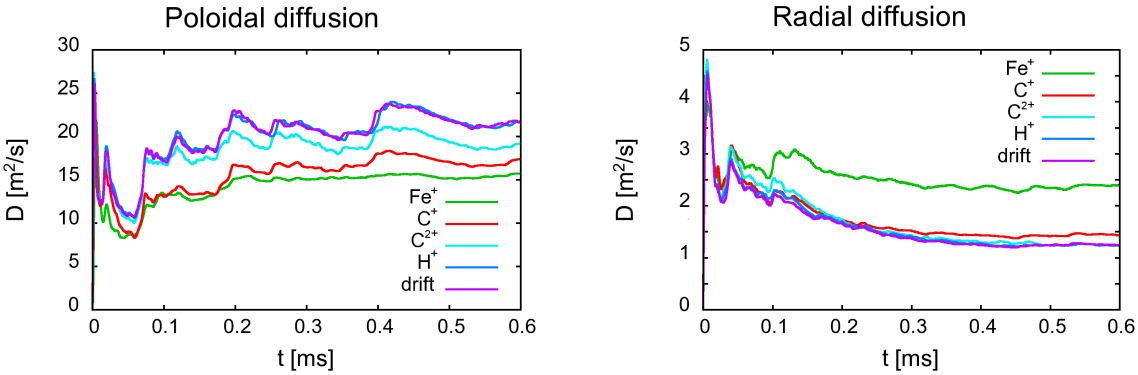


Figure 7.7: Diffusion coefficient computed for different particle species in poloidal (left) and radial (right) direction.

The opposite behaviour of diffusion coefficient with $m/q$ ratio for poloidal and radial direction can be explained as follows. Particles with small $m/q$ ratio are bound tu equipotentials and they are easily convected together with turbulent structures moving predominantly in poloidal direction. Moreover, the structures are poloidally elongated and also the equipotentials outside of the structures are

oriented predominantly in poloidal direction, which enhances poloidal movement of untrapped particles. The larger the ratio $m/q$, the larger Larmor radius and larger probability that: a) trapped particle becomes untrapped which reduces its poloidal convection together with potential structures; b) particle can jump radially between equipotentials which increases its radial diffusion.

In order to confirm that the poloidal diffusion can be described in the frame of Lévy walks, we have traced trajectories of all individual particles and reconstructed probability distribution function (PDF) $P(d_p)$ of lengths $d_p$ of jumps that particles undergo in the poloidal direction. First, each trajectory has been gyro-averaged in order to remove cyclotron rotation of particles. Then each jump was defined as a part of the trajectory in which corresponding poloidal velocity does not change its sign. The PDF of step lengths is shown in Fig. 7.8 and it consists of two parts - Gaussian distribution generated by particles wandering only short distances and the long tail that was expected from behaviour of $D_p$. The long tail is asymmetric with respect to direction of the jumps and long jumps in the direction of the poloidal flow have higher probability than those going against the flow. This is due to particle dragging by potential structures that supports positive jumps and disrupts the negative ones. Since particles with larger Larmor radius feel the dragging weaker (they have higher probability of untrapping from potential structures), their PDF decays faster in the direction of the flow and on the other hand jump lenghts against the flow are slightly increased. The assymetry of the PDF is further supported by the particles trapped on positive potential structures and further released due to Bellan instability. They circulate in such direction that when they become untrapped, their poloidal velocity is on average heading in the direction of the flow.

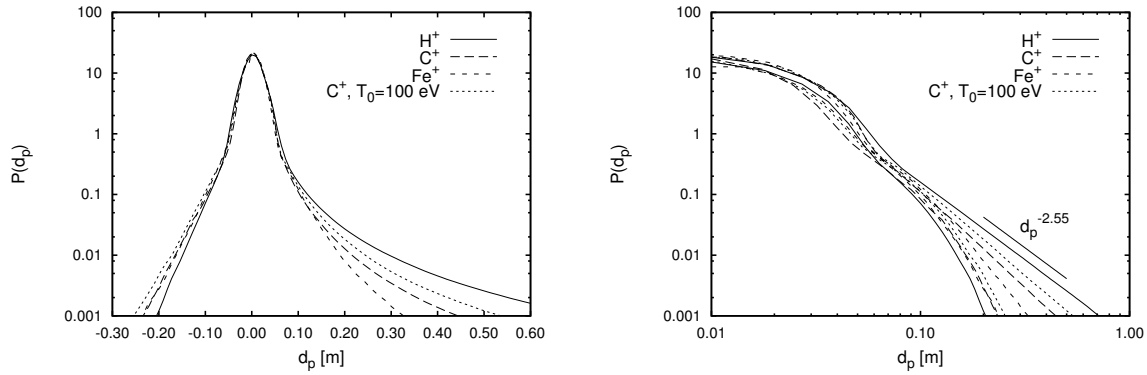


Figure 7.8: PDF of step lengths of particles in time-dependent turbulent potential in poloidal direction in semilogarithmic (left) and logarithmic (right) scale. Branch with higher probability of long jumps heads in the direction of mean poloidal plasma flow. [132]

Making power-law fit to the PDF of jumps in direction of the flow, $P(d_p) \sim d_p^{\alpha}$, we find $\alpha_{H^+} = -2.55$ and $\alpha_{C^+} = -2.93$. Both exponents fall into range $-3 < \alpha < -1$ which implies Lévy distribution (7.7). The tail of PDF of jumps against direction of the plasma flow decays exponentially and the distribution is bi-Gaussian.

### 7.5.3 Conclusion

Based on our results, the following conclusions can be drawn [132]. The presence of poloidally rotating turbulent structures in tokamak edge enhances poloidal transport of all types of particles. Asymmetry in distribution of poloidal particle step lengths $d_p$ was detected, with Lévy walk distribution of $d_p$ in the direction of poloidal flow. The overall poloidal transport is anomalous with running poloidal diffusion coefficient $D_p$ growing in time. Particles with larger $m/q$ ratio exhibit smaller poloidal diffusion since their larger Larmor radius $r_L$ implicates higher probability of particle untrapping from poloidally moving potential fluctuations. The radial particle diffusion is classical, with diffusion coefficient $D_r$ generally lower then $D_p$. The dependence on $m/q$ ratio is reversed in radial direction, compared to the poloidal one, and particles with larger $m/q$ ratio exhibit stronger radial diffusion. In the radial direction particles have to overcome larger local potential gradients which is more simple for particles with larger $m/q$ ratio and larger $r_L$, that enhances their transport. Impurities are typically generated at the edge where plasma interacts with material components. Our study reveals that heavier particles will penetrate into the plasma easier than those with small $m/q$, since their Larmor radius is able to 'bridge' equipotentials in radial direction and limit the effect of particle trapping in poloidally moving potential structures. As more electrons become stripped from the impurity ions, the $m/q$ ratio drops and their radial transport becomes supressed in favour of anomalous poloidal dragging by turbulent structures.

There are two main limitations of the used form of potential. First, the convective structures are poloidally rotating and therefore they are present in the simulation for a limited time only. The effect of particle trapping in the structures is therefore underestimated and the transport in direction of structure movement (which has both large poloidal and small radial component) is underestimated as well. Second, we have used isothermal approximation. Indeed, turbulent structures typically exhibit some fluctuation of electron temperature, however, if this fluctuation is in phase with fluctuation of potential (either by drift-wave origin of the structures or by sheath-dissipative coupling), the substitution of plasma potential $\phi$ by the measured floating potential $V_{fl}$ overestimates its fluctuations, but does not generally change its structure. As neither $T_e$ nor $\phi$ were measured, this assumption cannot be verified.

## 7.6 Clustering and radial pinch of impurities in Hasegawa-Wakatani potential

In this section we will focus on some specific properties of particle transport in modelled Hasegawa-Wakatani potential. Specifically, we will discuss effects of particle clustering in turbulent vortexes and their inward radial pinch that were found in fluid simulations of impurities with finite mass but zero Larmor radius in [122]. We will test validity of these effects for particles with non-negligible Larmor radius. First, our code for modelling drift wave turbulence is described in Secs. 7.6.1-7.6.2. Previous findings on effects of particle clustering and radial impurity pinch can be found in Sec. 7.6.4 and we present our results in Sec. 7.6.5.

### 7.6.1 Hasegawa-Wakatani equations

Hasegawa-Wakatani model is a basic model for description of drift waves in 2D drift plane perpendicular to magnetic field lines. 2D slab coordinates $x$ and $y$ represent radial and poloidal direction, respectively. The model is very simple, yet it still contains important parts of the drift-wave physics. It is based on fluid continuity (4.53) and vorticity (4.78) equations with momentum equation (4.45) reduced to $E \times B$, $\vec{v}_E$, and polarization, $\vec{v}_P$, drifts. Similarly to the ESEL model, the effect of second-order $\vec{v}_P$ is neglected in the continuity equation and it plays a role only through its compressibility in the vorticity equation. The standard version of the model is isothermal, $T_e = \text{const.}$, even though its advanced variants with non-constant $T_e$ were developed [140, 158, 83]. Magnetic field $B$ is taken as constant. The fluid equations are simplified by assumption of constant radial e-folding length $L_n$ of background density $n_0$,

$$n_0 \approx N_0 \exp\left(-\frac{x}{L_n}\right). \tag{7.43}$$

This allows to separate total density $n(t)$ to the fluctuating part $\tilde{n}(t) = n(t) - n_0$ and the background $n_0$. Then, assuming $\tilde{n}/n_0 \ll 1$, term $\mathrm{d}n/\mathrm{d}t$ in the continuity equation can be approximated as

$$\frac{1}{n}\frac{\mathrm{d}n}{\mathrm{d}t} = \frac{\mathrm{d}\ln n}{\mathrm{d}t} = \frac{\mathrm{d}\ln(n_0+\tilde{n})}{\mathrm{d}t} = \frac{\mathrm{d}\ln n_0}{\mathrm{d}t}\frac{\mathrm{d}\ln(1+\tilde{n}/n_0)}{\mathrm{d}t} = \tag{7.44}$$

$$= \frac{1}{L_n B_0}\frac{\partial\phi}{\partial y} + \frac{\mathrm{d}\ln(1+\tilde{n}/n_0)}{\mathrm{d}t} \approx \frac{1}{L_n B_0}\frac{\partial\phi}{\partial y} + \frac{1}{n_0}\frac{\mathrm{d}\tilde{n}}{\mathrm{d}t} \tag{7.45}$$

where it was used

$$\frac{\mathrm{d}\ln n_0}{\mathrm{d}t} = (\frac{\partial}{\partial t} + \vec{v}_E\cdot\vec{\nabla})\ln n_0 = (\frac{\partial}{\partial t} + \frac{-\vec{\nabla}\phi\times\vec{b}}{B_0}\cdot\vec{\nabla})(-\frac{x}{L_n}) = \frac{1}{L_n B_0}\frac{\partial\phi}{\partial y}. \tag{7.46}$$

Note that such separation of scales was not possible in the ESEL model because in the SOL, in contrast to the edge region, the relative fluctuations are of the order of background density $\tilde{n}/n_0 \approx 1$.

To close the vorticity equation, form of $\vec{\nabla}_\parallel \cdot \vec{J}_\parallel$ term must be specified. In the edge region where magnetic field lines are closed, small but still finite $1/L_\parallel \equiv k_\parallel \ll k_\perp$ is consistent with magnetic geometry [127]. A single dominant parallel mode is considered in H-W model and appropriate closure (4.95) of the $\vec{\nabla}_\parallel \cdot \vec{J}_\parallel$ was presented in Sec. 4.4.2.

From now on we will omit the tilde and understand symbols $n$ and $\phi$ as $\tilde{n}$ and $\tilde{\phi}$, respectively, and we will use normalization

$$\frac{\vec{x}}{\rho_s} \to \vec{x};\quad t\omega_{ci}\frac{\rho_s}{L_n} \to t;\quad \frac{e\tilde{\phi}}{T_e}\frac{L_n}{\rho_s} \to \phi;\quad \frac{\tilde{n}}{n_0}\frac{L_n}{\rho_s} \to n \tag{7.47}$$

where $\rho_s$ is hybrid ion gyroradius, $\omega_{ci}$ ion gyrofrequency and $T_e$ electron temperature.

After substitution of the drifts into (4.53) and (4.78), the final form of Hasegawa-Wakatani equations is

$$\left(\frac{\partial}{\partial t} - \frac{\vec{\nabla}_\perp \phi \times \vec{b}}{B_0} \cdot \vec{\nabla}_\perp\right) n + \frac{\partial \phi}{\partial y} = \quad \alpha(\phi - n) + (-1)^{d+1} \nu \vec{\nabla}_\perp^{2d} n \tag{7.48}$$

$$\left(\frac{\partial}{\partial t} - \frac{\vec{\nabla}_\perp \phi \times \vec{b}}{B_0} \cdot \vec{\nabla}_\perp\right) \left(\vec{\nabla}_\perp^2 \phi\right) = \quad \alpha(\phi - n) + (-1)^{d+1} \nu \vec{\nabla}_\perp^{2d+2} \phi \tag{7.49}$$

The factor $(-1)^{d+1}$ in front of dissipative terms in both equations guarantees that the dissipation acts as a sink of energy and enstrophy and not as a source.

The system is dependent on single adiabaticity parameter $\alpha$

$$\alpha = \frac{T_e L_n}{n_0 \omega_{ci} \rho_s L_\parallel^2 \eta_\parallel} \tag{7.50}$$

and has two basic limits [24]. For $\alpha \gg 1$ (adiabatic regime) the system reduces to more simple Hasegawa-Mima [62] system and for $\alpha \ll 1$ (hydrodynamic regime) it reduces to Navier-Stokes equations.

### 7.6.2 Numerical algorithm for solving Hasegawa-Wakatani equations

In order to solve system of coupled partial differential equations (7.48) and (7.49) we developed fully dealiased spectral numerical code. This is made possible by the fact that we use double-periodic boundary conditions that allow to make Fourier transform in both direction. Substituting Laplacian of the potential with vorticity $\Omega$ in accordance with Eq. (4.71),

$$\Omega = \vec{\nabla}_\perp^2 \phi, \tag{7.51}$$

and transforming all three equations (7.48), (7.49) and (7.51) into Fourier space, the code solves three coupled equations

$$\tilde{\phi} = -\frac{1}{k_x^2 + k_y^2} \tilde{\Omega}, \tag{7.52}$$

$$\frac{\partial}{\partial t}\tilde{n} - (k_y \tilde{\phi}) * (k_x \tilde{n}) + (k_x \tilde{\phi}) * (k_y \tilde{n}) + i k_y \tilde{\phi} = \alpha(\tilde{n} - \tilde{\phi}) - \nu(k_x^2 + k_y^2)^d \tilde{n}, \tag{7.53}$$

$$\frac{\partial}{\partial t}\tilde{\Omega} - (k_y \tilde{\phi}) * (k_x \tilde{\Omega}) + (k_x \tilde{\phi}) * (k_y \tilde{\Omega}) = \alpha(\tilde{n} - \tilde{\phi}) - \nu(k_x^2 + k_y^2)^d \tilde{\Omega}. \tag{7.54}$$

The tilde $\sim$ denotes fourier image of the original real-space quantities. Note that hyperviscosity terms are now always negative because the factors $(-1)^{d+1}$ used in real space compensate with the sign of Fourier transform of a derivation. All terms can be easily enumerated except the convective term that in the Fourier space has a form of convolution $(*)$. It would be costly to compute the convolution directly. Therefore we use fast Fourier transform (FFT) algorithm to transform

both involved fields back to the real space where they can be directly multiplied. The second FFT then brings the result back into Fourier space.

The computational grid is discretized equidistantly and to perform fast Fourier transform we use well-known open source library FFTW (Fastest Fourier Transform in the West) [1].

Chosen time stepping algorithm is a 3rd order explicit linear multistep method. It computes value $\vec{q}_n$ of vector of field quantities $\vec{q} = (n, \Omega)$ at given point in time $t_n$ based on its values and derivations $\frac{\partial \vec{q}}{\partial t} = \vec{f}(t, \vec{q})$ in three previous steps with constant time step $\Delta t$ as

$$\vec{q}_n = \frac{6}{11}\left(3\vec{q}_{n-1} - \frac{3}{2}\vec{q}_{n-2} + \frac{1}{3}\vec{q}_{n-3} + \Delta t\left[3\vec{f}(t_{n-1}, \vec{q}_{n-1}) - 3\vec{f}(t_{n-2}, \vec{q}_{n-2}) + \vec{f}(t_{n-3}, \vec{q}_{n-3})\right]\right). \tag{7.55}$$

There are four dynamical invariants of H-W equations (7.48) and (7.49) that can be combined into two quantities with simple physical interpretation [24]. It is the total energy density $E$ composed from kinetic energy $E_{kin}$ and potential energy $E_{pot}$

$$E = E_{kin} + E_{pot} = \frac{1}{2}\int\int \left(\vec{\nabla}_\perp \phi\right)^2 \mathrm{d}x\mathrm{d}y + \frac{1}{2}\int\int n^2 \mathrm{d}x\mathrm{d}y \tag{7.56}$$

and potential (or generalised) enstrophy

$$W = \frac{1}{2}\int\int \left(n - \vec{\nabla}_\perp^2 \phi\right)^2 \mathrm{d}x\mathrm{d}y. \tag{7.57}$$

Time evolution of these quantities is given by (7.48) and (7.49) as [24]

$$\frac{\partial E}{\partial t} = \Gamma_n - \Gamma_\alpha - D^E \tag{7.58}$$

$$\frac{\partial W}{\partial t} = \Gamma_n - D^W \tag{7.59}$$

where only radial density flux $\Gamma_n$

$$\Gamma_n = -\int\int n\left(\frac{\partial \phi}{\partial y}\right)\mathrm{d}x\mathrm{d}y \tag{7.60}$$

can work as a source of energy and potential enstrophy, extracting free energy from the background density gradient (see origin of the term $\frac{\partial \phi}{\partial y}$ in Eq. (7.46)). $\Gamma_\alpha$ defined as

$$\Gamma_\alpha = \alpha\int\int (n - \phi)^2 \mathrm{d}x\mathrm{d}y \tag{7.61}$$

is always positive and thus constitutes a sink of fluctuation energy being resistively dissipated. The remaining diffusion terms

$$D^E = \nu\int\int \left[\left(\vec{\nabla}_\perp^d n\right)^2 + \left(\vec{\nabla}_\perp^{d+1}\phi\right)^2\right]\mathrm{d}x\mathrm{d}y \tag{7.62}$$

$$D^W = \nu\int\int \left(\vec{\nabla}_\perp^d (n - \vec{\nabla}_\perp^2 \phi)\right)^2 \mathrm{d}x\mathrm{d}y \tag{7.63}$$

[1] http://www.fftw.org

are also sink terms. The factor $(-1)^{d+1}$ in front of the diffusive terms in (7.48) and (7.49) was chosen such that terms (7.62) and (7.63) are always positive.

The code computes these quantities and checks that evolution laws (7.58) and (7.63) are satisfied. Since only Fourier coefficients of the fields are stored in every time step and all these terms have a quadratic or generally multiplicative form, we use Parseval's theorem[2] to evaluate the integrals directly in Fourier space.

Fig. 7.9(left) shows time evolution of integral quantities $E$, $E_{kin}$, $E_{pot}$ and $W$ for a simulation that will be used in the following sections as a background for particle tracing. For better comparison with results presented in [122] we have chosen parameters such that $\alpha = 1$, $d = 1$, $D_n = D_\Omega = 10^{-2}$. The simulation was made with $512 \times 512$ Fourier nodes (after dealiasing) and normalized time step $dt = 10^{-4}$. Fig. 7.9(right) presents evolution of corresponding fluxes $\Gamma_n$, $\Gamma_\alpha$ and diffusive sinks $D^E$ and $D^W$ in this simulation. Time evolution of enstrophy is given by balancing $\Gamma_n$ with diffusive sink $D_W$ and since $\Gamma_n$ is nonzero in the saturated state the $D_W$ cannot disappear. Different behaviour works for $D_E$, because here the fluxes due to background density gradient $\Gamma_n$ are balanced by $\Gamma_\alpha$ and in principle, by increasing degree of hyperviscosity $d$ and by lowering diffusivities $D_n$ and $D_\Omega$ (and eventually refining computational grid), the effect of diffusive energy sink could be suppressed [24].

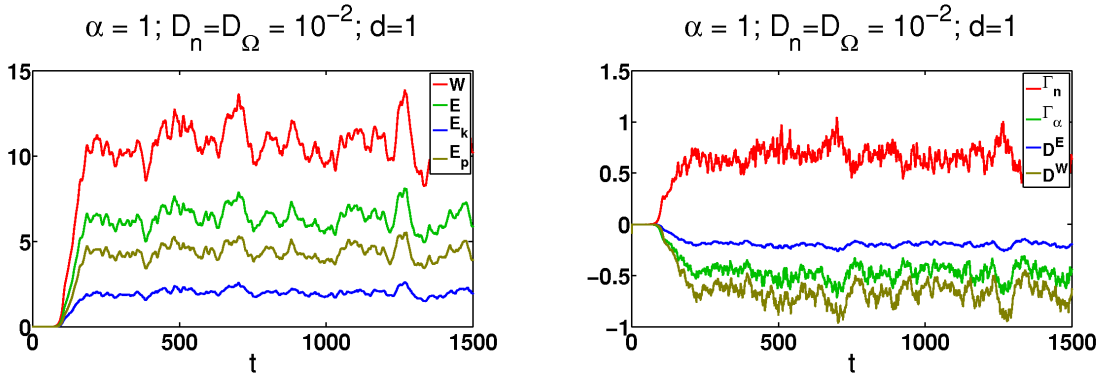


Figure 7.9: Time evolution of total energy and enstrophy (left) and corresponding fluxes and diffusive sinks (right) in the H-W model. Coupling parameter $\alpha = 1$ and order of diffusive terms $d = 1$.

### 7.6.3 Dimensionless parameter governing particle motion in the Hasegawa-Wakatani potential

In the following sections motion of individual particles in potential field of resistive drift waves given by solution of Hasegawa-Wakatani fluid equations (7.48)-(7.49) will be investigated. We will describe motion of the particles by equations of motion (7.25)-(7.28) derived in Sec. 7.3.

To express values of parameters $T$ and $R$ (Eqs. (7.33) and (7.34)) in terms of plasma parameters, we will substitute the normalization (7.47) of the H-W

[2] If $g(x)$ and $h(x)$ are $2\pi$-periodic integrable complex functions and $\tilde{g}_n, \tilde{h}_n$ coefficients of their Fourier series, then $\int_{-\pi}^{\pi} g(x)\overline{h(x)}\mathrm{d}x = 2\pi \sum_{n=-\infty}^{\infty} \tilde{g}_n \overline{\tilde{h}_n}$. Here the bar means complex conjugation.

equations. Then, one have

$$T = \frac{\omega_{c,imp}}{\omega_{ci}} \frac{L_n}{2\rho_s} = \frac{\omega_{c,imp}}{\omega_{ci}} \frac{L_n}{2} \frac{eB_0}{\sqrt{T_e m_i}} \sim \frac{q}{m} \tag{7.64}$$

$$R = \frac{2T_e}{eB_0 \rho_s^2 \omega_{ci}} = 2. \tag{7.65}$$

We remind that $L_n$ is a radial length-scale of background density, $\rho_s$ is hybrid gyroradius (5.7) of plasma ions, $T_e$ electron temperature, $B_0$ background magnetic field and $m_i$ mass of plasma ions. We further distinguish gyrofrequency of traced particles $\omega_{c,imp}$ from gyrofrequency of ion component of the plasma $\omega_{ci}$. As we can see, the parameter $R$ reduces to a constant and the whole dynamics is thus given by parameter $T$ which is combination of all plasma parameters and is proportional to charge/mass ratio of the traced particle. Indeed, the form of potential itself depends also on choice of adiabaticity parameter $\alpha$, which is the second parameter of the problem. In the following we will use $\alpha = 1$

In [122], a different form of the dimensionless parameter describing character of particle motion was used,

$$\xi = \frac{1}{2} \frac{1}{T} \sim m/q. \tag{7.66}$$

In order to be consistent with the cited work, we will mostly describe the type of traced particles using $\xi$ instead of $T$. The physical meaning of $\xi$ as a ratio of characteristic frequency of turbulent fluctuations to the particle's gyrofrequency can be seen from the definition of $T$ in Eq. (7.33). Particles with $\xi \ll 1$ (i.e. $\omega_{c,imp}^{-1} \ll t_0$) feel the potential as constant during one gyro-period while in the case $\xi \gg 1$ the potential is changing on faster scale than particles gyro-period. Another interpretation of $\xi$ arises when we combine (7.33), (7.34), (7.65) and (7.66) and get

$$\xi = \frac{\phi_0 m}{q B_0^2 x_0^2} \tag{7.67}$$

which agrees with the parameter $\alpha_B$ in (7.39) that describes particle untrapping due to Bellan instability.

For use in the following simulations it will be useful to evaluate reasonable values of the parameters $T$ and $\xi$. For values of radial background density length-scale in the tokamak edge region $L_n \approx 10^{-2} - 10^{-1}$ m, magnetic field $B_0 \approx 0.5 - 3$ T, electron temperature $T_e \approx 10 - 500$ eV [145] we get (for deuterium plasma) range of parameters $T \approx (1.5 - 66)\frac{q}{m}$. The dependence of $T$ on plasma parameters is shown in Fig. 7.10.

### 7.6.4 Inertial impurities, their clustering and radial pinch

In [122, 111] fluid model of passive transport of particles with finite mass (called inertial impurities) in H-W potential was developed and studied. Advection of impurity density $n_{imp}$ by two fluid drifts was considered - the dominant $E \times B$ drift $\vec{v}_E$ and polarization drift $\vec{v}_P$. Even though $\vec{v}_P$ is a second order drift, it was shown that its compressibility brings important effects that generate inward radial particle pinch.

The papers have shown that there is an approximate Lagrangian invariant

$$I_L = \ln n_{imp} - \xi\Omega \tag{7.68}$$

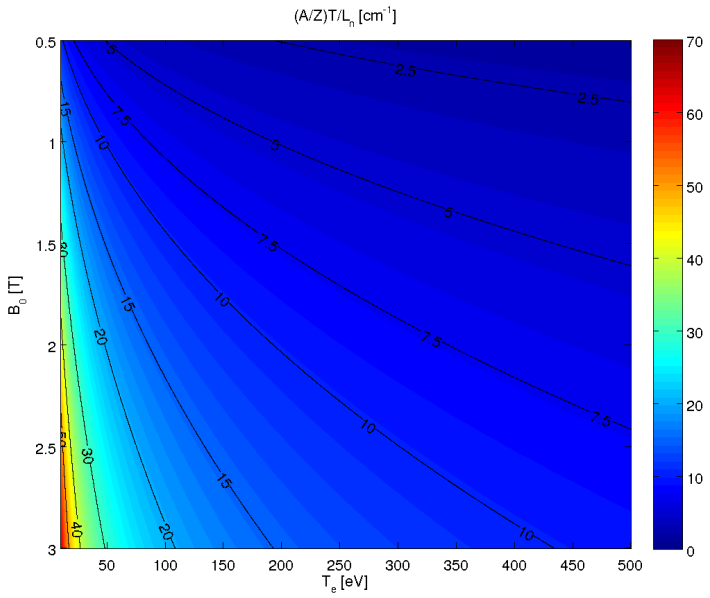


| $L_n$ [cm] | $B_0$ [T] | $T_e$ [eV] | $T_{H^+}$ - Eq. (7.64) | $\xi_{H^+}$ - Eq. (7.66) |
|---|---|---|---|---|
| 1 | 0.5 | 10 | 10.98 | $4.55 \times 10^{-2}$ |
| 1 | 0.5 | 500 | 1.55 | $3.22 \times 10^{-1}$ |
| 1 | 3 | 10 | 65.89 | $7.59 \times 10^{-3}$ |
| 1 | 3 | 500 | 9.32 | $5.37 \times 10^{-2}$ |

Figure 7.10: Values of parameter $T$ (for deuterium plasma) governing character of particle motion in Hasegawa-Wakatani potential and their dependence on plasma electron temperature $T_e$ and the strength of magnetic field $B_0$. In order to obtain value of $T$ for any specific case, the values in the figure need to be multiplied by $L_n$ (in centimetres) and by $A/Z$ ratio of the traced particle species. Several values of $T$ and $\xi$ evaluated for $H^+$ ions with $A = Z = 1$ are stated in the table.

that is approximately conserved during the $E \times B$ motion of inertial impurities. Here $\xi$ is a dimensionless parameter from Eq. (7.66) that parametrizes the dynamics. Due to turbulent mixing of particle trajectories the invariant becomes soon homogenized over the whole simulation, $I_L(x, y) = \text{const}$. When the impurity density is split into its mean and fluctuating part, $\langle n_{imp} \rangle$ and $\tilde{n}_{imp}$, respectively, and the logarithm is linearised, the conservation of the Lagrangian invariant shows that relative fluctuations of impurity density are correlated with local vorticity $\Omega$,

$$\frac{\tilde{n}_{imp}}{\langle n_{imp} \rangle} \approx 1 + \xi\Omega. \tag{7.69}$$

The positively charged particles are accumulated (clustered) in areas with positive vorticity (negative potential) and expelled from regions with negative vorticity (positive potential). We note that in the constant magnetic field that is considered in H-W model, the $E \times B$ drift is incompressible and the fluctuating part $\tilde{n}_{imp}$ arises solely from compressibility of the polarization drift, i.e. it is an effect of finite particle mass. Since $I_L$ is only approximate invariant (changed only by impurity advection by polarization drift and by collisional diffusion) and its spatial homogenization is dependent on turbulent mixing of particle trajectories, the relation

between $n_{imp}$ and $\Omega$ found in simulations in [122, 111] is not ideal,

$$\frac{\tilde{n}_{imp}}{\langle n_{imp}\rangle} = 1 + K\Omega \tag{7.70}$$

with $K = 0.82\xi$.

In the double periodic domain used in H-W model the total $E \times B$ drift is equal to zero. Therefore, if there would be no fluctuations of impurity density, the total $E \times B$ impurity flux would be zero as well. However, the compressibility of the impurity flow causes redistribution of $n_{imp}$ such that the total radial flux due to $E \times B$ drift becomes negative and the impurities experience net inward radial velocity (inward radial pinch)

$$\bar{v}_{imp,x} = \frac{\int n_{imp} v_{E,x} \mathrm{d}x\mathrm{d}y}{\int n_{imp} \mathrm{d}x\mathrm{d}y} \approx -0.09\xi. \tag{7.71}$$

The amplitude of the inward velocity grows with $\xi$ i.e., with particles' $m/q$ ratio. The fluid model, however, neglects Larmor radius, which may bring, especially for the case of large $m/q$ ratio, new effects competing with the inertial effects described. This topic will be investigated in the next section.

### 7.6.5 Effect of finite Larmor radius on the radial velocity pinch

The situation that will be modelled in this section is very similar to that examined in [122, 111] and discussed in Sec. 7.6.4. We use H-W model with $\alpha = 1, d = 1$ and $D_n = D_\omega = 10^{-2}$ and follow transport of particles with finite mass in the turbulent potential. In contrast to [122, 111] we do not neglect particle cyclotron gyration and follow full particle orbits described by Eqs. (7.25)-(7.28). We solve H-W equations for $512 \times 512$ dealiased Fourier modes and since particle trajectory is resolved on much finer spatial scale, the value of potential at particles' positions is obtained by Fourier interpolation. In order to model particle transport in test-particle approximation, we assume that both, particle density and density gradients, are much smaller than those of the main plasma so that the impurities do not enter the quasineutrality equation [111]. The same numerical scheme (fourth-order explicit Runge-Kutta) was used as for the particle tracing in experimentally measured potential in Sec. 7.5. The time step was chosen as either 1/1000 of particle cyclotron period or 1/10000 of characteristic time of turbulent fluctuations $t_0$, what was smaller. Again, all particles were initialized with zero initial velocity and gained energy from their interaction with the fluctuating turbulent potential. The particles were added into the H-W simulation after its initial phase when state of saturated turbulence was established.

First, we focus on the effect of impurity clustering in turbulent vortexes. Fig. 7.11(left) shows relative impurity density $(n_{imp}/\langle n_{imp}\rangle - 1)$ as a function of local turbulent vorticity for three different values of $\xi$. We can observe that the relationship is approximately linear, except the case $\xi \approx 0.1$ in which negative vortices (or positive potential hills) are less populated than predicted by linear relation (7.70). Nevertheless, the linear relation holds around $n_{imp}/\langle n_{imp}\rangle \approx 1$ for all cases and we estimate the regression coefficient $K$ in the region $0.75 < n_{imp}/\langle n_{imp}\rangle < 1.25$.

Dependence of $K$ on particle species expressed in terms of $\xi$ is shown in Fig. 7.11(right). Up to value $\xi = 0.1$ the estimated value of $K/\xi$ is constant, $K/\xi = 0.94$ and for higher $\xi$ it quickly drops. This value is closer to the ideal clustering described in Eq. (7.69) with $K = \xi$ than estimation made in [122, 111] for inertial impurities with neglected Larmor radius ($K = 0.82\xi$). We attribute this to the difference in particle collisions that change $I_L$ in time and that were taken into account in the cited works but not in our simulation. When $\xi \approx 0.1$, particles start to escape from positive potential structures (negative vortexes) due to Bellan instability described in Sec. 7.4, while their accumulation in potential valleys further grows. Therefore, for $0.1 < \xi < 0.5$ the correlation between impurity density and vorticity in Fig. 7.11(right) grows, but dependence of $K$ on $\xi$ is sublinear. When $\xi \approx 1$, particles start to escape from potential valleys and function $K(\xi)$ has a maximum at $\xi \approx 0.5$.

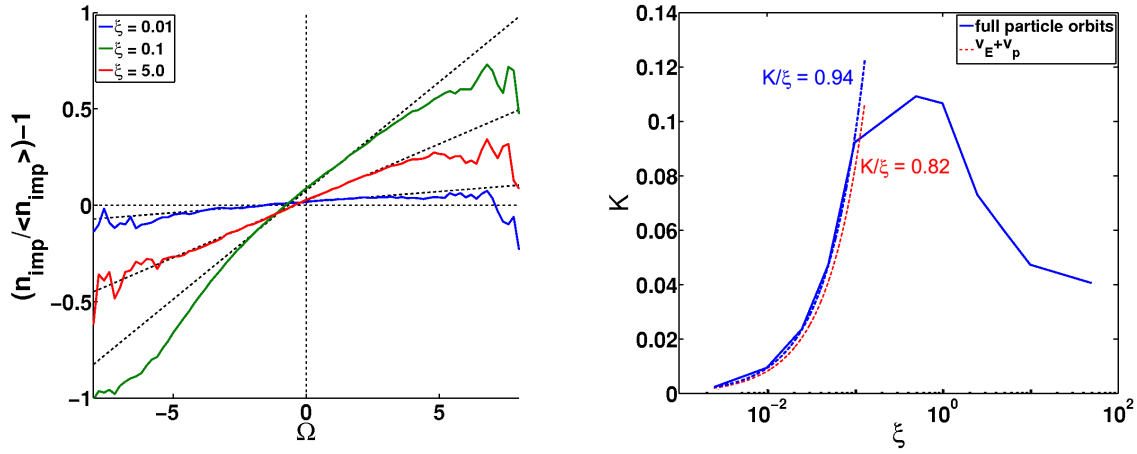


Figure 7.11: *Left:* Average value of relative particle density $(n_{imp}/\langle n_{imp}\rangle - 1)$ at place with local turbulent vorticity $\Omega$. Particle density is not readily available from the simulation and we compute it from average number of particles $N(\Omega)$ found at surroundings of turbulent vorticity $\Omega$. For better statistics, the relation was averaged over interval of length $50t_0$. The oscillations at the ends of lines are caused by poor vorticity statistics at these values. *Right:* Regression coefficient $K$ of the relation (7.70) as a function of $\xi$ (solid blue line). Linear relation $K = 0.94\xi$ is plotted as blue dashed line, $K = 0.82\xi$ as red dashed line.

The effect of particle trapping by potential structures is shown in Fig. 7.12 from two different points of view. Fig. 7.12(right) shows fraction of particles that are located in places with positive vorticity (or negative potential) as a function of $\xi$. For $\xi < 1$, accumulation of particles in positive vortexes (potential valleys) due to compressibility of $\vec{v}_P$ grows with $\xi$. However, the relative frequency of turbulent fluctuations increases with $\xi$ as well and it increases the probability that particles located at the edges of potential valley become untrapped. This balances the clustering effect at $\xi \approx 0.5 - 1$ and for $\xi > 1$ the effect of particle trapping by potential valleys weakens as the characteristic frequency of turbulent fluctuations rises over particles' gyrofrequency. Since all particles were initialized with zero velocity, the effect of finite Larmor radius can be seen also when time evolution of the regression coefficient $K$ is plotted (Fig. 7.12(left)). For $\xi = 0.01$, the effect of

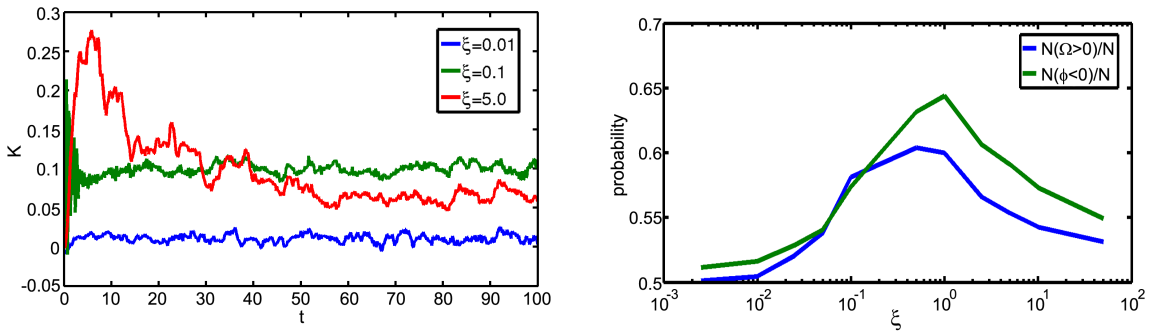


Figure 7.12: *Left:* Time evolution of the regression coefficient $K$ for three different values of $\xi$. *Right:* Fraction of particles found in the places with negative potential (green) and positive vorticity (blue).

Larmor radius is negligible and $K$ grows due to compressibility of $\vec{v}_P$ drift until it reaches its steady-state value. On the other hand, particles with $\xi = 5.0$ at first exhibit sharp increase of $K$. At this initial phase the particles remain cold with small Larmor radius and effect of the $\vec{v}_P$ compressibility dominates. During time the particles gain energy from turbulent fluctuations and as their Larmor radius grows, Bellan instability starts to release particles trapped in potential structures (preferentially from potential hills) which is reflected in a decrease of $K$. Saturated value of $K$ is then given by a balance between these two mechanisms.

Fig. 7.13 shows that for small values of $\xi$ the inward radial pinch, originally identified for inertial impurities in [122, 111], is present as well for particles with finite Larmor radius. In this regime the impurity density is redistributed such that regions with negative sign of radial part of $E \times B$ drift are more populated than the others. For $\xi > 0.01$ the inward radial velocity weakens and it changes its sign at $\xi = 0.1$. This reversal of radial velocity is qualitatively new behaviour brought by finite Larmor radius effects and therefore it could not be found in the fluid model of inertial impurities examined in [122, 111].

The net outward drift of heavier particles is connected with their unstable motion at potential hills. Due to asymmetric shape of the potential structures, the particles are released only at several spatially localized points and velocity of escaping particles is not isotropic, but it gains some preferential direction. First, we have tested whether the shape of turbulent structures present in H-W potential is favourable for the Bellan instability. An example of a structure frozen in time and motion of particles with four different values of $\xi$ is shown in Fig. 7.14. The typical threshold above which we found that particles on potential hills experience Bellan instability is in the range $\xi_{thr} \approx 0.05 - 0.1$, the actual number is, however, strongly dependent on shape of each individual potential structure. Nevertheless, the threshold is generally lower than the threshold found in the case of fully symmetric quadratic structures ($\xi_{thr,Bellan} \approx 0.31$ in [12]) and in case of nearly symmetric egg-crate potential ($\xi_{thr,egg} \approx 0.25$ in [89, 90]). The value $\xi_{thr}$ is well consistent with departure from ideal clustering ($K \approx \xi$) shown in Fig. 7.11(right). Figs. 7.14 and 7.15 demonstrate that particles escape from potential hills typically on their corners, in the places with high curvature of equipotentials. If the spatial region favourable for particle escape is narrow, only particles with certain phase of their

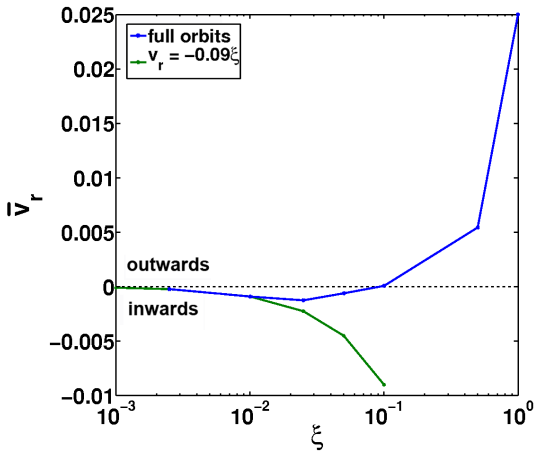


Figure 7.13: Dependence of net radial velocity of particles on $\xi$. The radial velocity was averaged over time interval of $50t_0$ to remove influence of turbulent potential oscillations. Dependence $\bar{v}_r = -0.09\xi$ found for inertial impurities neglecting Larmor radius [122] is plotted for comparison (green).

gyro-orbit can escape and particles gain a preferential sign of their velocity. From the point of view of stochastisation of phase space, this can be viewed as asymmetric stochastisation, where stochastic see of escaping particles is not symmetric in velocity component that represents the gyro-orbit. An example of Poincare's section of particle movement on potential hill in two different moments of its evolution is shown in Fig. 7.16. The left part of the figure shows asymmetrically stochastised phase space in which particle with negative sign of their radial velocity $v_r$ are trapped while those having positive sign of $v_r$ move in the stochastic see and are able to escape from the structure. Through this mechanism the potential hill quickly expels particles from half of its phase space. However, not all structures in all times generate such asymmetric stochastisation. Fig. 7.16(left) show the stochastisation of phase space of the same structure as shown in right, but in later time of its evolution. Here, the structure of phase space is almost symmetric with respect to $v_r$.

We have verified that even though the net radial velocity $\bar{v}_r$ fluctuates in time as the particles react on temporal changes of the potential, the mean value $\langle \bar{v}_r \rangle$ (averaged over several periods of the fluctuations) that was shown in Fig. 7.11(right) is stable in time.We note, that in the next step the model will be augmented by particle collisions in form of stochastic Langevin equation that may partially suppress the effect of the outward impurity outflux.

In this section we have evaluated limits of a model of inertial impurities [122] given by effects of finite Larmor radius (FLR). We have found that impurity clustering and net inward radial velocity of impurity particles predicted by the fluid model hold up to $\xi \approx 5 \times 10^{-2}$. For higher values of $\xi$ the FLR effects become important. In such case the phase space is stochastised and motion of particles on positive potential structures is unstable, generating reversal of sign of the net radial drift and at $\xi \approx 0.1$. The clustering of impurities inside turbulent vortex drops down for $\xi > 0.5$. In the future, further effects are expected to be brought into the model by including collisions with the main plasma and taking into account

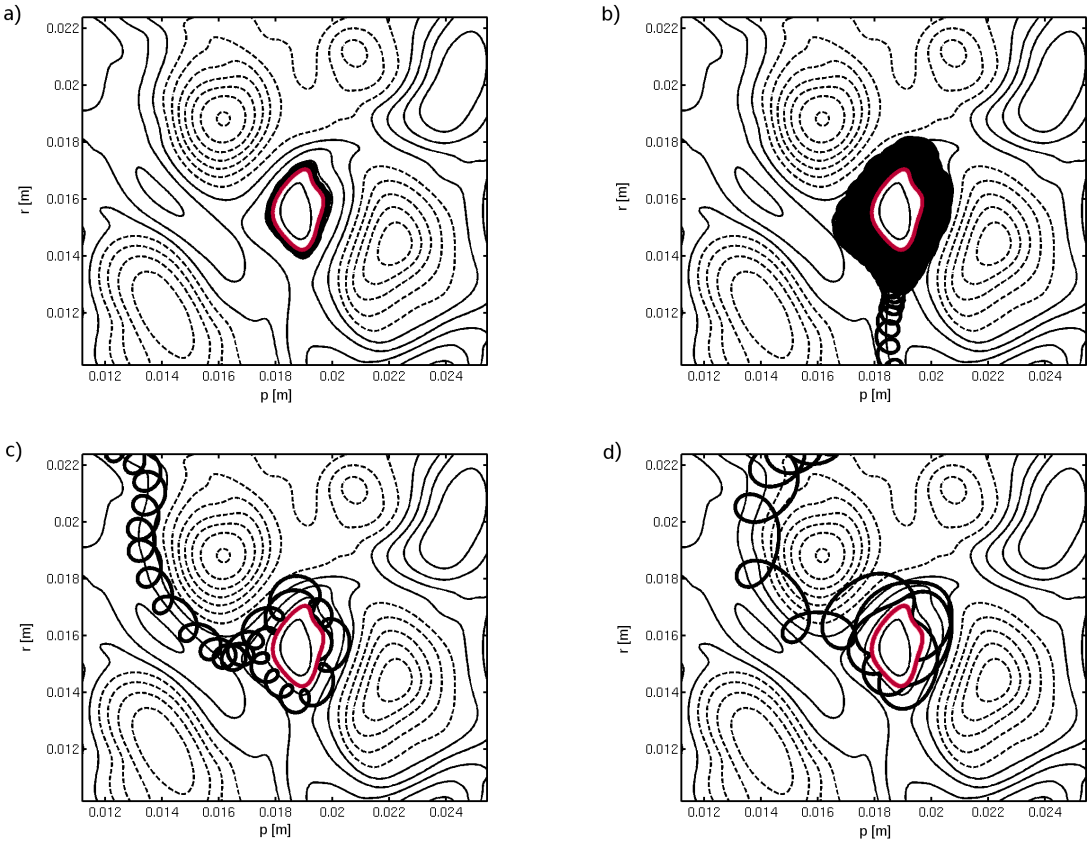


Figure 7.14: Trajectories of impurity particles (black bold solid lines) with identical starting positions and zero initial kinetic energy moving in frozen snapshot of H-W potential for different values of $\xi$ [91]. Positive equipotentials are plotted with thin solid line, the neagtive ones with dashed line. $\xi = 5{\cdot}10^{-2}$ (a), $\xi = 10^{-1}$ (b), $\xi = 1.5{\cdot}10^{-1}$ (c), $\xi = 3{\cdot}10^{-1}$ (d). With growing $\xi$, particles are repelled from the potential structure gaining energy. Due to asymmetry of turbulent structures the escape direction is not isotropic. Motion of ideal massless particle described by $E \times B$ drift is plotted in red.

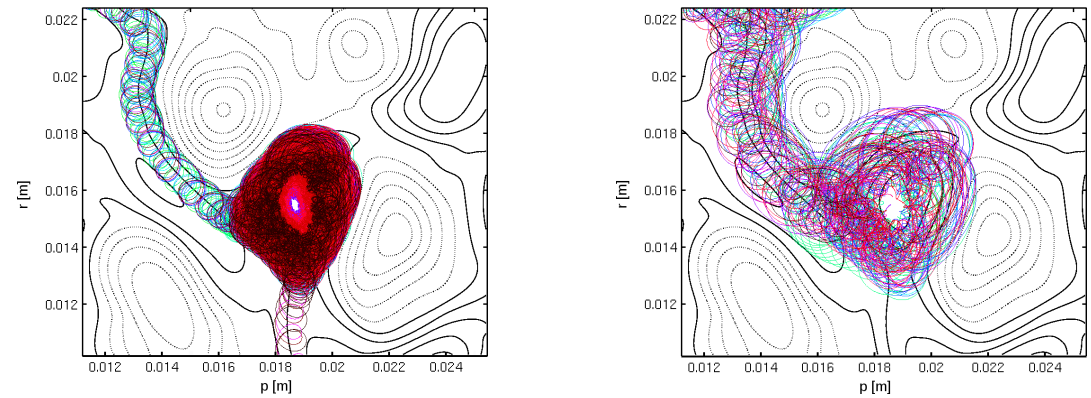


Figure 7.15: Trajectories of 30 particles (each color represents one trajectory) moving in frozen snapshot of H-W potential. All particles were initialized with zero kinetic energy, randomly distributed on a potential hill from Fig. 7.14. Two different values of $\xi$ vere used: $\xi = 1.5 \times 10^{-1}$ (left) and $\xi = 3 \cdot 10^{-1}$ (right).

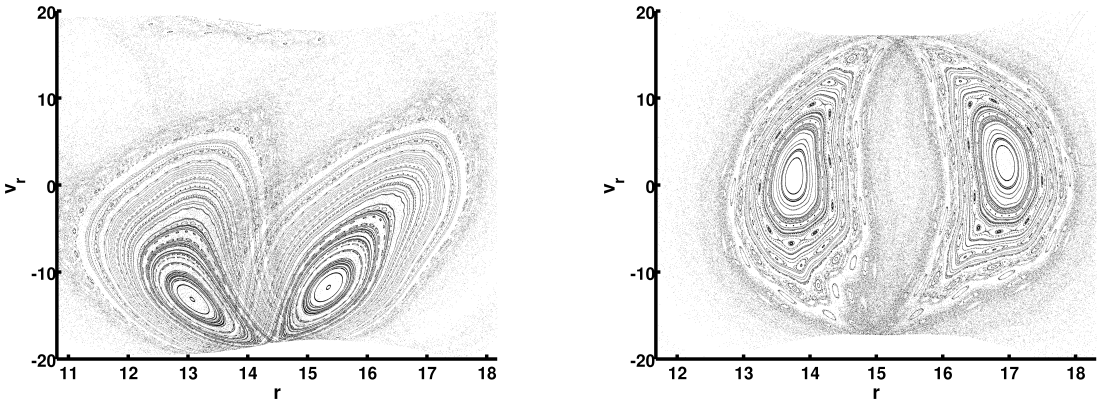


Figure 7.16: Poincare's sections of particle motion on positive potential structure in two different times of its evolution separated by $\Delta t = 0.75$. Particles with $\xi = 0.1$ and the same total energy $H = 40$ were tracked. During generation of the Poincare's section the structure was frozen in time. Spatial asymmetry of the structure may result in asymmetric stochastisation of the phase space (top). Plotted quantities are in dimensionless units with normalization (7.47).

inhomogeneous magnetic field. The latter will, however, require modification of the underlying turbulent model, because currently used H-W model assumes magnetic field homogeneity.

## 7.7 Particle motion in structures of interchange turbulence

The Hasegawa-Wakatani model of drift-wave turbulence presented in Sec. 7.6.1 is relevant mainly in the inner vicinity of LCFS where closed magnetic field lines allow presence of nonzero $k_\parallel$. According to recent understanding of tokamak edge turbulence [88, 31], in the SOL the turbulence should be dominated by interchange modes. In this section we will present two initial considerations about impurity behaviour in the interchange convective structures modelled by ESEL model (see Sec. 5.1).

### 7.7.1 Generation of asymmetric impurity flux by interaction with interchange structures

First, we have used our previous ESEL simulation #116 and used the blob-tracking algorithm to detect all turbulent structures with density fluctuation $\tilde{n}/\langle n \rangle > \sigma_n$. Then, by detecting amplitudes of positive and negative potential parts of each blob and their mutual distance, it was possible to estimate value of parameter $R \equiv \alpha_B$ according to (7.39). Radial profile of its mean and maximum value evaluated from the set of all blobs appearing in simulation is shown in Fig.7.17. In the SOL, mean value of $R$ occurs in a close vicinity of stochasticity threshold for $C^+$, while its maximum value can be almost 10 times higher. This indicates that not all blobs are capable of exhibiting Bellan instability, but on the other hand there exists

a group of blobs that are capable of destabilizing motion even of very light or multiply charged particles.

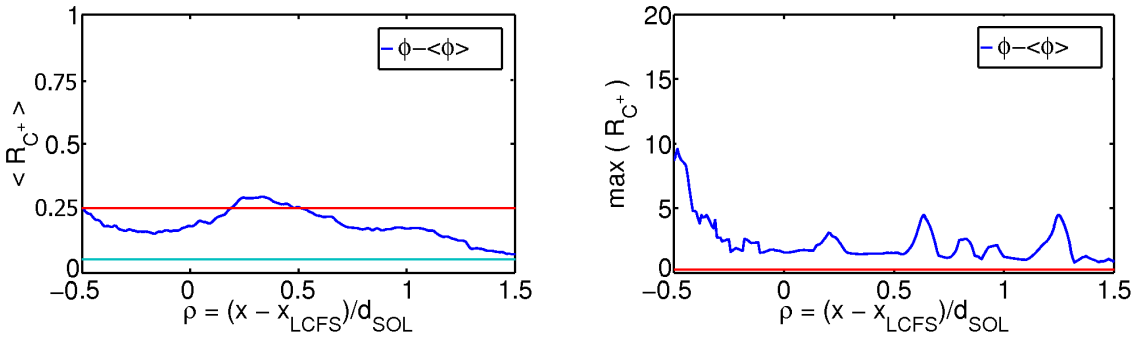


Figure 7.17: Mean (left) and maximum (right) value of stochasticity parameter $R$ estimated from properties of potential turbulent structures in ESEL simulation (blue curve). Red line marks stochasticity threshold for $C^+$ ions, cyan line for $Fe^+$.

It is necessary to note that such estimation of $R$ is limited by the fact that the stochasticity threshold was derived assuming symmetric shape of potential with leading quadratic term and slow motion of potential structures. These assumptions may be violated in the turbulent potential and the stochasticity threshold may be lower, similarly as was observed for particle motion in H-W potential in Sec. 7.6.5.

ESEL model shows that interchange structures are rare in the sense that in one time there are typically only one or two structures present in the SOL, surrounded by background plasma (see e.g. Fig. 5.6.) Such situation could be well described by egg-crate potential (7.36), but restricted to only one bipolar structure corresponding to a single blob bounded by separatrix $\phi = 1$. Such structure is divided into two parts, potential hill and valley, with significantly different type of motion. While the positive part can release and accelerate particles whenever the stochasticity threshold is reached, the negative part will some of them temporarily trap back. In a result, the potential valley can effectively screen out outflow of particles from the hill and total particle flux caused by Bellan instability will be predominantly heading in the opposite direction, away from the valley. Therefore, if the blob axes are aligned with radial and poloidal axes, the largest flux is in the poloidal direction. However, as can be seen in Fig. 7.18(left) taken from ESEL simulation, blobs in SOL are usually tilted due to shear of poloidal velocities, which rotates also the direction of maximum particle outflow to head more into inside. Therefore, this mechanism may enhance impurity transport from the wall region into the main plasma [133], causing negative effects such as diluting fuel or cooling the plasma down.

The situation is schematically depicted in Fig. 7.18 and the dependence of asymmetry strength on scaling of parameter $R$ and particle kinetic energy $E_k$ is shown in Fig.7.19. For particles with low initial energy and low value of $R$, the asymmetry between number of particles escaping through parts of separatrix labelled in Fig. 7.18 as 1 and 2 and those labelled as 3 and 4 can go up to $N_{1+2}/N_{3+4} \approx 3$. The asymmetry of particle outflux drops down with growing $R$ and $E_k$, because high-energy particles more-likely avoid being trapped when passing through the potential valley. These results indicate that the proposed mechanism of generation

of asymmetric impurity flows in SOL by interchange structures may be realistic and simulation with full time evolving potential generated by ESEL model is planned.

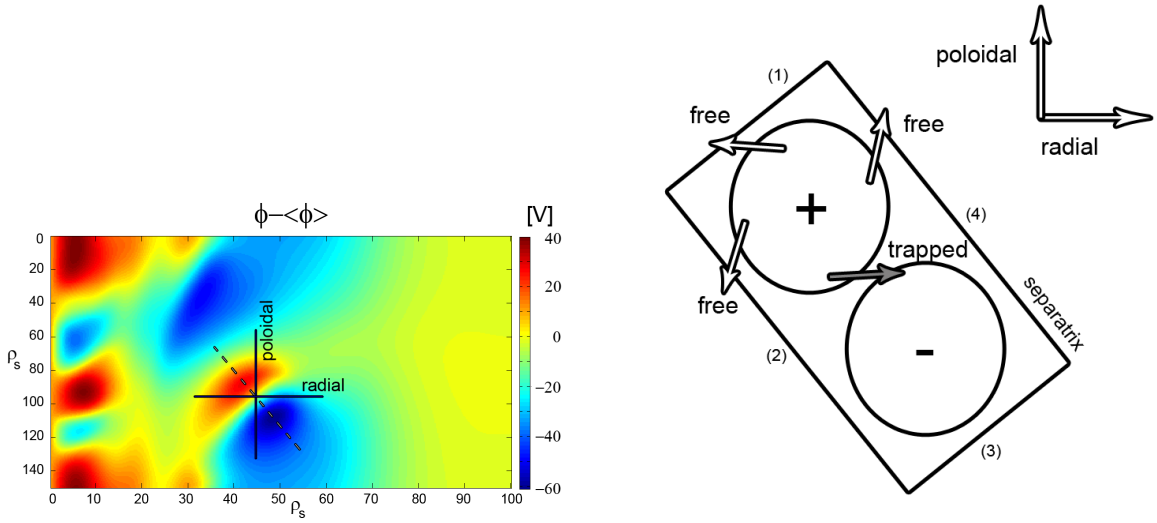


Figure 7.18: Snapshot of turbulent potential from the ESEL model (left part) showing that typical blobs in SOL are tilted, which leads to asymmetric outflow of particles due to Bellan instability (schematic picture on the right). Dashed line connects local minimum and maximum of blob's potential. [133]

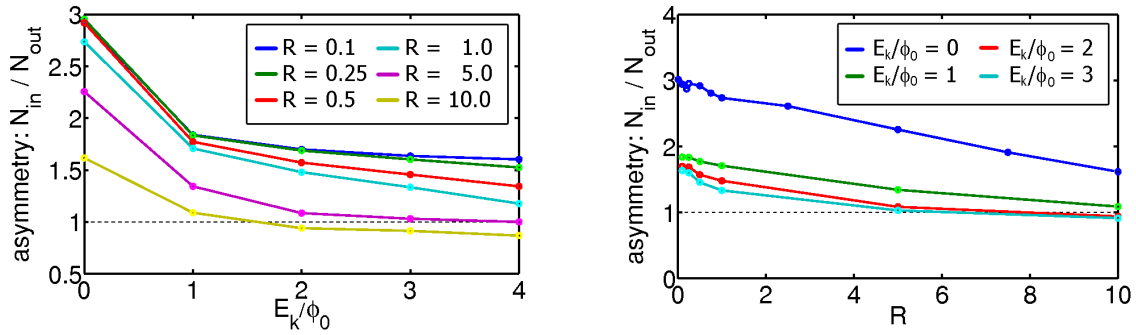


Figure 7.19: Asymmetry of particle outflow from a single blob structure. Harmonic potential profile (7.36) is assumed. $N_{in}$ is number of particles arriving at 1st and 2nd part of potential separatrix (see Fig. 7.18) and $N_{out}$ is number of particles reaching 3rd and 4th part of potential separatrix. Initial positions of particles in blob are distributed randomly with given kinetic energy $E_k$. [133]

### 7.7.2 Transport of particles by a single moving interchange structure

As a next step, we have used ESEL model to generate single radially moving interchange structure. We used so called seeded-blob approach and imposed small Gaussian perturbation on exponentially decaying pressure profile. Parallel plasma

losses have been neglected in this simulation. The time evolution of the generated structure is plotted in Fig. 7.20.

To investigate the difference between drift approximation and full particle motion we use the time evolution of blob shown in Fig. 7.20 as a background potential for tracing of $C^+$ ions. Assuming that $n_{C^+} \ll n$ and also $n_{C^+} \ll \tilde{n}$ we assume that impurities do not enter into quasineutrality condition and we neglect their influence on the turbulence itself and treat them as test particles. For the simplicity we also use constant magnetic field $B = 1$ T. At the beginning all particles were distributed randomly in space with initial energy 100 eV. The simulation was made for three different approximations of particle motion - massless particles advected by $\vec{v}_E$ only, particles advected by combination of $E \times B$ and polarization drift, $\vec{v}_E + \vec{v}_P$, and particles with full orbits governed by 2D Hamiltonian equations of motion (7.25)-(7.28).

Fig. 7.21 shows that the density significantly differs for all three cases. The density of particles moving only with $\vec{v}_E$ remains almost homogeneous (Fig. 7.21a). In other words, $E \times B$ drift motion is incompressible under these conditions ($B$ =const.). Nevertheless, mixing of the particles can be observed (see Fig. 7.23). Taking into account also polarization drift $\vec{v}_P$, the generic effect of flow compressibility in turbulent vortexes discussed in Sec. 7.6.4 takes place and particles are concentrated in the potential valley while repelled from potential hill (Fig. 7.21b). In the case of Hamiltonian particles this effect is even stronger because they feel in addition also the Bellan instability given by their finite Larmor radius and consequently they escape the potential hill much faster and become concentrated in the valley. Also particle mixing is larger than in the both drift cases, as can be seen in Fig. 7.23.

The results of our simulation provide somewhat unusual picture of particle transport in SOL. In contrast to fluid simulations of the plasma, where the positive density perturbation is covering symmetrically both lobes of the blob (see Fig. 7.20), the finite Larmor radius effects of particles with higher $m/q$ ratio together with polarization effects cause the impurity density distribution to by asymmetric, correlated with the plasma vorticity [134]. If we would take into account particle drifts $\vec{v}_E$ and $\vec{v}_P$ only, as is often done, the fluctuation of impurity density would be localized in smaller region and its amplitude underestimated in the negative part and overestimated in the positive one. This will overestimate local radial particle flux in the central region of the blob as shown in Fig. 7.22. On the other hand, in the SOL region where strong radial gradients of all quantities are typically present, the lower rate of mixing (Fig. 7.23) will result in underestimated radial transport of these gradients.

During our computation we have assumed that concentration of impurities is low and therefore they do not enter quasineutrality condition. However, this assumption may not be always fulfilled in tokamak plasmas. In such case the correlation of impurity concentration with plasma vorticity will lead to generation of inhomogeneous electric field capable of changing dynamics of the background turbulence. Since vorticity of the plasma flow is related to the electric potential, inhomogeneity of impurity density will affect rotation of the lobes of the blob and this may be transfered through Reynolds stress to poloidal plasma flows. These effects, however, need to be evaluated with self-consistent electric field influenced by both, the bulk plasma as well as impurities.

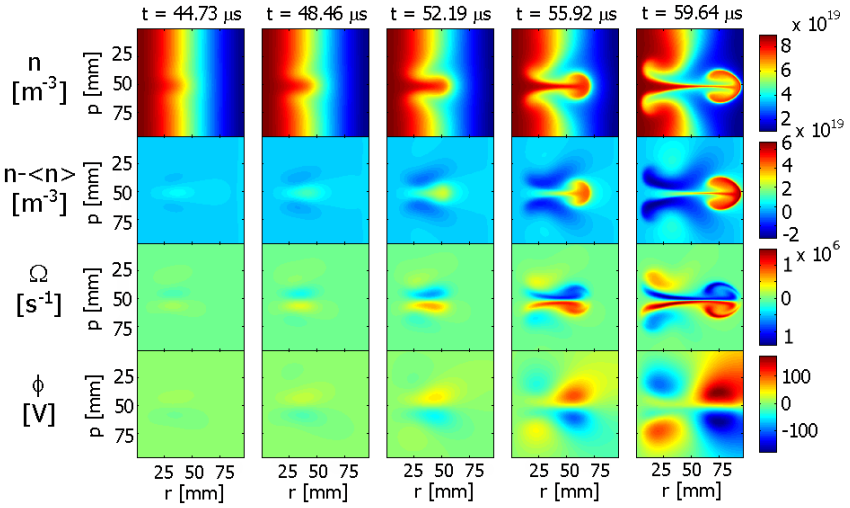


Figure 7.20: Isolated structure produced by interchange instability in ESEL model from small Gaussian perturbation imposed on exponentially decreasing pressure equilibrium p(r). The structure is accelerated by electric drift resulting from its bipolar nature. Two holes protruding into high density areas can be clearly seen.

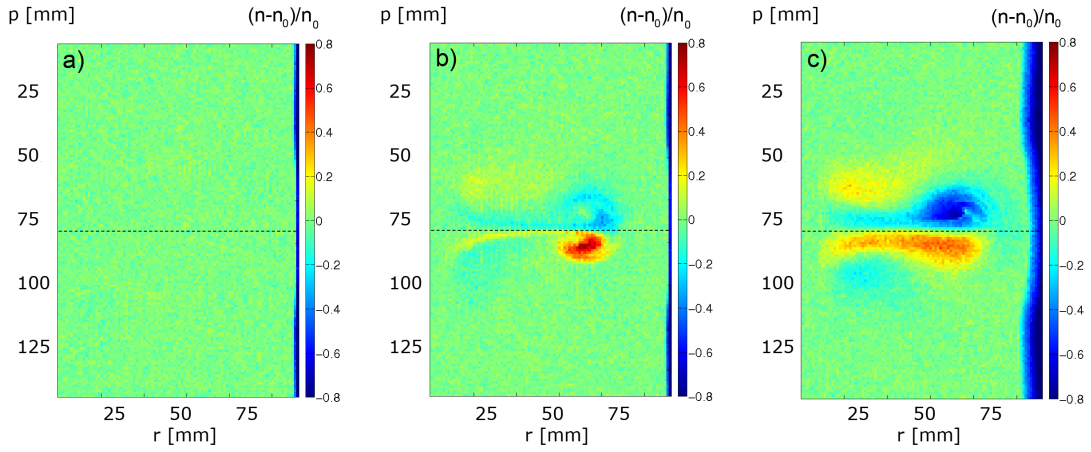


Figure 7.21: Relative fluctuation of particle density at t = 57.8 $\mu$s during transit of fast blob from Fig. 7.20 through spatially homogeneous cloud of $C^+$ ions with energy 100 eV. The density is homogeneous for particles advected by $E \times B$ drift only (left). Compressibility of polarization drift gives rise to density perturbation (middle) correlated with the plasma vorticity (see Fig. 7.20) with maximum $\max(\tilde{n}/n_0)_{drift} = 0.64$ and minimum $\max(\tilde{n}/n_0)_{drift} = -0.46$. Full tracking of particle orbits (right) shows even larger perturbation due to Bellan instability with $\max(\tilde{n}/n_0)_{full} = 0.55$ and $\max(\tilde{n}/n_0)_{full} = -0.75$. [134]

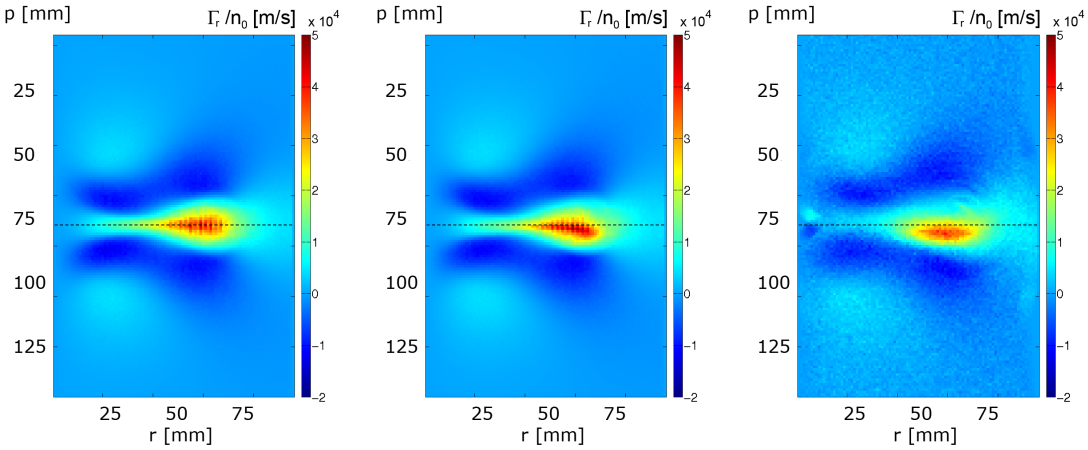


Figure 7.22: Radial part of instantaneous impurity flux $\Gamma_r$ at t = 57.8 $\mu$s normalized to initial density of particles $n_0$ for particles advected by $E \times B$ drift (left), $E \times B$ and polarization drift (middle) for particles with fully resolved cyclotron orbits (right). [134]

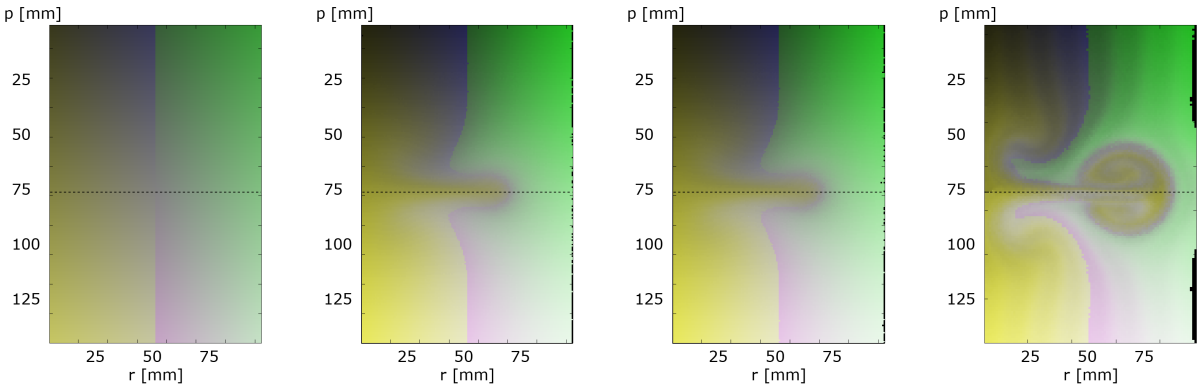


Figure 7.23: Mixing of $C^+$ tracers after 57.8 $\mu$s of blob evolution. Initial particle positions are marked by different colors (left). Particles moving by $E \times B$ drift (middle left) and by $E \times B$ and polarization drift (middle right) exhibit lower mixing (and smaller radial transport) than particles with their cyclotron orbits fully resolved (right). [134]

# Summary

Numerical turbulence modelling is an important part of efforts devoted to understanding of transport processes in tokamak edge region. On one side it allows investigation of non-linear models, providing results hardly reachable by purely analytical treatment, on the other side their comparison with experimental measurements is mutually beneficial. Experiment can serve as a rule of thumb for various approximations made during derivation of analytical models, while at the same time results of numerical models can provide interpretation of experimental observations.

In the frame of this thesis we have touched plasma turbulence in tokamak edge from three different points of view. In the first part, we have adopted and further developed fluid code ESEL, generously provided to us by researchers from Danish Technical University (DTU). The code allows modelling of turbulence driven by interchange instability that is considered main source of enhanced transport through tokamak scrape-off layer region. Parallelisation of the code allowed significant reduction of its running time, which could otherwise pose an issue in modelling of low collisionality conditions that require very fine spatial and temporal resolution of the simulations. Developed blob tracking algorithm allows characterisation of properties of turbulent structures in environment of fully developed turbulence in the SOL. Testing of the results by comparison with experimental measurements with Langmuir probes or gas puff imaging on tokamak COMPASS is envisaged and expected to provide feedback on assumptions of the model.

Character of parallel electric currents generated by bipolar nature of the blobs has been identified as a key factor influencing fluctuation statics in the scrap-off layer. The modelling of scrape-off layer plasmas in tokamak TCV was performed and mechanism of generation of parallel electric currents by field line bending by moving blobs was ruled out for these conditions. The drain of plasma vorticity by emitted Alfvén waves appears to be too strong, inhibiting poloidal flows and limiting blob motion through the SOL. On the other hand, assumption on presence of sheath dissipation, even in highly collisional plasmas, gives very promising results. In this regime, a new free parameter appears in the ESEL model which allows evaluation of influence of radial electric field around last closed flux surface on density fluctuation statistics observed in the SOL. With increasing radial electric field around LCFS the profiles steepen in a way that is consistent with experimental measurements, however agreement in density fluctuations worsens compared to the regime of subsonic vorticity advection. In order to unify both regimes, we propose a model in which response of sheath dissipation is delayed behind potential perturbations carried by blobs due to finite time necessary for the information to travel from the outer midplane to the divertor targets. In cooperation with researchers from DTU, corresponding terms are currently being implemented and tested in the ESEL code. Moreover, analysis of experimental data of electron temperature and plasma potential fluctuations measured on ASDEX Upgrade has started, with preliminary results confirming effects of the sheath-dissipative coupling of plasma potential and electron temperature. Detailed analysis of its impact, however, has yet to be assessed.

ESEL is 2D model with plasma transport along field lines simplified to sim-

ple analytical expressions. This may introduce significant error in estimation of parallel plasma losses. Comparison of the analytical model of parallel losses with predictions of code SOLF1D shows that density losses may be underestimated by an order of magnitude, while temperature losses are on average of the correct order. Based on this results, coupling of ESEL with 1D fluid code SOLF1D has been performed and tested. First physical results are expected soon. Moreover, enhancement of SOLF1D with full form of generalized Ohm's law is planned, which would make a large contribution to resolving the question on nature of parallel currents generated by turbulent structures.

In the second part, we have used fluctuation statistics modelled by the ESEL code to interpret several experimental results obtained by electrostatic probes in the SOL. In the wall shadow region on ASDEX Upgrade two different e-folding lengths of mean temperature profile has been measured simultaneously by swept Langmuir probe and by technique based on combination of floating Langmuir and ball-pen probes. We show that e-folding length measured by the latter is consistent with our turbulence modelling and provide physical arguments to explain steeping of the temperature profile in this region as a result of shortening of connection length from midplane to the nearest material surface. Moreover, we explain presence of a 'bump' in power spectra of plasma potential measured by the ball-pen probe as a result of appearance of blobs with some characteristic size and velocity. This confirms capability of the ball-pen probe to measure fast fluctuations of plasma potential in the range around $10^5$ Hz that is crucial for investigation of properties of turbulent structures in the SOL. We also show that power spectra of floating potential are dominated by fluctuations of electron temperature and not fluctuations of plasma potential, as could be expected.

On COMPASS, a probe head called U-probe is currently being installed. The U-probe is mounted with such combination of Langmuir probes that should evaluate plasma vorticity from simultaneous spatially separated measurement of floating potential. Based on the results of our simulations we document that interpretation of such measurement in the presence of interchange turbulence is ambiguous, distorted by possibly large fluctuations of temperature part of the floating potential.

As a last result of the second section we interpret divergence of cross-correlation of density signal measured by two spatially separated Langmuir probes inside velocity shear layer in the vicinity of last closed flux surface on tokamak CASTOR. We show that this divergence appears in the region where poloidal plasma velocity is comparable or smaller than radial velocity of the structures and we derive a formula for estimation of poloidal velocity from the cross-correlation even in this region.

In the last, third, section we handle the topic of transport of plasma impurities by their interaction with turbulent structures of the main plasma. It is convenient to describe this problem as a movement of test particles in background turbulent potential. This allows, compared to the common approach of tracking particle gyrocenters, to include important effects of finite size of Larmor radius. As a result, we find significant differences in transport of typical tokamak plasma impurities (such as $C^+$ ions) when the size of Larmor radius is/is not taken into account and we stress out that transport of heavier/less charged particles in the edge cannot be correctly evaluated by the drift approximation. The results show that character of particle transport changes with mass-to-charge ratio $m/q$ of the particle. The

particle tracing in experimentally measured potential allowed estimation of basic character of the transport in realistic shape of the potential, with limitation given mainly by short-term appearance of poloidally rotating turbulent structures in the field of view of the probe array. The study reveals that impurity particles with large $m/q$ that are generated by plasma-wall interaction will penetrate into the plasma easier than those with small $m/q$, since their Larmor radius is able to 'bridge' equipotentials in radial direction and limit the effect of particle trapping in poloidally moving potential structures. Then, with ionisation of the impurities increasing with the time spent in the plasma, the effect of radial diffusion will become suppressed.

Taking into account particle mass through polarization drift, the drift approximation predicts inward particle pinch of impurities moving in potential field of drift waves described by Hasegawa-Wakatani model. Strength of the pinch grows with the $m/q$ ratio. We have investigated limits of this mechanism and found threshold, described by dimensionless parameter $\xi$ (7.66), after which the direction of the pinch is reversed and particles are expelled radially outwards. Further simulations are being prepared to include effects of particle collisions and, if possible, also of inhomogeneous magnetic field.

Concluding the third section, several anomalous effects given by finite Larmor radius of the particles were found, especially enhanced particle diffusion in poloidal direction, reversal of direction of net radial particle flux in potential of drift waves from inward (particles with small $m/q$ ratio) to outward (particles with large $m/q$ ratio) or mechanism for generation of asymmetric impurity flux by bipolar interchange structures. In all three studied cases the comparison of transport in drift approximation and transport of particles with fully resolved cyclotron orbits shows significant differences for parameters of typical impurities.

Research made in the frame of this thesis was published as a part of papers in impacted scientific journals [132, 22, 2, 74, 65, 66], a book chapter [91], conference proceedings [133, 1, 37, 38, 134, 112, 84, 102] and it was presented on several other conferences that do not publish proceedings. Two papers covering results on influence of sheath dissipation term on interchange turbulence [115] and transport of heavy particles in Hasegawa-Wakatani potential [135] are currently in preparation.

# Appendix A

## Blob speed and size estimation from three-point probe measurements

Here we will derive equations for determination of speed and size of turbulent structures from time trace of three Langmuir probes. We will assume that the probes are in ion saturation mode and that typical waveform of blobs and holes can be in poloidal plane described as 2D Gaussian

$$I_{sat}(x,y) = I_{sat,0} e^{-\frac{r^2}{dr^2} - \frac{p^2}{dp^2}} \tag{7.72}$$

where $dr$ and $dp$ are radial and poloidal size, respectively, and amplitude of the structure $I_{sat,0}$ is positive for blobs and negative for holes. This may be understood either as a waveform of individual or an average structure.

Geometry of the problem is illustrated in fig. 7.24, where $x-y$ coordinates are aligned with axis of the structure, the structure is tilted with respect to the direction of its movement by angle $\pi - \alpha$ and the angle between its velocity and poloidal axis is $\epsilon$. The trajectory of the probe in the reference frame of the blob is then

$$x_T(t) = x_d + v_x t = \quad d\sin(\alpha) + v\cos(\alpha)t, \tag{7.73}$$
$$y_T(t) = y_d + v_y t = - \quad d\cos(\alpha) + v\sin(\alpha)t. \tag{7.74}$$

This gives signal on the triggering probe generated by the structure (7.72)

$$I_{sat,T}(t) = I_{sat,0} e^{-\frac{(d\sin(\alpha)+vt\cos(\alpha))^2}{dr^2} - \frac{(-d\cos(\alpha)+vt\sin(\alpha))^2}{dp^2}}. \tag{7.75}$$

Maximum of the triggering signal

$$I_{sat,T,max} = I_{sat,0} e^{-\frac{d^2}{\cos^2(\alpha)dy^2 + \sin^2(\alpha)dx^2}} \tag{7.76}$$

is found at time

$$t_{max} = \frac{d}{v}\frac{\sin(\alpha)\cos(\alpha)(dx^2 - dy^2)}{\cos^2(\alpha)dy^2 + \sin^2(\alpha)dx^2} = \frac{d}{v}\tau. \tag{7.77}$$

It is convinient to shift time origin by $t_{max}$, $t' = t - t_{max}$, to have maximum signal on the trigger at $t' = 0$,

$$I_{sat,T}(t') = I_{sat,0} e^{-\frac{(d\sin(\alpha)+(vt'+d\tau)\cos(\alpha))^2}{dr^2} - \frac{(-d\cos(\alpha)+(vt'+d\tau)\sin(\alpha))^2}{dp^2}}. \tag{7.78}$$

Position of the secondary probe is related to the postion of the trigering probe as

$$x_S(t') = x_T(t') + r\cos(\alpha+\beta-\epsilon) = x_T(t') + r\cos(\alpha+\delta) \tag{7.79}$$
$$y_S(t') = y_T(t') + r\sin(\alpha+\beta-\epsilon) = y_T(t') + r\sin(\alpha+\delta) \tag{7.80}$$

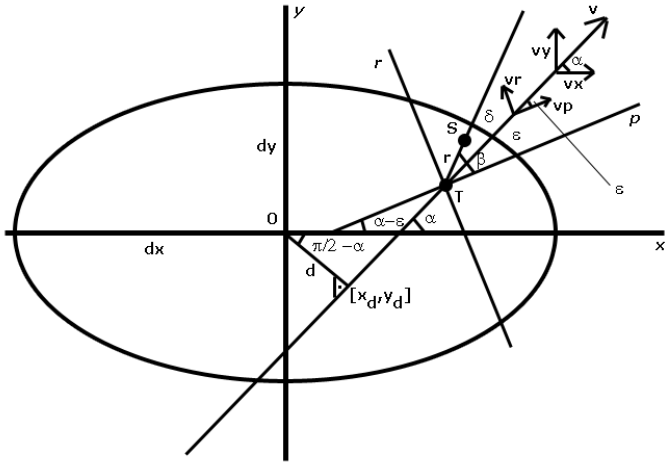


Figure 7.24: Geometry of Gaussian turbulent structure passing over pair of Langmuir probes - triggering probe $T$ and secondary probe $S$ in coordinates $x, y$ alligned with structure axis. $d$ is distance of center of the structure from triggering probe, $\pi - \alpha$ is tilt of the blob with respect to the direction of its velocity $v$ and $\epsilon = \tan(v_r/v_p)$ is angle between $v$ and poloidal direction $p$. Probes are located in mutual distance $r$ in angle $\beta = \epsilon + \delta$ from the poloidal axis and $\delta$ from the direction of $v$, respectively. $dx$ and $dy$ are dimensions of the structure.

which gives signal of the probe $S$

$$I_{sat,S}(t') = I_{sat,0} e^{-\frac{(d\sin(\alpha)+(vt'+d\tau)\cos(\alpha)+r\cos(\alpha+\delta))^2}{dr^2} - \frac{(-d\cos(\alpha)+(vt'+d\tau)\sin(\alpha)+r\sin(\alpha+\delta))^2}{dp^2}}. \quad (7.81)$$

## Conditional average

In conditional average, only blobs with maximum of the signal larger then some threshold, $I_{sat,T,max} \leq I_{thr}$ are considered. We find the range of $d$ in which the condition is fullfiled:

$$|d_{thr}| \leq \sqrt{-\ln\left(\frac{I_{thr}}{I_{sat,0}}\right)(\cos^2(\alpha)dy^2 + \sin^2(\alpha)dx^2)}. \quad (7.82)$$

Each structure will pass the probes in different distance $d$. We will therefore consider $d$ as uniformly distributed and conditionally averaged signal will be given by integration of (7.78) or (7.81), respectively, over the distance $d$ in the limits given by (7.82) normalized to the number of blobs given by length of the interval of $d_{thr}$

$$I_{sat,CA}(t') = \frac{1}{d_{thr,+} - d_{thr,-}} \int_{d_{thr,-}}^{d_{thr,+}} I_{sat}(t', d)\mathrm{d}d. \quad (7.83)$$

It is

$$I_{sat,CA,T}(t') = \frac{I_{sat,0}\sqrt{\pi}}{2}\frac{\mathrm{erf}\,(L)}{L}e^{-\frac{v^2t'^2}{dx^2dy^2}\Delta^2}, \tag{7.84}$$

$$\Delta^2 = dy^2\cos^2\alpha + dx^2\sin^2\alpha, \tag{7.85}$$

$$L = \sqrt{\ln\left(\frac{I_{sat,0}}{I_{thr}}\right)}, \tag{7.86}$$

for the triggering probe and

$$I_{sat,CA,S}(t') = \frac{I_{sat,0}\sqrt{\pi}}{4L}e^{-\frac{v^2\Delta^2(t'-t'_{max,S})^2}{dx^2dy^2}} \times \tag{7.87}$$

$$\times\left(\mathrm{erf}\left(\frac{r}{\Delta}\sin(\delta)+L\right)-\mathrm{erf}\left(\frac{r}{\Delta}\sin(\delta)-L\right)\right) \tag{7.88}$$

for the secondary probe. If the secondary probes are close enough to the triger compared to the size of the structure, $\sin(\delta)r/\Delta \ll 1$, factor in (7.87) simplifies, because

$$\frac{1}{2}\left(\mathrm{erf}(\frac{r}{\Delta}\sin(\delta)+x)-\mathrm{erf}(\frac{r}{\Delta}\sin(\delta)-x)\right)\approx\mathrm{erf}(x)+(O)((r/\Delta\sin(\delta))^2). \tag{7.89}$$

and ratio of signals on seconary and triggering probe in $t'=0$ is

$$\frac{I_{sat,CA,S}}{I_{sat,CA,T}}(t'=0) = e^{-\frac{v^2\Delta^2t'^2_{max,S}}{dx^2dy^2}}. \tag{7.90}$$

Maximum of $I_{sat,CA,S}$ is found at time

$$t'_{max,S} = -\frac{r}{v\Delta^2}(dy^2\cos(\alpha)\cos(\alpha+\delta)+dx^2\sin(\alpha)\sin(\alpha+\delta)). \tag{7.91}$$

### Radially and poloidally aligned probes

Here we will simplify the situation for the case of two secondary probes, one placed poloidally and one radially from the triggering probe. Such probe layout was used e.g. for reciprocating probe measurements on TCV [72]. This layout is described by relations

$$\beta_{Sp} = 0 \tag{7.92}$$

$$\beta_{Sr} = \frac{\pi}{2} \tag{7.93}$$

where subscripts $Sp$ and $Sr$ denote secondary probes placed poloidally and radially from the trigering probe. In the following, $r_r$ and $r_p$ will denote distance of $Sr$ and $Sp$ probe, respectively, from the trigger and angle $-\xi = \epsilon - \alpha$ is tilt of the structure with respect to $r-p$ axes.

Time lag $t'_{max,S}$ in this geometry is

$$t'_{max,Sp} = -\frac{r_p}{v\Delta^2}(dy^2\cos(\alpha)\cos(\xi)+dx^2\sin(\alpha)\sin(\xi)) = \tag{7.94}$$

$$= -\frac{r_p}{v}\left(\cos(\epsilon)+\sin(\epsilon)\left[\frac{1}{2}\frac{\sin(2\alpha)(dy^2-dx^2)}{\Delta^2}\right]\right),$$

$$t'_{max,Sr} = \frac{r_r}{v\Delta^2}(dy^2\cos(\alpha)\sin(\xi)-dx^2\sin(\alpha)\cos(\xi)) = \tag{7.95}$$

$$= \frac{r_r}{v}\left(\sin(\epsilon)+\cos(\epsilon)\left[\frac{1}{2}\frac{\sin(2\alpha)(dy^2-dx^2)}{\Delta^2}\right]\right).$$

If we use relation $\alpha = \mathrm{atan}(v_r/v_p) + \xi$, the ratio of estimated and real velocity is

$$\frac{v_{p,CA}}{v_p} = \frac{r_p}{t'_{max,Sp}}\frac{1}{v_p} = -\frac{dx^2(v_p\tan(\xi)+v_r)^2 + dy^2(v_p - v_r\tan(\xi))^2}{dx^2\tan(\xi)(v_p\tan(\xi)+v_r) + dy^2(v_p - v_r\tan(\xi))} \tag{7.96}$$

$$\frac{v_{r,CA}}{v_r} = \frac{r_r}{t'_{max,Sr}}\frac{1}{v_r} = -\frac{dx^2(v_p\tan(\xi)+v_r)^2 + dy^2(v_p - v_r\tan(\xi))^2}{dy^2\tan(\xi)(v_r\tan(\xi)-v_p) + dx^2(v_r + v_p\tan(\xi))} \tag{7.97}$$

This reduces for the blob without tilt ($\xi = 0$) to relations

$$\frac{v_{p,CA}}{v_p} = 1 + \frac{v_r^2}{v_p^2}\frac{dx^2}{dy^2} \tag{7.98}$$

$$\frac{v_{r,CA}}{v_r} = 1 + \frac{v_p^2}{v_r^2}\frac{dy^2}{dx^2} \tag{7.99}$$

used in Sec. 6.4.

Solving equations (7.95) and (7.96) allows to determine $\epsilon$ and $v_p/v_r$, respectively, as a function of $\sin(2\alpha)(dy^2 - dx^2)/(2\Delta^2)$. Then, assumption that blobs moves in direction of one of its axes $\alpha = 0$ will close the set of equations and both components of blob velocity can be determined from three-point probe measurements. Adding further probes will not provide any aditional information in this model, because equation (7.91) with new angle $\beta$ would provide only linear combination of information provided by the two previous probes. Obtaining additional information would be possible only if non-Gaussian waveform of the blob is considered.

# Bibliography


[1] Adámek, J., Horacek, J., Rohde, V., Müller, H. W., Ionita, C., Schrittwieser, R., Mehlmann, F., Stöckel, J., Weinzettl, V., Seidl, J., Peterka, M.: ELM studies with ball-pen and Langmuir probes on ASDEX Upgrade. *36th European Physical Society Conference on Plasma Physics - Contributed Papers*:P-1.140 (2009).

[2] Adámek, J., Horacek, J., Müller, H.W., Rohde, V., Ionita, C., Schrittwieser, R., Mehlmann, F., Kurzan, B., Stöckel J., Dejarnac, R., Weinzettl, V., Seidl, J., Peterka, M., ASDEX Upgrade Team: Ball-pen probe measurements in L-mode and H-mode on ASDEX Upgrade, *Contributions to Plasma Physics*, **50**(9):854 (2010).

[3] Angus, J.R., Umansky, M., Krasheninnikov, S.I.: Effect of Drift Waves on Plasma Blob Dynamics. *Physical Review Letters*, **108**(21):1 (2012).

[4] Angus, J.R., Krasheninnikov, S.I., Umansky, M.V.: Effects of parallel electron dynamics on plasma blob transport. *Physics of Plasmas*, **19**(8):082312 (2012).

[5] Arakawa, A.: Computational Design for Long-Term Numerical Integration of the Equations of Fluid Motion: Two-Dimensional Incompressible Flow. Part I. *Journal of Computational Physics*, **135**(2):103 (1997).

[6] ASDEX Team: The H-mode on ASDEX. *Nuclear Fusion* **29**(11):1959 (1989).

[7] Atkinson, R., Houtermans, F.G.: *Zur Frage der Aufbaumöglichkeit der Elemente in Sternen*. Springer, Berlin (1929).

[8] Atzeni, S., Schiavi, A., Temporal, M.: Converging geometry Rayleigh-Taylor instability and central ignition of inertial confinement fusion targets. *Plasma Physics and Controlled Fusion*, **46**(12B):B111 (2004).

[9] Audi, G., Wapstra, A.H. and Thibault, C.: The Ame2003 atomic mass evaluation: (II). Tables, graphs and references. *Nuclear Physics A*, **729**(1):337 (2003).

[10] Balescu, R.: *Aspects of Anomalous Transport in Plasmas*. Institute of Physics Publishing, Bristol and Philadelphi (2005).

[11] Basu, R., Jessen, T., Naulin, V., Rasmussen, J.J.: Turbulent flux and the diffusion of passive tracers in electrostatic turbulence. *Physics of Plasmas*, **10**(7):2696 (2003).

[12] Bellan, P.M.: Transport inferred from consideration of particle orbits in drift turbulence. *Plasma Physics and Controlled Fusion*, **35**(2):169 (1993).

[13] Berionni, V., Gürcan, O.D.: Predator prey oscillations in a simple cascade model of drift wave turbulence. *Physics of Plasmas*, **18**(11):112301 (2011).

[14] Bian, N., Benkadda, S., Paulsen, J.-V., Garcia, O.E.: Blobs and front propagation in the scrape-off layer of magnetic confinement devices. *Physics of Plasmas*, **10**(3):671 (2003).

[15] Bisai, N., Das, A., Deshpande, S., Jha, R., Kaw, P., Sen, A., Singh, R.: Edge and scrape-off layer tokamak plasma turbulence simulation using two-field fluid model. *Physics of Plasmas*, **12**(7):072520 (2005).

[16] Bisai, N., Singh, R., Kaw, P.K.: Scrape-off layer tokamak plasma turbulence. *Physics of Plasmas*, **19**(5):052509 (2012).

[17] Biskamp, D.:*Magnetohydrodynamic turbulence*. Cambridge University Press, Cambridge (2011).

[18] Boedo, J.A.: Edge turbulence and SOL transport in tokamaks. *Journal of Nuclear Materials*, **390-391**:29 (2009).

[19] Braginskii, S. I. (1965): Transport processes in a plasma. *Reviews of Plasma Physics*, **1**:205.

[20] Brotankova, J., Adámek, J., Stöckel, J., Martines, E., Popa, G., Costin, C., Schrittwieser, R., Ionita, C., Van Oost, G., Peppel, L.: A probe-based method for measuring the transport coefficient in the tokamak edge region. *Czechoslovak Journal of Physics*, **56**(12):1321 (2006).

[21] Brotankova, J., Stöckel, J., Hron, M., Ďuran, I., Horacek, J.: Detailed Measurements of Poloidal Velocity of Density and Floating Potential Fluctuations in the Edge Plasma of the CASTOR Tokamak. *WDS08 Proceedings of Contributed Papers: Part II - Physics of Plasmas and Ionized Media* (eds. J. Safrankova and J. Pavlu), Prague, Matfyzpress (2008).

[22] Brotankova, J., Stöckel, J., Horacek, J., Seidl, J., Duran, I., Hron, M., Oost, G.V.: Measurement of sheared flows in the edge plasma of the CASTOR tokamak. *Plasma Physics Reports*, **35**(11):980 (2009).

[23] Brotankova, J.: Study of high temperature plasma in tokamak-like experimental devices. *PhD thesis*, Charles University in Prague (2006).

[24] Camargo, S.J., Biskamp, D., Scott, B.D.: Resistive drift-wave turbulence. *Physics of Plasmas*, **2**(1):48 (1995).

[25] Chandrasekhar, S.: Stochastic problems in physics and astronomy. *Reviews of Modern Physics*, **15**:1 (1943)

[26] Connor, J.W.: Tokamak turbulence-electrostatic or magnetic? *Plasma physics and controlled fusion* **35B**:293 (1993).

[27] Connor, J.W., Wilson, H.R.: Survey of theories of anomalous transport. *Plasma physics and controlled fusion*, **36**(5):719 (1994).

[28] Conway, G. D.: Turbulence measurements in fusion plasmas. *Plasma Physics and Controlled Fusion*, **50**(12):124026 (2008).

[29] Chankin, A.V., Coster, D.P., Corrigan, G., Erents, S.K., Fundamenski, W., Kallenbach, A., Lackner, K., Neuhauser, J., Pitts, R. the ASDEX Upgrade Team and JET-EFDA Contributors: Fluid code simulations of radial electric field in the scrape-off layer of JET. *Plasma Physics and Controlled Fusion*, **51**(6):065022 (2009).

[30] Chen, F.F. *Introduction to Plasma Physics and Controlled Fusion*. Plenum-Press, New York, London (1984).

[31] D'Ippolito, D.A., Myra, J.R., Zweben, S.J.: Convective transport by intermittent blob-filaments: Comparison of theory and experiment. *Physics of Plasmas*, **18**(6):060501 (2011).

[32] Diamond, P.H., Itoh, S.-I., Itoh, K., Hahm, T.S.: Zonal flows in plasma - a review. *Plasma Physics and Controlled Fusion*, **47**(5):R35 (2005).

[33] Endler, M., Niedermeyer, H., Giannone, L., Holzhauer, E., Rudyj, A., Theimer, G., Tsois, N.: Measurements and modelling of electrostatic fluctuations in the scrape-off layer of ASDEX. *Nuclear Fusion*, **35**(11):1307 (1995).

[34] Estrada, T., Hidalgo, C., Happel, T., Diamond, P.: Spatiotemporal Structure of the Interaction between Turbulence and Flows at the L-H Transition in a Toroidal Plasma. *Physical Review Letters*, **107**(24):3 (2011).

[35] Farina, D., Pozzoli, R., Ryutov, D.D.: Effect of the magnetic field geometry on the flute-like perturbations near the divertor X point. *Nuclear Fusion* **33**(9):1315 (1993).

[36] Frisch, U.: *Turbulence: The Legacy of A. N. Kolmogorov*. Cambridge University Press, Cambridge, (1995).

[37] Fuchs V., Gunn J. P., Petržílka V., Horacek J., Seidl J., Ekedahl A., Goniche M., Hillairet J.: Landau damping of the LH grill spectrum by tokamak edge electrons. *AIP Conference proceedings*, **1187**:383 (2009).

[38] Fuchs V., Gunn J., Petržílka V., Horáček J., Seidl J., Ekedahl A., Goniche M., Hillairet J.: A note on the Radial Extent of LH wave – tokamak SOL interaction. *36th European Physical Society Conference on Plasma Physics - Contributed Papers*:P-5.201 (2009).

[39] Fundamenski, W., Garcia, O. E., Naulin, V., Pitts, R. A., Nielsen, A. H., Rasmussen, J. J., Horacek, J., Graves, J.P.: Dissipative processes in interchange driven scrape-off layer turbulence. *Nuclear Fusion*, **47**(5):417 (2007).

[40] Fundamenski, W., Militello, F., Moulton, D., McDonald, D.C.: A new model of the L-H transition in tokamaks. *Nuclear Fusion*, **52**(6):062003 (2012).

[41] Garcia, O. E.: Two-field transport models for magnetized plasmas. *Journal of Plasma Physics*, **65**(02):81 (2001).

[42] Garcia, O.E.: Collective motions in non-uniformly magnetized plasmas. *European Journal of Physics*, **24**(4):331 (2003).

[43] Garcia, O.E., Naulin, V., Nielsen, A.H., Rasmussen, J.J.: Computations of Intermittent Transport in Scrape-Off Layer Plasmas. *Physical Review Letters*, **92**(16):165003 (2004).

[44] Garcia, O.E., Naulin, V., Nielsen, A.H., Rasmussen, J.J.: Turbulence and intermittent transport at the boundary of magnetized plasmas. *Physics of Plasmas*, **12**(6):062309 (2005).

[45] Garcia, O.E., Bian, N.H.: Shear dispersion and turbulence decorrelation by differential rotation. *Physics of Plasmas*, **12**(1):014503 (2005).

[46] Garcia, O. E., Horacek, J., Pitts, R. A., Nielsen, A. H., Fundamenski, W., Graves, J. P., Naulin, V., Rasmussen, J.J.: Interchange turbulence in the TCV scrape-off layer. *Plasma Physics and Controlled Fusion*, **48**(1):L1 (2006).

[47] Garcia, O.E., Bian, N.H., Fundamenski, W.: Radial interchange motions of plasma filaments. *Physics of Plasmas*, **13**(8):082309 (2006).

[48] Garcia, O.E., Naulin, V., Nielsen, A.H., Rasmussen, J.J.: Turbulence simulations of blob formation and radial propagation in toroidally magnetized plasmas. *Physica Scripta*, **T122**:89 (2006).

[49] Garcia, O.E., Bian, N.H., Naulin, V., Nielsen, A.H., Rasmussen, J.J.: Two-dimensional convection and interchange motions in fluids and magnetized plasmas. *Physica Scripta*, **T122**:104 (2006).

[50] Garcia, O.E., Horacek, J., Pitts, R.A., Nielsen, A.H., Fundamenski, W., Naulin, V., Rasmussen, J.J.: Fluctuations and transport in the TCV scrape-off layer. *Nuclear Fusion*, **47**(7):667 (2007).

[51] Garcia, O.E., Pitts, R., Horacek, J., Nielsen, A.H., Fundamenski, W., Graves, J.P., Naulin, V., Rasmussen, J.J.: Turbulent transport in the TCV SOL. *Journal of Nuclear Materials*, **363-365**:575 (2007).

[52] Garcia, O.E., Pitts, R.A., Horacek, J., Madsen, J., Naulin, V., Nielsen, A.H., Rasmussen, J.J.: Collisionality dependent transport in TCV SOL plasmas. *Plasma Physics and Controlled Fusion*, **49**(12B):B47 (2007).

[53] Garcia, O.E.: Blob Transport in the Plasma Edge: a Review. *Plasma and Fusion Research*, **4**:019 (2009).

[54] Golant, V.E., Zhilinsky, A.P., Sakharov, I.E., Brown, S.C.: *Fundamentals of plasma physics*. John Wiley & sons, New York (1980).

[55] Goodall, D.H.J.: High speed cine film studies of plasma behaviour and plasma surface interactions in tokamaks. *Journal of Nuclear Materials*, **111-112**:11 (1982).

[56] Graves, J.P., Horacek, J., Pitts, R., Hopcraft, K.I.: Self-similar density turbulence in the TCV tokamak scrape-off layer. *Plasma Physics and Controlled Fusion* **47**(3):L1 (2005).

[57] Gruber, O. (2007). Overview of ASDEX Upgrade results. *Nuclear Fusion*, **47**(10):S622 (2007).

[58] Grulke, O., Terry, J.L., LaBombard, B., Zweben, S.J.: Radially propagating fluctuation structures in the scrape-off layer of Alcator C-Mod. *Physics of Plasmas*, **13**(1):012306 (2006).

[59] Gunn, J.P., Boucher, C., Dionne, M., Ďuran, I., Fuchs, V., Loarer, T., Nanobashvili, I., Pánek, R., Pascal, J.-Y., Saint-Laurent, F., Stöckel, J., Van Rompuy, T., Zagorski, R., Adámek, J., Bucalossi, J., Dejarnac, R., Devynck, P., Hertout, P., Hron, M., Lebrun, G., Moreau, P., Rimini, F., Sarkissian, A., Van Oost, G.: Evidence for a poloidally localized enhancement of radial transport in the scrape-off layer of the Tore Supra tokamak. *Journal of Nuclear Materials*, **363-365**:484 (2007).

[60] Gustafson, K., Ricci, P.: Lévy walk description of suprathermal ion transport. *Physics of Plasmas*, **19**(3):032304 (2012).

[61] Heines, M.G.: A review of the dense Z-pinch. *Plasma Physics and Controlled Fusion*, **53**(9):093001 (2001).

[62] Hasegawa, A., Mima, K.: Stationary Spectrum of Strong Turbulence in Magnetized Nonuniform Plasma. *Physical Review Letters*, **39**(4):205 (1977).

[63] Hasegawa, A., Wakatani, M.: Plasma Edge Turbulence. *Physical Review Letters* **50**(9): 682 (1983).

[64] Havlíčková, E.: Computer modelling of plasma processes and transport for selected applications. *PhD thesis*, Charles University in Prague (2009).

[65] Havlíčková, E., Fundamenski, W., Naulin, V., Nielsen, A.H., Zagórski, R., Seidl, J., Horacek, J.: Steady-state and time-dependent modelling of parallel transport in the scrape-off layer. *Plasma Physics and Controlled Fusion*, **53**(6):065004 (2011).

[66] Havlíčková, E., Fundamenski, W., Naulin, V., Nielsen, A.H., Wiesen, S., Horacek J., Seidl, J.: The effect of plasma fluctuations on parallel transport parameters in the SOL. *Journal of Nuclear Materials*, **415**:S471.

[67] Hazeltine, R.D., Meiss, J.D.: *Plasma confinement*. Dover Publications, Inc., New York (2003).

[68] Helander, P., Sigmar, D.J.: *Collisional Transport in Magnetized Plasmas*. Cambridge University Press, Cambridge (2002).

[69] Hidalgo, C., Gonc, B., Hron, M., Loarte, A., Erents, K., Matthews, G.F., Pitts, R.: Experimental evidence of fluctuations and flows near marginal stability and dynamical interplay between gradients and transport in the JET plasma boundary region. *Journal of Nuclear Materials*, **316**:863.

[70] Hinton, F.L., Hazeltine, R.D.: Theory of plasma transport in toroidal confinement systems. *Reviews of Modern Physics* **48**(2):239 (1976).

[71] Horacek, J., Pitts, R.A., Stangeby, P.C., Batishchev, O., Loarte, A.: Predicted effects of parallel temperature gradients on the overestimation of TCV divertor target Langmuir probe Te measurements. *Journal of Nuclear Materials*, **313-316**:931 (2003).

[72] Horacek, J.: Measurement of edge electrostatic turbulence in the TCV tokamak plasma boundary. *PhD thesis*, Ecole Polytechnique Fédérale de Lausanne (2006).

[73] Horacek, J., Nielsen, A.H., Pitts, R.A., Zajac, J., Seidl, J., Garcia, O.E., Gulejova, B.: Fast temperature fluctuation measurements in SOL of tokamak TCV. *Book of Abstracts of the 13þEU-US Transport Taks Force Workshop*, Copenhagen (2008).

[74] Horacek, J., Adámek, J., Müller, H. W., Seidl, J., Nielsen, A. H., Rohde, V., Mehlmann, F., Ionita, C., Havlíčková, E.: Interpretation of fast measurements of plasma potential, temperature and density in SOL of ASDEX Upgrade. *Nuclear Fusion*, **50**(10):105001 (2010).

[75] Horacek, J., Adámek, J., Seidl, J., Bílková, P., Stöckel, J., Naydenkova, D., Šesták, D., Dejarnac, R.: *Investigation of turbulent plasma boundary of tokamak COMPASS using two deeply-reciprocating probes, interpreted by numerical models*. Grant of the Czech Science Foundation nr. GAP205122327.

[76] Huba, J.D.: *NRL Plasma Formulary*, Naval Research Laboratory, Washington DC (2011).

[77] Hutchinson, I.H.: A fluid theory of ion collection by probes in strong magnetic fields with plasma flow. *Physics of Fluids*, **30**(12):3777 (1987).

[78] Itoh, S.-I., Itoh, K.: Model of the H-mode in tokamaks. *Nuclear Fusion*, **29**(6):1031 (1989).

[79] Jardin, S.: *Computational Methods in Plasma Physics*. CRC Press, Boca Raton (2010).

[80] Komm, M.: Studies of tokamak edge plasma and its interaction with the first wall. *PhD thesis*, Charles University in Prague (2011).

[81] Komm, M., Adamek, J., Pekarek, Z., Panek, R.: Transport of electrons in the tunnel of an ion sensitive probe. *Plasma Physics and Controlled Fusion*, **53**(1):015005 (2011).

[82] Korsholm, S.B., Michelsen, P.K., Naulin, V., Rasmussen, J.J., Garcia, L., Carreras, B.A., Lynch, V.E.: Reynolds stress and shear flow generation. *Plasma physics and* **43**(10):1377 (2001).

[83] Korsholm, S.B.: Coherent structures and transport in drift wave plasma turbulence. *PhD thesis*, Technical University in Denmark (2008).

[84] Kovařík, K., Ďuran, I., Stöckel, J., Brotánková, J., **Seidl, J.**, Šesták, D., Spolaore, M., Martines, E., Vianello, N., Hidalgo, C., Pedrosa, M. A.: U-probe for the COMPASS tokamak. *WDS11 Proceedings of Contributed Papers: Part II - Physics of Plasmas and Ionized Media* (eds. J. Safrankova and J. Pavlu), Prague, Matfyzpress (2011).

[85] Krasheninnikov, S.I.: On scrape off layer plasma transport. *Physical Letters A*, **283**(5-6):368 (2001).

[86] Yu, G.Q., Krasheninnikov, S.I., Guzdar, P.N.: Two-dimensional modelling of blob dynamics in tokamak edge plasmas. *Physics of Plasmas*, **13**(4):042508 (2006).

[87] Krasheninnikov, S.I., Smolyakov, A.I.: Dynamics and generation mechanisms of mesoscale structures in tokamak edge plasmas. *Physics of Plasmas*, **15**(5):055909 (2008).

[88] Krasheninnikov, S.I., D'Ippolito, D.A., Myra, J.R.: Recent theoretical progress in understanding coherent structures in edge and SOL turbulence. *Journal of Plasma Physics*, **74**(05):679 (2008).

[89] Krlin, L., Stöckel, J., Svoboda, V.: Stochastic (ExB) diffusion of ions in a spatially periodical potential field. *Plasma Physics and Controlled Fusion*, **41**(3):339 (1999).

[90] Krlin, L., Paprok, R., Svoboda, V.: Modelling of Lévy walk kinetics of charged particles in edge electrostatic turbulence in tokamaks. *The European Physical Journal D*, **48**(1):95 (2008).

[91] Krlin, L., Paprok R., Seidl J., Panek R., Stockel J., Petrzilka V.: Anomalous Diffusion of Particles in Edge Plasma Turbulence in Tokamaks and Random and Lévy Walk Distributions. In: Skogseid A., Fasano V., eds. *Statistical Mechanics and Random Walks: Principles, Processes and Applications*. Nova Science Publisher, Inc., New York (2012), pp. 65.

[92] Lawson, J.D.: Some Criteria for a Power Producing Thermonuclear Reactor. *Proceedings of the Physical Society B*, **70**(1):6 (1957).

[93] Lipschultz, B., Bonnin, X., Counsell, G., Kallenbach, A., Kukushkin, A., Krieger, K., Leonard, A., et al.: Plasma–surface interaction, scrape-off layer and divertor physics: implications for ITER. *Nuclear Fusion*, **47**(9):1189 (2007).

[94] Mahdizadeh, N., Greiner, F., Ramisch, M., Stroth, U., Guttenfelder, W., Lechte, C., Rahbarnia, K.: Comparison of Langmuir and emissive probes as diagnostics for turbulence studies in the low-temperature plasma of the torsatron TJ-K. *Plasma Physics and Controlled Fusion*, **47**(4):569 (2005).

[95] Manfredi, G., Dendy, R. O.: Transport properties of energetic particles in a turbulent electrostatic field. *Physics of Plasmas*, **4**(3):628 (1997).

[96] Manz, P., Ramisch, M., Stroth, U.: Long-range correlations induced by the self-regulation of zonal flows and drift-wave turbulence. *Physical Review E*, **82**(5):056403 (2010).

[97] Maqueda, R.J., Stotler, D.P., Zweben, S.J.: Intermittency in the scrape-off layer of the National Spherical Torus Experiment during H-mode confinement. *Journal of Nuclear Materials*, **415**(1):S459 (2011).

[98] Martines, E., Hron, M., Stöckel, J.: Coherent structures in the edge turbulence of the CASTOR tokamak. *Plasma Physics and Controlled Fusion*, **44**:351 (2002).

[99] Martines, E., Vianello, N., Sundkvist, D., Spolaore, M., Zuin, M., Agostini, M., Antoni, V., Cavazzana, R., Ionita, C., Maraschek, M., Mehlmann, F., Müller, H.W., Naulin, V., Rasmussen, J.J., Rohde, V., Scarin, P., Schrittwieser, R., Serianni, G., Spada, E.: Current filaments in turbulent magnetized plasmas. *Plasma Physics and Controlled Fusion*, **51**(12):124053 (2009).

[100] Matthews, G.F.: Tokamak plasma diagnostic by electrical probes. *Plasma Physics and Controlled Fusion*, **36**():1595 (1994).

[101] Menard, J.E., Bromberg, L., Brown, T., Burgess, T., Dix, D., El-Guebaly, L., Gerrity, T., Goldston, R.J., Hawryluk, R.J., Kastner, R., Kessel, C., Malang, S., Minervini, J., Neilson, G.H., Neumeyer, C.L., Prager, S., Sawan, M., Sheffield, J., Sternlieb, A., Waganer, L., Whyte, D., Zarnstorff, M.: Prospects for pilot plants based on the tokamak, spehrical tokamak and stellarator. *Nuclear Fusion*, **51**(10):103014 (2011).

[102] Mlynar, J., Petržílka, V., Duran, I., Odstrcil, M., Bilkova, P., Horacek, J., Hron M., Janky F., Kovarik, K., Seidl J., JET EFDA contributors: Participation of IPP Prague in the international fusion energy research at Joint European Torus JET. *Proceedings of the 17th conference of Czech and Slovak Physicist*, Žilina (2011).

[103] Monk, D., Loarte, A., Chankin, A., Clement, S., Davies, J., Ehrenberg, K., Lingertat, J., Matthews, F., Stamp, F., Stangeby, C.: Interpretation of ion flux and electron temperature profiles at the JET divertor target during high recycling and detached discharges. *Journal of Nuclear Materials*, **241-243**(1):396 (1997).

[104] Müller, H.W., Adamek, J., Cavazzana, R., Conway, G.D., Fuchs, C., Gunn, J.P., Herrmann, A., Horacek, J., Ionita, C., Kallenbach, A., Kočan, M., Maraschek, M., Maszl, C., Mehlmann, F., Nold, B., Peterka, M., Rohde, V., Schweinzer, J., Schrittwieser, R., Vianello, N., Wolfrum, E., Zuin, M.: Latest investigations on fluctuations, ELM filaments and turbulent transport in the SOL of ASDEX Upgrade. *Nuclear Fusion*, **51**(7):073023 (2011).

[105] Myra, J.R., D'Ippolito, D.A.: Edge instability regimes with applications to blob transport and the quasicoherent mode. *Physics of Plasmas*, **12**(9):092511 (2005).

[106] Myra, J.R., Russell, D.A., D'Ippolito, D.A.: Collisionality and magnetic geometry effects on tokamak edge turbulent transport. I. A two-region model with application to blobs. *Physics of Plasmas*, **13**(11):112502 (2006).

[107] Myra, J.R., Russell, D.A., D'Ippolito, D.A.: Transport of perpendicular edge momentum by drift-interchange turbulence and blobs. *Physics of Plasmas*, **15**(3):032304 (2008).

[108] Myra, J.R., Davis, W.M., D'Ippolito, D.A., LaBombard, B., Russell, D.A., Terry, J.L., Zweben, S.J.: Edge Sheared Flows and Blob Dynamics. *Contributed Papers to the 24th IAEA Fusion Energy Conference*:THD/P4-23 (2012).

[109] Naulin, V., Nielsen, A.H., Rasmussen, J.J.: Dispersion of ideal particles in a two-dimensional model of electrostatic turbulence. *Physics of Plasmas*, **6**(12):4575 (1999).

[110] Naulin, V., Kendl, A., Garcia, O.E., Nielsen, A.H., Rasmussen, J.J.: Shear flow generation and energetics in electromagnetic turbulence. *Physics of Plasmas*, **12**(5):052515 (2005).

[111] Naulin, V., Garcia, O.E., Priego, M., Rasmussen, J.J.: The application of passive tracers for investigating transport in plasma turbulence. *Physica Scripta*, **T122**:129 (2006).

[112] Naulin, V., Fundamenski, W., Havlíčková, E., Maszl, Chr., Xu, G., Nielsen, A.H., Rasmussen, J.J., Schrittwieser, R., Horacek, J., Seidl, J., JET-EFDA contributors: Progress in Turbulence Modeling JET SOL and edge phenomena. *Contributed Papers to the 23rd IAEA Fusion Energy Conference*:THD/P3-03 (2010).

[113] Naulin, V., Xu, G., Vianello, N., Madsen, J., Schrittwieser, R., Ionita, C., Maszl, C., Mehlmann, F., Yan, N., Nielsen, A.H., Rasmussen, J.J.: Profiles and Fluctuations in Edge and SOL Turbulence. *Contributions to Plasma Physics*, **52**(5-6):391 (2012). doi:10.1002/ctpp.201210022

[114] Nielsen, A.H., Seidl, J., Horacek, J., Madsen, J., Naulin, V., Rasmussen, J.J.: Investigations of Parallel Dynamics in the ESEL Model. Poster at 13th European Fusion Theory Conference, Riga (2009).

[115] Nielsen, A.H., Seidl, J., Horacek, J., Madsen, J., Naulin, V., Rasmussen, J.J., Garcia, O.E.: Investigation into parallel dynamics in the ESEL model. *To be published in 2013.*

[116] Pánek, R., Krlín, L., Tendler, M., Tskhakaya, D., Kuhn, S., Svoboda, V., Klíma, R., Pavlo, P., Stöckel, J., Petržílka, V.: Anomalous Ion Diffusion and Radial-Electric-Field Generation in a Turbulent Edge Plasma Potential Weakly Correlated in Time and Space. *Physica Scripta*, **72**(4):327 (2005).

[117] Papřok, R.: Anomální difúze iontú v modelech turbulentního okrajového plazmatu tokamaku. *Msc thesis*, Charles University in Prague (2007).

[118] Parks, B., Sessions, W.D., Baylor, L.R.: Radial displacement of pellet ablation material in tokamaks due to the grad-B effect. *Physics of Plasmas*, **7**(5):1968 (2000)

[119] Pégourié, Brosset, C., Tsitrone, E., Beauté, A., *et. al*: Overview of the deuterium inventory campaign in Tore Supra: Operational conditions and particle balance. *Journal of Nuclear Materials*, **390-391**:550 (2009).

[120] Pitts, R.A., Coad, J.P., Coster, D.P., Federici, G., Fundamenski, W., Horacek, J., Krieger, K., Kukushkin, A., Likonen, J., Matthews, G.F., Rubel, M., Strachan, J.D.: Material erosion and migration in tokamaks. *Plasma Physics and Controlled Fusion*, **47**(12B):B303 (2005).

[121] Popov, T.K., Ivanova, P., Stockel, J., Dejarnac, R.: Electron energy distribution function, plasma potential and electron density measured by Langmuir probe in tokamak edge plasma. *Plasma Physics and Controlled Fusion*, **51**(6):065014 (2009).

[122] Priego, M., Garcia, O.E., Naulin, V., Rasmussen, J.J: Anomalous diffusion, clustering, and pinch of impurities in plasma edge turbulence. *Physics of Plasmas*, **12**(6):062312 (2005).

[123] Rakhlin, D. A: Enhanced diffusion in smoothly modulated superlattices. *Physical Review E*, **63**(1):1 (2000).

[124] Rozhansky, V., Veselova, I., Voskoboynikov, S.: Evolution and stratification of a plasma cloud surrounding a pellet. *Plasma Physics and Controlled Fusion*, **37**(4):399 (1995).

[125] Sarazin, Y., Ghendrih, P., Attuel, G., Clement, C., Garbet, X., Grandgirard, V., Ottaviani, M., Benkadda, S., Beyer, P., Bian, N.: Theoretical understanding of turbulent transport in the SOL. *Journal of Nuclear Materials*, **313-316**:796 (2003).

[126] Scott, B.D.: Modelling Toroidal Curvature in Slab Coordinates. *http://home.rzg.mpg.de/ bds/fusion.html*

[127] Scott, B.D.: Global consistency for thin flux tube treatments of toroidal geometry. *Physics of Plasmas*, **5**(6):2334 (1998).

[128] Scott, B.D.: The nonlinear drift wave instability and its role in tokamak edge turbulence. *New Journal of Physics*, **4**:52 (2002).

[129] Scott, B.D.: Free-energy conservation in local gyrofluid models. *Physics of Plasmas*, **12**(10):102307 (2005).

[130] Scott, B.D.: Drift wave versus interchange turbulence in tokamak geometry: Linear versus nonlinear mode structure. *Physics of Plasmas*, **12**(6):062314 (2005).

[131] Scott, B.D.: Coordinate Systems for Tokamak Geometry. *http://home.rzg.mpg.de/ bds/lectures/gotit/day4.pdf*. Scott, B.D.: Basics of turbulence computation for magnetically confined plasmas. *http://home.rzg.mpg.de/ bds/lectures/iter072.pdf*

[132] Seidl, J., Krlín, L., Pánek, R., Pavlo, P., Stöckel, J., Svoboda, V.: Simulations of anomalous ion diffusion in experimentally measured turbulent potential. *The European Physical Journal D*, **54**(2):399 (2009).

[133] Seidl, J., Krlin, L.: Interchange Driven Turbulence and Bellan Instability in Tokamak Scrape-off Layer. *WDS09 Proceedings of Contributed Papers: Part III - Physics* (eds. J. Safrankova and J. Pavlu), Prague, Matfyzpress (2009).

[134] Seidl, J., Krlín, L.: Impurity Dynamics in Turbulent Plasma in Tokamak Scrape-off Layer. *WDS10 Proceedings of Contributed Papers: Part III - Physics* (eds. J. Safrankova and J. Pavlu), Prague, Matfyzpress (2010).

[135] Seidl, J., Krlín, L., Papřok, R.: Effects of finite Larmor radius on transport of impurities in Hasegawa-Wakatani model. *To be published in 2013.*

[136] Shafranov, V.D., Bondarenko, B.D., Goncharov, G.A.: On the history of the research into controlled thermonuclear fusion. *Physics-Uspekhi*, **44**(8):835 (2001).

[137] Schirmer, J., Conway, G.D., Zohm, H., Suttrop, W.: The radial electric field and its associated shear in the ASDEX Upgrade tokamak. *Nuclear Fusion*, **46**(9):S780 (2006).

[138] Shlesinger, M.F., Zaslavsky, G.M., Klafter, J.: Strange kinetics. *Nature*, **363**:31 (1993).

[139] Shukla, P.K., Yu,M.Y., Rahman, H.U., Spatschek, K.H.: Nonlinear convective motion in plasmas. *Physical Reports*, **105**(4-5):227 (1984).

[140] Shukla, P.K., Murtaza, G., Weiland, J.: Electron-temperature gradient-driven drift waves and anomalous electron energy transport. *Journal of Plasma Physics*, **44**(3):393 (1990).

[141] Schrittwieser, R., Adámek, J., Balan, P., Hron, M., Ionita, C., Jakubka, K., Kryška, L., Martines, E., Stöckel, J., Tichý, M., Van Oost, G.: Measurements with an emissive probe in the CASTOR tokamak. *Plasma Physics and Controlled Fusion*, **44**(5):567 (2002).

[142] Snyder, P.B., Wilson, H.R., Ferron, J.R., Lao, L.L., Leonard, A.W., Mossessian, D., Murakami, M., Osborne, T.H., Turnbull, A.D., Xu, X.Q.: ELMs and constraints on the H-mode pedestal: peeling–ballooning stability calculation and comparison with experiment. *Nuclear Fusion*, **44**(2):320 (2004).

[143] Spolaore, M., Vianello, N., Agostini, M., Cavazzana, R., Martines, E., Scarin, P., Serianni, G., Spada, E., Zuin, M., Antoni, V.: Direct Measurement of Current Filament Structures in a Magnetic-Confinement Fusion Device. *Physical Review Letters*, **102**(16):1 (2009).

[144] Spolaore, M., Vianello, N., Agostini, M., Cavazzana, R., Martines, E., Serianni, G., Scarin, P., Spada, E., Zuin, M., Antoni, M.: Magnetic and electrostatic structures measured in the edge region of the RFX-mod experiment. *Journal of Nuclear Materials* **390-391**:448 (2009).

[145] Stangeby, P., McCracken, G.: Plasma boundary phenomena in tokamaks. *Nuclear Fusion*, **30**(7):1225 (1990).

[146] Stangeby, P.C.: *The plasma boundary of magnetic fusion devices.* IOP Publishing, Bristol (2000).

[147] Stöckel, J., Adámek, J., Balan, P., Bilyk, O., Brotankova, J., Dejarnac, R., Devynck, P., Ďuran, I., Gunn, J.P., Hron, M., Horacek, J., Ionita, C., Kocan, M., Martines, E., Panek, R., Peleman, P., Schrittwieser, R., Oost, G. Van, Zacek, F.: Advanced probes for edge plasma diagnostics on the CASTOR tokamak. *Journal of Physics: Conference Series*, **63**:012001 (2007).

[148] Stoica, P., Moses, R.L.:*Introduction to Spectral Analysis*, Prentice-Hall, New Jersey (1997).

[149] Umansky, M.V., Krasheninnikov, S.I., LaBombard, B., Terry, J.L.: Comments on particle and energy balance in the edge plasma of Alcator C-Mod. *Physics of Plasmas* **5**(9):3373 (1998).

[150] Vianello, N., Naulin, V., Schrittwieser, R., Müller, H., Zuin, M., Ionita, C., Rasmussen, J.J., Mehlmann, F., Rohde, V., Cavazzana, R., Maraschek, M.: Direct Observation of Current in Type-I Edge-Localized-Mode Filaments on the ASDEX Upgrade Tokamak. *Physical Review Letters*, **106**(12):1 (2011).

[151] Vayakis, G.: Anomalous Transport in the Tokamak Edge. *PhD thesis*, University of Oxford (1991)

[152] Vondráček, P.: Study of edge plasma physics of tokamak COMPASS by means of two reciprocating probes. *MsC thesis (in Czech)*, Czech Technical University in Prague (2012).

[153] Weiland, J.: *Collective Modes in Inhomogeneous Plasma: Kinetic and Advanced Fluid Theory*, Institute of Physics Publishing, Bristol and Philadelphia (2000).

[154] Wesson, J.A.: *Tokamaks*. Clarendon Press, Oxford (2004).

[155] Xu, G.S., Naulin, V., Fundamenski, W., Hidalgo, C., Alonso, J.A., Silva, C., Goncalves, B., Nielsen, A.H., Rasmussen, J.J., Krasheninnikov, S.I., Wan, B.N., Stamp, M.: Blob/hole formation and zonal-flow generation in the edge plasma of the JET tokamak. *Nuclear Fusion*, **49**(9):092002 (2009).

[156] Yamazaki, K., Oishi, T., Mori, K.: Environmental and economic assessments of magnetic and inertial fusion energy reactors. *Nuclear Fusion*, **51**(10):103004 (2011).

[157] Yu, G.Q., Krasheninnikov, S.I., Guzdar, P.N.: Two-dimensional modelling of blob dynamics in tokamak edge plasmas. *Physics of Plasmas*, **13**(4):042508 (2006).

[158] Zeiler, A., Drake, J.F., Biskamp, D.: Electron temperature fluctuations in drift-resistive ballooning turbulence . *Physics of Plasmas*, **4**(4):991 (1997)

[159] Zimbardo, G., Greco, A., Veltri, P.: Superballistic transport in tearing driven magnetic turbulence. *Physics of Plasmas*, **7**(4):1071 (2000).

# List of used abbreviations

| | | |
|---|---|---|
| BPP | ball-pen probe | Advanced concept of electrostatic probe specialized on measurement of plasma potential (see Sec. 6.1). |
| CA | conditional average | See Eq. (3.22). |
| ELM | edge localized mode | Large transport event occurring in tokamak. edge due to collapse of pedestal. |
| H-W model | Hasegawa-Wakatani model | Basic model of drift-wave turbulence. Introduced in Sec. 7.6.1. |
| LCFS | last closed flux surface | Magnetic surface separating regions of closed and open field lines. |
| PDF | probability distribution function | |
| PSD | power spectral density | |
| RFP | reversed field pinch | |
| SOL | scrape-off layer | Region of open field lines at the boundary of tokamak plasmas. From region of close field lines it is separated by magnetic separatrix (last closed flux surface). |
| VSL | velocity shear layer | |